Grazing Incidence X-ray Scattering from Magnetic Thin Films and Nanostructures

EASTWOOD, DAVID,SAMUEL

Grazing Incidence X-ray Scattering from Magnetic Thin Films and Nanostructures

David Samuel Eastwood

A thesis submitted in partial fulfilment of the requirements

for the degree of Doctor of Philosophy

University of Durham

2009

Abstract

Grazing incidence scattering of synchrotron x-rays has been used to characterize the structure of magnetic thin films and periodic nanostructures. The combined metal and metal oxide films have been chosen to clarify the effects of growth processing techniques in technologically important magnetic and magnetoresistive thin film materials, and have particular relevance to the magnetic tunnel junction (MTJ) class of magnetic sensor.

Co/Al_2O_3 thin films and Co/MgO multilayer thin films have been characterized using x-ray reflectivity and diffuse scatter analysis to explain how preparatory oxidation of the lower ferromagnet in an MTJ can reduce Néel interlayer coupling and improve the consistency of magnetoresistance. Measurements reveal differing effects for Al_2O_3 and MgO tunnel barrier materials. In Co/Al_2O_3 systems, preoxidation is found to reduce significantly chemical interdiffusion at the interface between the two layers, implying a more uniform oxidation of the barrier layer. In Co/MgO multilayers, an increased in-plane correlation length of the inherited interface roughness is seen after preoxidation. This implies that preoxidation suppresses the short wavelength undulations on both sides of the tunnel barrier that cause Néel coupling.

Grazing incidence in-plane diffraction measurements on epitaxial Fe/MgO/Fe [001] and Fe/Au/MgO/Fe [001] films during annealing to 600 K have shown that, in both cases, the MgO lattice is initially strained towards being commensurate with the iron and gold layers, but relaxes after annealing towards a typical bulk MgO lattice. The iron and gold layers display linear thermal expansion at rates consistent with the bulk material. These in-plane lattice measurements demonstrate how the strain and strain dispersion in an epitaxial MgO barrier layer can be relieved under controlled annealing conditions.

Finally, patterned thin film surfaces with submicron periodic symmetries have been studied by grazing incidence x-ray scattering. A novel semi-kinematical theory has been developed into a numerical algorithm capable of simulating the scatter from a wide range of arbitrary and disordered nanoscale arrays. This has allowed key structural parameters including array periodicity, symmetry and array coherence lengths to be extracted from experimental data.

Declaration

Unless explicitly stated otherwise, the work presented in this thesis is solely that of the author and has not been submitted for examination for other degree at any University.

Synchrotron experiments were coordinated by the author, but were performed with the assistance of several team members. The measurements in chapter 4 were made at the XMaS beamline of the European Synchrotron Radiation Facility by the author with Professor Brian Tanner, Dr Alexander Pym and Dr Thomas Hase, and at the I-16 beamline at Diamond by the author and Dr Del Atkinson, Alexis Ridler, Dr Thomas Hase, Professor Brian Tanner and Dr Alexander Pym. In chapter 5 measurements were made at XMaS by the author with Professor Brian Tanner and Dr Thomas Hase and at I-16 by the author, Professor Brian Tanner, Dr Thomas Hase and Dr Madjid Abes. Chapter 6 contains measurement taken at XMaS by the author, Professor Brian Tanner, Dr Thomas Hase, Dr Alexander Pym and Dr Del Atkinson.

The samples examined in chapter 4 were provided by Dr Bill Egelhoff Jr and colleagues from the Metallurgy Division in the Materials Science and Engineering Laboratory at NIST in Gaithersburg, Maryland, United States. The samples studied in chapter 5 were produced by Dr Mannan Ali in the Department of Physics and Astronomy at the University of Leeds. The lithographic arrays studied in chapter 6 were fabricated in Durham by the author with the support of Dr Del Atkinson. The self-assembled arrays in chapter 6 were made by Professor Manfred Albrecht and colleagues at the Universität Konstanz in Germany. Earlier experimental measurements from the sample shown in section 6.5.2 of chapter 6 were presented in a Master in Science project report [1].

Table of Contents

List of Figures

List of Tables

List of Publications

Chapter 4 contains work partially summarized in the following journal article:

Eastwood, D.S., Egelhoff, W.F., and Tanner, B.K., 'The role of preoxidation on the interface structure of Co/MgO multilayers', *IEEE Transactions on Magnetics* **44** (2008) 3594-3596.

Chapter 6 contains work partially summarized in the following journal article:

Eastwood, D.S., Hase, T.P.A., van Kampen, M., Bručas, R., Hjörvarsson, B., Atkinson, D., and Tanner, B.K., 'X-ray scattering from two-dimensionally patterned magnetic thin film nanoscale arrays', *Superlattices and Microstructures* **41** (2007) 163-167.

Work from chapter 6 was also published as:

Eastwood, D.S., Hase, T.P.A., van Kampen, M., Bručas, R., Hjörvarsson, B., Atkinson, D., Tanner, B.K., Thompson, P., and Brown, S.D., 'Coherent X-ray scattering from two-dimensionally patterned thin film nanoscale arrays', *ESRF Newsletter: Scientific Highlights* **43** (2006) 21.

Related work which has been co-authored by the candidate during the period of doctoral study has appeared in the following peer-reviewed publications:

Lamperti, A., Pym, A.T.G., Eastwood, D.S., Cardoso, S., Wisniowski, P., Freitas, P.P., Anderson, G.I.R., Marrows, C.H., and Tanner, B.K., 'Interface stability of magnetic tunnel barriers and electrodes', *Physica Status Solidi A* **204** (2007) 2778-2784.

Bogart, L.K., Eastwood, D.S., and Atkinson, D., 'The effect of geometrical confinement and chirality on domain wall pinning behavior in planar nanowires', *Journal of Applied Physics* **104** (2008), art. no. 033904.

Atkinson, D., Eastwood, D.S., and Bogart, L.K., 'Controlling domain wall pinning in planar nanowires by selecting domain wall type and its application in a memory concept', *Applied Physics Letters* **92** (2008), art. no. 022510.

Notation

The following is a list of repeatedly used symbols and their definitions. Less frequent terms are defined in the text where required.

α	Grazing angle of the x-ray beam relative to the sample surface
α_c	Critical angle
$\bar{\alpha}$	Mean linear thermal expansion coefficient
β	Imaginary component of the deviation of *n* from unity
δ	Real component of the deviation of *n* from unity
ε	Strain
ε_0	Permittivity of free space
2θ	Angle of the detector relative to the incident beam at the sample
κ	Root-mean-square displacement
λ	Wavelength
μ	Linear attenuation coefficient
ξ	In-plane correlation cut-off length
ϕ	Phase *or* sample orientation about the surface normal
ρ	Electron density
ζ	Out-of-plane correlation cut-off length
$\tau_{1/e}$	1/e penetration depth
σ	Interface width
ω	Angular frequency
$\mathbf{a_1}, \mathbf{a_2}, \mathbf{a_3}$	Real space lattice vectors
a_0	Lattice parameter
B_+, B_-	Real and imaginary parts of the complex critical angle
$\mathbf{b_1}, \mathbf{b_2}, \mathbf{b_3}$	Reciprocal space lattice vectors
C	Height-height correlation function
c	Speed of light in vacuum
D	Diffusion coefficient *or* detector resolution function

d	Interplanar period
$d\Omega$	Solid angle element
$\mathbf{E}$	Electric field vector
E	Energy
E_a	Activation energy
E_F	Fermi energy
e	Charge of the electron
f^0	Atomic form factor (non-resonant)
f', f''	Corrections to the atomic form factor (real and imaginary)
g	Height difference function
h	Fractal exponent
I	Intensity
$\mathbf{k}$	Wavevector
k_B	Boltzmann constant
m_e	Mass of an electron
N	Number of coherently scattering objects
n	Index of refraction *or* number of repeats
P	Polarization
p	Phase
$\mathbf{q} = (q_x, q_y, q_z)$	Wavevector transfer (scattering vector)
R	Reflection coefficient *or* radial distance *or* electrical resistance
r_0	Thomson scattering length
$\mathbf{r}$	Relative position vector
r	Reflection amplitude
r_V, r_S	Scattering amplitude from volume element *dV*, or surface element *dS*
T	Transmission coefficient *or* temperature
t	Transmission amplitude
w	Width

Acknowledgements

Throughout my doctoral studies Professor Brian Tanner has made advice, facilities and research contacts readily available. For his supervision I express my gratitude. I also thank Dr Del Atkinson, who as my secondary supervisor has given breadth to my studies in many ways, providing electron microscopy and electron beam lithography as well as his expertise.

I have received a great deal of help from the staff and students in the Department of Physics, as well as the members of Grey College, and I acknowledge both organisations.

Much of my work has relied upon the provision of samples of thin film multilayers and nanostructured surfaces by researchers from other academic institutions. I acknowledge the considerable time and expense given freely by Dr Bill Egelhoff Jr and colleagues at NIST, Dr Maanan Ali and colleagues at the University of Leeds, and from Universität Konstanz by Professor Manfred Albrecht (now at the Chemnitz University of Technology) and colleagues. The transmission electron microscopy images were provided by Dr Damien McGrouther at the University of Glasgow.

Any research at synchrotron facilities inevitably builds upon foundations laid by innumerable scientists, engineers and support staff. From the European Synchrotron in Grenoble I would especially like to thank the XMaS beamline support staff, namely Dr Laurence Bouchenoire, Dr Danny Mannix, Dr Simon Brown, Dr Peter Normile, Dr Paul Thompson, David Paul, Sandra Beaufoy, Dr Chris Lucas and Professor Malcolm Cooper. From the Diamond Light Source in Didcot I am grateful to Professor Steve Collins, Dr Alessandro Bombardi and Dr Guillaume Beutier.

Financial support for my studies was given by the UK Engineering and Physical Sciences Research Council through the NASCHARS project, and through a travel bursary allocated by the Magnetism Group of the Institute of Physics.

It has also been my great fortune to participate in the Spin@RT network, the members of which have taught me a great deal about current research in room temperature spintronics. Through a Royal Society funded UK-China collaboration arranged by Dr Del Atkinson I have had the opportunity to visit and collaborate with the group of Professor X-F Han at the Institute of Physics in the Chinese Academy of Sciences, Beijing, and observe their sputtering equipment in operation. I would especially like to thank Dr H-X Wei and Z-C Wen for their hospitality. I am grateful to Dr Tamzin Lafford and Dr Matthew Wormington from Bede plc for their advice on x-ray characterization techniques. Furthermore, I thank Dr Matts Björck from the Swiss

Light Source at the Paul Scherrer Institut in Villigen, Switzerland for discussions on and resources for the analysis of x-ray reflectivity.

It has been a privilege to study within the stimulating academic community in Durham. I must thank Dr Thomas Hase (now at the University of Warwick) for introducing the discipline of x-ray scattering to me, and for acting as a supplementary supervisor on many occasions. I would also like to thank John Dobson and Norman Thompson for the provision of laboratory facilities in Durham. During my studies I have had many informative discussions with Durham colleagues, especially Professor Peter Hatton, Dr Ian Terry, Dr Tom Beale and Dr Michael Hunt. It has been a pleasure to work alongside Dr Alexander Pym, Dr Alessio Lamperti, Dr Arnaud Serres, Dr Jennifer King, Alexis Ridler, Rachael Houchin, Lara Bogart, Dr Madjid Abes, Dr Miriana Vadala and Helen Armstrong.

I express my ultimate thanks to my family and to Amy for all their support and encouragement.

David Samuel Eastwood
Durham, June 2009

1. Introduction

Recent concurrent advances in thin film fabrication and surface-sensitive characterization techniques have given rise to a rich and rewarding field of science. The controlled deposition of thin films of metals and metal oxides possessing ultrasmooth surfaces has been achieved through precise control over the rates and thermodynamics of the evaporation and adsorption processes. Ultra-high vacuum techniques like molecular beam epitaxy allow some materials to be grown in thin films that are smooth and ordered on the atomic scale and extend laterally over many centimetres. There remain, however, many challenging combinations of materials for which film deposition processes are subject to ongoing study and refinement.

The patterning of thin films in order to create additional degrees of spatial confinement has not yet attained such a degree of atomic precision over large areas, but nevertheless it has radically improved over the last decade. Established patterning techniques from the semiconductor industry (e.g. ultraviolet lithography and electron-beam lithography) have been joined by a range of more novel self-assembly techniques relying upon atomic, molecular and nanoscale interactions between constituent 'building-block' units. Such assembly processes present unique advantages and challenges, and demand new methods of structural characterization.

X-ray scattering is particularly appropriate in the study of structure on the atomic and nanometre scales because the x-ray wavelength range (10^{-10} – 10^{-8} m) spans the typical interatomic separations in solids. A beam of x-rays can illuminate an area of several square millimetres with a radiation that can be considered parallel and, to some extent, coherent. They can probe material within a solid to a depth of several microns, and are generally non-destructive.

The condition of grazing incidence shall be defined as occurring when the angle of incidence between the impinging x-ray and the sample surface is either at, or just above, the critical angle for transmission into that material. Importantly, this geometry allows reflective and refractive phenomena from within the surface layers to be observed. Grazing incidence x-ray scattering is a reciprocal space technique: the scattered intensity from an ensemble of scattering points is measured at some distance, and the observed interference pattern depends upon the spatial distribution and scattering power of these points. Since the scattered intensity rather than field amplitude is measured, a direct inversion of data to reveal the scattering potential is not normally possible – a consequence known as the 'phase problem'. However with an *a priori* model of the

structure, many important material parameters can be quantified to a high degree of precision. The phase problem together with the large illuminated volume necessarily means that measurements tend to be statistical in nature, applying to an extended region of the sample rather than specific points.

There are several techniques that provide similar information to grazing incidence x-ray scattering, but frequently they offer complementary localised measurements rather than complete replacements. Cross-sectional techniques (e.g. transmission electron microscopy and atom probe measurements) can give two and three dimensional element-sensitive atomic profiles through the layers in a sample, but require careful and destructive sample preparation. Scanning probe microscopies (scanning electron microscopy or atomic force microscopy) provide real space images, limited to the very near-surface region of the sample. They can provide atomic resolution over a limited extent of the sample surface. One reciprocal space technique often favoured for monitoring during thin film growth is reflection high energy electron diffraction (RHEED). Electrons of energies 5 – 40 keV are seen to diffract from crystal lattice, but only from the uppermost few atomic planes, since such electrons provide very limited penetration.

Grazing incidence x-ray scattering offers a unique combination of advantages for the structural analysis of magnetic thin film materials. The resulting measurements are:

1. Statistical: a large surface of sample can be probed in a single measurement, and the resulting scattering interpreted to determine the statistical distribution of key material parameters.
2. Non-destructive: when suitable simple precautions are taken, a properly performed measurement does not permanently change the sample. Meticulous sample preparation is not required before a measurement.
3. Rapid: a single x-ray scan can establish a number of important structural parameters, and a simple combination of scans can give a highly comprehensive characterization.
4. Penetrative: at grazing incidence, buried layers and interfaces in metallic thin films can be measured at depths up to a few hundred nanometres into the sample, and the depth sensitivity of measurements quantified.

This thesis demonstrates that grazing incidence x-ray scattering can determine film thicknesses from sub-Angstrom to sub-micron length scales. Interface widths varying from sub-Angstrom to several nanometres (in root-mean-square amplitude) are separated into interdiffuse and topologically rough components. The interplanar crystal

lattice spacings (both parallel and perpendicular to the film surface) are measured with extremely high precision. Mesoscale surface patterning is quantitatively analysed.

Chapter 2 introduces the different types of magnetic thin film structures under study. It describes the fabrication techniques used to produce the samples subject to later characterization, and by explaining the desired material functionality provides an understanding of typical structural requirements. This chapter serves as a motivation and a justification for the structural analysis of magnetic and magnetoresistive thin film structures.

In chapter 3 a theory of non-resonant grazing incidence x-ray scattering is reviewed and developed. Different models are introduced to allow the different types of surface sensitive measurements to be interpreted, including specular reflectivity, diffuse scattering, high-angle and grazing incidence in-plane x-ray diffraction, and diffraction by a periodic submicron grating.

Chapter 4 is an investigation of the effect of a process of preoxidation of the lower electrode in a magnetic tunnel junction prior to the deposition of subsequent layers. X-ray scattering from both Co/Al_2O_3 films and Co/MgO repeated 'multilayer' interfaces is presented, both in the form of specular reflectivity and as diffuse x-ray scatter.

Chapter 5 comprises a study of annealing to 600 K in Fe/MgO and Fe/Au/MgO epitaxial thin film structures of the type exploited in some of the most recent generations of MTJ. Both specular reflectivity and diffuse scattering are considered, but the key information on lattice relaxation is extracted from measurements of grazing incidence diffraction from the lattice planes lying perpendicular to the film surface.

In chapter 6, a theoretical re-examination of grazing incidence scattering from nanostructures that form two-dimensional submicron patterns in $Ni_{81}Fe_{19}$ and Co/Pt thin films is introduced, and a semi-kinematical model allowing simulation of the transverse diffuse scatter is developed. The validity of this model is tested by the study of a range of different regular and irregular arrays prepared both by electron beam lithography and self-assembly.

The thesis concludes with a summary of the results found for specific materials and growth processes studied, and goes on to consider the significance of these results, and that of grazing incidence x-ray scattering techniques within the broader field of thin film device manufacture and characterization.

2. The preparation and properties of ferromagnetic thin films and periodic nanostructured surfaces

In this chapter the methods used to fabricate thin films, thin film devices, and nanostructured thin films are introduced. Some physical properties of these structures are discussed in order to clarify compositional requirements.

2.1. Introduction

Advances in nanoscale fabrication during the last twenty years have allowed the controlled confinement of electrons on the scale where quantisation effects become apparent. When the confinement is of the order of the Fermi wavelength of the electron[*] the electron wavefunction can be considered (in a crude quantum model) as a standing wave within a box, allowing the electronic band structure and therefore electronic and optical properties to be manipulated. The semiconductor industry has extensively developed the design and manufacture of such materials by tailoring microscopic and crystal structure and chemical composition. Over recent decades the magnetic recording industry has investigated novel magnetic and magnetoresistive metals and metal oxides in the pursuit of improved data storage densities, together with the necessary sensor sensitivity and spatial resolution.

The purview of this thesis concerns spintronic structures engineered on the nanoscale to enable the manipulation and detection of electronic spin primarily for sensing applications. In order to characterize the relevant materials it is necessary to understand the techniques and underlying processes by which they are formed and the functions for which they are designed.

[*] The Fermi wavelength for an electron (assuming $n = 10^{25}\,\mathrm{m}^{-3}$) is $\lambda_F = 2\pi/k_F = 2\pi/(3\pi^2 n)^{1/3} \approx 20$ nm.

2.2. Crystallographic structure in thin films

Continuous films of material may be deposited in thicknesses down to single, and even partial, atomic layers. This thickness control, often used in combination with lateral patterning of the film, can lead to various degrees of electron confinement, and is achieved by monitoring the rate and duration of deposition, whilst the lateral patterning of these films is performed by either 'top-down' techniques such as lithography or focussed ion-beam milling, or by 'bottom-up' processes relying on physical or chemical self-assembly or surface relaxation.

A crystal is defined by a lattice, the regular repetition of units of atoms over an extended region of space. In a thin film, this crystal is extensive in the two dimensions parallel to the substrate surface, and limited in the direction out of the surface. The degree of crystallinity of the sample and the topology and sharpness of interfaces between materials are factors modifying the electronic structure of the material.

Epitaxy refers to the growth of a crystalline layer onto a single crystal substrate such that the geometry of the substrate lattice is inherited by the new atomic layers. For films which are not perfectly lattice matched to the substrate this can introduce strain which deforms films into crystal structures which would be impossible for bulk material. The most common form of epitaxy is heteroepitaxy, where the deposited epilayer has either a different chemical composition or a different crystallographic structure to the substrate. The lattice misfit *e* between epilayer and substrate is defined by:

$$e = \frac{a_{epilayer} - a_{substrate}}{a_{substrate}} \tag{2.1}$$

Where here *a* refers to the surface lattice spacing of the layers.

High vacuum deposition conditions are required to control the purity and structural perfection of the films. The degree of strain and strain dispersion within a sample can be controlled through the growth dynamics of the crystal, and in particular by optimising the substrate temperature and the chamber pressure at the different stages of deposition. The resulting thin film structures can either be highly epitaxial single crystals or polycrystalline films. Polycrystalline films can, depending upon the degree of preferred orientation and the extent of the crystallite grains, exhibit many of the desirable properties occurring in perfect epitaxial systems.

This chapter serves to explain the sample fabrication techniques that have been used in the later experimental chapters. First, different techniques for evaporating and depositing a thin film of material will be introduced. Secondly, the growth mechanisms will be described on atomistic and macroscopic scales. Finally, the physics underlying the functionality of magnetoresistive devices will be outlined.

2.3. Deposition techniques

The deposition of a thin film can be considered in three distinct stages. First, the material to be deposited must be produced as an atomic (or small molecular) species. Methods for such production include evaporative processes like thermal evaporation and molecular beam epitaxy, and sputtering due to ion bombardment. Secondly, the released species must be transported to the substrate. Finally, there is a growth stage involving condensation and relaxation of the species onto the substrate.

2.3.1. Thermal evaporation

Thermal evaporation, or simply 'vacuum deposition' is performed at pressures around 10^{-4} Pa, and uses either resistive heating for low melting point elements (shown in Figure 2-1), or electron beam evaporation for higher melting point substances. The latter method permits the simultaneous evaporation of materials with different evaporation temperatures.

A large separation between the substrate and the crucible (greater than 0.5 m) permits a stable and uniform deposition over the entire substrate surface. Although this most simple of deposition techniques is capable of depositing relatively smooth and dense films, when elements with different evaporation temperatures are heated within the same crucible the composition of evaporated material may not match that of the source material.

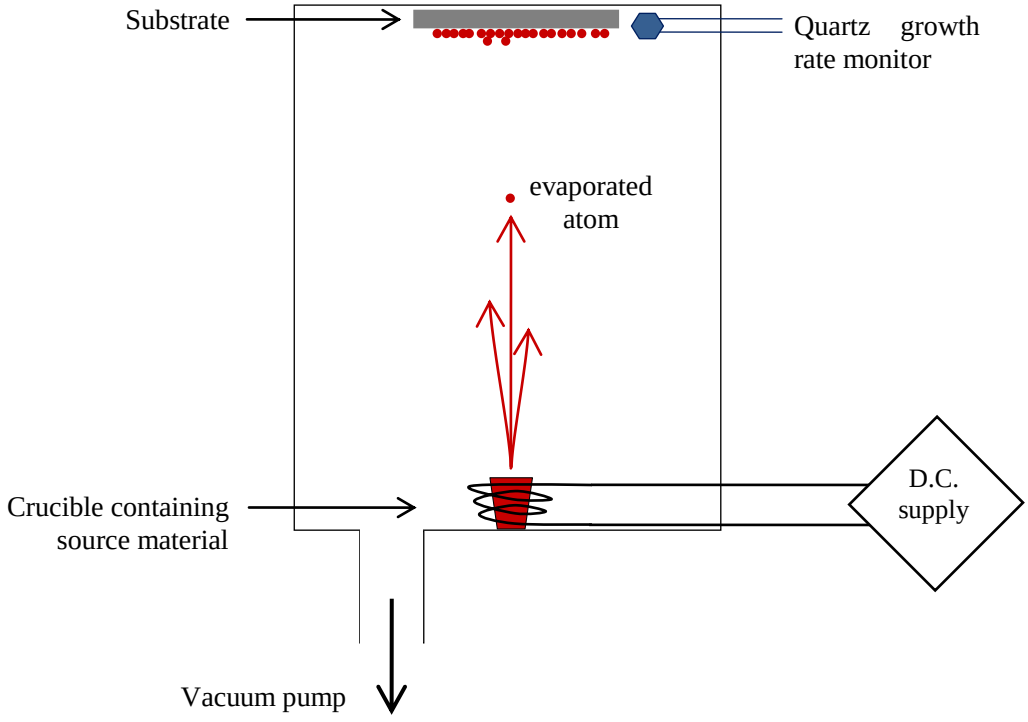

Figure 2-1. Schematic diagram of the thermal evaporation process.

The growth thickness is controlled by varying the power dissipated in the crucible, and can be monitored by a quartz crystal oscillator. As material is deposited onto the quartz crystal its resonant frequency changes slightly (being inversely proportional to the square root of the mass of the oscillator). This allows deposition monitoring down to the sub-nanogramme level.

2.3.2. Molecular beam epitaxy

A commonly used technique in research and development is molecular beam epitaxy (MBE) [see, for example ref. 2]. Fundamental to this process is the generation of a uniform flux or beam of atomic or molecular species which travel ballistically from the source to condense on the substrate. Molecular beam epitaxy is performed in ultra high vacuum, usually less than 10^{-9} Pa, and a typical deposition rate is 0.01 nm s^{-1}

Knudsen–type effusion cells are used to evaporate individual species; precise temperature control creates a highly stable flux. Deposition of mixed composition films can be achieved by co-evaporation from multiple cells, or by evaporation from a cell of mixed composition itself (for example, MgO). Monitoring of the thickness and surface crystallography is often performed by reflection high-energy electron diffraction (RHEED). The basic components of an MBE apparatus are shown in Figure 2-2.

To promote uniformity of growth the substrate is rotated during deposition. The grain size can also be increased by post-deposition annealing, the effect being most significant for thicker films.

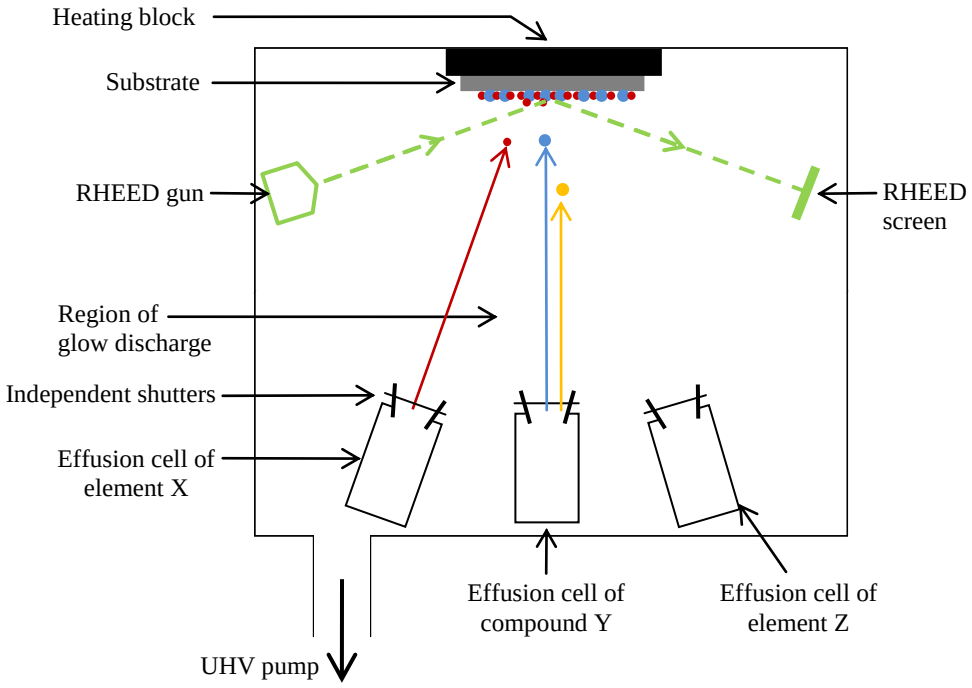

Figure 2-2. Schematic diagram of a molecular beam epitaxy system.

2.3.3. Sputter deposition

Sputtering is a deposition method favoured in many high-throughput industrial situations because it has excellent stability, scalability and rapid deposition and processing times, although MBE can ultimately achieve more perfect epitaxial growth.

In direct current (d.c.) sputter deposition, gaseous ions are accelerated towards a target of source material held at a negative potential, causing the ejection of sputtered atoms which then condense on the substrate. A high vacuum (10^{-8} – 10^{-6} Pa) is prepared, into which a low-pressure gas, typically argon at 10^{-1} Pa is introduced (see Figure 2-3). This supports a chain reaction 'Townsend' ionisation process. Initially a large potential difference (approximately 2 kV) is applied between the target cathode and the substrate anode, which is large enough to emit electrons from the cathode and to initiate breakdown of the argon gas to form a plasma. (This is visible as a characteristic 'glow discharge' due to the recombination of Ar^+ cations with electrons, shown in Figure 2-4.) The Ar^+ cations from the plasma are accelerated towards the target cathode, and on impact eject both target atoms/ions and secondary electrons. The secondary electrons maintain the plasma and enable a self-sustaining sputtering cycle, whilst the sputtered target particles condense on the substrate anode. The sputtered atoms are generally neutral monatomic particles, though these may be partially ionised whilst passing through the plasma.

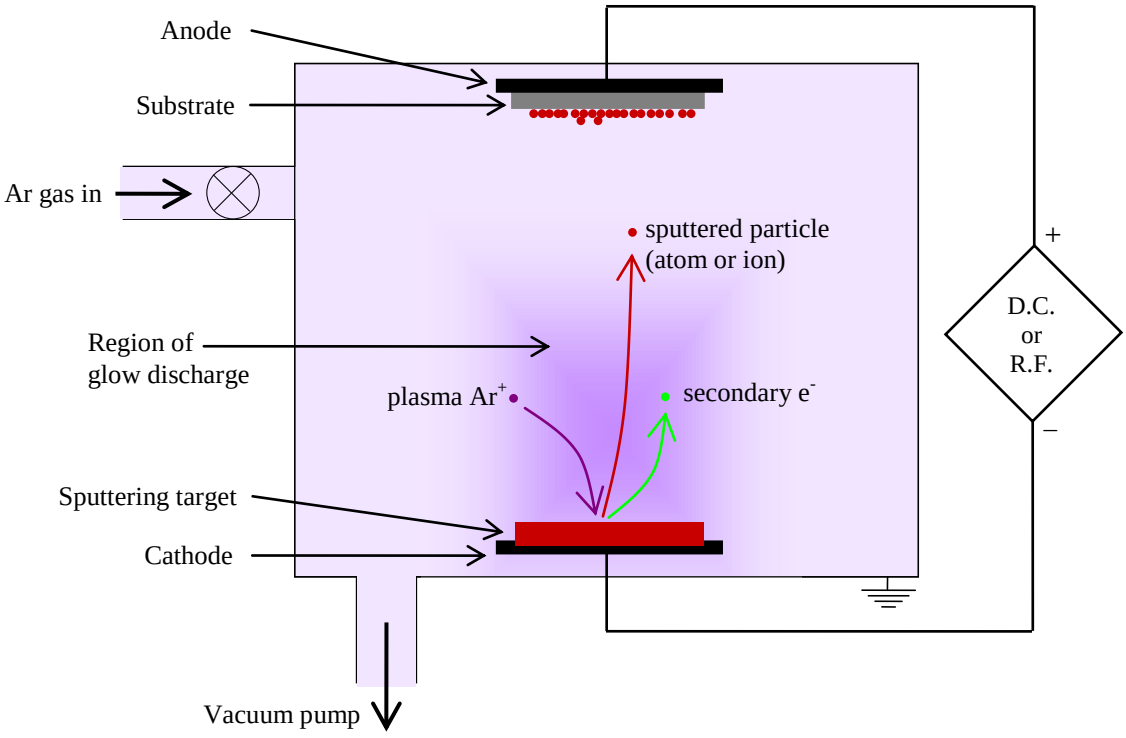

Figure 2-3. Schematic diagram of the sputter deposition process using an argon sputtering gas.

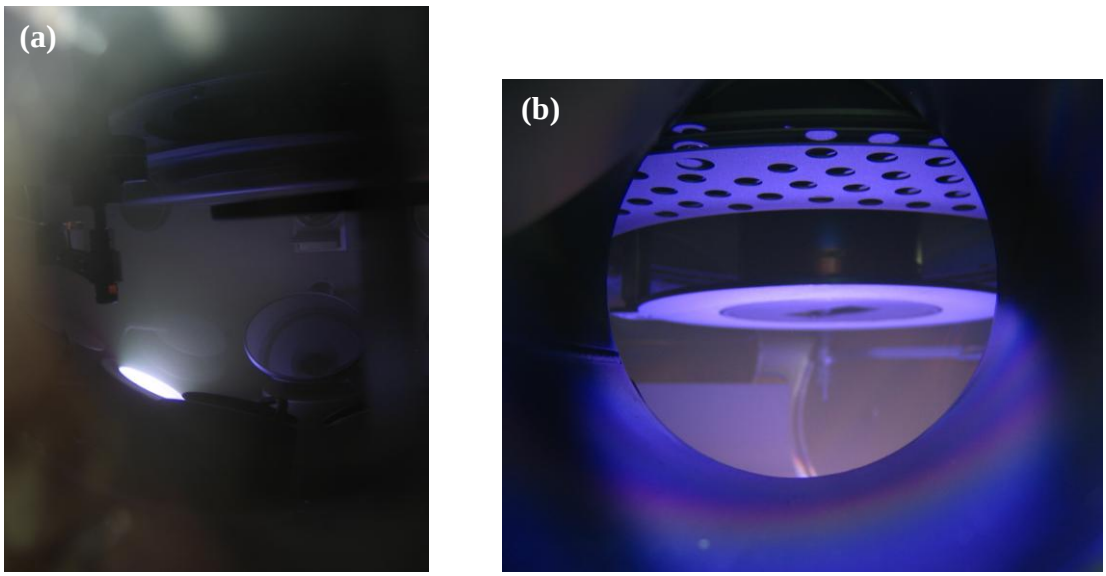

Figure 2-4. Photographs through the chamber window of (a) a sputter target (with the substrate visible in the mirror), and (b) the mounted substrate. (Sputtering equipment shown is at the M02 research group in the Institute of Physics, Chinese Academy of Sciences, Beijing, courtesy of Prof. X-F. Han. Photography by the author.)

The pressure of the argon plasma is critical in determining the breakdown voltage and the rate of production of ions by collisions. It may also act to moderate the kinetic energy and mean free path of the sputtered particles, resulting in entirely ballistic or partially diffusive motion from the target to the substrate.

The sputtering target may develop surface inhomogeneity as material is progressively sputtered away, which can cause significant variation in the evaporation rate. The target may be rotated or heated in order to reduce this effect, though targets must be replaced when the surface becomes highly irregular. Under a direct current, targets of insulating material soon acquire a surface charge which repels incident sputtering ions from the discharge region, disrupting the sputtering cycle. A high frequency (R.F.) sputtering current is therefore necessary. For complex multilayer structures like magnetic tunnel junctions, a combination of different sputtering techniques is often needed to deposit metallic and dielectric layers.

The substrate is mounted on a rotating plate promoting a uniform film thickness, and a magnetic field can be applied across the substrate to introduce magnetic anisotropy via directional order in a magnetic alloy [3, 4] . The growth temperature of the substrate may be determined by the kinetic energy of the incident particles, or controlled by electrical heating in order to produce highly epitaxial growth. Deposition thickness is controlled by shutter mechanisms across both the substrate and the sputter target and deposition rate monitors.

Magnetron sputtering

In order to increase the deposition rates and reduce substrate heating effects the sputter target can be incorporated into a magnetron [5]. Magnets are arranged such that one pole is below the central axis of the target, and the other pole forms a ring around the edge, generating a closed magnetic field over the target surface (see Figure 2-5). The superposition of the electric field into the target and the magnetic field radial from the target centre causes a cycloidal motion of electrons and ions close to the surface, generating a dense local plasma. The increased bombardment of the target allows lower sputtering gas pressures (~ 10^{-3} Pa) and potential differences (~ 0.5 kV) to be used, reducing the collisions in the region between target and substrate.

One further refinement in magnetron sputtering is the use of an unbalanced magnetron. By weakening the central pole compared to the outer ring of magnetic poles, magnetic field lines are not fully closed but extend from the target towards the substrate. This allows the sputtered ion beam to escape confinement close to the target, and creates a high flux of low energy sputtered particles to the substrate. Unbalanced magnetron sputtering is found to produce high density, stress free films.

Reactive sputtering

In many thin film devices (including the magnetic tunnel junction or MTJ, as discussed fully in section 2.6.3) control of the chemical composition of each layer, particularly at interfaces in devices, determines the operating efficiency. In the case of a MTJ, quantum tunnelling occurs between two electrodes through an insulating metal-oxide barrier, and the method of oxidation of the barrier has been found to affect strongly the device performance. Such metal oxide layers may be deposited by reactive sputtering, where the component species are simultaneously evaporated from a metal target and introduced with oxygen gas. This is found to produce the closest stoichiometry of oxide material [6].

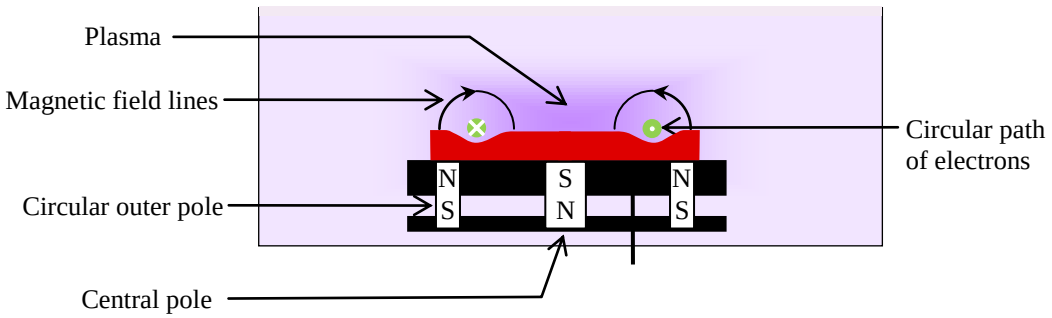

Figure 2-5. Schematic diagram of a balanced magnetron in cross-section. The grooves in the target are part of the circular path of the erosion track.

Epitaxial sputtering

Epitaxial films may be sputtered under ultra-clean conditions at very slow deposition rates. A high surface mobility is achieved by heating the substrate close to the evaporation temperature of the deposited material, so that extensive adatom reordering permits the formation of extremely large grains. The crystallography of the substrate and buffer layer is highly influential on the crystallographic properties of subsequent layers. Close lattice matching between successive layers supports epitaxial growth, and compatible combinations of metallic buffers and epilayers have been tabulated in papers by Harp and Parkin [7, 8].

2.4. Growth models

As the free atom or ion meets the substrate surface, the momentum perpendicular to the substrate is lost and the particle undergoes *adsorption* onto the surface. This has two forms: *physisorption* where reversible bonding occurs via the relatively weak van der Waals mechanism which depends upon the temperature; and *chemisorption* in which the adatom reacts chemically with the substrate or existing film and a more permanent bonding occurs.

A freshly deposited physisorbed atom will possess significant kinetic energy and will traverse the surface, interacting with other particles to nucleate and expand clusters. Clusters will move and grow until they are thermodynamically stable entities – a point known as the *nucleation* stage. As the number of nuclei with this critical size increases, the film growth will enter the *coalescence* stage in which islands agglomerate in order to reduce the total surface area. The degree of agglomeration is sensitive to the substrate temperature which determines the thermal diffusion of the adsorbed species. As islands grow they become less mobile.

The diffusion length of an adsorbed atom l_s is temperature dependent, and can be described by:

$$l_s = \sqrt{2 D_s \tau_s} \tag{2.2}$$

Where τ_s is the mean residence time of an adatom, and the diffusion coefficient D_s is given by:

$$D_s = D_0 \exp\left(-E/k_B T\right) \tag{2.3}$$

Here E is the hopping barrier between sites on the substrate. By increasing the growth temperature, the mobility increases and the adatom is more likely to find a global minimum in the energy of the surface in the most thermodynamically stable structure.

2.4.1. Adatom interactions on the film surface

A deposited epilayer experiences two interactions: the adatom-adatom interaction which favours the lattice parameter of the epilayer; and the substrate-adatom interaction which acts to force the epilayer to be commensurate with the substrate lattice. Following the growth mode categorisation presented by Bauer [9, 10], these can be characterized in terms of the surface energies of the material, which is a macroscopic measure of the strength of bonding at a surface. The surface free energy is defined as the work done per unit area in dividing a perfect crystal into two crystals with perfectly smooth surfaces [ref. 11, pp. 20-21].

If the deposited layer has a surface free energy lower than that of the substrate, the adatoms are likely to form continuous atomic layers (known as wetting the substrate) to create a continuous film. Neglecting any strain in the film, the condition for growth of a continuous epitaxial layer (Frank – van der Merwe growth [12, 13]) can be written mathematically as [ref. 2, p. 302]:

$$E_S > E_F + E_I \tag{2.4}$$

Here E_S, E_F and E_I are the substrate energy, the surface free energy of the epilayer, and the interface energy respectively. For the reverse inequality there is no wetting of the substrate; adatoms form islands or droplets which minimises the surface energy, and island (or Volmer-Weber) growth is favoured.

An intermediate growth mode is Stranski-Krastanov growth which occurs when there is initial wetting of the substrate, but as the epilayer becomes thicker strain causes the interface energy to increase, introducing island growth. These three modes are illustrated in Figure 2-6.

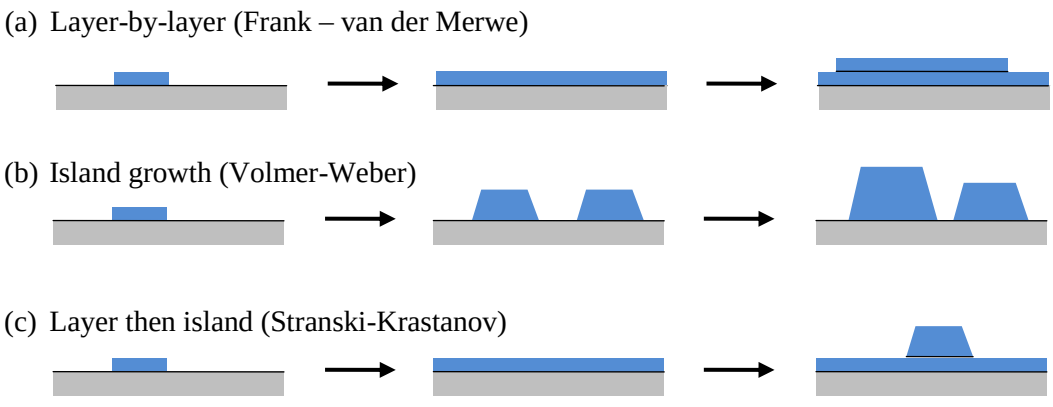

Figure 2-6. Schematic representation of the three general modes of growth. (a) Layer by layer growth occurring when wetting of the substrate is favoured, (b) island growth, and (c) the intermediate Stranski-Krastanov growth mode in which after an initial wetting phase, island growth occurs.

Under standard growth conditions the crystallographic orientations of individual nuclei are independent, and grain boundaries are formed between islands during coalescence. By increasing the substrate temperature and the kinetic energy of particles to be deposited, the mobility of adsorbed atoms is increased. Using a low vapour pressure, and when the nucleation barrier is high, the density of nucleation sites is decreased. These three strategies allow the growth of larger grains.

Finally, subsequent layers are formed upon the first layer of islands; in general for thin films *columnar growth* leads to grain sizes determined by the density of initial nucleation sites and the degree of coalescence between islands.

2.4.2. The critical thickness of an epitaxial layer

A strained epitaxial layer can grow commensurate with a single crystal substrate until it exceeds a critical thickness, beyond which the strain energy exceeds the bonding energy adhering it to the underlying lattice, and it relaxes towards its bulk lattice. This may be understood in the model of van der Merwe [14], which applies at thermodynamic equilibrium and assumes that the final configuration of the epitaxial system has the minimum overall energy. There are two competing energy terms considered: the *homogeneous strain energy* E_H of the epilayer due to a strain e, and a dislocation energy E_D due to the introduction of misfit dislocations within the epilayer in order to relieve this strain. The total interface energy is described by [ref. 2, p. 290]:

$$E_I = E_H + E_D = 2\mu t e^2 \frac{1+\upsilon}{1-\upsilon} + \mu b \frac{|e + f_0|(1-\upsilon\cos^2\beta)}{2\pi(1-\upsilon)\cos\gamma\sin\beta}\ln\left(\frac{\rho R}{b}\right) \qquad (2.5)$$

Here t is the epilayer thickness, μ is the interfacial shear modulus, υ is Poisson's ratio, f_0 is the natural misfit between the substrate and epilayer, b is the magnitude of the Burgers vector, β is the angle between the Burgers vector and the dislocation line, γ is the angle between the glide plane of the dislocation and the interface and R is the radius of the dislocation strain field.

This equation is introduced here to highlight the dependencies of the two energy terms. The dislocation energy is proportional to $|e + f_0|$, and when $e = -f_0$ the epilayer is fully strained to the substrate. The strain energy E_H is directly proportional to the thickness of the film, and to the square of the strain. It therefore becomes dominant as the deposited film thickness increases, and induces dislocations when the thickness exceeds a critical thickness. For interfaces with $E_H \sim E_D$, the resulting equilibrium is reached with a partial relaxation of the strain.

2.4.3. Development and propagation of roughness

As islands coalesce to form a continuous film, voids of uncovered substrate will remain. In addition, boundaries between islands can lead to defects in the crystal structure. Grain boundary formation can also lead to the propagation and evolution of surface roughness as successive layers are deposited.

It is found that large, coarse grain sizes allow higher amplitude surface roughness to propagate. High surface mobility generally makes surfaces smoother by filling in concave regions. Interfaces in thin films are well described as self-affine fractal surfaces, which are self-similar under scale transformations in certain directions [a concept described further in section 3.4.3 and ref. 15].

2.5. Patterning methods

Techniques for nanoscale patterning of extended areas of thin films can be assigned to one of two categories. 'Top-down' direct writing of patterns (for example by electron beam lithography, projection lithography or focussed ion beam milling) can achieve large coherent areal coverage of nanoscale structures, but generally requires a serial exposure of either the structures or a template for the structures, which is a slow process. 'Bottom-up' self-assembly or self-organisation methods where short-range interactions between large numbers of atomic, molecular or nanoscale objects lead to long-range ordering can produce more rapid areal coverage and higher resolution features, but may also suffer from poorer long-range coherency. There are techniques combining the advantages of both top-down and bottom-up methods, including for example the self-assembly of anodized aluminium oxide pores within a lithographically defined macro-template [16].

Progressive increases in the data density held by magnetic recording media have resulted in individual bit volumes which approach the so-called 'superparamagnetic limit', where thermal fluctuations can exceed the bit switching field and inadvertently reverse the binary state. One way to increase the magnetic anisotropy of a bit is to confine it within a nanostructure possessing strong shape anisotropy. This can increase the switching field, and the magnetization state can reduce the stray field which may act to switch neighbouring bits [e.g. ref. 17]. By arranging nanostructures in close proximity, interactions can be controlled [see, e.g. ref. 18]. Patterned devices may be required for the controlled production of nano-device arrays, for example of MRAM elements [6] or for microwave generation [19]. In general, smaller structures approach the length scales of 'artificial atoms', where the electronic density of states can be tailored to produce controlled radiative or electrical behaviour. Because the energy dissipated by a single nanostructure typically scales with area, large numbers of

structures are required (often coherently) to operate. Their physical arrangement is fundamental.

Two techniques will be outlined here that are used to prepare the patterned samples studied in chapter 6. These techniques are electron beam lithography, and the self-assembly of silica spheres.

2.5.1. Electron beam lithography

Electron beam lithography (EBL) involves the serial writing of nanostructures in an electron-sensitive resist, and as such is relatively slow. In research applications, EBL is often performed using a scanning electron microscope. The basic features of the EBL system are shown in Figure 2-7. A tungsten cathode or field emission gun produces a beam of electrons which is focussed and deflected by a series of magnetic lenses to a specific point on the resist. The lenses are usually multipolar so that astigmatism of the beam can be eliminated. The beam spot size is determined by the degree of focussing; typical diameters are between five and ten nanometres.

The exposure region is primarily controlled by deflecting the beam using local high frequency magnetic fields from deflectors, but large sample areas may be spanned by translating the sample and tiling together several exposure regions. Imaging of the surface is performed by measuring the intensity of scattered electrons as the beam is rastered across the sample.

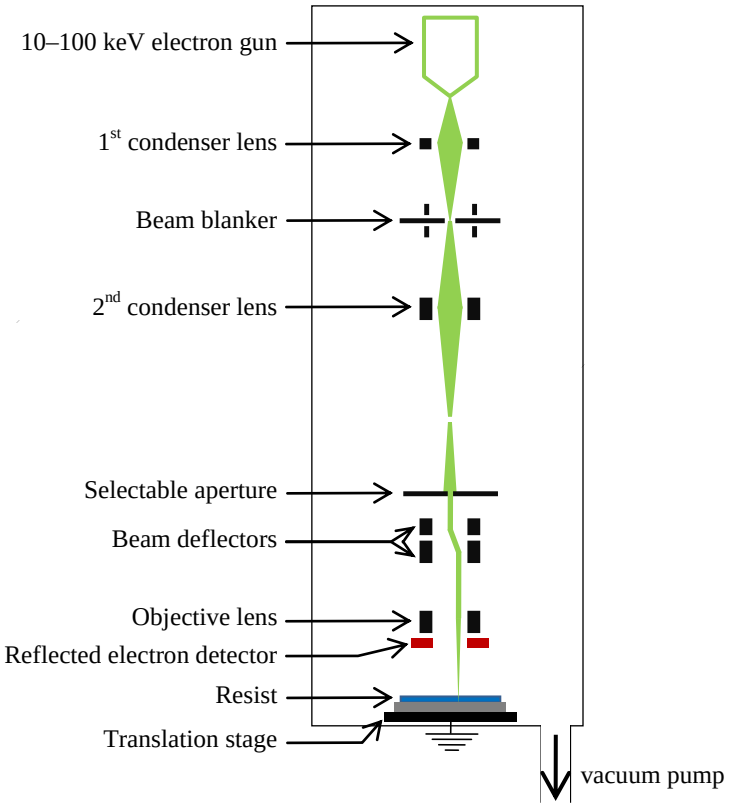

Figure 2-7. A simplified schematic cross-section of an electron beam lithography system.

The exposure process

The electron beam causes a chemical or physical change in the resist which allows it to be selectively removed. In positive lithography, the exposed regions of resist are the areas where features remain at the end of the process (see Figure 2-8). This is achieved using an organic resist such as polymethylmethacrylate (PMMA), which is spin-coated onto the substrate to a thickness of approximately 50 nm. The electron beam causes the long carbon backbone of the polymer to be divided into chains of lower molecular weight, which are more soluble in a developing solution (for PMMA, methylisobutylketone or MIBK in isopropanol is commonly used). Higher resolution lithography can be achieved with inorganic resists such as AlF_3 [20], but these have much lower sensitivities to e-beam exposure and are impractical for coverage of large areas. Higher acceleration voltages, and thinner resist layers are also found to increase the resolution [21]. A more specialist resist is hydrogen silsesquioxane (HSQ), which has a much smaller molecular weight than PMMA, and has enabled patterning of structures just five nanometres in lateral extent [22].

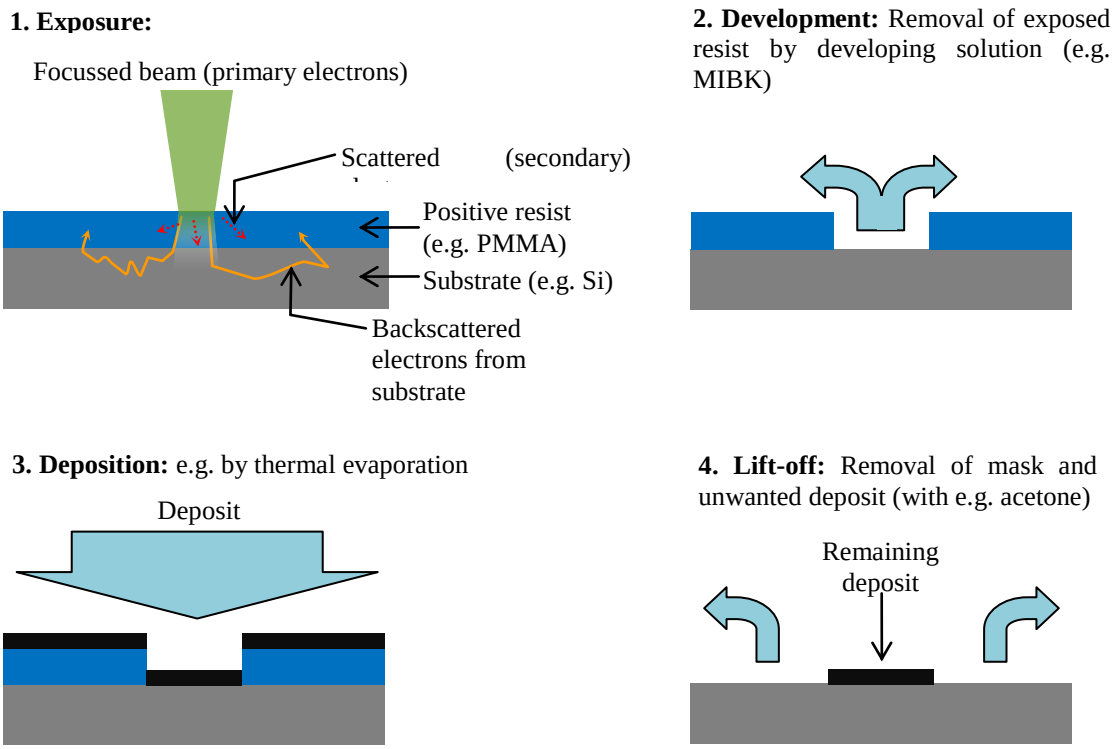

Figure 2-8. The four stages of electron beam lithography using a positive resist followed by lift-off.

The scission of polymer chains occurs with interaction energies greater than 5 eV, meaning that most successful exposure of the resist is not by the primary electrons of the e-beam, but secondary scattering events as the beam energy is dissipated in the resist through an electron cascade. This leads to a broadening of the exposed region relative to the focused beam, an occurrence known as the *proximity effect*. The region of energy dissipation can be accurately calculated by Monte Carlo simulations, and these demonstrate that backscattered electrons from the substrate cause exposure at radial distances of up to 10 μm from the beam spot.

There are many techniques for reducing for the proximity effect, including calculating the unintentional overexposure and compensating by a complementary background [23], and simulating the exposure received at each location prior to irradiation, then modifying the initial dose [24]. These corrections are beyond the scope of this introduction.

The contrast between exposed and unexposed regions is also degraded by the proximity effect, which tends to amplify the edge roughness of structures. Edge roughness may originate from random variations in the beam position, or from inhomogeneities in the resist material which may include clustering of molecules, density variations, and impurities. Details of the electron beam lithography process used in Durham have been given by Atkinson [25].

2.5.2. Self-assembly of submicron spheres

Self-assembly occurs when unit structures experiencing short-range interactions spontaneously assume some order which extends over much longer scales, and generally occurs close to thermal equilibrium. In case presented here, submicron electrically insulating spheres are considered, for which the most space-filling ground state is a hexagonal close-packed single film.

In a detailed paper, Denkov *et al* [26] identified the underlying mechanisms of the self-assembly of micron-sized spheres immersed in a liquid surface, determining that capillary action between the spheres induced coalescence. This capillary attraction is much stronger for particles partially immersed in a liquid layer as compared to particles on the surface or fully in suspension. Indeed, with thick liquid layers electrostatic repulsive forces dominate, and only when the liquid layer is shallower than the sphere diameter does capillary attraction overwhelm any repulsion. For two spheres in close proximity, the meniscus of the fluid rises up more on the facing surfaces than on the outwards faces (as Figure 2-9).

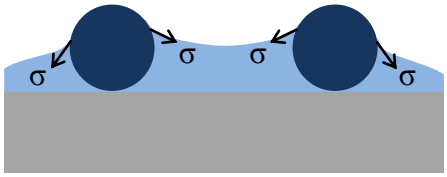

Figure 2-9. Two spheres partially immersed in a liquid film are drawn together due to the capillary effect and the in-plane component of the surface tension vector σ at the point of contact with the sphere. Arrows indicate the local direction of the surface tension [adapted from ref. 26, figure 9].

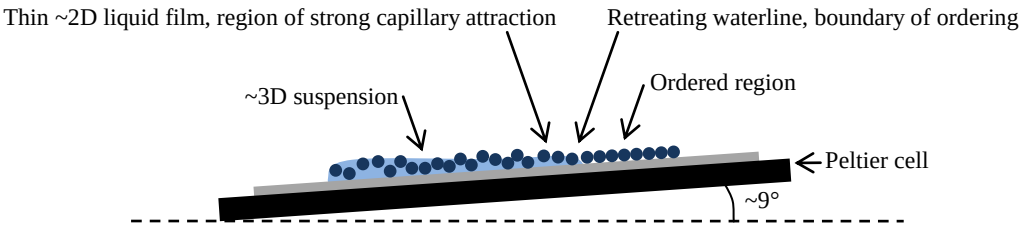

Figure 2-10. Schematic of the technique for controlled self-assembly described by Micheletto et al [27].

This results in a net in-plane component of the surface tension F_x acting to bring the spheres together. The in-plane component of the force upon the sphere at any point is [according to ref. 26]:

$$F_x \approx \frac{2\pi\sigma r_c^2 \sin^2 \Psi}{L} \quad \text{for} \quad r_c \ll L \tag{2.6}$$

Here σ is the inherent surface tension of the liquid, r_c is the radius of curvature of the liquid at the sphere surface, Ψ is the mean meniscus slope angle at the point of contact with the sphere, and L is the distance between the two spheres. Denkov *et al* report that this interaction is greater than electrostatic interactions and thermal fluctuations.

Denkov *et al* observed the spheres gathering into a regular hexagonal close packed lattice as the liquid (water) evaporated, and that the rate of the evaporation determined whether a monolayer or a multilayer of spheres were formed.

The technique was refined by Micheletto *et al* [27], who mounted a glass slide on a Peltier cell (to prevent temperature fluctuations), held at an angle of 9° to the horizontal. The slow, controlled evaporation of the water at a precisely controlled 295 K started at the most elevated end of the sample where the liquid film was thinnest due to gravity. As the thin liquid layer evaporated, the waterline retreated down the slope to leave a region highly ordered spheres.

Some of the largest coherent arrays have been produced by the group of Weekes *et al* [28]. Using polystyrene spheres coated in carboxyl groups, they were able to balance

the mobility of spheres due to electrostatic repulsion and the capillary attraction between them. By introducing a single layer of 390 nm diameter spheres onto a water surface they observed a spontaneous coherent hexagonal lattice extending over an area of 1 cm^2. The raft was sufficiently resilient to be captured onto the surface of a variety of substrates including metals, glasses and polymers. Weekes *et al* demonstrate that these spheres can be used as a protective resist in reactive ion etching to produce arrays of 120 nm circular magnetic dots.

Another important study was performed in 2005, when Albrecht *et al* [29] allowed 270 nm diameter polystyrene nanospheres to self-assemble slowly as their solvent evaporated. They deposited cobalt/palladium MBE multilayers directly onto these spheres to produce dense arrays of magnetically isolated 'caps' which exhibited perpendicular magnetic anisotropy. Later, the same group performed self-assembly using SiO_2 spheres, depositing iron platinum [30] and observing similar results, achieving good epitaxy by MBE directly onto the spheres.

2.6. Magnetoresistance

Magnetoresistance (MR) is the variation of electrical resistance in a conductor or semiconductor with magnetisation, and can have various physical origins. Any magnetic field will deflect a moving charge as described by the Lorentz force:

$$\mathbf{F} = q(\mathbf{v} \times \mathbf{B}) \tag{2.7}$$

This force can act to lengthen the path of the electron in the material and therefore increase the resistance. The magnetoresistance of a semiconductor is understood using this model. The magnitude of the relative change in resistance for a given applied field is highly dependent upon the geometry of the material, but is too small to be widely used in sensor applications.

2.6.1. Anisotropic magnetoresistance

Kelvin first reported *anisotropic* magnetoresistance (AMR) in a ferromagnet in 1857 [31] by arranging a nickel bar (with approximate dimensions 330 × 130 × 30 mm^3) into a magnetic field aligned along the long axis. Current passing transverse to the field experienced a fractional reduction of 1/192 in electrical resistance, whereas current parallel to the field experienced a fractional increase of 1/144. With a modern understanding of magnetism this is attributed to spin-orbit coupling changing the electron scattering cross-sections when a current is parallel or perpendicular to the magnetic polarisation of the atoms.

Figure 2-11 shows a schematic density of states diagram for the 3d band in a transition metal using Mott's two current model [32]. Magnetisation of the material causes the 3d band to be exchange split into two channels, with spins parallel to the magnetisation being energetically favourable, and therefore preferentially filled compared to the antiparallel channel. Conduction is primarily through the weakly bound 4s shell, which does not experience such exchange splitting. Resistance is dominated by scattering from the 4s states to the 3d states (in this analysis, whilst the spin orientation is conserved). The scattering probability is therefore proportional to the density of states at the Fermi energy of the 3d sub-band being scattered into, which is different for the two spin channels. Therefore they experience a different resistance. In the specific case of nickel, the 3d+ sub-band lies below E_F, so scattering of minority spins from 4s → 3d– is more probable.

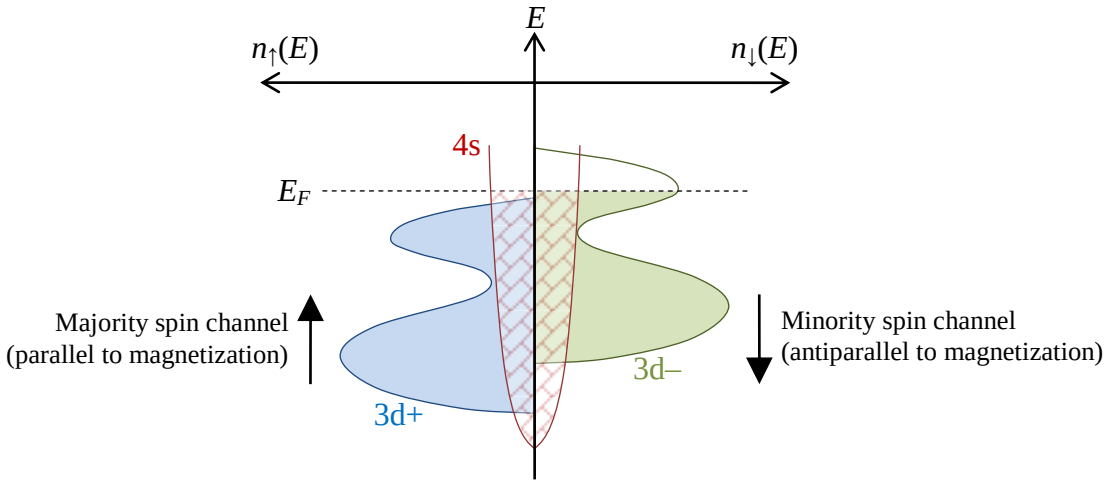

Figure 2-11. A schematic two-channel density of states curve for nickel, used to explain anisotropic magnetoresistance. Shaded regions represent the occupied states below the Fermi energy, E_F. [Adapted from ref. 33, figure 1.10b].

In the case of AMR, the change in scattering lengths results in the overall resistance along the magnetisation direction being higher than the resistance perpendicular to the magnetization. The relative AMR is typically a few percent, and was applied in the majority of magnetic hard disk drive read heads until the mid-1990s. The commercial demand for greater data storage densities motivated the development of more sensitive read heads. These relied upon *giant* magnetoresistance, or GMR.

2.6.2. Giant magnetoresistance

The discovery of giant magnetoresistance (GMR) around 1988 is accredited to Grünberg [34] and Fert [35], who made independent reports of a large MR in iron/chromium thin films. An excellent review article documenting the discovery was written by Thompson in 2008 [36] to commemorate the award of the Nobel prize in Physics to Fert and Grünberg for their work on GMR.

Whereas AMR is seen in a bulk ferromagnet, GMR only became apparent when advances in thin film deposition (in particular MBE) allowed the construction of thin iron electrode layers separated by a very thin nonmagnetic layer. The principal stimulus for GMR came in 1986, when Grünberg *et al* [37] reported antiferromagnetic exchange coupling in Fe/Cr/Fe trilayers, which provided a mechanism for arranging an antiparallel alignment of two ferromagnetic thin films.

In 1988, Grünberg *et al* went on to measure the change in electrical resistivity of iron-chromium-iron sandwich structures as the relative magnetisation of the iron layers was switched from antiparallel to parallel by an external field. Concurrent studies were made by Fert *et al*, on iron-chromium sixty-repeat multilayers. In the following description GMR will be introduced in simple two-current terms using a trilayer structure.

Shown in Figure 2-12, the current passes perpendicularly to the plane of the thin films (CPP geometry). As discussed in the section on AMR, electrons with spins aligned antiparallel to the magnetisation experience are strongly scattered, hence experience a high resistance. This causes the first electrode to act as a ‘spin filter’, polarising the current. For thin spacer layers (Grünberg used 1 nm of Cr) the spin imbalance remains as electrons enter the second ferromagnet. In zero external magnetic field, the magnetisation of the second ferromagnet is antiparallel to the first due to exchange coupling, therefore the favoured spin orientation in the first electrode is the unfavoured in the second, and vice-versa (as shown below in (a)). Through the entire structure, the total resistance of the two spin orientations is identical.

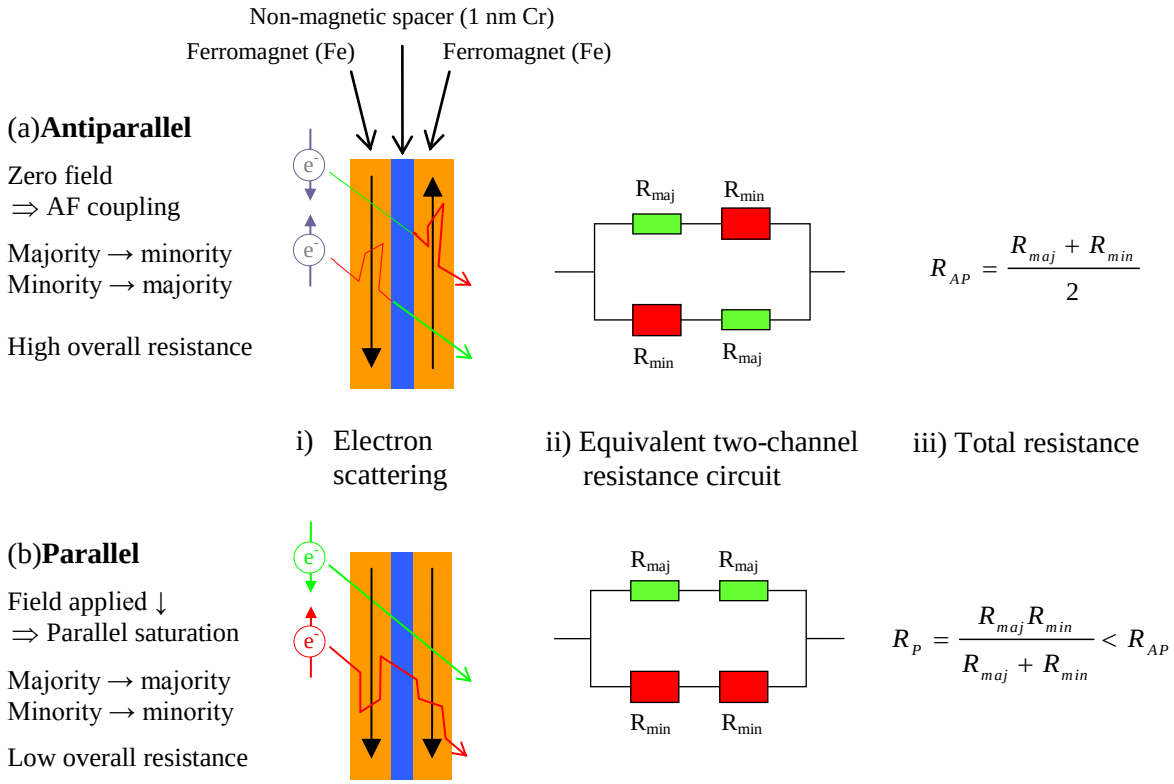

Figure 2-12. Schematic two current explanation of the (a) antiparallel, and (b) parallel states of a GMR trilayer structure. From left to right: (i) The scattering of the spin up and spin down channels, (ii) the equivalent resistance circuit, (iii) the resulting overall resistance.

When a large external magnetic field is applied (0.4 T), the exchange coupling is overcome and both electrodes align parallel to the field and each other (shown in (b)). Now the majority spin channel has the same spin alignment in both electrodes, and therefore one spin orientation experiences a lower resistance than the other. The overall resistance is lowered, hence the structure can act as a binary sensor.

The relative change in magnetoresistance is described by a magnetoresistance ratio:

$$\frac{\Delta R}{R} = \frac{R_{AP} - R_P}{R_{AP}} \tag{2.8}$$

Here the denominator represents the resistance in the default, zero-field state.

Understanding the nature of coupling between the electrodes was essential in developing effective GMR sensors. The nature of the interlayer exchange coupling in various materials was systematically explored by Parkin [38], who observed an oscillation of the coupling strength and polarity as the spacer thickness was varied with a universal period of approximately 1 nm. This was attributed to wavefunction interference effects occurring in the spacer layer, as understood in the Ruderman-Kittel-Kasuya-Yosida (RKKY) model [39], and became known as *oscillatory exchange*

coupling. The strength of this coupling made Grünberg's simple 'sandwich' sensor structures too magnetically hard to switch. Dieny *et al* [40] developed the idea of the spin valve, in which antiparallel alignment of layers is achieved by coupling one of the ferromagnetic layers to a neighbouring hard layer through direct exchange coupling, whilst allowing the other 'free' layer to switch in much lower external fields.

The fixed reference layer is said to be 'pinned'. Pinning lowers the switching field of the free layer whilst preventing inadvertent reversal of the hard layer (either by application of a large saturating field or by the nucleation of local misaligned domains during lower field sweeps [6]). This was originally achieved by direct exchange coupling to a neighbouring antiferromagnetic layer, but a more recent development is the synthetic antiferromagnet, where there is an RKKY interaction between a directly pinned, third ferromagnetic layer. This creates a 'flux-closure' state of the pinned electrode, reducing any dipolar coupling between the two electrodes [for further information, see ref. 6].

Magnetically isolating the two electrodes has a further advantage; by inducing different magnetic anisotropies in the electrodes, the zero-field magnetizations can be set perpendicular to one another. This elicits a linear magnetoresistance response to an applied field, by which opposite polarities of applied field yield opposite resistance change [41]. This is the optimal arrangement for read head sensors in hard disk drives.

In an important experiment where thin surface layers of a second ferromagnetic material were inserted at the electrode-space interface, Parkin demonstrated that it is the electronic structure very close to the interface which determines spin dependent scattering [42], rather than the bulk scattering model as developed above. Therefore the electron wavefunction (described as Bloch states in the electrodes and evanescently decaying wavefunctions through the spacer) must be considered when performing rigorous calculations of thin film magnetoresistance. This also implies that the magnetoresistance ratio is especially sensitive to the interface structure.

In the original 1988 paper of Fert *et al* [35], the magnetoresistance ratio was increased by repeating the ferromagnet/non-magnet unit to create a multilayer structure. One of the highest values for $\Delta R/R$ achieved with such multilayer GMR sensors at room temperature is 70%, obtained by Parkin *et al* in 1991 [43] with a structure of the form [0.8 nm Co / 0.8 nm Cu]$_{\times 60}$.

The summary given above represents the simplest self-consistent description of current perpendicular to the plane GMR. A similar MR effect is seen when current is passed in the plane of the films, again due to spin dependent scattering. There are many factors (including interface structure and crystallographic orientation and perfection) which influence the magnitude of GMR and the switching field of the device. Accurate

quantitative predictions of magnetoresistance require rigorous numerical calculations which account for the full electronic band structure throughout all atomic layers in the structure, but this extends beyond the scope of this thesis. For further information the interested reader is referred to the review article on GMR by Thompson [36].

2.6.3. Tunnelling magnetoresistance

Tunnelling magnetoresistance occurs when the non-magnetic spacer layer is replaced by an insulating layer, in a structure known as a magnetic tunnel junction (MTJ). With a bias voltage applied across the barrier, a current can flow through the junction by quantum mechanical tunnelling. The principal motivation for using an insulating spacer layer is that extremely large values of TMR – potentially exceeding 1000% – have been predicted from calculations of spin dependent tunnelling probabilities [44, 45].

The typical components of an MTJ are shown in Figure 2-13. Here the synthetic antiferromagnet pins the lower electrode through the RKKY interaction, whilst the upper electrode is free to switch with the external field. The film material is usually patterned laterally to dimensions 10 × 10 μm^2 or smaller [41].

The first observation of TMR in thin Co/Ge/Fe films was published by Jullière in 1975 [46], although the measurement of only 14% change in resistance at cryogenic temperatures (4.2 K) was impractical for sensor applications.

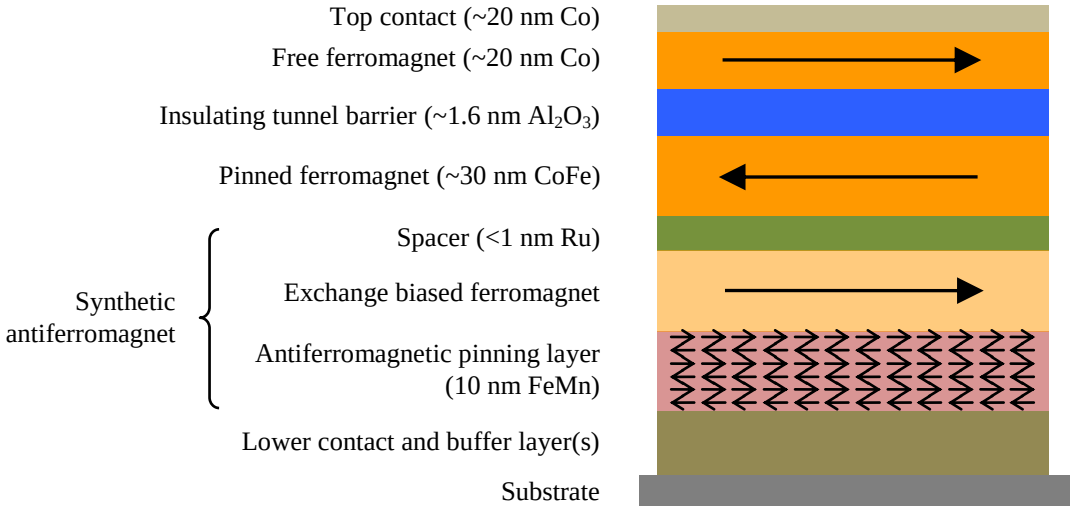

Figure 2-13. A schematic diagram of the layers present in magnetic tunnel junction structures. The lower electrode is pinned by indirect exchange coupling. Typical thicknesses and materials are indicated.

Following Jullière's discovery, the TMR effect lay largely unexploited for many years. In 1995 two reports of large room temperature MR in tunnel junctions were made. Moodera *et al* [47] reported an 11.8% tunnelling magnetoresistance ratio (TMR) in $CoFe/Al_2O_3/Co$ and $CoFe/Al_2O_3/NiFe$ films, where the alumina tunnel barrier was evaporated as ~1.3 nm aluminium and then oxidized by an oxygen plasma. Miyazaki and Tezuka [48] obtained 18% room temperature TMR in an $Fe/Al_2O_3/Fe$ structure. With improved film deposition and patterning techniques, optimised Al_2O_3 tunnel barriers produce room temperature TMR typically around 50% [36].

In his original work, Jullière proposed a relatively simple two-current model for his results. The Jullière tunnelling process is shown in Figure 2-14. In this case, the spin-up channel has a higher density of states at the Fermi energy. When the electrodes are parallel the majority-to-majority (spin up) electrons have a high tunnelling probability – much higher than the minority-minority (spin down) channel, and also higher than the majority-minority and minority-majority channels in the antiparallel arrangement. This higher tunnelling probability for the majority-majority channel lowers the overall junction resistance in the parallel alignment as compared to the antiparallel alignment.

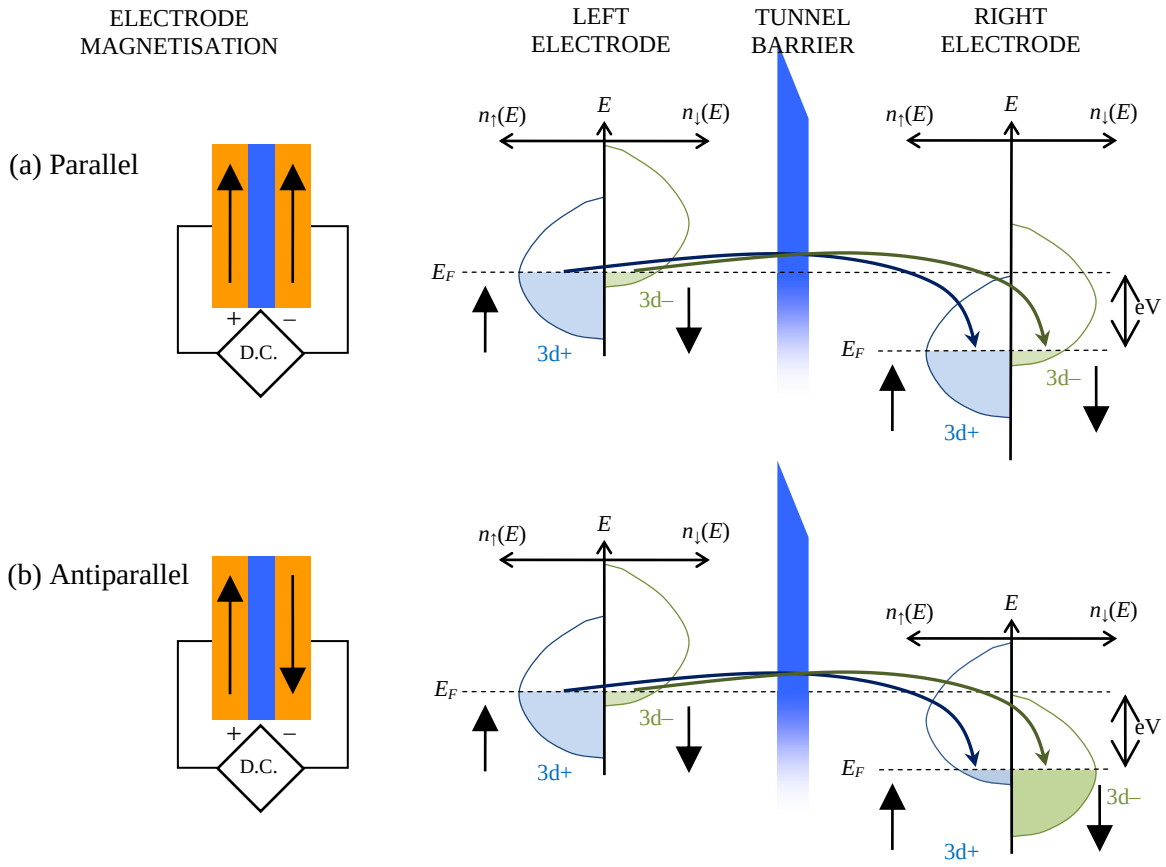

Figure 2-14. A schematic density of states model for Jullière's explanation of TMR in the two opposite magnetization states (left). Shown for the (a) parallel and (b) antiparallel alignments of the electrodes in a magnetic tunnel junction [Redrawn from ref. 49].

Quantitatively, by assuming spin conservation through the barrier the tunnelling current is considered proportional to the product of the density of states at the Fermi energy, $n(E_F)$, of the two spin channels in each electrode:

$$I \propto n_{\uparrow}^{L}(E_F)\, n_{\uparrow}^{R}(E_F) + n_{\downarrow}^{L}(E_F)\, n_{\downarrow}^{R}(E_F) \tag{2.9}$$

The magnitude of TMR is characterized by the tunnelling magnetoresistance ratio, which depends only upon the spin polarisation at the Fermi level in each ferromagnetic electrode:

$$\mathrm{TMR} = \frac{2P_1P_2}{(1 - P_1P_2)} \tag{2.10}$$

The polarisation in one electrode is defined as:

$$P = \frac{n_{\uparrow}(E_F) - n_{\downarrow}(E_F)}{n_{\uparrow}(E_F) + n_{\downarrow}(E_F)} \tag{2.11}$$

Using Jullière's formula (2.10) with a nominal spin polarisation $P = 0.6$, the predicted TMR is 63%.

When established band structures are used to calculate the electrode polarisations, the predicted MR ratios are inconsistent with observed TMR values. Much better agreement is obtained when the polarisations are measured using ferromagnet / Al_2O_3 / superconductor tunnel junctions, which allow the polarisation of the tunnelling current to be determined directly [50]. This indicates that the structure of the tunnel barrier is also important in determining the magnitude of TMR, a complication beyond Jullière's model.

To explain how the barrier influences spin dependent tunnelling, it is necessary to abandon the Jullière model, and to introduce Bloch states representing the solutions of Schrödinger's wave equation for an electron moving in the potential of the crystal lattice. The electron wavefunctions contain information on the momentum and phase of the tunnelling electrons, and are periodic in a metallic conductor such as iron or nickel, but decay as an evanescent wave in the insulating barrier.

The different Bloch states have different symmetries, labelled Δ_1, Δ_2 etc. The Δ_1 symmetry contains hybridized s-p-d states, which have a large (and positive) spin polarization at the Fermi energy [51]. The Δ_2 are d states, and often have small and negative polarizations at E_F. In Jullière's simplified model, these different states have equal tunnelling probabilities. In reality, the direct measurement of tunnelling polarisations suggests that different Bloch states tunnel with differing probabilities. In an amorphous barrier such as Al_2O_3, there is no overall symmetry and all the Bloch

states have a finite tunnelling probability. In a fully crystalline barrier such as MgO, coherent tunnelling may be expected due to the periodic potential of the barrier. This acts to enhance the spin-dependency of the tunnelling and enhance the TMR.

Theoretical predictions of extremely large TMR in fully epitaxial (001) orientated Fe/MgO/Fe tunnel junctions were made in 2001 by Butler *et al* [44] and Mathon and Umerski [45]. These materials received attention because the [100] interplanar spacing of iron conforms very well to the [110] spacing of MgO. Under a 45° rotation about the (001) axis, and with a relatively small 3.9% compression of the MgO, growth of a perfectly coherent MTJ was thought feasible. From first principle calculations, these nominally perfect epitaxial structures were predicted to give 1000% TMR or greater, a value which would in principle increase without limit as the barrier thickness increased (although the junction resistance would also increase.)

The realisation of epitaxial Fe/MgO/Fe tunnel junctions was reported in 2004 by Yuasa *et al* [52]. Similar TMR performance was obtained with CoFe/MgO/CoFe systems, which were produced at the same time by Parkin *et al* using sputtering [53]. The MgO barrier in this case had a strong preferential alignment in the plane (texture), but was not genuinely single crystal. Djayaprawira, Yuasa *et al* [54] later produced 230% TMR in an MTJ with a crystalline MgO barrier between amorphous CoFeB ferromagnetic layers. This unusual structure was commercially important because it was compatible with industrial sputtering processes. The paradox of tunnelling between amorphous electrodes was resolved when Yuasa *et al* [55] observed that the CoFeB layers in contact with the MgO barrier had crystallized upon annealing at 523K, adopting the bcc structure of the barrier through a process called *solid phase epitaxy*.

Due to the commercial potential of magnetoresistive sensors, there has been an extensive focus on the optimisation of layers and interfaces. One of the initial difficulties in producing Fe/MgO/Fe MTJs was that the iron atoms at the interface were easily oxidized [56]. It was shown that this disrupted the coupling of the iron Δ_1 Bloch states with corresponding evanescent Δ_1 states in the MgO barrier, reducing the spin-dependency of the tunnelling [57]. The effect of interdiffusion at the interface has been calculated by Tsymbal and Pettifor [58] and by Mathon and Umerski [59], with results which explain the discrepancy between measured TMR and the extremely large theoretical values.

2.6.4. Magnetic random access memory

Magnetic tunnel junctions have been arranged into an array of memory cells known as MRAM [for a review on the development of MRAM, see ref. 6]. This technology combines the non-volatility of magnetic recording with a purely electronic mechanism to address each bit of data. Each memory element must be integrated with one transistor, giving rise to challenges in production, and providing the principal limiting factor to the areal bit density. A method for increasing the data storage density by storing multiple bits per memory element (and therefore per transistor) was proposed in 2008 by Atkinson, Eastwood and Bogart [60].

2.6.5. Magnetoresistive sensors

A substantial review of magnetoresistance applications in field sensing was written in 2007 by Freitas *et al* [41].

Magnetoresistive sensors are engineered on the microscale, nanoscale and atomic scale in order to increase both the sensitivity to external magnetic fields, and the lateral resolution of measurements. In many applications including hard disk read heads the sensor is required to give a linear change in output voltage with varying external field. This means that the magnetoresistance of the device changes slowly as the relative orientation of the easy and hard magnetic layers switches, in contrast with the sharp binary response that may be desired in memory applications (for example, MRAM).

In order to linearize the sensor output, the easy axes of the free and pinned layers are set orthogonal to each other by applying a magnetic field during film deposition to induce different magnetic anisotropies. Normally, the device is patterned with a high shape aspect ratio (as Figure 2-15a), and the pinned ferromagnetic layer is pinned perpendicular to the long axis. The zero-field state of the free layer follows the natural shape anisotropy along the long axis (Figure 2-15b), and rotates when exposed to an external field to be either more parallel or more antiparallel to the pinned reference layer, as shown in Figure 2-15(c) for the case of a hard disk read head. This provides an approximately linear response since the change in output voltage is proportional to $\langle \cos(\Theta_R) \rangle$ where Θ_R is the relative magnetization angle and $\langle ... \rangle$ denotes a spatial average over the sensor area [41].

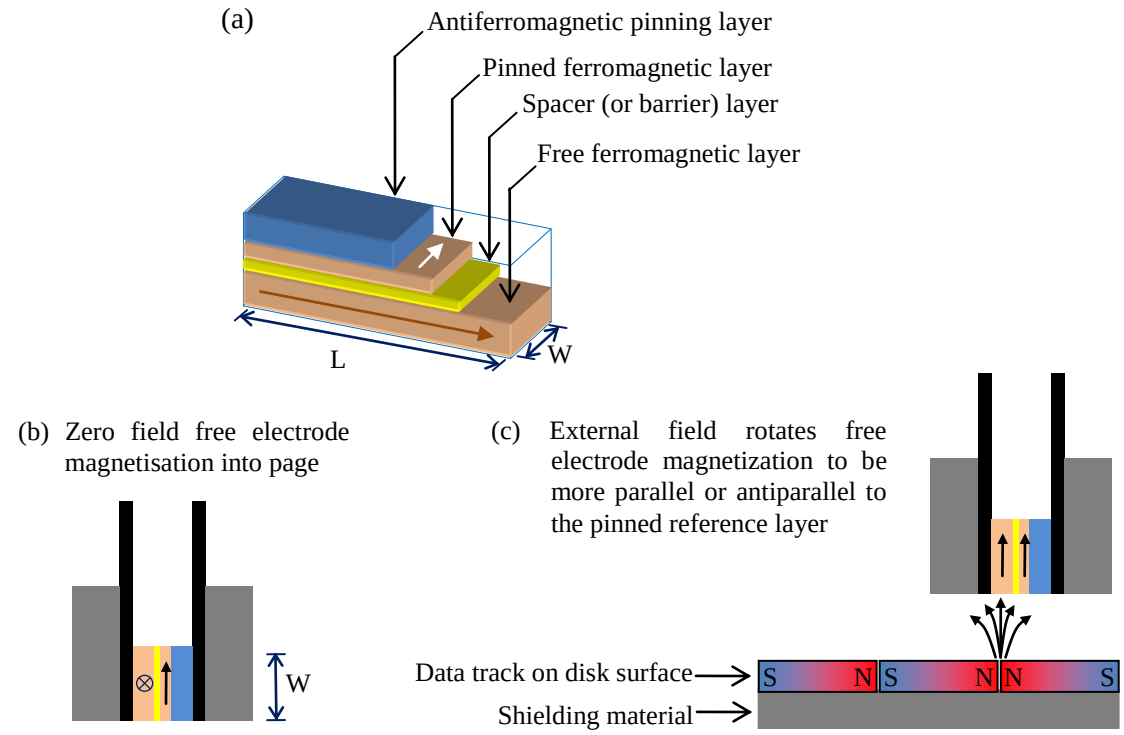

Figure 2-15. (a) Schematic cut-away of a simplified spin valve or tunnel junction structure with easy axes orthogonal to one another, so as to give a linear change in output voltage with applied field. Arrows indicate easy axis magnetizations, set by inducing a magnetic anisotropy during film deposition. (b) Schematic diagram of a current-perpendicular-to-plane MR sensor used as a read head in the zero field state. (c) Read head sensor when exposed to external field, causing a rotation of the free layer [adapted from ref. 41, figure 6].

There is often a zero-field offset present in the linear response due, primarily, to interlayer coupling between the free and pinned electrodes. There are a variety of mechanisms, including magnetostatic coupling due to stray fields, and Néel coupling due to topological undulation. This coupling can be compensated for by the application of a biasing field, although the direct limitation of coupling is a key design requirement (and was one motivation for the development of the synthetic antiferromagnet discussed earlier in section 2.6.2). The reduction of Néel coupling by controlling interface topology is the subject of chapter 4.

3. The theory of grazing incidence x-ray scattering

Grazing incidence x-ray scattering is sensitive to key structural properties of nanoscale thin films, including layer thicknesses, interface topology, interdiffusion at material boundaries, in-plane crystal structure and engineered surface patterning.

In this chapter a theoretical foundation is laid for the experimental studies in later chapters. The interaction of x-rays with matter is introduced, and the different formulations and calculation methods required to interpret x-ray scattering from structures over varying length scales and dimensions are presented.

3.1. Introduction

The interaction of the photon with the electron has provided many crucial insights into the structure of matter, playing a starring role in the development of new physics during the twentieth century. The process is fundamentally understood using quantum electrodynamics. The subject of this thesis, however, is not the behaviour of the electron or the internal structure of the atom but the structural characterization of atomic layers in nanoscale thin films. The measurements observe the scattering of x-rays by large numbers of electrons confined within atoms bound together in a solid.

X-ray generation occurs in two distinct physical processes: acceleration and fluorescence. An accelerating (or decelerating) charge emits radiation, and when the charged particles are of sufficient energy this radiation is in the x-ray regime. Such a sharp acceleration occurs when electrons rapidly decelerate after impact with a solid material, resulting in x-rays termed *Bremsstrahlung* or braking radiation. Acceleration also occurs when relativistic electrons circulate under the constraint of strong magnetic fields within electron storage rings (where it is termed *synchrotron* radiation.) The second process is x-ray fluorescence, and occurs when an incident electron causes core-shell ionisation in a target material. The subsequent relaxation of an outer shell electron to fill the inner shell vacancy causes the release of an x-ray with energy characteristic of the electronic transition.

X-rays were first reported by Röntgen in 1895 [61], who famously captured a shadow image of the bones in his wife's ring-bearing hand. Experimental studies of materials by x-ray diffraction started with Friedrich and Knipping and von Laue in 1912 [62], who measured the diffraction pattern of rock salt. In the same year, and following the work of his father, W.L. Bragg [63] described x-ray diffraction with the law $n\lambda = 2d\sin\theta$. Over the next few years further advances in the understanding of x-ray diffraction were made by von Laue [64], Ewald [e.g. ref. 65], Debye, Compton and many of their contemporary physicists. The total external reflection of x-rays was first reported by Compton in 1923 [66], but the exploitation of x-ray reflectivity as an analysis technique evolved more slowly than the field of diffraction.

The characteristic penetration length of x-rays into a bulk material depends upon the energy of the beam, and is usually of the order of ten to a hundred micrometers. This is significantly deeper than most thin film structures which range from single atomic layers to several hundred nanometres thick. In order to maximise the interaction of x-rays with the layers of interest, it is common to arrange a very small *grazing* angle of incidence for the incident beam. In this geometry, two common measurements are *x-ray reflectivity* where reflections from layer interfaces are observed, and *grazing incidence x-ray diffraction* when atomic planes perpendicular to the surface are set to diffract.

In addition to geometrically increasing the path of the x-rays within the uppermost layers, grazing incidence scattering gives enhanced surface sensitivity due to the evanescent wave which occurs for totally externally reflected x-rays. This chapter presents a formalism describing refraction, reflection, transmission and elastic scattering under grazing incidence, and explains how these phenomena are exploited to provide structural information from varying length scales and orientations.

3.1.1. A summary of background literature

Whilst primary references are attributed wherever possible in this chapter, many of the well understood principles of grazing incidence x-ray scattering have been compiled in excellent textbooks and review articles. The electromagnetic theory of light is comprehensively detailed in the seminal book of Born and Wolf [67]. Als-Nielsen and McMorrow [68] provide an excellent introduction to the whole field of x-ray scattering, whilst Birkholz [69], Pietsch, Holý and Baumbach [70] and Tolan [71] all describe methods suited to thin films and nanostructures. Bowen and Tanner [72] cover the application of x-ray scattering techniques for precision quality control. Robinson and Tweet [73] review the diffraction of x-rays from surfaces, and Stoev and Sakurai [74] cover the development of grazing incidence reflectometry and fluorescence. The use of

x-rays to study self-assembled nanostructures is discussed in a review by Stangl, Holý, and Bauer [75] and a book by Schmidbauer [76].

3.2. The interaction of x-rays with matter

3.2.1. Scattering from a free electron

In the simple classical model of elastic charge scattering (also called Thomson scattering), the electric field of an x-ray interacting with an electron causes the electron to oscillate, and re-radiate an electric field. The acceleration *a* of the electronic dipole observed at a distance *R* is:

$$a(t') = \frac{F}{m_e} = \frac{-e}{m_e} E_0 \exp(-i\omega t') \cos\psi \tag{3.1}$$

Where $t' = t - R/c$ allows for the time the scattered wave takes to reach the observer and ψ is the angle within the incident plane of polarisation relative to the direction of propagation.

Since the energy density at a distance *R* from a point source must decrease as $1/R^2$, the electric field amplitude decreases as $1/R$. The field radiated is also proportional to the charge of the electron, and must be normalized by a factor $1/4\pi\varepsilon_0 c^2$ for SI unit calculations. In the plane of polarization the re-radiated wave is:

$$\begin{aligned} E_{rad}(R) &= -\frac{1}{4\pi\varepsilon_0 c^2}\frac{-e}{R} a(t') \\ &= -\frac{1}{4\pi\varepsilon_0 c^2}\frac{-e}{R}\frac{-e}{m_e} E_0 \exp\left(\frac{i\omega R}{c}\right)\cos\psi \end{aligned} \tag{3.2}$$

The constant terms are general for a classical free electron. They are collected together as the Thomson scattering length:

$$r_0 = \left(\frac{e^2}{4\pi\varepsilon_0 m_e c^2}\right) = 2.8179 \times 10^{-15}\,\mathrm{m} \quad (5\ \text{s.f.}) \tag{3.3}$$

The remaining term, $\exp(ikR)/R$ describes a spherically emanating wave.

The electric field scattered within the incident plane of polarisation (termed π-polarisation) is therefore written:

$$E_{rad}(R) = -E_0 \frac{r_0}{R} \exp(ikR) \cos\psi \tag{3.4}$$

When the observation direction is perpendicular to the polarisation direction (σ-polarization), the $\cos\psi$ term becomes unity and the entire dipole moment is projected onto the detector window.

π and σ polarisations are both naturally obtained from bending magnet synchrotron radiation, the first is observed in the plane of the storage ring, and the second perpendicular to the plane of the storage ring. In the case of a laboratory fluorescence source, the completely unpolarized radiation is an incoherent combination of the two.

The general scattered electric field from an electron is written:

$$E_{rad}(R) = -E_0 \frac{r_0}{R} \exp(ikR)\, P \tag{3.5}$$

where the polarization term is given by:

$$P = \begin{cases} \cos\psi & \text{observed in the plane of polarization } (\pi\text{–polarized}) \\ 1 & \text{observed perpendicular to the plane of polarization } (\sigma\text{–polarized}) \\ \sqrt{\frac{1}{2}\left(1+\cos^2\psi\right)} & \text{for randomly polarized incident x-rays} \end{cases}$$

The minus sign in Eq. (3.5) implies that the scattered wave has a π phase shift with respect to the incident wave.

3.2.2. Definitions of scattering in real and reciprocal space

Before the scattering from an assembly of electrons can be considered, some geometrical definitions require introduction.

The reciprocal space lattice is described by the three perpendicular primitive vectors $\mathbf{b_1}$, $\mathbf{b_2}$ and $\mathbf{b_3}$, which are related to the real space lattice vectors $\mathbf{a_1}$, $\mathbf{a_2}$ and $\mathbf{a_3}$ by the conventional relations:

$$\mathbf{b}_1 = \frac{\mathbf{a}_2 \times \mathbf{a}_3}{\mathbf{a}_1 \cdot \mathbf{a}_2 \times \mathbf{a}_3}, \mathbf{b}_2 = \frac{\mathbf{a}_3 \times \mathbf{a}_1}{\mathbf{a}_1 \cdot \mathbf{a}_2 \times \mathbf{a}_3}, \mathbf{b}_3 = \frac{\mathbf{a}_1 \times \mathbf{a}_2}{\mathbf{a}_1 \cdot \mathbf{a}_2 \times \mathbf{a}_3} \tag{3.6}$$

For the experimental geometry where the scattering plane is normal to the sample surface (as defined in Figure 3-1), the incident wavevector $\mathbf{k_{in}}$ makes an angle α_i with the surface, and the scattered wavevector $\mathbf{k_{out}}$ makes an angle ($2\theta - \alpha_i$) with the surface. For elastic scattering $\mathbf{k_{in}}$ and $\mathbf{k_{out}}$ have the same magnitude: $|\mathbf{k}| = 2\pi/\lambda$.

For historical reasons the label (2θ) is given to the scattering angle; in an experiment this is the angle of the detector in the scattering plane relative to the incident beam.

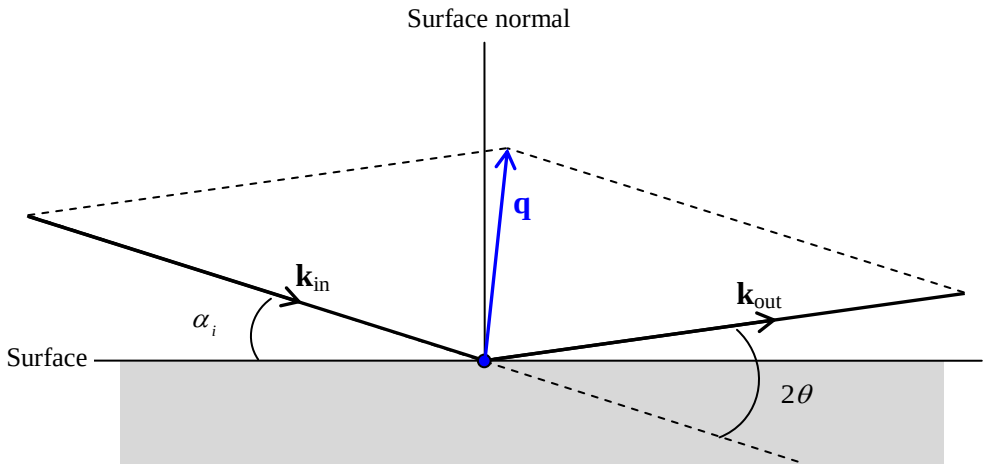

Figure 3-1. The relation of wavevectors to the experimental geometry.

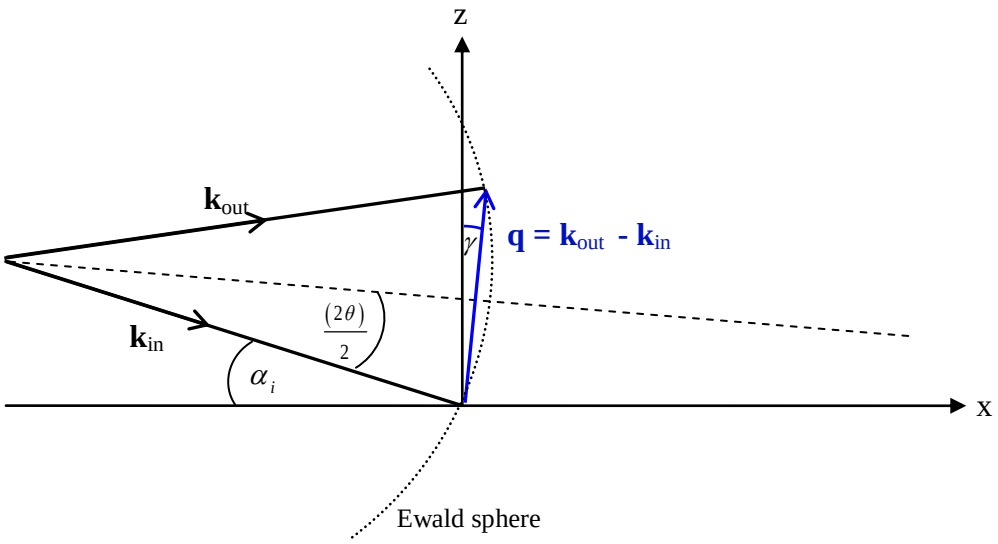

Figure 3-2. A geometrical construction relating coordinate systems and defining the scattering vector, **q**.

The scattering vector $\mathbf{q} = (q_x, q_y, q_z) = q_x \mathbf{b_1} + q_y \mathbf{b_2} + q_z \mathbf{b_3}$ is the difference between $\mathbf{k_{in}}$ and $\mathbf{k_{out}}$, as shown in Figure 3-2.

From the geometrical construction in the previous figure, it is possible to derive a trigonometric conversion between angular coordinates and the reciprocal space scattering vector in the plane containing the incident and scattered directions:

$$q_x = 2k \sin\left(\frac{2\theta}{2}\right)\sin(\gamma) \tag{3.7}$$

$$q_z = 2k \sin\left(\frac{2\theta}{2}\right)\cos(\gamma) \tag{3.8}$$

A grazing incidence scan for which the incident and exit angles are equal (meaning that $\gamma = \left[\alpha_i - (2\theta)/2\right] = 0$) defines a *specular reflectivity scan*: $\mathbf{q} = (0, 0, q_z)$ and only the

structure normal to the sample surface is probed. Sensitivity to the in-plane sample structure plane is gained when there is a component of the scattering vector in the plane of the sample. This is commonly found by a sample only (or *transverse diffuse*) scan, where the detector is fixed (2θ is constant, γ varies).

Occasionally the third dimension q_y is also varied. The in-plane vectors must then be redefined as:

$$\begin{aligned} q_x &= k\left[\cos(2\theta - \alpha_i)\cos(\psi) - \cos(\alpha_i)\right] \\ q_y &= k\left[\cos(2\theta - \alpha_i)\sin(\psi) + \cos(\alpha_i)\right] \end{aligned} \tag{3.9}$$

where ψ is the angle in the plane of the sample surface (the *x*-*y* plane) measured from the direction of incidence. The out of plane component q_z is unchanged.

Now that the reciprocal space coordinate system has been defined, it is useful to introduce the Ewald sphere construction. In Figure 3-3(a) the locus of points describing all possible scattering vectors forms a circle (with an equivalent sphere in three dimensions) relative to the vector of incidence. It can be seen that as $\mathbf{k}_{out}$ changes, **q** varies in direction, and can range in magnitude from zero to *2k*. Figure 3-3(b) shows the maximum extent of reciprocal space from [0,0,0] that can be accessed by orientating both the incident and exit wavevectors.

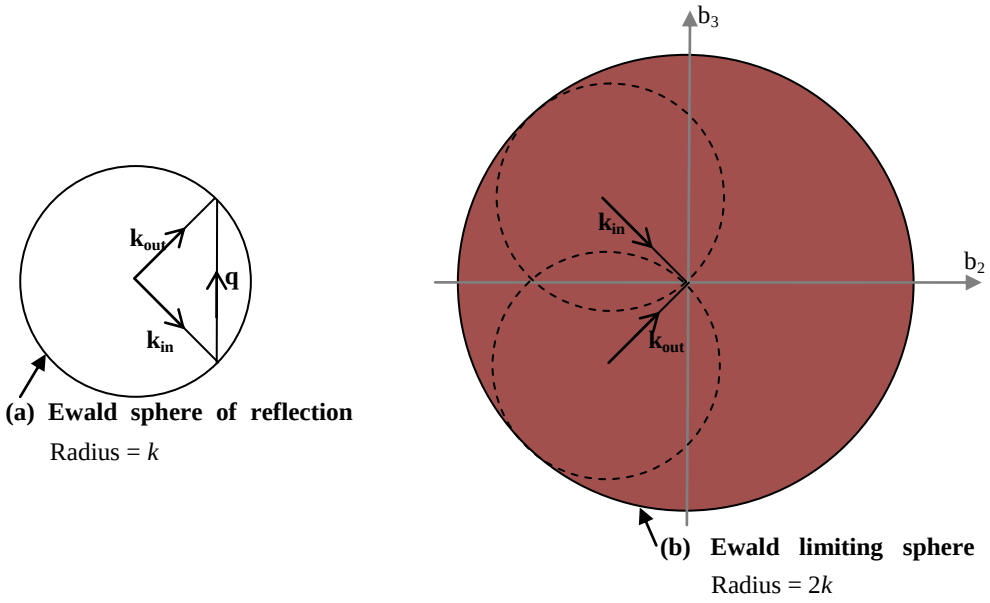

Figure 3-3. (a) Ewald's sphere of reflection, which defines the surface of possible scattering vectors for a fixed incidence vector, (b) Ewald's limiting sphere, which contains the volume of reciprocal space which is accessible by varying both incidence and exit vector relative to the sample. After Born and Wolf [ref. 67, p. 701].

From Eqs. (3.7) – (3.9) and Figure 3-2 it can be deduced that scattering vector is limited by the conditions $-2k \le q_x, q_y \le 2k$ and $0 \le q_z \le 2k$. The simultaneous solution of these equations also requires that $q_x^{\,2} + q_y^{\,2} + q_z^{\,2} \le 4k^2$, which defines the Ewald limiting sphere.

There is an additional constraint due to the sample surface: that if $\alpha_i < 0$ or $(2\theta)/2 < \alpha_i$, all possible beam paths from source to detector pass through the sample in transmission. These constraints are incorporated onto the Ewald limiting sphere in the following figures, represented by the purple regions. (In small angle scattering techniques the transmission zones can be treated as fixed in reciprocal space during one scan). Although diffraction occurring in transmission is a well established field known as Laue diffraction, it is beyond the scope of this thesis.

Onto the Ewald limiting sphere, an arbitrary wavevector diagram is superimposed. During a scan, one or both of the incident and exit wavevectors are varied systematically to achieve an appropriate trajectory of the scattering vector **q**.

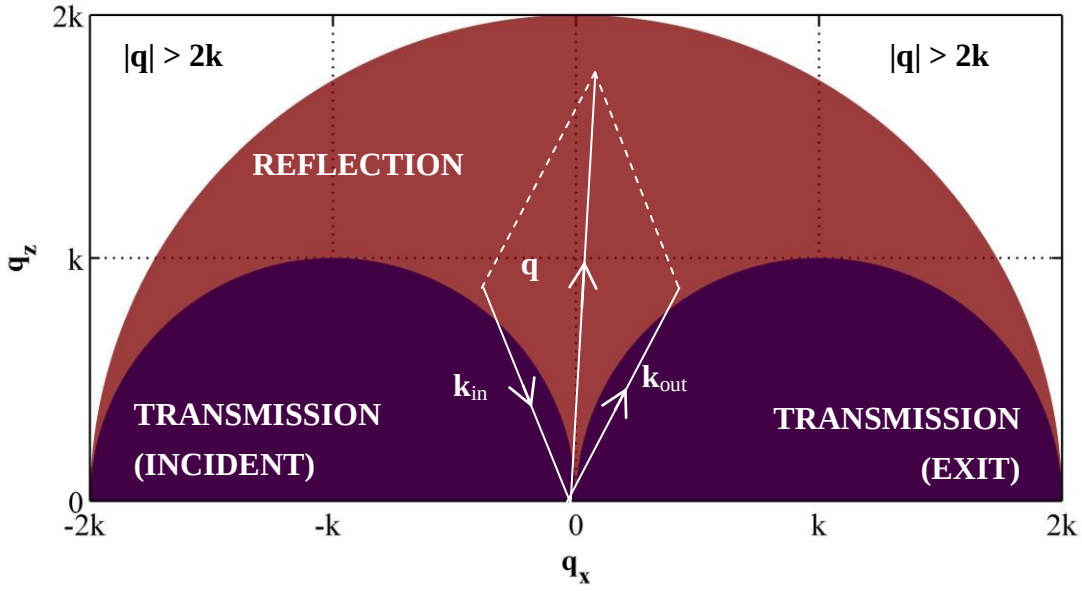

Figure 3-4. The plane of momentum transfer in the x-z plane of the Ewald limiting sphere. The purple areas are the Laue zones for transmission; on the left the incident angle is below the sample surface, on the right the exit angle is below the sample surface. After Schmidbauer [ref. 76, p. 76].

The trajectories of the scattering vector for three common scans are shown on Figure 3-5. In the symmetric case $\alpha_i = (2\theta)/2$, $q_x = 0$ and it is again seen that the scan probes only q_z.

It should be noted that the range of q_x is severely limited by the sample surface, especially at low q_z. Figure 3-6 shows that the range of q_y is not restricted in the same way, and offers an alternative in-plane scan trajectory. Furthermore, in a scan of q_y, the incidence angle remains constant and the penetration depth is unchanged. However an important experimental consideration often favours the q_x-q_z scan: the resolution in the q_x direction is typically an order of magnitude finer than in the q_y direction.

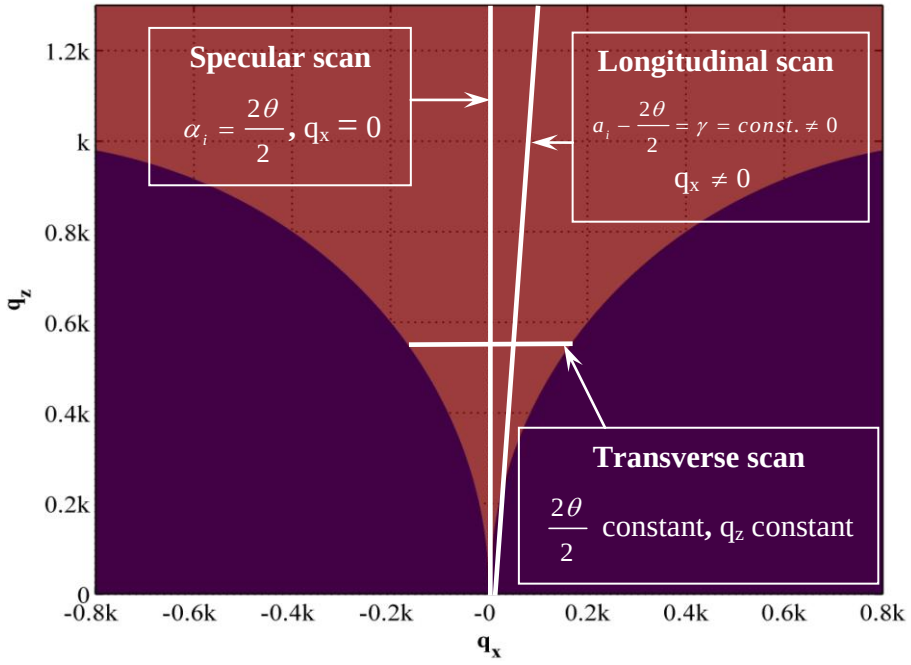

Figure 3-5. An expanded region of Figure 3-4 showing the path of the scattering vector **q** *during scans in reciprocal space.* γ *is typically 0.1°.*

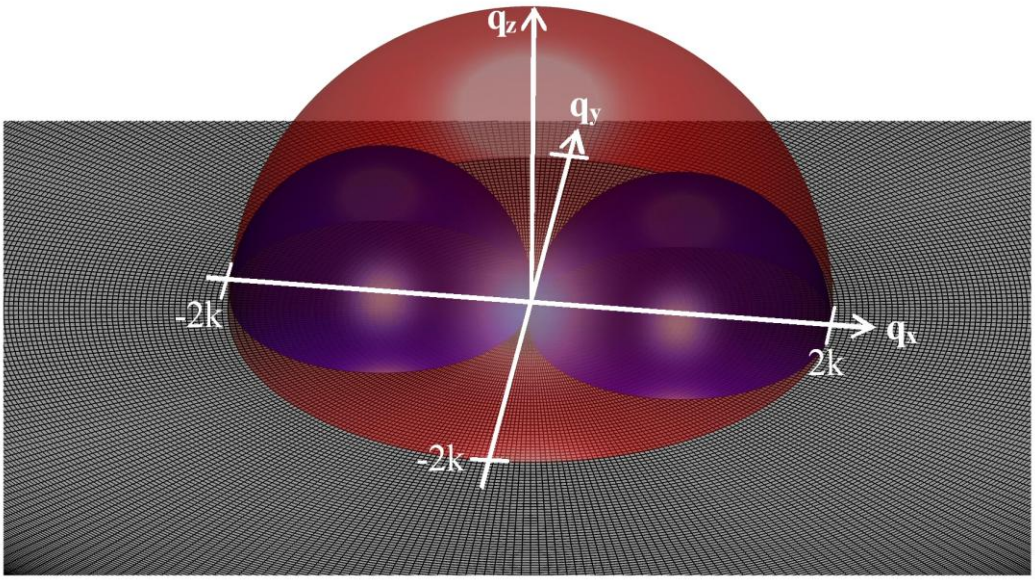

Figure 3-6. A three-dimensional representation of the Ewald limiting sphere. The blue hemispheres represent the region of reciprocal space where the x-rays are transmitted into the sample. The red hemisphere represents the limit of the region accessible by x-rays with incident wavevector **k**.

3.2.3. Scattering from electrons in an atom

The discussion now returns to scattering from an ensemble of electrons in a solid. Electrons are arranged according to the atomic lattice, and in a quantum description are also bound in discrete energy levels.

Initially, consider a classical atom with a uniform electronic structure with electron density $\rho(\mathbf{r})$. The relative phase difference between a wave scattered at the origin of the atom and one at the relative position **r** is:

$$\Delta\phi(\mathbf{r}) = (\mathbf{k}_{out} - \mathbf{k}_{in}).\mathbf{r} = \mathbf{q}.\mathbf{r} \tag{3.10}$$

where **q** is the scattering vector defined earlier as $\mathbf{q} = (\mathbf{k}_{out} - \mathbf{k}_{in})$.

The scattering contributions from the entire atom are found by integrating the atom over **r** to determine the total atomic scattering length:

$$-r_0 f^0(\mathbf{q}) = -r_0 \int \rho(\mathbf{r}) \exp(i\mathbf{q}.\mathbf{r})\, d\mathbf{r} \tag{3.11}$$

Here, $f^0(\mathbf{q})$ is the atomic form factor and is seen to be the Fourier transform of the electron density. For $|\mathbf{q}| \to 0$ the entire atom scatters in phase and f^0 is equal to the atomic number of the atom. For $|\mathbf{q}| \to \infty$, the wavelength of the x-ray is small compared to the atom, and the electrons scatter incoherently.

To a good approximation, f^0 follows the empirical model [ref. 69, p. 18]:

$$f^0 = \sum_{n=1}^{4} a_n \exp\left(-b_n \frac{\sin^2\left(2\theta/2\right)}{\lambda^2}\right) + c = \sum_{n=1}^{4} a_n \exp\left(-b_n \frac{|q|^2}{16\pi^2}\right) + c \qquad (3.12)$$

where a_n, b_n and c are empirical constants which have been tabulated for selected atomic and ionic species [77]. For $2\theta/2 \to 0$, this relation must (and does) give $f^0 \to Z$.

In reality the assumption of a uniform distribution of electrons is invalid, and it is necessary to modify this classical theory to account for the binding of electrons in atomic shells using the energy-dependent dispersion corrections f' and f''. Electrons in the innermost K shell will be strongly bound and therefore have a heavily damped response if the incident energy is less than the binding energy of that electron. The amplitude damping is reflected in the f' term, which is nonzero below the binding energy of the electron, and drops to zero well above the binding energy.

The binding of electrons can also cause an additional phase lag, which is described by the f'' term. These are combined as:

$$f(\mathbf{q}, E) = f^0(\mathbf{q}) + f'(E) + if''(E) \qquad (3.13)$$

The dispersion corrections are most influential when the x-ray energy is tuned to an absorption edge of the inner shell electrons, and can provide element specificity to diffraction measurements. In this thesis, scattering is considered to be well away from absorption edges, in the non-resonant regime.

Scattering is observed most strongly when many atoms scatter in phase. X-ray metrology most commonly uses x-ray diffraction, where the scattering vector matches the interplanar spacing of a crystal (to be described in section 3.5). Much of this thesis however is concerned with reflectivity and diffuse scatter measurements from thin films, where the scattering vector is sensitive to the nature of coherent scattering from surfaces and interfaces on much longer length scales than the crystal lattice. In order to achieve both an appropriate scattering vector and a high sensitivity to surface layers, scattering at grazing incidence to the sample surface is applied.

3.2.4. Absorption and the penetration depth of x-rays

Before moving to a description of reflectivity, an understanding of the penetration of x-rays into bulk material must be developed.

Initially, the exponential decay of the x-ray intensity into any sample can be characterized simply by the 1/*e* penetration depth for the incident intensity measured perpendicularly into the sample, labelled $\tau_{1/e}$.

The absorption of x-rays with energy less than 10 keV is dominated by photoelectric ionisation, where the energy carried by the x-ray is transferred to an ejected electron. At higher energies, elastic (Thomson) or inelastic (Compton) scattering become dominant interactions, and at very high energies (greater than 1 MeV) electron-positron pair production occurs.

The linear attenuation coefficient characterizes the strength of the absorption process. Values are tabulated for all elements at varying incident energies and are published [e.g. in ref. 78]; as an example, the penetration depth into silicon is given in Figure 3-7.

Penetration increases with energy, following an approximately E^3 dependence except at transition edges where a new photoionisation process becomes possible and the penetration decreases sharply. The overall trend of decreasing absorption with increasing energy can be attributed to the scattering mechanisms. The atom is understood as a driven oscillator with multiple resonant frequencies. As the incident energy increases above a transition, the electron's oscillatory response decreases as E^{-3}. Below the transition, the electron is tightly bound and has a negligible response.

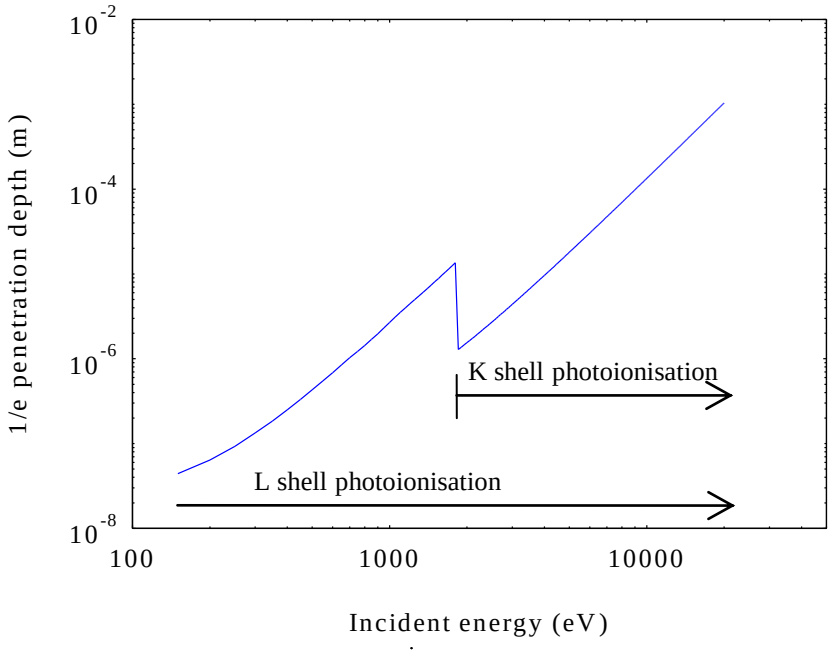

Figure 3-7. 1/e penetration depth into silicon for x-rays of varying incident energy [plotted using data from ref. 78].

For grazing incidence geometries, the penetration depth may be defined in terms of the grazing incidence angle α_i and the linear attenuation coefficient μ through the equation:

$$\tau_{1/e} = \frac{\sin \alpha_i}{\mu} \tag{3.14}$$

An alternative definition is the depth from which (1–1/*e*) of the incident intensity is measured leaving the sample. This is calculated using the grazing exit angle α_f as:

$$\tau_{1-1/e} = \frac{1}{\mu g_\alpha} = \frac{\sin \alpha_i \sin \alpha_f}{\mu \left(\sin \alpha_i + \sin \alpha_f \right)} \tag{3.15}$$

where g_α is a geometrical path length factor given by

$$g_\alpha = \frac{1}{\sin \alpha_i} + \frac{1}{\sin \alpha_f} \tag{3.16}$$

The *probe* depth, which is the average depth from which scattered information is detected from film of thickness *t*, can be calculated by integrating the intensity scattered over all depths into the film:

$$\bar{\tau}_\alpha = \frac{1}{\mu g_\alpha} + \frac{t}{1 - \exp\left(\mu t g_\alpha \right)} \tag{3.17}$$

For an infinitely thick film, the limiting value of this probe depth is $\tau_{1\text{-}1/e.}$ As the grazing incidence angle increases so that attenuation in the thin surface film becomes negligible, the film probe depth tends to half the film thickness, *t*/2.

This description neglects the deformation of the wavefront due to the change of refractive index upon entering a material. It includes only the geometry of the scattering and the linear absorption of the material, providing a simple method for normalizing a signal scattered by the grazing angle. For a fuller understanding, the refractive index as a bulk material property must be considered.

3.3. The refractive index and specular reflectivity

X-ray reflectivity is often used to measure the interference of x-rays scattered from the interfaces in thin film structures. The strength of reflectivity from a single interface is determined by the difference in refractive index above and below the interface, and by the width of the interface region. The refractive index is intimately related to the scattering factor of a medium, as will be demonstrated. First, the concept of the refractive index will be introduced.

3.3.1. The refractive index of a medium

The absolute index of refraction n is defined as the ratio of the phase velocity of an electromagnetic wave in vacuum c to the phase velocity in matter v,

$$n \equiv \frac{c}{v} \tag{3.18}$$

For visible light n is greater than unity; for x-rays, n can be ~ 1×10^{-5} less than unity. This is observed as total external reflection at very shallow angles of incidence, below a critical angle. Above the critical angle the electromagnetic wave will penetrate into a film, and partial reflection from each interface can be observed and interpreted to characterize multiple internal interfaces.

The deviation of n from unity is expressed in the terms δ and β, which are dispersion and absorption terms respectively, so that $n = 1 - \delta + i\beta$. The refractive index varies with the energy of the electromagnetic wave and displays resonant behaviour close to the electronic transitions in the material. The resulting long-range trend is one of decreasing δ with increasing energy, as shown for silicon and iron in Figure 3-8. This means that by tuning the incident energy close to a binding energy of a material, it is possible to increase n dramatically. β is approximately two orders of magnitude smaller than δ, and exhibits stepped increases at binding energies, where new absorption processes become possible.

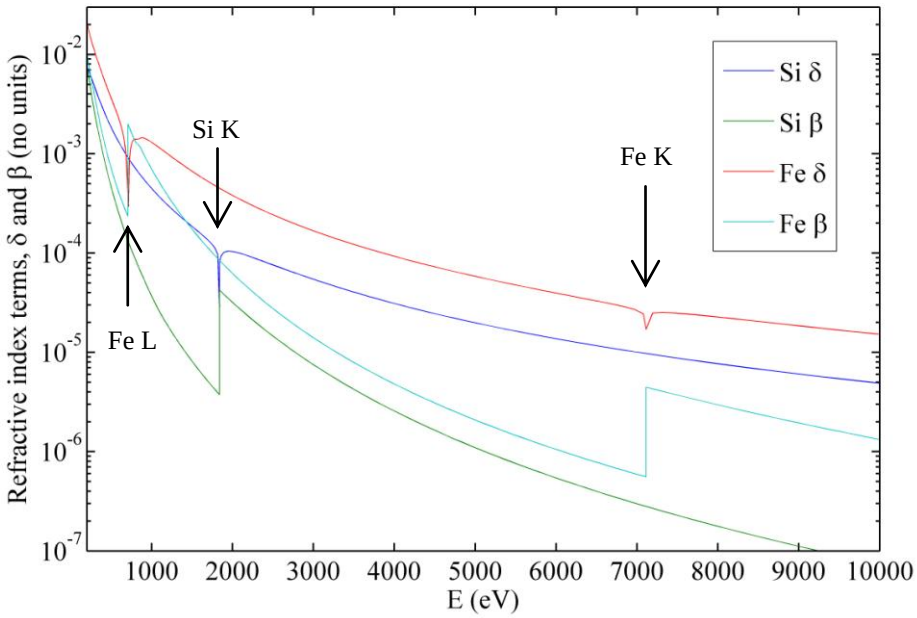

Figure 3-8. The real and imaginary refractive index terms δ and β for silicon and iron. Labels relate to absorption edges.

It can be seen that the refractive index is related to the scattering strength of a material. A complete derivation is given by Als-Nielsen and McMorrow [ref. 68, pp. 64-70], but here the result will simply be stated:

$$n = 1 - \frac{r_e}{k^2}\sum_A \rho_A \left(Z_A + f_A' - if_A''\right) \tag{3.19}$$

This is valid for a compound material where A denotes the parameters relating to element A and ρ_A is the atomic number density of element A. The electronic density of material A is therefore $\rho_A Z_A$, where the atomic number Z_A is a good approximation to f^0 for the small angles used in grazing incidence scattering.

3.3.2. Transmission and reflection of x-rays at a single interface

The time-independent component of the propagating electric field has the form $\mathbf{E} = \mathbf{E}_0 \exp(i\mathbf{k}.\mathbf{r})$. The incident, reflected and transmitted electric fields at the interface shown in Figure 3-9 are described by $\mathbf{E}_i$, $\mathbf{E}_r$ and $\mathbf{E}_t$ respectively.

From the definition of the refractive index:

$$\left|\mathbf{k}_{vacuum}\right| = \frac{\left|\mathbf{k}_i\right|}{n_0} = \frac{\left|\mathbf{k}_r\right|}{n_0} = \frac{\left|\mathbf{k}_t\right|}{n_1} \tag{3.20}$$

Continuity of the electromagnetic field and its derivative at the interface requires that:

$$\left|\mathbf{E}_i^0\right| + \left|\mathbf{E}_r^0\right| = \left|\mathbf{E}_t^0\right| \tag{3.21}$$

And:

$$\mathbf{k}_i\left|\mathbf{E}_i^0\right| + \mathbf{k}_r\left|\mathbf{E}_r^0\right| = \mathbf{k}_t\left|\mathbf{E}_t^0\right| \tag{3.22}$$

In the case of specular reflection $\alpha_i = \alpha_r$, and with $\mathbf{k}_i = \mathbf{k}_r$, resolving (3.22) parallel and perpendicular to the interface produces:

$$\mathbf{k}_{i,r}\left(\left|\mathbf{E}_i^0\right| + \left|\mathbf{E}_r^0\right|\right)\cos\alpha_{i,r} = \mathbf{k}_t\left|\mathbf{E}_t^0\right|\cos\alpha_t \tag{3.23}$$

and:

$$\mathbf{k}_{i,r}\left(\left|\mathbf{E}_i^0\right| - \left|\mathbf{E}_r^0\right|\right)\sin\alpha_{i,r} = \mathbf{k}_t\left|\mathbf{E}_t^0\right|\sin\alpha_t \tag{3.24}$$

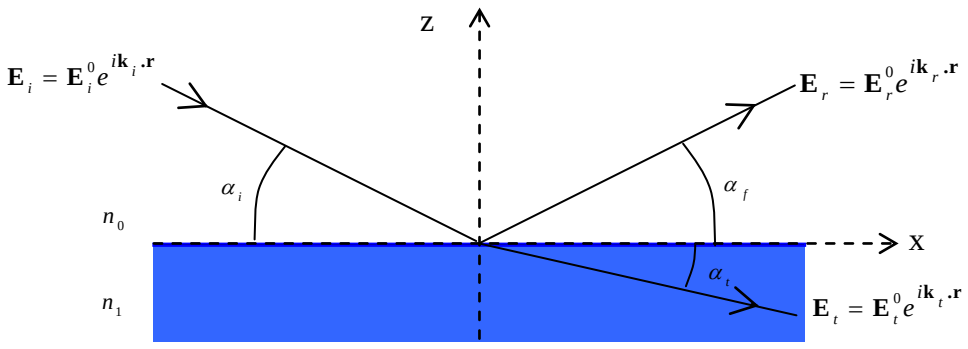

Figure 3-9. Reflection and transmission at an interface with a single, infinite thin film layer.

Substitution of (3.20) and (3.21) into (3.23) yields Snell's law:

$$n_0 \cos \alpha_{i,r} = n_1 \cos \alpha_t \tag{3.25}$$

The critical angle α_c where $\alpha_t = 0$, can be expressed as $\cos \alpha_c = n_1$ (assuming $n_0 = n_{air} \approx n_{vacuum} = 1$, $\cos x \approx 1 - x^2/2$, and negligible absorption, i.e. $\beta_1 \approx 0$), which implies that:

$$\alpha_c \approx \sqrt{2(1-n_1)} \approx \sqrt{2\delta} = \sqrt{\frac{4\pi\rho_e r_e}{k^2}} \tag{3.26}$$

Equation (3.26) allows a simple measurement of the electron density close to the surface of the sample from the position of the critical angle.

Furthermore, combining (3.21) and (3.24) leads to:

$$\frac{E_i^0 - E_r^0}{E_i^0 + E_r^0} = \frac{|\mathbf{k}_t| \sin \alpha_t}{|\mathbf{k}_{i,r}| \sin \alpha_{i,r}} = \frac{n_1 \sin \alpha_t}{n_0 \sin \alpha_{i,r}} \tag{3.27}$$

From (3.27) the Fresnel amplitude reflectivity is expressed (in angular terms) as:

$$r = \frac{E_r^0}{E_i^0} = \frac{n_0\alpha_{i,r} - n_1\alpha_t}{n_0\alpha_{i,r} + n_1\alpha_t} \tag{3.28}$$

And the Fresnel amplitude transmission coefficient is:

$$t = \frac{E_t^0}{E_i^0} = 1 + \frac{E_r^0}{E_i^0} = 1 + \frac{n_0\alpha_{i,r} - n_1\alpha_t}{n_0\alpha_{i,r} + n_1\alpha_t} = \frac{2n_0\alpha_{i,r}}{n_0\alpha_{i,r} + n_1\alpha_t} \tag{3.29}$$

Equivalently, the Fresnel coefficients may be expressed in terms of the *z*-components of the propagating wavevectors in the neighbouring media,

$$r = \frac{E_r^0}{E_i^0} \approx \frac{k_z^{i,r} - k_z^t}{k_z^{i,r} + k_z^t} \tag{3.30}$$

and:

$$t = \frac{E_t^0}{E_i^0} \approx \frac{2k_z^{i,r}}{k_z^{i,r} + k_z^t} \tag{3.31}$$

The corresponding intensity coefficients for reflection and transmission, *R* and *T* are found as the absolute squares of the amplitude coefficients *r* and *t*. Typical theoretical trends for these parameters are plotted in Figure 3-10 for the case of iron. The critical angle is approximately 0.38˚, above which the incident beam is predominantly transmitted into the sample and reflectivity drops sharply as α_i^{-4}. The increase in *T* at the critical angle is due to the coherent summation of the reflected and transmitted electric field vectors. As absorption becomes negligible ($\beta \to 0$), the maximum of $T \to 4$.

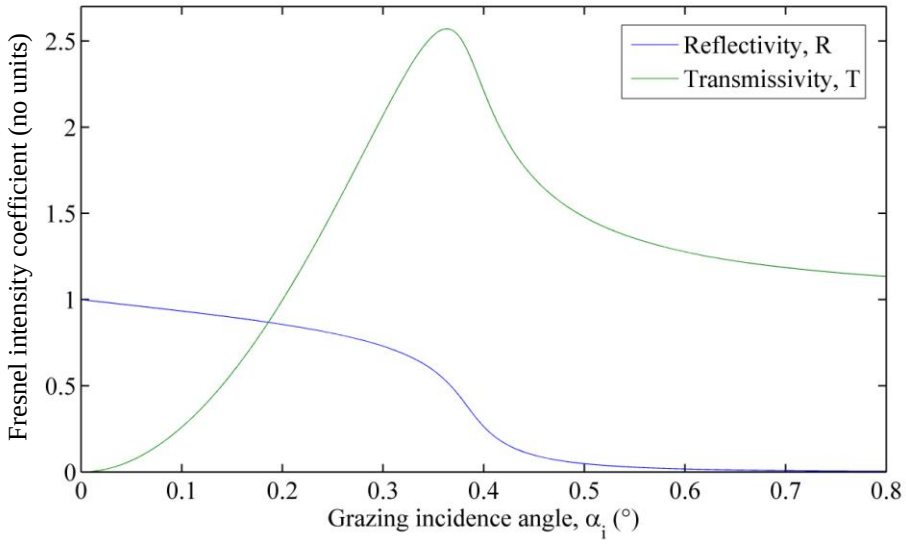

Figure 3-10. Calculated Fresnel transmissivity and reflectivity for iron at 8.051 eV.

3.3.3. The penetration depth due to refraction

Consider again Snell's law, now using the complex refractive index. The angle of transmission can be expressed as (the complex angle):

$$\alpha_t = \sqrt{\alpha_i^2 - \alpha_c^2 - 2i\beta} \tag{3.32}$$

By separating this into real and imaginary parts,

$$\alpha_t = \mathrm{Re}(\alpha_t) + \mathrm{Im}(\alpha_t) = B_+ - iB_- \tag{3.33}$$

Where [following ref. 69, p. 163] the terms B_+ and B_- are given by:

$$B_\pm^2 = \frac{1}{2}\left[\sqrt{\alpha_i^2 - \alpha_c^2 + 4\beta^2} \pm \left(\alpha_i^2 - \alpha_c^2\right)\right] \tag{3.34}$$

Inserting these into the exponential form for the electric field in a medium,

$$E_t = E_0 \exp\left\{-ik_t\left(x\cos\alpha_i - zB_+\right)\right\}\exp\left\{-xk_tB_-\right\} \tag{3.35}$$

By inspection, when $\alpha_i < \alpha_c$ this predicts a plane wave that propagates along x, but decays exponentially into the material with z. Including these refraction effects, $\tau_{1/e}$ may be written:

$$\tau_{1/e} = \frac{1}{2k_tB_-} = \frac{1}{k_t\sqrt{2}}\left[\sqrt{\left(\alpha_i^2 - \alpha_c^2\right)^2 + 4\beta^2} - \left(\alpha_i^2 - \alpha_c^2\right)\right]^{-1/2} \tag{3.36}$$

The resulting calculation for of the penetration depth is shown in Figure 3-11, and compared with the simple exponential absorption dependency of Eq. (3.14).

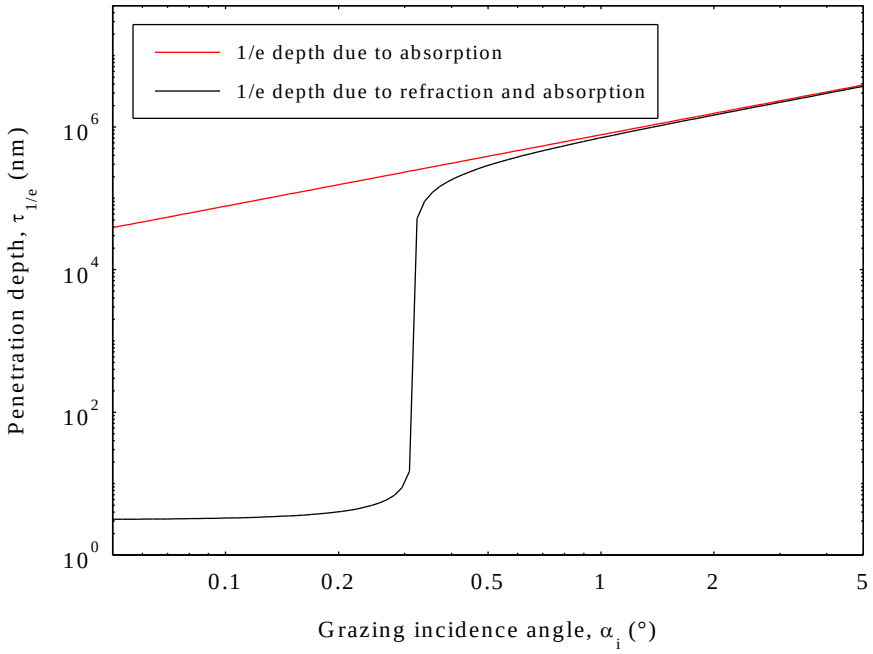

Figure 3-11. The penetration depth against angle of incidence calculated with and without consideration of refractive effects close to the critical angle. Shown for silicon at incident energy 10 keV.

At low α_i, the incident beam experiences total external reflection; there is only an evanescent surface electric field in the sample, and the penetration depth is a few nanometres. The penetration rapidly increases above the critical angle, reaching a maximum at normal incidence.

The penetration depth into a multilayer sample is not such a trivial calculation; refraction and transmission at each interface, as well as multiple reflections within layers must be included through the calculation of the electric field, and the process becomes increasingly complicated.

3.3.4. Dynamical description of transmission and reflection in a thin film

For the slab of infinite thickness presented in Figure 3-9, there is only one possible reflection-transmission process. In the study of thin film structures, the possibility of transmission and reflection from multiple interfaces must be introduced. Different possible beam paths are illustrated in Figure 3-12 where Δ is the thickness of layer 1.

The total reflectivity of the layer is an infinite sum of all possible reflections:

$$r_{total} = r_{10} + t_{01}r_{21}t_{10}p^2 + t_{01}r_{21}r_{10}r_{21}t_{10}p^4 + \ldots = r_{10} + t_{01}r_{21}t_{10}p^2\sum_{m=0}^{\infty}\left(r_{21}r_{01}p^2\right)^m \qquad (3.37)$$

Where p^2 is a phase factor given by:

$$p^2 = \exp\left(iq_1\Delta\right) \text{ with } q_1 = 2k_1\sin\alpha_1 \qquad (3.38)$$

The summation of the total reflectivity can be evaluated as a geometric series to be:

$$r_{total} = r_{10} + \frac{t_{01} r_{21} t_{10} p^2}{1 + r_{10} r_{21} p^2} \tag{3.39}$$

An example of the simulated reflectivity for an iron layer on silicon is shown in Figure 3-13. The resulting interference fringes are known as Kiessig fringes, named after the author of the first experimental reports of this phenomenon [79].

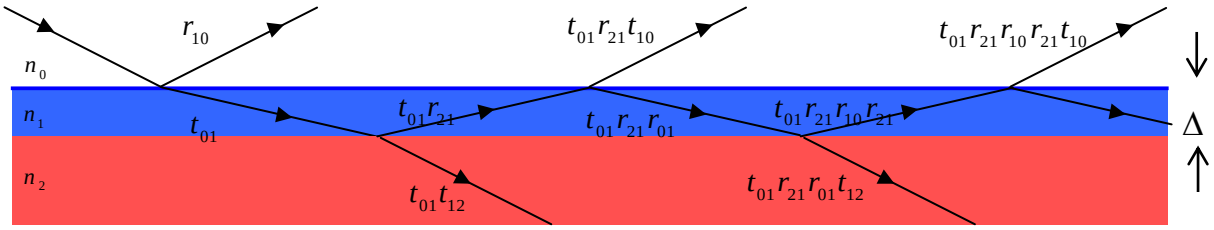

Figure 3-12. Reflection and transmission in the case of a finite layer of thickness Δ and refractive index n_1 upon an infinitely thick substrate layer with refractive index n_2.

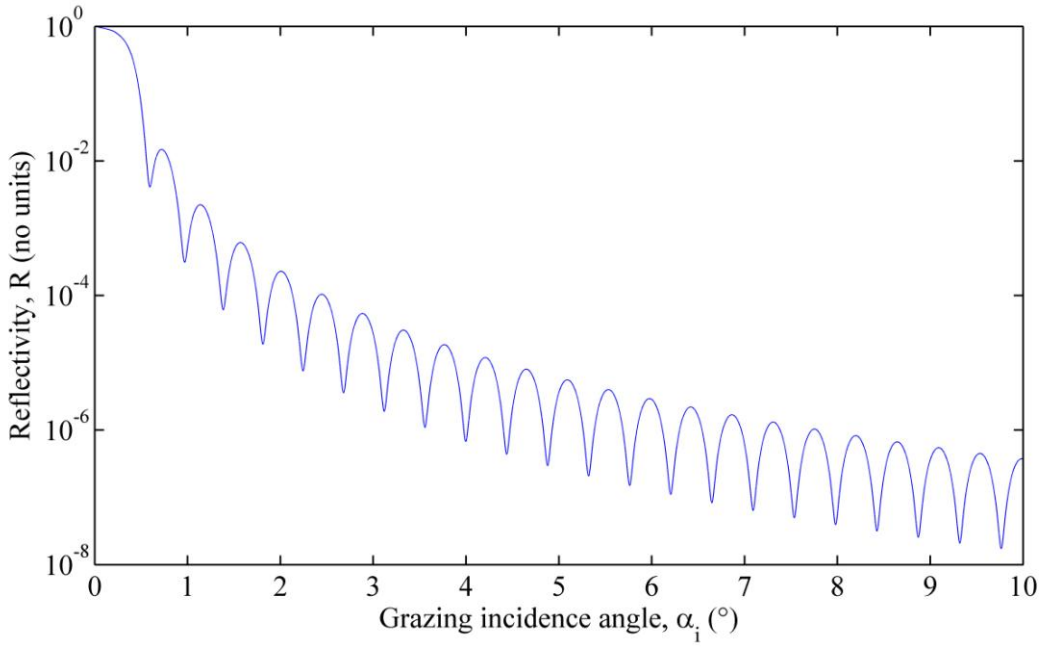

Figure 3-13. Simulated specular reflectivity from a single 10 nm film of iron on silicon with a perfectly sharp interface.

Far from the critical angle, for a simple single film the period of the Kiessig fringes is inversely related to the film thickness Δ through:

$$\Delta = \frac{\lambda}{\theta_{m+1} - \theta_m} \tag{3.40}$$

Where θ_m is the location of the m^{th} fringe.

3.3.5. Parratt's recursive calculation of specular reflectivity from a multilayer

Functional thin film devices, such as the magnetic tunnel junction, usually require more than the single layer considered above. These multilayers (a term used here to describe a structure of many arbitrary layers) can be modelled by extending the above analysis using the formalism of Parratt [80]. A consideration of N layers grown on an infinitely thick substrate, where the j^{th} layer has thickness Δ_j and refractive index n_j, starts with a calculation of the Fresnel reflectivity coefficient for the interface between the substrate and lowermost, N^{th}, layer. The expression derives from the Fresnel reflection coefficient, Eq. (3.30), expressed in terms of the z-component of the wavevector,

$$r_{N,\infty} = \frac{k_z^N - k_z^\infty}{k_z^N + k_z^\infty} \tag{3.41}$$

The reflectivity from interface between the j^{th} and $(j\text{-}1)^{\text{th}}$ layer is simply a re-indexed Eq. (3.30).

$$r_{j-1,j} = \frac{r_{j,j-1} + r_{j+1,j} p_j^2}{1 + r_{j,j-1} r_{j+1,j} p_j^2} \tag{3.42}$$

Where the phase factor is indexed here as:

$$p_j^{\,2} = \exp\left(i q_j \Delta_j\right) \text{ with } q_j = 2k_j \sin\alpha_j \tag{3.43}$$

Applying (3.42) recursively from the N^{th} buried layer up to the surface allows the reflected intensity from the sample to be calculated as:

$$\frac{I_R}{I_0} = \left|r_{1,0}\right|^2 \tag{3.44}$$

3.3.6. Interface widths and specular reflectivity

In real thin film systems the interface between two materials is neither perfectly smooth nor chemically sharp. These two interface broadening mechanisms (shown in Figure 3-14) are indistinguishable in a specular x-ray reflectivity measurement, which is sensitive only to the average refractive index as a function of depth, z.

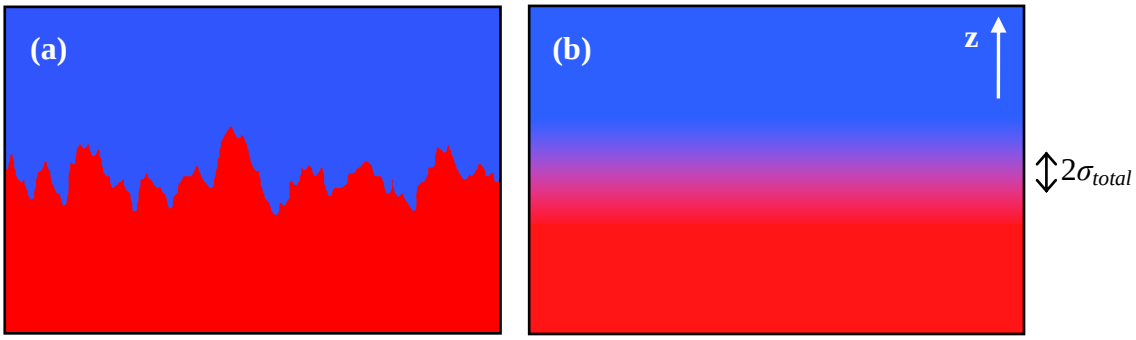

Figure 3-14. Schematic cross-section of (a) a sharp but topologically rough surface, and (b) a graded but perfectly flat surface, both described by an average out-of-plane interface width 2σ.

Over an extended interface the phase of the incident radiation will vary, and this is incorporated into the reflection coefficient through the term:

$$\int_{-\infty}^{\infty} \frac{1}{\rho_1} \frac{d\bar{\rho}(z)}{dz} \exp(-iqz)\, dz \tag{3.45}$$

Where ρ_1 is the electron density of the bulk material and $\bar{\rho}(z)$ is the mean electron density at depth *z*. Within the central limit theorem, the distribution of the electron density over a suitably large area can be considered Gaussian, such that $\bar{\rho}(z)$ has the form of an error function, and it is found that:

$$r_\sigma = r_{ideal} \exp\left\{-2\left(k_z^{i,r}\sigma_{total}\right)^2\right\} \tag{3.46}$$

Here $\sigma_{total} = \sqrt{\sigma_{topological}^{\ 2} + \sigma_{interdiff}^{\ 2}}$ is the total interface width, averaged out-of-plane.

Névot and Croce [81] proposed separate modifying damping terms for the reflected and transmitted Fresnel coefficients, in order better to account for effects at the critical angle:

$$r_\sigma = r_{ideal} \exp\left(-2k_z^{i,r}k_z^{t}\sigma_{total}^{\ 2}\right) \quad \text{and} \quad t_\sigma = t_{ideal} \exp\left\{\frac{-\sigma_{total}^{\ 2}}{2}\left(k_z^{i,r} - k_z^{t}\right)^2\right\} \tag{3.47}$$

Neither form is universally correct; de Boer [82] found both models to be valid in the limits of the more general distorted wave Born approximation. De Boer states that the Névot-Croce term is more valid around the critical angle and for high spatial frequencies of roughness, otherwise the Debye-Waller form is more valid.

3.3.7. Calculation and fitting of specular reflectivity

Upon detection of the reflected wave, any phase information is lost. This, together with the complexity of the interference pattern resulting from multiple reflections from all interfaces, means that for all but the most trivial structures a recursive fitting procedure

is necessary to interpret data. With many layers each characterized by a thickness, electron density and interface width, there is a large parameter space from which the optimum (and physically realistic) model must be found. Fitting starts with an initial best estimate of the structure, and proceeds using an automated algorithm to improve the agreement between the model simulation and the experimental measurement.

This agreement is evaluated by a so-called 'error function'. Wormington *et al* [83] found that the most suitable error function for x-ray scattering data (in which the detected intensity often varies by several orders of magnitude in a single scan) was the mean average error of the difference of the log of the intensity:

$$\frac{1}{N-1}\sum_{j=1}^{N}\left|\log I_{simulated} - \log I_{measured}\right| \tag{3.48}$$

Here N is the number of independent data points in the comparison.

The interferometric nature of a specular reflectivity measurement means that many local minima exist in the error function parameter space. For efficient optimisation of the error function, an algorithm which takes into account the gradient of the error function at each trial location is needed. Wormington *et al* applied an evolutionary algorithm for this purpose [83].

This fitting method was commercialised in the Bede REFS computer package [84], which has been used for much of the specular reflectivity analysis in this thesis. Similar open-source software is also available [e.g. ref. 85].

3.4. Off-specular scattering from random rough surfaces

Away from the specular reflection the scattering vector **q** gains an in-plane component q_x. This allows the in-plane nature of the interface to be probed.

As previously introduced, an interface may be sharp or diffuse. Furthermore, there may be a random undulation of the interface, the amplitude of which may have a spatial frequency dependence. In the case of entirely random undulation, only a statistical description of the correlation between two points as the distance between them increases is definable, and the concept of the height-height correlation function becomes a valuable idea.

First, the scattering from a sharp but rough surface is derived in the weak-scattering kinematical (first) Born approximation. Later, a more advanced solution known as the distorted wave Born approximation is described, which incorporates the stronger scattering which occurs around the critical angle.

3.4.1. Scattering in the kinematical Born approximation

In the kinematical first order Born approximation it is assumed that x-rays are weakly scattered, meaning that the intensity is constant throughout the scattering volume, and multiple scattering paths are ignored. It is further assumed that the observation distance is much greater than the coherent scattering radius, and that scattered waves from different points in the sample are parallel at the detector. This means that the scattering amplitude can be modelled as the Fourier transform of the scattering potential [ref. 67, p. 700]. These assumptions greatly simplify the mathematical description, but are not valid in regions of strong scattering such as close to the critical angle, or in periodic multilayer systems.

Consider an x-ray beam illuminating a semi-infinite slab at grazing incidence. The incident beam illuminates a volume V of the sample. Similarly to Eq. (3.11), we may sum the scattering from all the volume elements dV, taking into account the phase factors, to find the total scattered amplitude r_V.

$$r_V(\mathbf{q}) = r_0 \int_V \rho(\mathbf{r}) \exp(i\mathbf{q}.\mathbf{r})\, dV \tag{3.49}$$

$\rho(\mathbf{r})\, dV$ is the total number of electrons within the volume dV centred at $\mathbf{r}$.

This volume integral is converted to a surface integral using Gauss's theorem. It is assumed that the relevant surface is solely the uppermost surface of incidence, since the beam is assumed to be fully absorbed before reaching the lower bound of V, and the negligible thickness of the sample compared to the large beam footprint means the lateral surfaces are insignificant.

$$\begin{aligned} r_V(\mathbf{q}) = -r_0 \int_V \rho\, dV \exp(i\mathbf{q}.\mathbf{r}) &= -r_0 \rho \left(\frac{1}{iq_z}\right) \int_S \mathbf{z}.d\mathbf{S} \exp(i\mathbf{q}.\mathbf{r}) \\ &= -r_0 \rho \left(\frac{1}{iq_z}\right) \int_S \exp(i\mathbf{q}.\mathbf{r})\, dx\, dy \end{aligned} \tag{3.50}$$

Consider the scalar product of the local scattering vector $\mathbf{q}$ with the position vector $\mathbf{r}$:

$$\mathbf{q}.\mathbf{r} = q_x x + q_y y + q_z Z(x, y) \tag{3.51}$$

where Z is the local surface height at (x, y). So the scattered amplitude from volume element dV can be written:

$$r_S = -r_0 \rho \left(\frac{1}{iq_z}\right) \int_S \exp\left\{i\left(q_x x + q_y y\right)\right\} . \exp\left\{iq_z Z(x, y)\right\}\, dx\, dy \tag{3.52}$$

The scattering cross-section $(d\sigma/d\Omega)$ is the absolute square of the scattering amplitude:

$$\left(\frac{d\sigma}{d\Omega}\right) = \left(\frac{r_0\rho}{q_z}\right)^2 \int_S \exp\left\{i\left[q_x(x-x') + q_y(y-y')\right]\right\}.\exp\left\{iq_z\left[Z(x,y) - Z(x',y')\right]\right\} dx\,dx'\,dy\,dy'$$

$$= \left(\frac{r_0\rho}{q_z}\right)^2 \left(\frac{A}{\sin\alpha_i}\right) \int_S \exp\left\{i\left[q_x x + q_y y\right]\right\}.\left\langle \exp\left\{iq_z\left[Z(0,0) - Z(x,y)\right]\right\}\right\rangle dx\,dy \qquad (3.53)$$

In Eq. (3.53) A is the illuminated area, so the term (A/sin α_i) is the illuminated surface area originating from the evaluation of $\int dx'\,dy'$. It is assumed that the surface is homogeneous such that only the relative coordinates between two points ($x - x'$, $y - y'$) = (X, Y) are relevant. Using these relative coordinates, a statistical height difference function is introduced,

$$g(X,Y) = \left\langle \left[Z(0,0) - Z(x,y)\right]^2 \right\rangle \qquad (3.54)$$

If the statistical distribution of height variations $g(X,Y)$ is assumed to be Gaussian the cross section can be simplified to:

$$\left(\frac{d\sigma}{d\Omega}\right) = \left(\frac{r_0\rho}{q_z}\right)^2 \left(\frac{A}{\sin\alpha_i}\right) \int_S \exp\left\{-i\left[q_x X + q_y Y\right]\right\}.\exp\left\{-q_z^2\, g(X,Y)/2\right\} dx\,dy \qquad (3.55)$$

To demonstrate limiting cases of the above expression, consider two special cases.

In the case of Fresnel reflectivity from a flat, sharp interface, $g(X,Y) = 0$ for all X and Y, so the above equation reduces to:

$$\begin{aligned}\left(\frac{d\sigma}{d\Omega}\right)_{Fresnel} &= \left(\frac{r_0\rho}{q_z}\right)^2 \left(\frac{A}{\sin\alpha_i}\right) \int_S \exp\left\{i\left[q_x x + q_y y\right]\right\} dx\,dy \\ &= \left(\frac{r_0\rho}{q_z}\right)^2 \left(\frac{A}{\sin\alpha_i}\right) \delta(q_x)\,\delta(q_y)\end{aligned} \qquad (3.56)$$

which describes an infinitely sharp specular reflection at $q_x = q_y = 0$.

For a rough but completely uncorrelated surface the heights of two points separated by (X,Y) are statistically independent no matter how close together they are. The height difference function becomes:

$$g(X,Y) = \left\langle \left[Z(0,0) - Z(x,y)\right]^2 \right\rangle = \left\langle Z(0,0)\right\rangle^2 + \left\langle Z(X,Y)\right\rangle^2 + 2\left\langle Z(0,0)\right\rangle\left\langle Z(X,Y)\right\rangle = 2\sigma^2 \qquad (3.57)$$

So that the scattering cross section is:

$$\begin{aligned}\left(\frac{d\sigma}{d\Omega}\right)_{\substack{rough\\uncorrelated}} &= \left(\frac{r_0\rho}{q_z}\right)^2 \left(\frac{A}{\sin\alpha_i}\right) \exp\left\{-q_z^2\sigma^2\right\} \int_S \exp\left\{-i\left[q_x X + q_y Y\right]\right\} dx\,dy \\ &= \left(\frac{d\sigma}{d\Omega}\right)_{Fresnel} \exp\left\{-q_z^2\sigma^2\right\}\end{aligned} \qquad (3.58)$$

This is identical to the Fresnel reflectivity given in (3.56), except for the modifying $\exp\left\{-q_z^2\sigma^2\right\}$ term which shows that increasing the interface width reduces the specular reflectivity. This was previously presented in (3.46). Here, σ represents the total interface width, composed of topology and interdiffusion.

3.4.2. Simplified roughness estimation in the Born approximation

Within the first order Born approximation there exists a simple method for estimating the degree of topological roughness [ref. 72, p. 130]. It has been shown above that the integrated reflected intensity is reduced by a nonzero interface width as:

$$I_{\substack{specular,\\measured}} = I_{Fresnel}\exp\left\{-q_z^2\sigma_{total}^2\right\} = I_{Fresnel}\exp\left\{-q_z^2\left(\sigma_{topological}^2+\sigma_{interdiffusion}^2\right)\right\} \tag{3.59}$$

Importantly, the electron density gradient due to a slowly varying chemical composition will scatter x-rays out of phase, resulting in destructive interference which reduces the overall Fresnel reflectivity. In contrast, a perfectly sharp but undulating interface will scatter in phase, increasing the diffuse scatter at the expense of specular scatter.

Using a conservation of energy argument, for a perfectly sharp interface the loss of specular intensity must have been scattered diffusely, (into regions of $q_x \neq 0$) such that

$$I_{\substack{specular,\\measured}} = I_{\substack{specular,\\smoooth}} - I_{diffuse} \tag{3.60}$$

This implies that:

$$\frac{I_{diffuse}}{I_{\substack{specular,\\measured}}} = \exp\left(q_z^2\sigma_{topological}^2\right) - 1 \tag{3.61}$$

This offers a way to estimate the topological roughness from a transverse diffuse scan (for which q_z is constant to a close approximation), provided that the specular intensity can be distinguished from the underlying diffuse scatter. Further to this analysis, if the total interface width can be established by fitting the specular reflectivity, then the amount of interdiffusion can be established since:

$$\sigma_{total\ interface\ width}^2 - \sigma_{topological}^2 = \sigma_{interdiffusion}^2 \tag{3.62}$$

It should be noted that the integrated diffuse scatter will be underestimated since the angular range of reflection is limited by the sample surface. This means that the simple Born approximation will slightly underestimate the topological roughness.

3.4.3. The height-height correlation function for a self-affine surface

Sinha *et al* [86] introduced the idea of the self-affine fractal interface into the description of diffuse x-ray and neutron scattering. As has been seen in chapter 2, the atomic scale processes occurring during thin film deposition can result in random growth which is well described using fractal terminology.

A perfectly self-affine surface is self-similar on different in-plane length scales. In this case, the height difference function $g(R)$ is given the form

$$g(R) = AR^{2h} \tag{3.63}$$

Here the surface is assumed isotropic so that any in-plane distance can be represented simply by $R = \sqrt{X^2 + Y^2}$.

The fractal static scaling or Hurst exponent, $0 < h < 1$, describes the jaggedness of the surface. For $h \to 1$ the surface has more rounded features, and is described as increasingly two-dimensional. As $h \to 0$ the surface becomes increasingly jagged and three-dimensional, as shown in simulations in Figure 3-15 for surfaces with identical amplitude roughness.

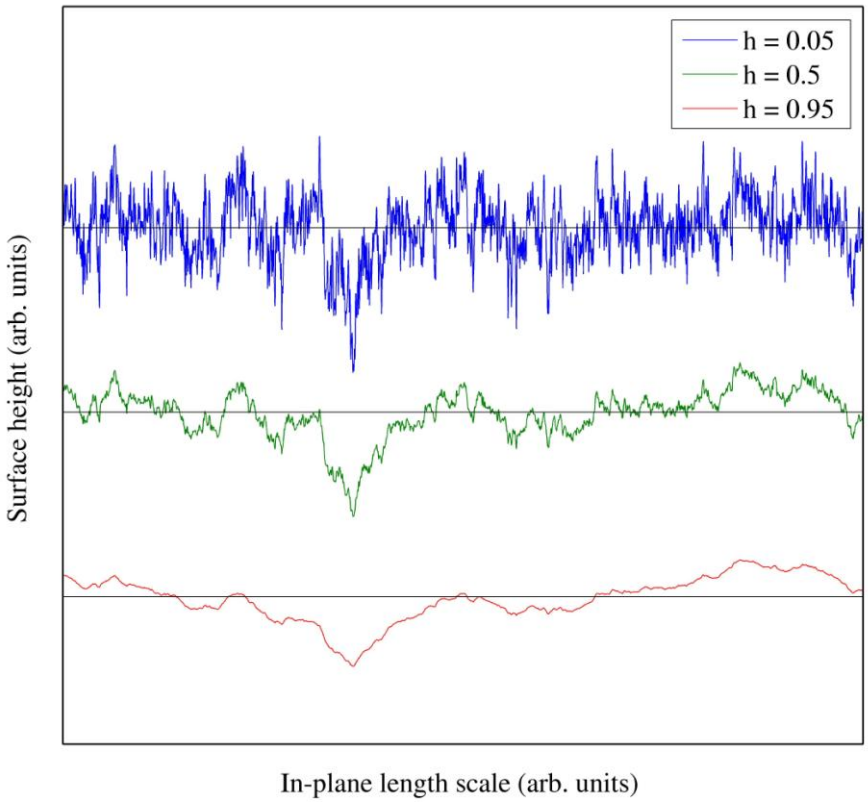

Figure 3-15. Numerical simulations of self-affine surfaces with different dimensionality D = 3 – h, where h is the Hurst fractal parameter. All surfaces have the same root mean square roughness, and were simulated using the Wierstrass-Mandelbrot algorithm [87] with component wavelengths spanning three orders of magnitude.

3.4.4. A semi-kinematical analytical calculation of diffuse scattering

Using the simple height difference function, Eq. (3.55) can be evaluated analytically for the special case of $h = 0.5$ [ref. 86, p. 2299] as:

$$\left(\frac{d\sigma}{d\Omega}\right) = (r_0\rho)^2 \left(\frac{A}{\sin\alpha_i}\right) \frac{B}{2\left[q_x^2 + \left(\frac{B}{2}\right)^2 q_z^4\right]} \tag{3.64}$$

Here the function has a Lorentzian lineshape with a full width at half maximum of $Bq_z^2/2$. This result is shown in Figure 3-16, where it is combined with the dynamical Fresnel reflectivity (in a *semi-kinematical* model) to show a recognisable transverse measurement†.

Unfortunately, for arbitrary h and more complicated forms of $g(R)$ the integral in the scattering cross section cannot be evaluated analytically, and a numerical calculation is often computationally intensive. (Note however, the perfect agreement of this simple model to the more complicated DWBA theory to be outlined in section 3.4.6 and shown in Figure 3-18, which suggests that this height function is valid in certain regimes).

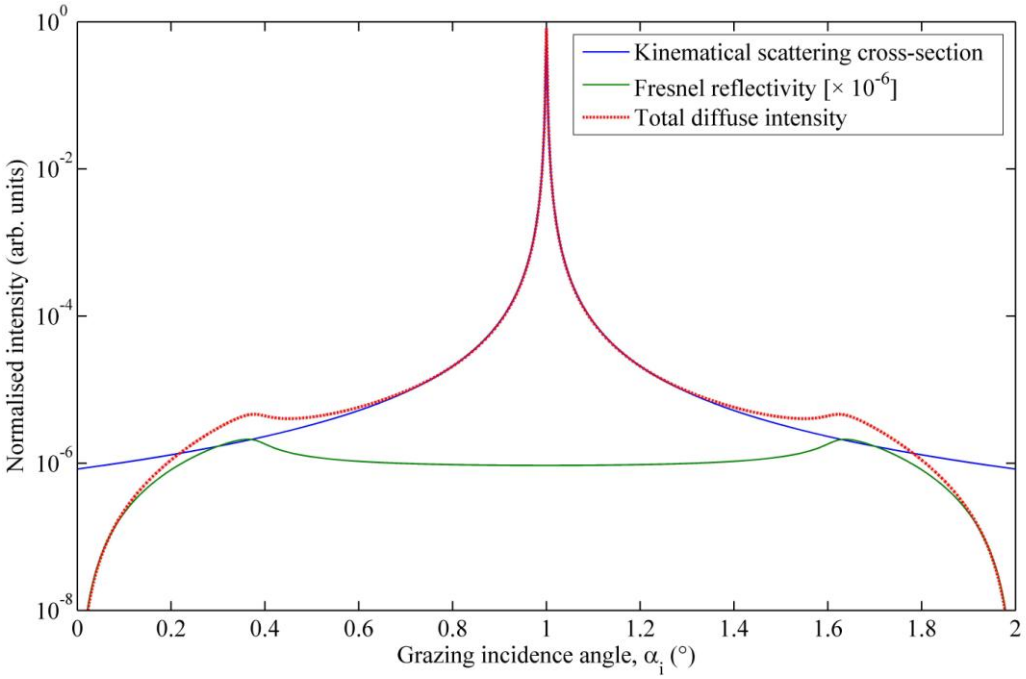

Figure 3-16†. Purely analytical calculation of the diffuse x-ray scatter from an iron surface using 8.047 keV x-rays and a detector angle of 2˚. The analytical model uses equation (3.63) with h *= 0.5. The components due to the kinematical scattering and Fresnel reflectivity are shown for comparison, and the geometrical footprint term excluded.*

† The MATLAB code used to simulate the diffuse intensity in this figure is included in Appendix A.

The wings occurring at the critical angles for incidence and exit originate from the Fresnel reflection, and were first experimentally studied by Yoneda [88] after whom they are named. This enhancement of the diffuse scattering occurs at these angles because the electric field amplitude at the surface is twice that of the incident field, being equal to the sum of the incident and refracted waves.

The assumption of perfect self-affinity is unphysical, since for $h > 0.5$, $g(R)$ diverges at large R. In reality, there will be a saturation roughness, σ. Sinha *et al* proposed a modified form for $g(R)$:

$$g(R) = 2\sigma^2 \left[1 - \exp\left\{ -\left(R/\xi \right)^{2h} \right\} \right] \tag{3.65}$$

Here ξ is the in-plane cut-off length for self-affinity. For large R, $g(R) \to \sigma^2$ whereas for small R, $g(R) \propto R^{2h}$.

Surfaces are more generally characterized in terms of a *correlation* (or *autocovariance*) function $C(R)$ rather than a height-height difference function. The two are related through:

$$C(R) = \left\langle \left[Z(0,0)\, Z(x,y) \right] \right\rangle = \sigma^2 - \frac{1}{2} g(R) \tag{3.66}$$

The effect of the two parameters ξ and h on $C(R)$ are illustrated in Figure 3-17.

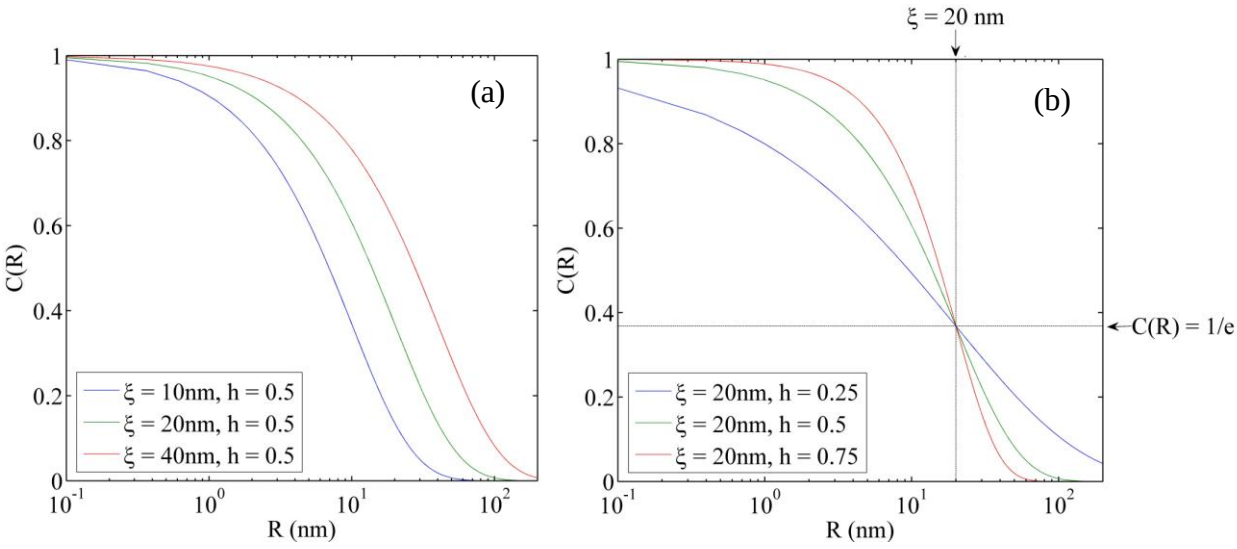

Figure 3-17. The height-height correlation function as a function of in-plane distance R given in Eq. (3.65). (a) for different cut-off lengths, and (b) for different fractal exponents.

3.4.5. A summary of scattering in the kinematical approximation

By evaluating their form of the correlation function within Eq. (3.55), Sinha *et al* [86] showed that the scattering cross section can be written:

$$\left(\frac{d\sigma}{d\Omega}\right)_{\substack{TOTAL\\kinematical}} = \left(\frac{r_0\rho}{q_z}\right)^2 \left(\frac{A}{\sin\alpha_i}\right) \exp\left\{-q_z^2\sigma^2\right\} \int_S \exp\left\{-i\left[q_r R\right]\right\} \exp\left\{q_z{}^2 C\left(R\right)\right\} dx\, dy \tag{3.67}$$

This can be evaluated as the sum of two distinct terms describing the specular and diffuse components:

$$\left(\frac{d\sigma}{d\Omega}\right)_{\substack{specular\\kinematical}} = \left(\frac{r_0\rho}{q_z}\right)^2 \left(\frac{A}{\sin\alpha_i}\right) \exp\left\{-q_z^2\sigma^2\right\} \int_S \exp\left\{i\left[q_r R\right]\right\} dR \quad = \exp\left\{-q_z^2\sigma^2\right\} \left(\frac{d\sigma}{d\Omega}\right)_{Fresnel} \tag{3.68}$$

and:

$$\left(\frac{d\sigma}{d\Omega}\right)_{\substack{diffuse\\kinematical}} = \left(\frac{r_0\rho}{q_z}\right)^2 \left(\frac{A}{\sin\alpha_i}\right) \exp\left\{-q_z^2\sigma^2\right\} \int \left(\exp\left\{q_z^2 C\left(R\right)\right\} - 1\right) \exp\left(q_x X + q_y Y\right) dx\, dy \tag{3.69}$$

After explicit insertion of the correlation function this becomes,

$$\left(\frac{d\sigma}{d\Omega}\right)_{\substack{diffuse\\kinematical}} = \left(\frac{r_0\rho}{q_z}\right)^2 \left(\frac{A}{\sin\alpha_i}\right) \exp\left\{-q_z^2\sigma^2\right\} \int \left(\exp\left\{ q_z^2\sigma^2 \exp\left\{ -\left(\frac{R}{\xi}\right)^{2h} \right\} \right\} - 1 \right) J_0\left(q_r R\right) dR \tag{3.70}$$

Where J_0 is a spherical Bessel function of the first kind. It should be noted that the diffuse scatter has a component present at $q_r = 0$, i.e. at the condition for specular reflection. This is sometimes termed 'forward diffuse scatter', and must be accounted for when a measurement of the true specular component is attempted.

3.4.6. Scattering in the distorted wave Born approximation

In the kinematical first order Born approximation above, the rough surface is considered as a perturbing potential acting on the incident wavefront. This model is entirely kinematical, and has limited validity when multiple scattering becomes important, such as close to the critical angle and with periodic multilayer structures.

The distorted wave Born approximation (DWBA) starts with the exact (dynamical) Fresnel solution for the perfect interface, and calculates the effect on the wavefront of the perturbing potential due to interface roughness. The concept was outlined in the seminal paper by Sinha *et al* [86]. The scattering potential is separated into two terms V_1 and V_2 where the total potential $V = V_1 + V_2$. The ideal surface located at $z = 0$, is described as:

$$V_1 = \begin{cases} k_0^2\left(1-n^2\right) & z<0 \\ 0 & z>0 \end{cases} \tag{3.71}$$

The perturbing potential at depth *z* due to roughness is described by

$$V_2 = \begin{cases} k_0^2\left(1-n^2\right) & \text{for } 0<z<Z\left(x,y\right) \\ -k_0^2\left(1-n^2\right) & \text{for } 0>z>Z\left(x,y\right) \\ 0 & \text{otherwise} \end{cases} \tag{3.72}$$

where $Z\left(x,y\right)$ is the actual rough surface. Use of this perturbing potential allowed Sinha *et al* to establish the diffuse scattering cross section within the DWBA as:

$$\left(\frac{d\sigma}{d\Omega}\right)_{\substack{diffuse \\ DWBA}} = \left(\frac{r_0\rho}{q_z^t}\right)^2\left(\frac{A}{\sin\alpha_i}\right)\left|t\left(\mathbf{k}_1\right)\right|^2\left|t\left(\mathbf{k}_2\right)\right|^2\left(1-n^2\right)\exp\left\{-\frac{\sigma^2}{2}\left[\left(q_z^t\right)^2+\left(q_z^{t*}\right)^2\right]\right\}$$
$$\times\int\left(\exp\left\{\left|q_z^t\right|^2 C\left(R\right)\right\}-1\right)\exp\left\{i\left(q_x X+q_y Y\right)\right\}dxdy \tag{3.73}$$

Here $|t\ (\mathbf{k}_i)|$ is the Fresnel transmission coefficient from medium *i* as defined earlier in (3.31). q_z^t is the wavevector transfer in the medium. Above the critical angle, $q_z^t \approx q_z$.

By comparing this expression with the Born approximation from Eq. (3.69) the two modifications are clear: (i) the Fresnel transmission coefficients, and (ii) the use of the modified wavevector q_z^t inside the medium. As in the Born approximation, for the general case the integral must be evaluated numerically.

Exemplary results (determined using a commercial software package [84]) are shown in Figure 3-18 for varying correlation cut-off lengths together with the simple analytical cross-section of Eq. (3.65), which matches perfectly at very long correlation length. It can be seen that larger ξ values cause diffuse scatter to be focussed around the specular condition, where q_x is small.

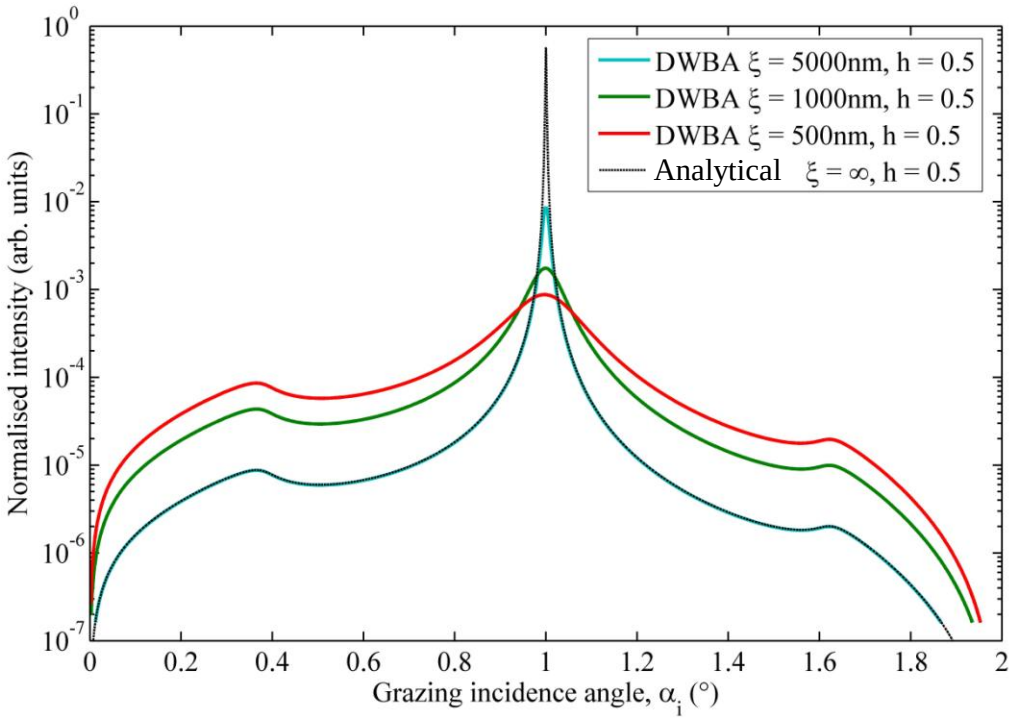

Figure 3-18. Simulated transverse diffuse intensity from an iron surface with 8.047 keV x-rays and detector at 2°. In the DWBA simulations the surface has a topological roughness σ = 0.1 nm. Note that the kinematical and 5000 nm DWBA lines perfectly overlap except at very short q_x values around 1°.

3.4.7. Interface grading within the DWBA

Sinha *et al* [86] explain that a graded but perfectly smooth interface will reduce specular scattering whilst producing no diffuse scatter, whereas a sharp but topologically rough surface will identically reduce the specular intensity, but will produce an equal amount of diffuse intensity. This idea was used in section 3.4.2, for the relatively crude Born analysis of the integrated intensity.

In order to incorporate this principle into the DWBA, Wormington *et al* [89] proposed that the an electron density gradient be described through the expression $\left|\int \left(d\rho_e(z)/dz\right)\exp\left(iq_z^t z\right)dz\right|^2$, so that the diffuse scattering cross-section in the presence of a graded interface described by $\rho_e(z)$ becomes:

$$\left(\frac{d\sigma}{d\Omega}\right)_{\substack{diffuse\\DWBA}} = \left(\frac{r_0\rho}{q_z^t}\right)^2\left(\frac{A}{\sin\alpha_i}\right)\left|t\left(k_{1,z}\right)\right|^2\left|t\left(k_{2,z}\right)\right|^2\left(1-n^2\right)\exp\left\{-\frac{\sigma^2}{2}\left[\left(q_z^t\right)^2+\left(q_z^{t*}\right)^2\right]\right\} \times\left|\int\left(\frac{d\rho_e(z)}{dz}\right)\exp\left(iq_z^t z\right)dz\right|^2\int\left(\exp\left\{\left|q_z^t\right|^2 C(X)\right\}-1\right)\cos q_x X dx \tag{3.74}$$

The effect of grading is shown in Figure 3-19, where the overall interface width is constant, but a greater proportion of interdiffusion is seen to lower the diffuse scatter and leave the specular reflectivity unchanged.

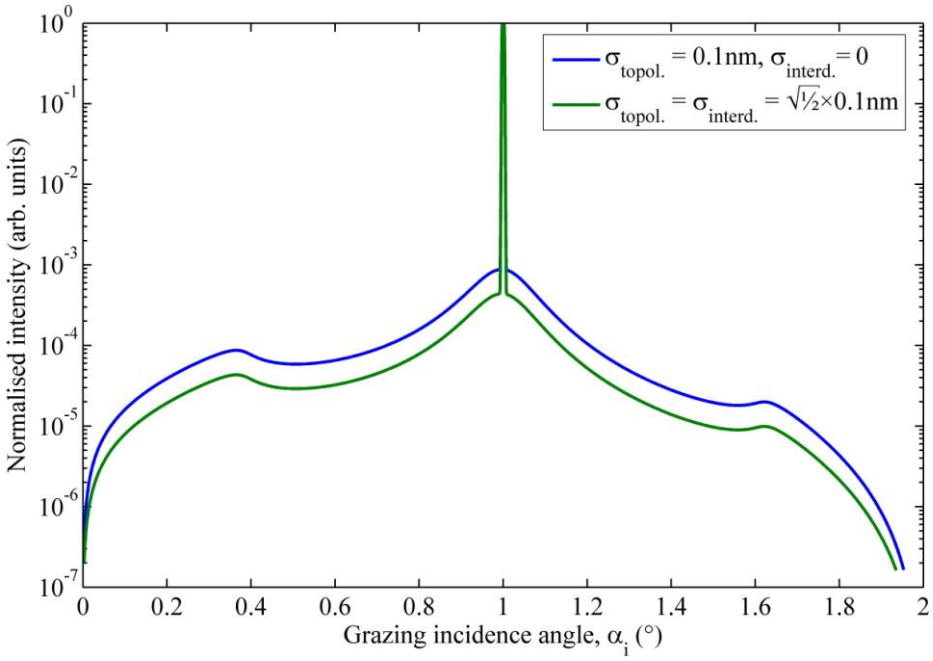

Figure 3-19. Simulated transverse intensity (specular and diffuse) within the DWBA for an iron surface with 8.047 keV incident x-rays and a detector at 2°. The total interface width is the same for both lines, but the relative proportion of grading is varied. Correlation parameters are ξ = 500 nm, h = 0.5. The specular reflection is shown here to be invariant with the balance of topology and interdiffusion.

3.4.8. Diffuse scatter from multilayer structures

Many thin film samples have several thin layers of different materials. The reflectivity from any interface is dependent upon the difference in refractive index between the neighbouring materials. Diffuse scatter is normally dominated by the uppermost air-sample interface, but diffuse scatter from buried interfaces can be enhanced by periodic repetition of the interface. Indeed, specular reflectivity displays a similar enhancement by periodic repetition of the layers, with Bragg peaks appearing amongst the Kiessig fringes. This feature is easily reproduced within the Parratt formalism.

If the roughness is highly conformal (correlated out-of-the-plane between layers), then diffuse scatter will interfere constructively at points related to the repeat periodicity through Bragg's law. Using this idea, the conformality of topological roughness can be probed. Figure 3-20 gives a graphic representation of conformal and non-conformal roughness. There is more often an intermediate degree of conformality, where characteristics are inherited from one layer to the next with a statistical probability dependent upon the growth processes.

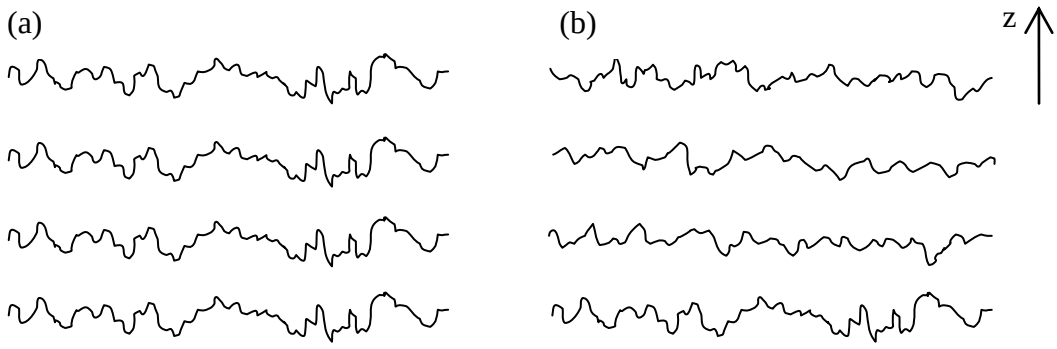

Figure 3-20. Schematic of (a) fully conformal, and (b) non-conformal topological roughness.

Holý *et al* [90, 91] introduced a *covariance* function with a corresponding out-of-plane covariance length ζ at which the correlation between the j^{th} and k^{th} layers is 1/e.

$$C_{j,k}(R) = \sigma_{j,k}^{2} \exp\left\{-\frac{R^{2h}}{\xi_{j,k}^{2h}}\right\} \exp\left\{\frac{-\left|z_j - z_k\right|}{\zeta}\right\} \tag{3.75}$$

$\sigma_{j,k}^{2}$ is the sum in quadrature of the topological roughness of the two interface and $\xi_{j,k}^{2h}$ is the mean of ξ_{j}^{2h} and ξ_{k}^{2h}.

This covariance function is used in place of the correlation (autocovariance) function to evaluate the scattering cross section of each pair of interfaces *j*, *k* in the chosen formulation of $(d\sigma/d\Omega)_{\substack{diffuse \\ DWBA}}$. All pairs of interfaces are summed over to find the total scattering cross-section of the multilayer. The interested reader is referred to Pietsch *et al* [ref. 70, pp. 252-260] for more detail.

As an example, Figure 3-21 shows the simulated specular and diffuse scatter in a longitudinal scan (where the sample is offset -0.1° from the reflection condition) for a Fe/MgO ten repeat bilayer on an MgO substrate. For fully conformal roughness, strong Bragg peaks are seen in the diffuse scatter at points in q_z related to the 5 nm layer thickness (this example is a special case; because the Fresnel coefficients are symmetric into and out of the sample, the Bragg peaks relating to the 10 nm period are suppressed).

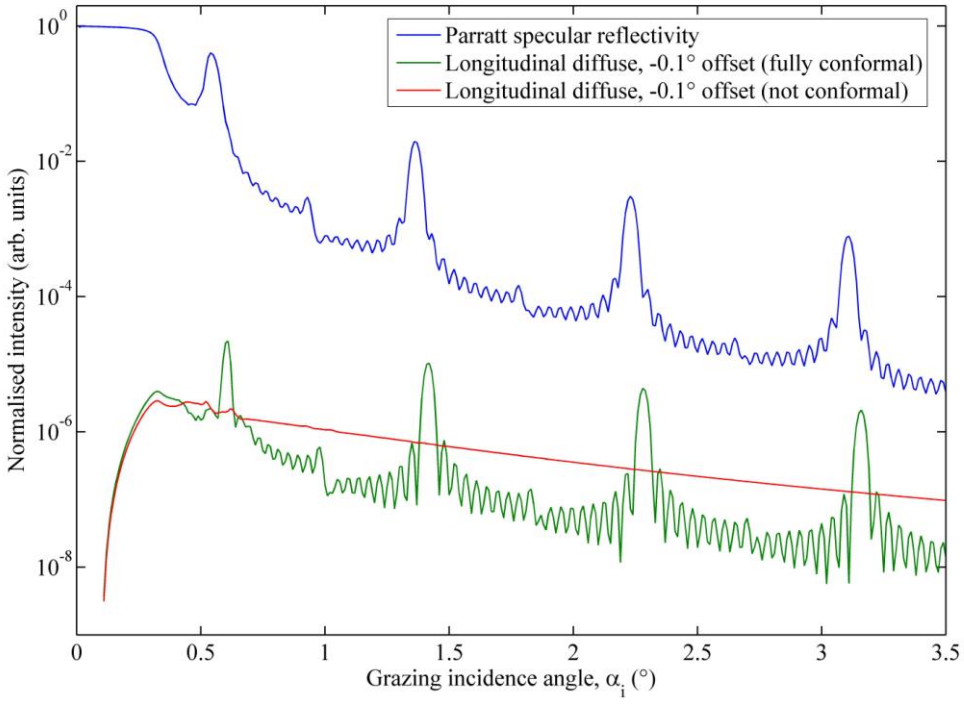

Figure 3-21. Simulated specular and longitudinal diffuse scatter from a repeat multilayer of [MgO (5 nm) / Fe (5 nm)]×10 on an MgO substrate, with 0.1 nm topological roughness throughout the stack.

3.4.9. Power-law analysis of diffuse scatter

The scattering cross-section as derived up to this point allows simulations of the diffuse scatter from a statistical model of each layer and interface. For increasingly complicated (and realistic) structural models, these simulations soon become computationally intensive and contain a large number of free fitted parameters, undermining confidence in the uniqueness of any given solution.

A simpler method of analysis for self-affine multilayer structures was introduced by Salditt *et al* [92] who considered diffuse scattering in the q_y direction and found that a universal power-law scaling occurred for $q_y \geq 2\pi/\xi$. Above this correlation cut-off frequency, the scattering cross-section falls off following a power law $\propto q_y^{-\gamma}$, where the fractal scaling parameter *h* is related to γ through:

$$\gamma = 2 + 2h - \left(\left|q_z\right|\sigma\right)^2 \tag{3.76}$$

Furthermore, because the sharpness of the Bragg peaks depends upon the coherency of scattering from each repeated interface in the multilayer, the full width at half maximum can be used to estimate an out-of plane coherence length ζ, by:

$$\zeta = \frac{2\pi}{\Delta q_z^{FWHM}} \tag{3.77}$$

This analysis was successfully applied to Fe/Au multilayer repeats by Paniago *et al* [93], who used the decay as a function of q_y of the Bragg peaks in the diffuse scatter to understand the growth kinetics of the film.

3.5. Scattering from a crystal lattice: principles of x-ray diffraction

To this point the discussion has focussed on interfacial scattering, transmission, reflection and refraction. A much more widely studied phenomenon is x-ray diffraction, the interference of waves scattered coherently from regularly arranged point scatterers. Historically, x-ray diffraction has exploited the scattering from a regular atomic crystal lattice. In this context, the incident wave is assumed to be a plane wave, i.e. the phase is constant over an extended wavefront perpendicular to the direction of travel. When this wave interacts with a crystal lattice, each atom is assumed to re-radiate a spherical wavefront. In most directions, these wavefronts will sum in amplitude to zero. However, in a few specific directions with relation to the lattice, wavefronts interfere constructively to produce diffraction peaks. This phenomenon is most apparent when the wavelength of the incident radiation is similar to the periodicity of the point scatterers, as is the case for x-rays and crystals.

The simplest mathematical construction of diffraction phenomena is that given by Bragg [63]. Consider Figure 3-22. When the path difference (highlighted in red) is equal to an integer number of wavelengths $n\lambda$, the x-rays scattered from the two centres will be in phase, and will interfere constructively in the far-field.

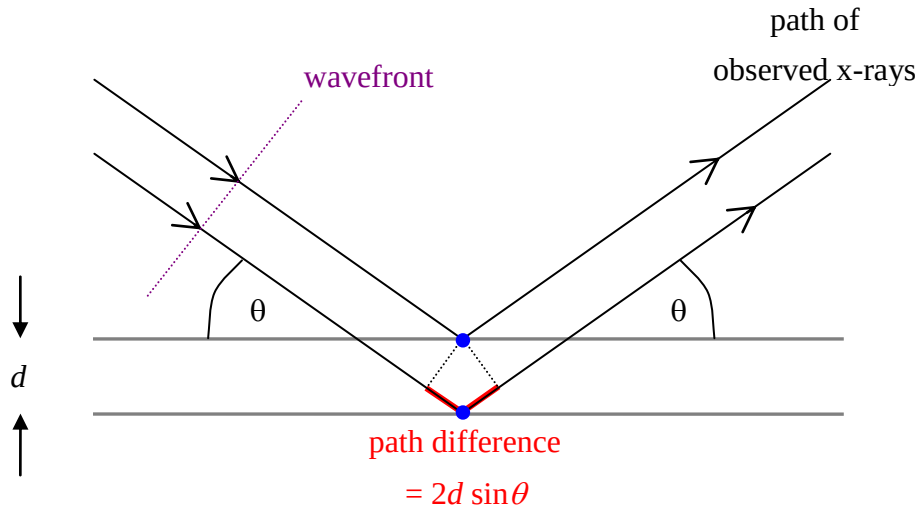

Figure 3-22. Geometrical construction for the derivation of Bragg's law. Scattering centres are shown as blue dots.

This diffraction condition occurs at the Bragg angle θ_B, and is encapsulated in Bragg's law, Eq. (3.78).

$$n\lambda = 2d_{hkl}\sin\theta_B \tag{3.78}$$

Because in a regular lattice this condition will be simultaneously true for all point scatterers related by the same translational symmetry, there will be a dramatic increase of the x-ray amplitude, producing diffraction peaks. From the position of these peaks it is possible to determine the periodicity d_{hkl} of the points scattering in phase.

3.5.1. Analysis of diffraction peak position

In vector notation, the lattice is defined by the set of vectors $\{\mathbf{R}_\mathbf{n}\}$ where

$$\mathbf{R}_\mathbf{n} = n_1\mathbf{a}_1 + n_2\mathbf{a}_2 + n_3\mathbf{a}_3 \tag{3.79}$$

Where $\mathbf{a}_i$ are the lattice vectors and n_i are integers. Planes of unit cells are defined by Miller indices, where the plane closest to (but not containing) the origin intersects the axes $(\mathbf{a}_1, \mathbf{a}_2, \mathbf{a}_3)$ at $(a_1/h, a_2/k, a_3/l)$. It should be noted that the point scatterers considered may be single atoms or complex polyatomic unit cells. The interplanar spacing (for the case of a cubic lattice) is given by:

$$d_{hkl} = \frac{a_0}{\sqrt{h^2 + k^2 + l^2}} \tag{3.80}$$

where a_0 is the lattice parameter.

Using the same formalism as in section 3.2, the scattering from each unit cell is summed over the crystal lattice to find the scattering amplitude for the crystal:

$$-r_0 F(\mathbf{q}) = -r_0 \underbrace{\sum_j f_j(\mathbf{q}) \exp\left(i\mathbf{q}.\mathbf{r}_j\right)}_{\text{unit cell structure factor}} \underbrace{\sum_n \exp\left(i\mathbf{q}.\mathbf{R}_\mathbf{n}\right)}_{\text{sum over lattice}} \tag{3.81}$$

The sum over the lattice will result in constructive interference when the term $\mathbf{q}.\mathbf{R}_\mathbf{n} = 2\pi m$, where m is an integer. In the same way that the real space lattice is defined by Eq. (3.79), the reciprocal lattice is defined $\mathbf{G}_{hkl} = h\mathbf{b}_1 + k\mathbf{b}_2 + l\mathbf{b}_3$ where the reciprocal lattice basis $\{\mathbf{b}_\mathbf{i}\}$ was given in Eq. (3.6). Diffraction occurs at the *Laue condition* where the scattering vector is equal to a reciprocal lattice vector:

$$\mathbf{q} = \mathbf{G} \tag{3.82}$$

because at this point:

$$\mathbf{G}.\mathbf{R}_\mathbf{n} = 2\pi\left(hn_1 + kn_2 + ln_3\right) = 2\pi m \tag{3.83}$$

The Laue condition defines the location of diffraction peaks in reciprocal space relative to the crystal lattice. It can be seen from (3.81) that the amplitude of scattering is also dependent upon the unit cell structure summation. When this summation is zero (the extinction condition), the reflection is forbidden. This can limit the number of diffraction peaks which may be measured. For a polyatomic unit cell the atomic structure factors may be summed in various combinations to give diffraction peaks of different amplitudes [e.g. ref. 72, p. 160]. There are many other factors which determine the integrated intensity of a diffraction peak, including the geometry factor, any preferred crystallite orientation, and the polarization factor. The work presented in this thesis interprets peak positions and widths but not amplitudes, so these factors will not be discussed. Further information can be found in the book by Birkholz [ref. 69, pp. 25-28].

3.5.2. Analysis of diffraction peak width

For a bulk single crystal, the peak width in θ-2θ is associated with the strain dispersion, $\Delta\varepsilon$. By differentiating Bragg's law [Eq. (3.78)], the following expression for the full width at half maximum is obtained:

$$\Delta(\theta)_{\text{strain dispersion}} = \left(\frac{\Delta d}{d}\right)\tan\theta = \Delta\varepsilon\tan\theta \quad \text{or} \quad \Delta(2\theta)_{\text{strain dispersion}} = 2\Delta\varepsilon\tan\theta \tag{3.84}$$

However, if the sample is polycrystalline the coherent scattering path can be limited in length by the grain size (or if a thin film is probed at high angle of incidence, the film thickness). This introduces an additional peak broadening mechanism:

$$\Delta\left(2\theta\right)_{\text{grain size}} = \left(\frac{\lambda}{L\cos\theta}\right) \tag{3.85}$$

where L is the grain size. With measurements of many diffraction peaks these two broadening mechanisms can be separated due to their different angular dependencies by using the Williamson-Hall equation (3.86) to produce a linear plot with gradient $2\Delta\varepsilon$ and intercept λ/L .

$$\Delta\left(2\theta\right)_{\text{total}}\cos\theta = 2\Delta\varepsilon\sin\theta + \frac{\lambda}{L} \tag{3.86}$$

3.5.3. Analysis of rocking curve width

Relaxation of strained epitaxial layers often results in mosaicity, where the local crystallites are tilted with respect to the substrate. In analogy with the way that topological roughness introduces diffuse scatter around the specular reflection, this mosaicity results in scattering around the nominal diffraction condition, as is seen during a sample-only rocking curve. Contrasting the rocking curve width to the coupled scan width can be used to differentiate mosaicity from strain dispersion; with mosaicity, the integrated intensity of the rocking curve is often greater since many more individual crystallites have the opportunity to diffract. This can be described as the crystallites self-selecting the diffraction condition, rather than the fixed $\theta - 2\theta$ motion selecting only symmetrically 'flat' crystallites.

3.5.4. Conclusion regarding the principles of x-ray diffraction

This discussion gives a brief overview of the principles behind the high-angle x-ray diffraction measurements presented in the following chapters. The analyses are most reliably used in comparative studies, rather than for absolute characterization. For more comprehensive coverage the reader is referred to established texts on the subject [for example, refs. 68, 70, 72]. The special case of diffraction at grazing incidence and exit follows in the next section.

3.6. Grazing incidence in-plane x-ray diffraction

Grazing incidence diffraction (GID) was first reported in 1979 by Marra, Eisenberger and Cho [94]. As discussed in detail by Doerner and Brennan [95], the technique combines the surface sensitivity at grazing incidence due to refraction with the atomic lattice measurement possible with diffraction. In this thesis, the symmetric case of equal grazing incidence and exit angles is considered, as is shown in Figure 3-23. This is a special case of GID, called grazing-incidence in-plane x-ray diffraction or GIIXRD, and the planes diffracting are assumed to be perpendicular to the surface.

For a single crystal with planes lying normal to the surface the diffraction condition can never be perfectly satisfied. However, the presence of the surface extends the points over which diffraction will occur: in reciprocal space, these are described as *crystal truncation rods*, and are elongated perpendicular to the surface. As the grazing angle α increases the scattering vector moves up the crystal truncation rod, and the diffraction becomes weaker.

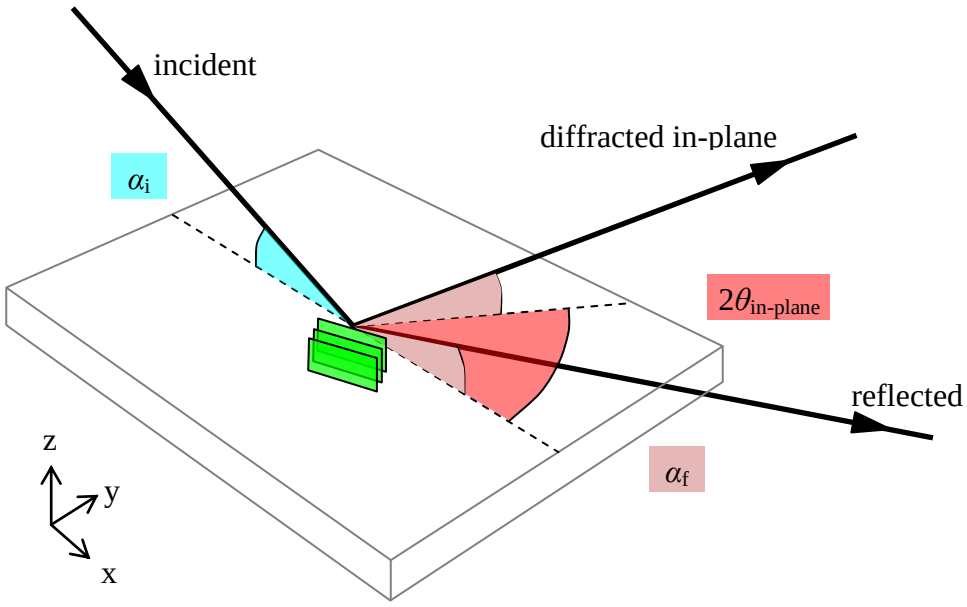

Figure 3-23. Diagram of the grazing incidence in-plane diffraction geometry. The grazing angles of incidence and exit, α_i and α_f are in the plane perpendicular to the sample surface, and the diffraction angle $2\theta_{in\text{-}plane}$ is in the plane of the sample. The sample is orientated such that $\alpha_i = \alpha_f$, and a vertical (z-parallel) plane is at the Bragg angle θ with both the source and detector.

The second consideration which is obvious from the earlier discussion on reflectivity is that close to the critical angle, the incident wave will be refracted along the surface. Together, these two factors imply that as the incidence angle increases, the diffraction peak will increase sharply as the critical angle is exceeded and the x-ray is transmitted into the sample, but will then slowly decrease with angle as the scattering vector and the lattice vector diverge.

The peak position and width can be subject to a similar analysis as high-angle diffraction using the equations given previously, but must be applied with an appreciation that material properties in-plane may require different interpretations. For example, whilst atomic layers may grow predominantly in the [001] direction normal to the substrate, the crystallites may be highly misorientated in the plane of the sample, about the surface normal. This twist mosaic is analogous to tilt mosaic measured by high-angle diffraction.

3.7. Grazing incidence x-ray scattering from a reflection grating

The discussion now moves to nanostructured periodic surfaces, where there is an in-plane engineering of the thin films typically on the length scale of 0.1 – 1 μm. Under appropriate irradiation, an extensive and periodic arrangement of nanostructures will act like an artificial crystal lattice or a two-dimensional diffraction grating. The periodicity of these arrays is much greater than the interatomic distances studied by conventional diffraction; this fact favours grazing incidence geometries, where the projection of the beam onto the sample increases the coherent footprint. Indeed, the coherence of the beam requires explicit consideration for these length scales since the number of coherently scattering elements can no longer be considered infinite. Gibaud *et al* [96] evaluate fully the geometrical and beam coherence considerations.

Morrison [97] provides a derivation of scattering of x-rays by one-dimensional gratings using a diffraction model from optics, which was successfully applied by Clarke to reflection gratings [98, 99]. The theory makes two key assumptions: (i) that each structure is much larger than the x-ray wavelength, and (ii) that polarization may be ignored. Fraunhofer diffraction conditions are applied, so the reflection amplitude is proportional to the Fourier transform of the scattering amplitude profile $f(\mathbf{r})$:

$$E_d(\mathbf{q}) = E_0 \int_{-\infty}^{\infty} f(\mathbf{r}) \exp(-i\mathbf{q}.\mathbf{r})\, d\mathbf{r} \tag{3.87}$$

For a one-dimensional single surface reflection grating, $f(\mathbf{r})$ is equated to the physical grating profile in the scattering plane $Z(x)$, which is set as unity in the presence of a structure and zero in between structures as shown in Figure 3-24.

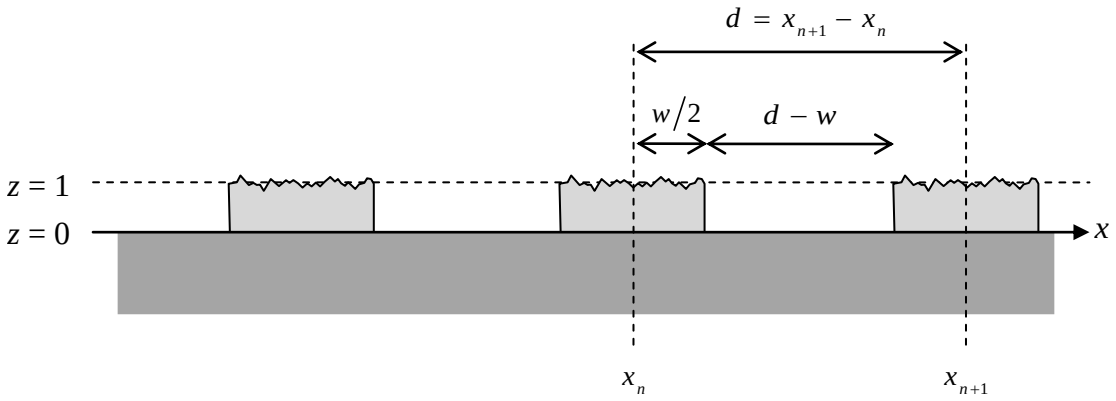

Figure 3-24. Schematic cross-section in the scattering plane through a one-dimensional grating.

The local profile of the n^{th} structure is:

$$z_n(x) = \begin{cases} 1 & x_n - \dfrac{w}{2} < x < x_n + \dfrac{w}{2} \\ 0 & \text{otherwise} \end{cases} \tag{3.88}$$

And the entire grating profile can be described by $z_N(x)$ convoluted by a 'comb' of Dirac delta functions centred on each structure:

$$Z(x) = z_n(x) \otimes \sum_{m=1}^{N} \delta(x - x_m) \tag{3.89}$$

The diffracted amplitude from *N* coherently scattering structures becomes:

$$E_d(q_x) = E_0 \int_{-\infty}^{\infty} Z(x) \exp(-iq_x x)\, dx = E_0 \int_{-\infty}^{\infty} \sum_{n=1}^{N} z_n(x) \otimes \delta(x - x_n) \exp(-iq_x x)\, dx \tag{3.90}$$

Since the Fourier transform of a convolution is equivalent to a multiplication of the individual convolutions, this can be separated as:

$$E_d(q_x) = E_0 \int_{-\infty}^{\infty} z_n(x) \exp(-iq_x x)\, dx \;\times\; \int_{-\infty}^{\infty} \sum_{n=1}^{N} \delta(x - x_n) \exp(-iq_x x)\, dx \tag{3.91}$$

The first integral is the Fourier transform of a single element

$$\begin{aligned} \Im\left[z_n(x)\right] &= \int_{-d/2}^{(w-d)/2} 1.\exp(-iq_x x)\, dx + \int_{d/2}^{(d-w)/2} 1.\exp(-iq_x x)\, dx \\ &= \frac{-2}{q_x}\left\{\frac{\exp[iq_x(d-w)/2] - \exp[-iq_x(d-w)/2]}{2i}\right\} + \frac{2}{q_x}\left\{\frac{\exp(iq_x d/2) - \exp(-iq_x d/2)}{2i}\right\} \\ &= \frac{\sin(q_x d/2) - \sin[q_x(d-w)/2]}{q_x/2} \end{aligned} \tag{3.92}$$

The second integral can be evaluated, first using the 'sifting' property of the delta function [e.g. ref. 67, p. 893], and secondly by using a standard geometric sum:

$$\int_{-\infty}^{\infty} \sum_{n=1}^{N} \delta(x - x_n) \exp(-iq_x x)\, dx = \sum_{n=1}^{N} \exp(-iq_x x_n) = \frac{\sin\{Nd\, q_x/2\}}{\sin\{d\, q_x/2\}} \tag{3.93}$$

In a similar way to the semi-kinematical modelling of diffuse scatter from random, rough surfaces in section 3.4, the Fresnel reflectivity coefficient can be used as a prefactor in order to account for critical angle phenomena. Hence, the diffraction intensity from an ideal reflection grating can be expressed as

$$I(q_x, q_z) = I_0 \left|R(q_z)\right|^2 \left|F(q_x)\right|^2 = I_0 \left|R(q_z)\right|^2 \left[\frac{\sin(q_x d/2) - \sin[q_x (d-w)/2]}{q_x/2}\right]^2 \left[\frac{\sin\{N d\, q_x/2\}}{\sin\{d\, q_x/2\}}\right]^2 \quad (3.94)$$

The result of this theory is shown for typical structural parameters in Figure 3-25, which includes the analytical calculation of the diffuse scatter derived in section 3.4.4.

There are several qualifications which apply to this ideal picture. The coherent beam footprint, and therefore the value of N will in general depend upon q_z (as will the experimental resolution). Any dispersion in either d or w can reduce the coherent scattering.

The section presented above is the theory of scattering from reflection gratings as published by Morrison [97] and developed by Clarke [98, 99]. An original extension to this theory is the subject of chapter 6, where the discussion continues with scattering from disordered two-dimensional arrays and self-assembled structures.

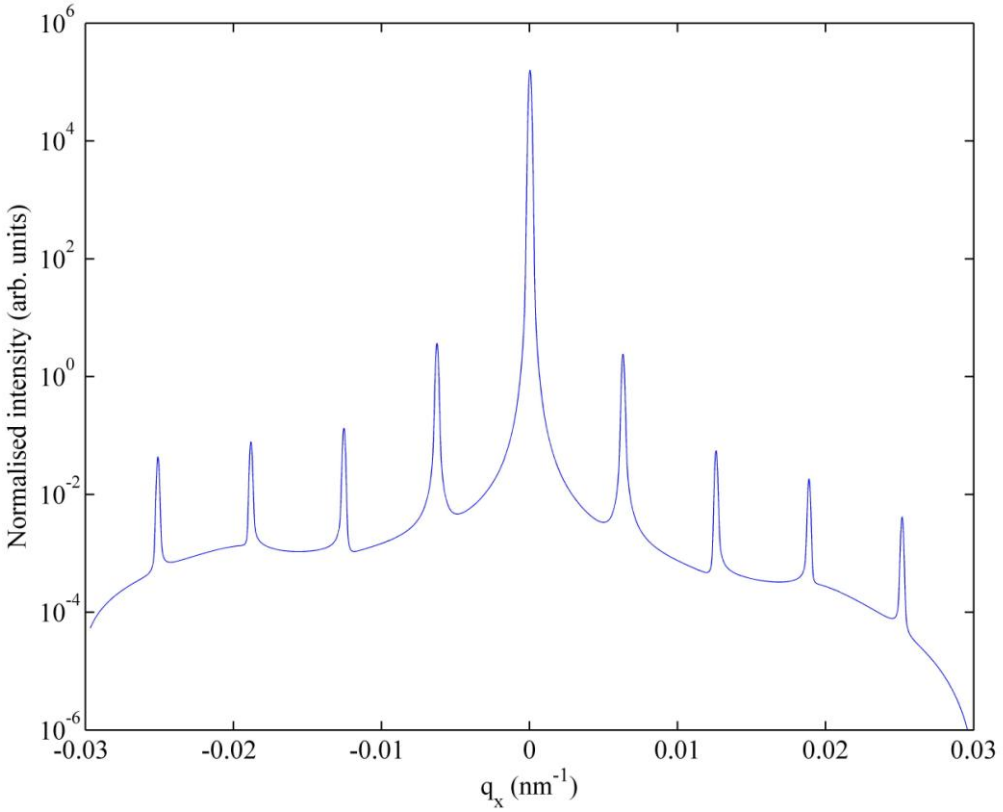

Figure 3-25. Simulated GIXS from an ideal reflection grating made of one hundred coherently scattering iron stripes of width 400 nm on a 1 μm pitch. The model incorporates the diffuse scatter simulation from section 3.4.4. The result is convolved with a constant resolution function of width Δq_x = 1 μm^{-1}.

3.8. Chapter summary

The sensitivity of grazing incidence scattering to the atomic and mesoscale characterization of thin films and nanostructures has been established theoretically. The specular reflectivity from a thin film has been derived in the dynamical Parratt formalism, incorporating the effect of a finite interface width. The complex relationship of diffuse x-ray scattering to the nature of interfaces has been shown able to separate topological roughness from interdiffusion, to characterize the self-affine fractalinity and in-plane length scale of interface topology, and to measure the conformality of roughness from one interface to the next. A brief explanation of x-ray diffraction (with particular focus on diffraction at grazing incidence and exit angles) has been given, in order that the measurements shown in later chapters can be understood.

These different surface-sensitive measurements are summarized in Table 3-1, which includes methods needed for data analysis, and indicators of the technique sensitivity.

Table 3-1. A summary of the surface-sensitive x-ray scattering techniques demonstrated in this thesis.

MEASUREMENT		METHOD OF ANALYSIS	SENSITIVITY
Specular X-ray Reflectivity (XRR)		Recursive fitting to a realistic initial model of the layer structure.	Precise measurements of layer thicknesses and interface widths (film thicknesses 0.1 nm – 500 nm).
Diffuse x-ray scattering at grazing incidence	Distorted Wave Born Approximation (DWBA) analysis	Computationally intensive simulation and fitting, only possible with prior knowledge of the out-of-plane layer structure.	Separates topological roughness and interdiffusion. Quantifies in-plane and out-of plane roughness correlations.
	Born analysis	Quantification of the ratio of the specular intensity to the integrated transverse diffuse scatter.	Provides an average of the interface topological roughness, weighted according to electron density contrast.
	Power law GISAXS analysis	Fitting of power laws to the integrated diffuse scatter.	Provides a weighted average measure of the in-plane and out-of-plane roughness correlations.
High-Angle X-ray Diffraction (HAXRD)		Diffraction peak position and width fitting.	Absolute measurement of out-of-plane crystal lattice *d*-spacings and dispersion, averaged over the uppermost 1-100 μm.
Grazing-Incidence In-plane X-Ray Diffraction (GIIXRD)		Analysis of diffraction peak position and width as a function of grazing incidence angle.	Absolute measurement of in-plane crystal lattice *d*-spacings and dispersion, with depth selectivity up to 100 nm.
Grazing-incidence x-ray scattering (GIXS) from periodic nanostructures		Fitting a semi-kinematical model of GIXS as a function of azimuthal sample orientation.	Measurement of repeat period and element profile of periodic nanostructures. Sensitive on in-plane length scales of 10 nm – 10 μm.

4. The effect of preoxidation on the interface structure of Co/Al_2O_3 and Co/MgO multilayers

Preoxidation is a process used in the fabrication of GMR spin valves and magnetic tunnel junctions. After deposition of the first ferromagnetic electrode, the surface is exposed to a low pressure of oxygen gas prior to deposition of the nonmagnetic layer. It has been reported that this reduces interlayer magnetic coupling and enhance magnetoresistance, although the mechanisms are not well understood.

In this chapter, x-ray reflectivity and diffuse scatter was analysed to understand changes occurring due to preoxidation at interfaces in sputtered Co/Al_2O_3 and Co/MgO trilayers and multilayers. For Co/Al_2O_3 systems, a chemical sharpening of the interface was observed, together with a more uniform oxidation of the Al_2O_3 layer. In Co/MgO multilayers no similar change in interface width or in layer thicknesses was detected, but a distinct increase in the in-plane correlation cut-off length of the interface roughness suggested a possible mechanism for the reduction in interlayer coupling.

4.1. Introduction

4.1.1. Interlayer coupling mechanisms

Interlayer coupling between ferromagnetic electrodes in magnetoresistive sensors can cause nonlinear or hysteretic response to an external field and degrade the operational sensitivity. At the end of chapter 2, some the design features used in magnetoresistive sensors were briefly introduced.

There are several mechanisms which can cause interlayer coupling between thin ferromagnetic films. Oscillatory exchange coupling is thought to be a manifestation of the Ruderman-Kittel-Kasuya-Yosida (RKKY) interaction, which itself has been

explained in terms of the electron wavefunction within the spacer layer [39]. It can encourage either parallel or antiparallel alignment of two adjacent ferromagnetic electrodes depending upon the distance separating them.

A second type of coupling can occur with very thin spacer layers, when pinholes directly linking the two ferromagnetic layers can lead to very strong ferromagnetic coupling (Figure 4-1a). (This is also likely to cause a catastrophic loss of magnetoresistance as the spacer is short-circuited.) As the dimensions of the thin films are laterally constrained, stray field coupling between the layers occurs when flux closure at the edges supports an antiparallel alignment of the electrodes (Figure 4-1b).

The final coupling mechanism discussed here, and the one of primary interest in this chapter is Néel (or "orange-peel") interlayer coupling.

4.1.2. Néel interlayer coupling

This coupling mechanism was first proposed by Néel in 1962 [100], and is illustrated in Figure 4-2. It is associated with free poles created in the ferromagnetic electrodes at undulations in the interface with the spacer layer.

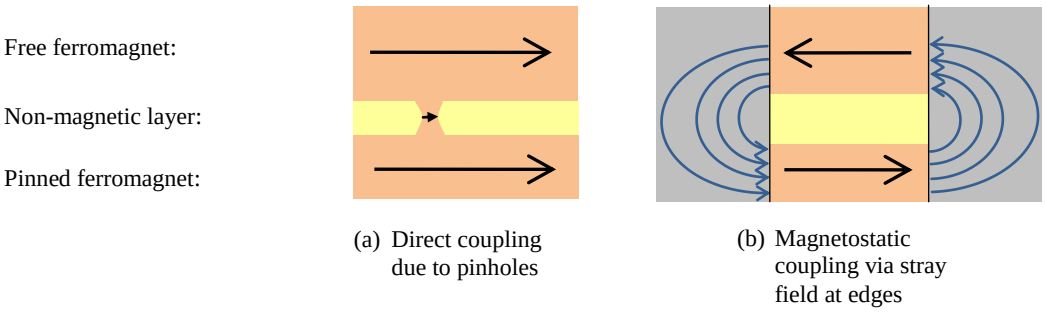

Figure 4-1 (above). Schematic diagram of (a) direct coupling due to pinholes, and (b) stray field coupling at edges of a small sensor element.

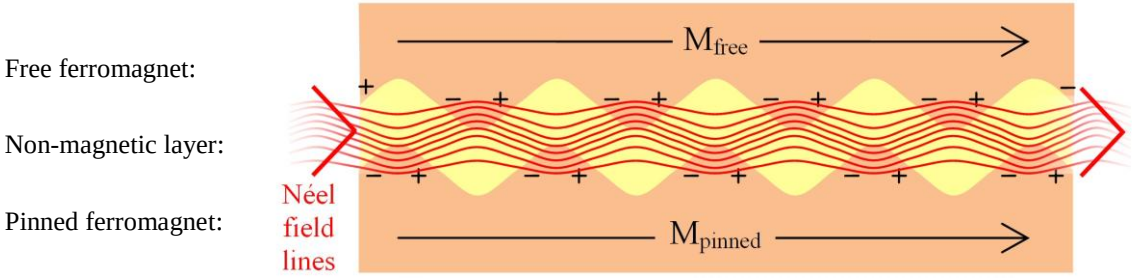

Figure 4-2 (above). Schematic diagram of the Néel magnetic field which couples two thin ferromagnetic electrodes, acting to favour a parallel alignment of the electrodes. The interfaces shown are sinusoidal and have fully conformal interfaces.

Néel proposed a simple model that assumed a sinusoidal and fully conformal interface [100], which was subsequently interpreted by Kools *et al* [101]. It predicts a variation of the coupling field $H_{\text{Néel}}$ which increases with roughness amplitude σ but also depends on the in-plane characteristic length of the roughness, λ, through:

$$H_{\text{Néel}} = \frac{\pi^2 \sigma^2 M_p}{\sqrt{2}\lambda t_f} \exp\left(\frac{-2\sqrt{2}\pi t_b}{\lambda}\right) \tag{4.1}$$

Here M_p is the saturation magnetisation of the electrodes, t_f is the thickness of the free electrode, and t_b is the barrier (or spacer) layer thickness.

The coupling field is phenomenologically defined as the shift from zero of the centre of the easy axis hysteresis loop. The overall trend of H_f with barrier thickness is in good agreement with the variation observed in Co/MgO/Co/IrMn MTJs [e.g. ref. 102]. From this above model, it is clear that minimisation of the coupling field requires control of both the amplitude of interface roughness and its in-plane length scale. These parameters can be statistically and non-destructively determined by grazing incidence x-ray scattering.

In this chapter, both grazing incidence specular and diffuse x-ray scattering are used to determine the layer and interface parameters of Al_2O_3 based MTJ structures and Co/MgO multilayers. Diffuse scatter is observed in both the conventional q_x-q_z geometry and also in the out-of plane q_y direction in the grazing incidence small angle x-ray scattering geometry.

4.1.3. Reported effects of preoxidation on MR and interlayer coupling

It has previously been reported that preoxidation of the bottom electrode prior to deposition of the Al_2O_3 or MgO barrier in magnetic tunnel junctions acts to suppress orange-peel coupling between cobalt electrodes.

One research group in particular have performed extensive studies of preoxidation during their development of low field sensors. In 1997, Egelhoff *et al* at NIST inadvertently discovered improvements in spin valve sensitivity after oxygen contamination during growth [103]. They reported that when 6.5×10^{-7} Pa of O_2 was present in the chamber during magnetron sputter deposition of the bottom (pinned) cobalt electrode onto NiO, the GMR increased significantly. Their paper proposed that "oxygen appears to act as a surfactant during growth, suppressing mixing at the Co/Cu interface and increasing the extent of specular electron scattering…". Furthermore, Egelhoff *et al* showed that Néel interlayer coupling was reduced, proposing that oxidation of cobalt protrusions makes them non magnetic, hence eliminating the exposed magnetic poles.

In 2000, Schrag *et al* published evidence that Néel coupling was present in Al_2O_3 based MTJs [104]. This led to preoxidation being studied in tunnel junction structures, where dramatic reductions in Néel coupling together with small increases but improved consistency in TMR values have been reported by Egelhoff *et al* [102, 105]. The precise microscopic role of preoxidation is not yet fully understood.

4.2. Study of preoxidation and the Co/Al_2O_3 interface

The first grazing incidence x-ray scattering experiments in this chapter focus upon the differences between aluminium oxide layers deposited onto preoxidized and unpreoxidized cobalt surfaces. These were grown on a sequence of layers designed to replicate faithfully the Co/Al_2O_3 interface that would appear in an MTJ.

4.2.1. Sample preparation and the preoxidation process

All the thin film structures studied in this chapter were prepared in the group of Dr William Egelhoff Jr. in the Metallurgy Division of the Materials Science and Engineering Laboratory at NIST in Gaithersburg, Maryland, United States. The films were deposited by d.c.-magnetron sputtering at room temperature in a deposition chamber with base pressure of 7×10^{-8} Pa. The process was similar to that published by Egelhoff *et al* [102, 105]. The $Ni_{77}Fe_4Cu_5Mo_4$ alloy is used in low field sensors because it is magnetically very soft, and by direct exchange coupling with the cobalt electrode can result in large changes in output voltage for small changes in external field [106].

The nominal structure of the cobalt-aluminium oxide layers studied in this section is shown in Figure 4-3. Two samples were prepared. For the sample not preoxidized, aluminium was deposited onto the cobalt layer and then oxidized by an oxygen plasma. For the preoxidized sample, the cobalt surface was dosed with O_2 gas at 10^{-3} Pa for ten seconds prior to the reactive sputtering of Al_2O_3. Because this layer was resistant to further atmospheric degradation, no additional capping layer was needed.

Figure 4-3. Schematic outline of the nominal structure of the Co/Al_2O_3 thin films.

Preoxidized surface →

	SAMPLE COMPOSITION		
	Material	**Thickness (nm)**	**Nominal layer function**
	Al_2O_3	3	Barrier
	Co	2.5	Lower (free) electrode
	$Ni_{77}Fe_4Cu_5Mo_4$	30	Soft sensing layer
	SiO_2	~ 300	Substrate layers
	Si	~ ∞	

4.2.2. Experimental method

Measurements were made on the XMaS beamline (BM28) at the European Synchrotron Radiation Facility in Grenoble, France, which is described in the paper by Brown *et al* [107]. X-rays produced from the bending magnet were monochromated to a fixed energy of 7.00 keV, and close to the sample the beam had a height of 200 μm and a width of 500 μm. The incident divergence determined by fitting the incident and reflected line shape was 0.005°.

The reflection from the sample surface was orientated in the diffractometer such that it lay in the vertical scattering plane. During exposure to the beam, nitrogen gas was blown over the sample surface to minimise beam damage.

The specular reflection of x-rays by thin films was interpreted as the Fresnel reflectivity modified by a function describing the interface width, as described in chapter 3, section 3.3. Since the wavevector transfer is entirely perpendicular to the surface, specular scattering is only sensitive to the averaged in-plane structure. By measuring the diffuse scatter away from the specular condition it is possible to examine the nature of the roughness in terms of both an in-correlation cut-off length, and a fractal scaling exponent *h* (parameters introduced in chapter 3, section 3.4).

4.2.3. X-ray scattering results: without preoxidation

The reflectivity and longitudinal diffuse measurements for the sample prepared without preoxidation are shown in Figure 4-4 together with best fit simulations. The Kiessig fringes present in the longitudinal diffuse scatter indicate that the roughness is highly conformal between layers.

Figure 4-5 shows transverse diffuse (rocking curve) measurements at two detector angles. Excellent correspondence between data and simulations within the distorted wave Born approximation (DWBA) is achieved by manually optimising the in-plane correlation cut-off length and fractal parameter, and by altering the relative contribution of topological undulation and chemical interdiffusion to the interface width. By fitting data at different detector angles there is a high degree of confidence in the uniqueness of the model parameters.

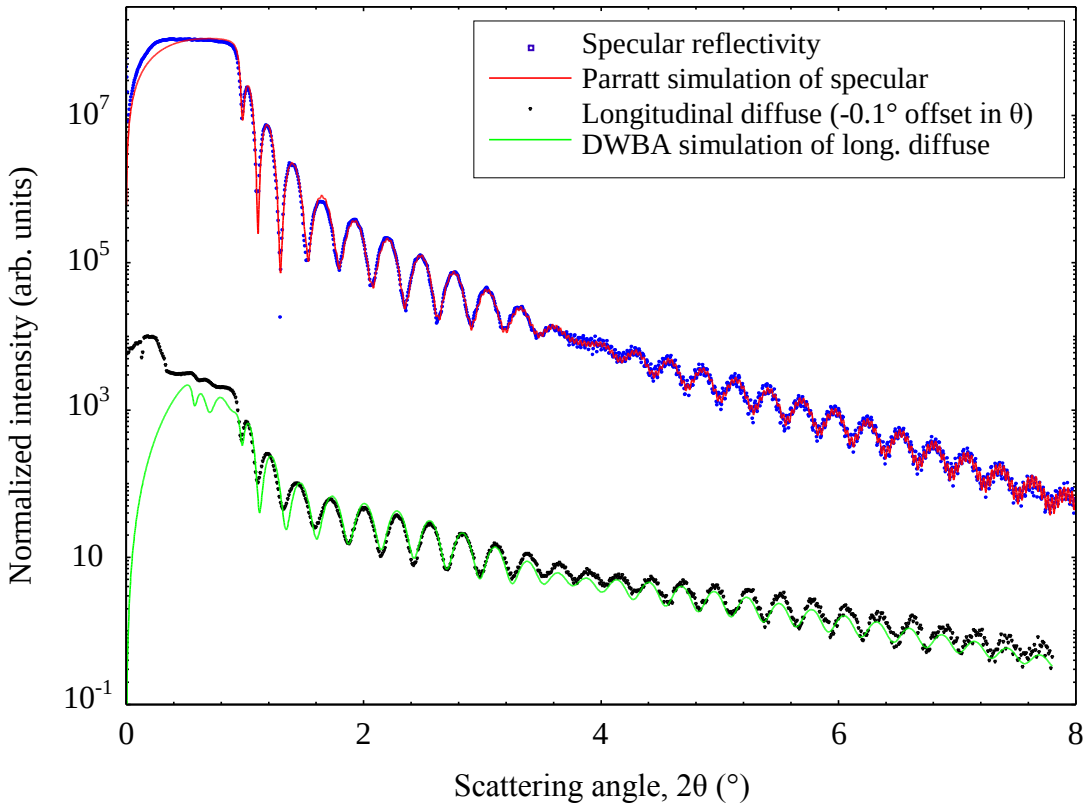

Figure 4-4. Specular reflectivity and longitudinal diffuse scatter from a Co/Al_2O_3 structure without preoxidation. Parameters used to produce the best fit simulations are given in Table 4-1. The in-plane correlation cut-off length used to fit all curves was 7.5 nm, and Hurst fractal parameter h = 0.17.

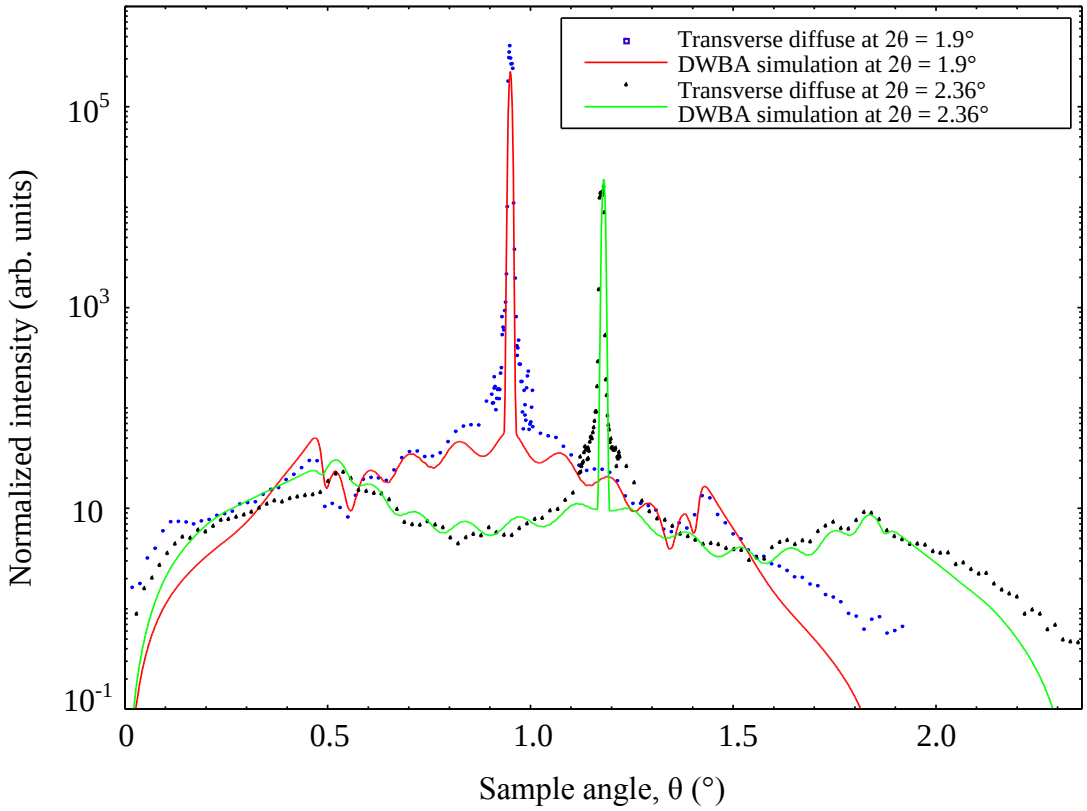

Figure 4-5. Transverse diffuse scatter measurements at a Kiessig maximum (2θ = 1.9°) and a Kiessig minimum (2θ = 2.36°), together with simulations made within the DWBA for the Co/Al_2O_3 sample without preoxidation. The in-plane correlation cut-off length used to fit all curves was 7.5 nm, with a Hurst fractal parameter h = 0.17.

Table 4-1. Best fit parameters used in the simulation of specular reflectivity and longitudinal diffuse scatter for the Co/Al_2O_3 interface without preoxidation shown in Figure 4-4 and the transverse diffuse scatter in Figure 4-5.

MATERIAL PARAMETERS		**RECURSIVELY FITTED PARAMETERS**			**MANUALLY ADJUSTED PARAMETERS**	
Chemical composition	**Bulk density (g cm^{-3})**	**Thickness (nm)**	**Packing density (%)**	**Interface width (nm)**	**Topological roughness (nm)**	**Interdiffusion (nm)**
Al_2O_3	3.97	1.53 ± 0.01	30.9 ± 0.8	0.44 ± 0.01	0.4	0.0
Al	2.700	2.19 ± 0.01	79.1 ± 1.9	0.40 ± 0.01	0.1	0.4
Co	8.860	1.63 ± 0.28	90.6 ± 1.9	0.94 ± 0.01	0.4	0.9
$Ni_{77}Fe_{14}Cu_5Mo_4$	8.900	30.34 ± 0.28	99.2 ± 0.1	2.04 ± 0.14	0.8	1.9
$Ni_{77}Fe_{14}Cu_5Mo_4$	8.900	1.20 ± 0.02	103.2 ± 0.1	0.00 ± 0.01	–	–
SiO_2	2.533	300.17 ± 0.01	103.9 ± 0.4	0.30 ± 0.01	0.2	0.2
Si	2.328	substrate	100 (fixed)	0.00 ± 0.00	0.0	0.0

The fitted parameters are given in Table 4-1. The interfaces most influential upon the goodness of fit are those which divide regions of strongly contrasting electron density. Here these are the $SiO_2/Ni_{77}Fe_{14}Cu_5Mo_4$, the Co/Al, and the Al_2O_3/air interfaces.

Fitting started with the nominal structure, but was adapted to incorporate two additional layers in order to improve the fit. The soft magnetic layer has been separated into two independent layers in order to simulate the lower interface more realistically than the simple error function interdiffusion model in the modified Parratt formalism. The alumina layer has been separated into an oxidized and an unoxidized layer, although in reality there is likely to be a single layer with an extended composition gradient.

There is a low level of topological roughness inherited from the substrate. The soft magnetic layer is deposited close to the bulk density, with an accurate thickness. The density of the cobalt layer is slightly lower than the bulk value for this metal; this can be attributed to the thinness of the layer, which equates to only a few atomic layers. Fits to the diffuse scatter suggest that the $Ni_{77}Fe_{14}Cu_5Mo_4$/Co interface may be diffuse, with the 3d transition metals alloying readily.

The interface of most interest is the Co/Al boundary. From the level of diffuse scatter relative to the specular reflectivity it was determined that the interface width was mainly composed of interdiffusion. The topological roughness value is consistent with inheritance from the substrate.

4.2.4. X-ray scattering results: with preoxidation

The specular reflectivity and longitudinal diffuse scatter from a preoxidized sample is shown in Figure 4-6. The high frequency fringes resulting from interference from the top and bottom surfaces are shown in the inset graph (and were also present in the previous sample, though less clear due to coarser sampling during the scan). The transverse diffuse measurements and simulations are shown in Figure 4-7, displaying close agreement.

Away from the interface of primary interest, the fitted parameters are broadly similar to the previous sample. There is evidence of reduced interdiffusion of the NiFeCuMo and Co into the barrier layer leading to a significant reduction in the overall interface width.

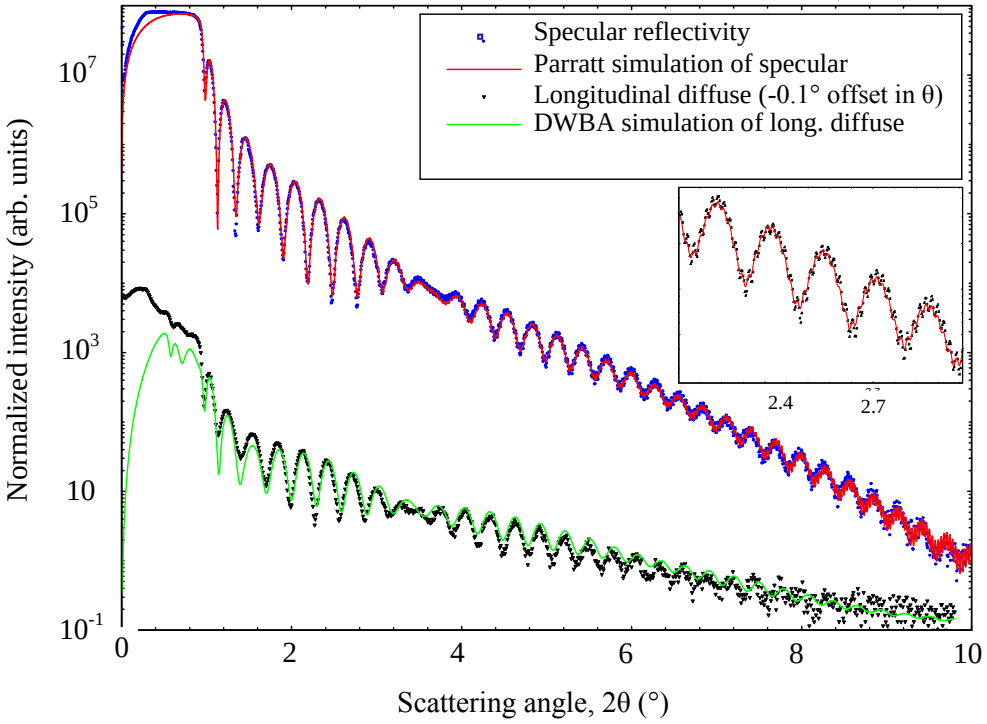

Figure 4-6 (above). Specular reflectivity and longitudinal diffuse scatter from a Co/Al_2O_3 structure with preoxidation. Parameters used to produce the best fit simulations are given in Table 4-2. Inset: high frequency fringes originating from the total stack thickness.

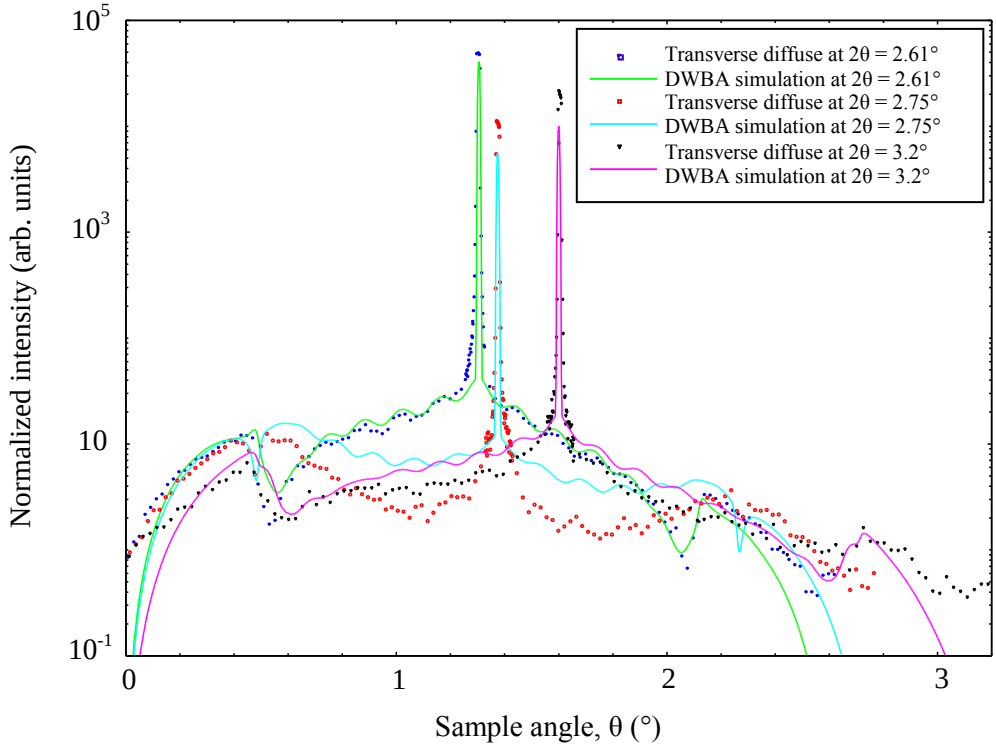

Figure 4-7. Transverse diffuse scatter measurements at Kiessig maxima (2θ = 2.61°, 2θ = 3.2 °) and a Kiessig minimum (2θ = 2.75°), together with simulations made within the DWBA for the Co/Al_2O_3 sample with preoxidation. The in-plane correlation cut-off length used to fit all curves was 7.5 nm, and the Hurst fractal parameter h = 0.17.

Table 4-2. Best fit parameters used in the simulation of specular reflectivity and longitudinal diffuse scatter for the interface with preoxidation shown in Figure 4-6 and the transverse diffuse scatter in Figure 4-7.

MATERIAL PARAMETERS		**RECURSIVELY FITTED PARAMETERS**			**MANUALLY ADJUSTED PARAMETERS**	
Chemical composition	**Bulk density ($g\ cm^{-3}$)**	**Thickness (nm)**	**Packing density (%)**	**Interface width (nm)**	**Topological roughness (nm)**	**Interdiffusion (nm)**
Al_2O_3	3.97	1.65 ± 0.05	33.3 ± 1.1	0.40 ± 0.00	0.40	0
Al	2.700	2.27 ± 0.05	117.8 ± 3.2	1.10 ± 0.07	1.10	0
Co	8.860	0.67 ± 0.08	60.0 ± 4.9	0.58 ± 0.02	0.5	0.28
$Ni_{77}Fe_{14}Cu_5Mo_4$	8.900	29.57 ± 0.08	99.0 ± 0.1	0.85 ± 0.03	0.45	0.72
$Ni_{77}Fe_{14}Cu_5Mo_4$	8.900	1.02 ± 0.01	103.9 ± 0.3	0.16 ± 0.01	–	–
SiO_2	2.533	298.10 ± 0.01	87.2 ± 0.4	0.35 ± 0.00	0.35	0
Si	2.328	substrate	100 (fixed)	0.09 ± 0.03	0.09	0

4.2.5. Interpretation of results for the Co/Al_2O_3 interface

The primary effect of preoxidation on the Co/Al_2O_3 interface is to reduce the interdiffusion and therefore the overall interface width. There is no observable change in layer thicknesses or topological roughness propagating through the stack. This is a somewhat surprising result; the deliberate oxidation of the cobalt electrode prior to barrier deposition could naively be expected to roughen the interface. There is no evidence that preoxidation increases the thickness of the aluminium oxide layer or reduces the amplitude or in-plane correlation cut-off length of the interface topology.

One may propose that this fabrication process leads to more uniform oxidation of the aluminium oxide barrier, and less intermixing of aluminium and cobalt. Buchanan *et al* have previously shown that this interface intermixes by up to 1 nm [ref. 108]. A sharpening of the contrast in electron density at this interface would be consistent with the observation that the junction resistance increases significantly and that the TMR both increases and is more reproducible [105]. A second proposition, previously made by Egelhoff *et al* [105] is that preoxidation causes oxidation (and therefore loss of ferromagnetism) in cobalt prominences on the surface of the electrode, reducing the stray field from exposed magnetic poles that contributes to Néel interlayer coupling. This idea would imply a smearing of the electron density at the Co/Al_2O_3 interface, which is in contradiction to the measurements presented here in Table 4-1 and Table 4-2.

4.3. Study of preoxidation and Co/MgO multilayers

The preoxidation method was also shown to be effective in reducing the coupling field in MgO based tunnel junctions, in addition to spin valves and aluminium oxide MTJs [102]. Following the investigation of aluminium oxide based layers, a second study exploring the effect of preoxidation at the Co/MgO interface was undertaken.

4.3.1. Sample preparation

Repeat layers of the Co/MgO interface were grown upon a 20 nm $Ni_{77}Fe_{14}Cu_5Mo_4$ seed layer deposited on thermally oxidized silicon wafers, under the same growth conditions specified in section 4.2.1. To preoxidize samples, 10^{-3} Pa O_2 was admitted to the chamber and there was a ten second delay prior to turning on the magnetron gun and depositing the MgO layer by reactive sputtering. For samples not preoxidized, magnesium metal was deposited and subsequently oxidized in an oxygen plasma (as is common practice with aluminium oxide barriers). The nominal structure, Si / SiO_2 / $Ni_{77}Fe_{14}Cu_5Mo_4$ [20 nm] / (Co [10 nm] / MgO [2 nm])$_{\times n}$ / Co [2.5 nm] / Al_2O_3 [1 nm], is shown in Figure 4-8. This was grown for n = 3 and 5.

Figure 4-8. Schematic outline of the nominal Co/MgO multilayer structure.

	MULTILAYER COMPOSITION		
	Material	**Thickness (nm)**	**Nominal layer function**
	Al_2O_3	1	Capping layer
	Co	2.5	Electrode
Preoxidized surface →	MgO	2	Electrode-barrier repeated bilayer
	Co	10	
	$Ni_{77}Fe_4Cu_5Mo_4$	20	Soft sensing layer
	SiO_2	~ 300	Substrate layers
	Si	~ ∞	

In order to enhance the sensitivity to this key Co/MgO interface, multilayer structures were fabricated to reinforce scattering at angles relating to Bragg interference [109]. Not only is the scattered intensity repeated, but constructive interference occurs most strongly when the interface conforms from one layer to the next, i.e. undulations propagate up through the stack of layers. This is precisely the type of correlated corrugation which can trap adjacent magnetic dipoles on either side of the tunnel barrier and increase Néel coupling.

In studies of multilayer samples it is preferable to use very high repeats of the interface of interest, often up to $n = 50$, since the coherently scattered intensity scales with n^2. Unfortunately samples incorporating many repeats of metal oxide layers are very time consuming to fabricate since after each oxide deposition unadsorbed oxygen must be pumped out of the vacuum system before the subsequent metallic layers can be grown. In order to reduce the evacuation volume and time, the sample may be transferred to an adjoining oxidation chamber which is isolated from the main sputtering chamber. Even using this technique, the turnaround time for a single oxide layer is still of the order of a few hours. For this study, samples with three and five repeats were grown.

4.3.2. Experimental method

X-ray reflectivity and coplanar diffuse scatter measurements in the vertical reflectivity geometry were undertaken on beamline I16 of the Diamond Synchrotron Light Source near Didcot during its first period of user beam delivery in January 2007. These measurements used an incident energy of 7.0 keV with a beam height of 200 μm.

Out-of-plane measurements of the diffuse scatter from the same samples were performed using the MAR two dimensional detector at the XMaS beamline at the ESRF. These measurements were performed with 10 keV incident x-rays with a square beam cross section 200 μm × 200 μm.

4.3.3. X-ray reflectivity and coplanar diffuse scatter results

The specular and diffuse scatter from the $n = 5$ multilayer structures with and without preoxidation are shown in Figure 4-9 and Figure 4-10 respectively. Insets to both Figures show transverse diffuse measurements and fits for fixed detector angles of $2\theta = 3.3°$ and 3.4°.

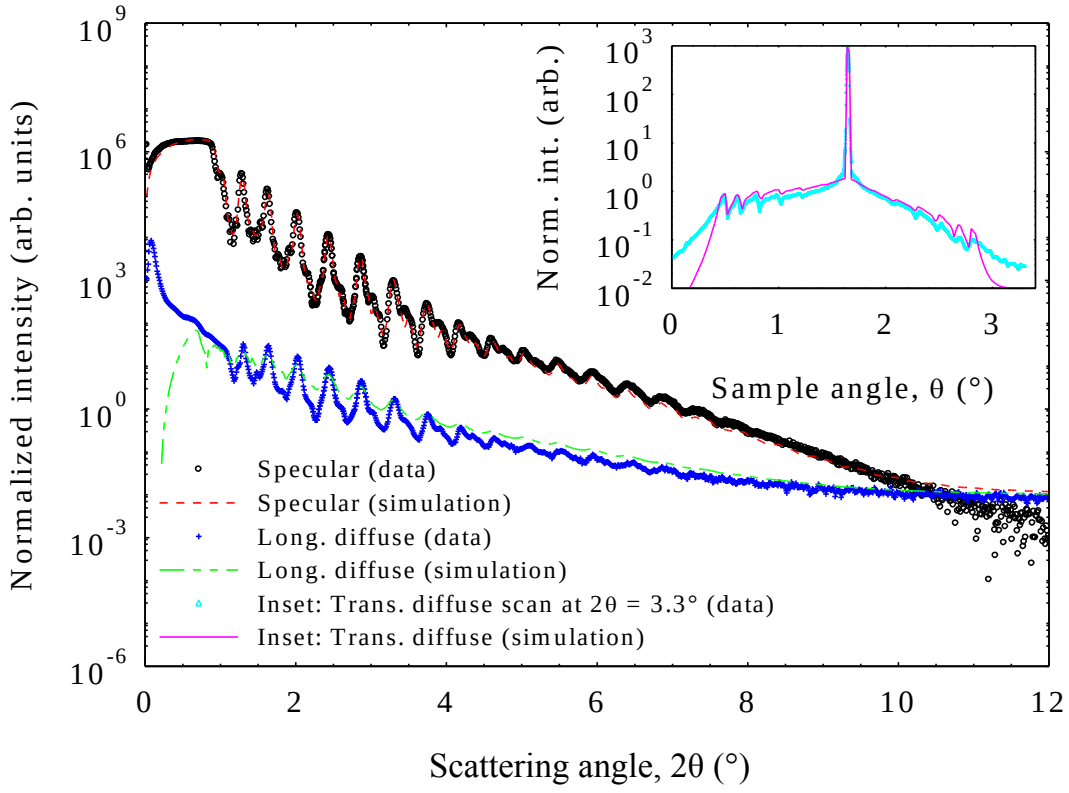

Figure 4-9. Specular and diffuse scatter from a structure nominally of the form Si / SiO_2 / NiFeCuMo [20 nm] / (Co [10 nm] / MgO [2 nm])×5 / Co [2.5 nm] / Al_2O_3 [1 nm] without pre-oxidation of the Co surface prior to MgO deposition. Inset: transverse diffuse scan and simulation for 2θ = 3.3°. Simulation parameters are consistent for all scans in the figure.

Table 4-3. Fitted parameters for the specular, longitudinal and transverse diffuse measurements on the (Co/MgO)×5 multilayer without preoxidation, as shown in Figure 4-9. In the diffuse scatter fits, the in-plane correlation length = 7 nm, and the fractal exponent = 0.2.

MATERIAL PARAMETERS		**RECURSIVELY FITTED PARAMETERS**			**MANUALLY ADJUSTED PARAMETERS**	
Chemical composition	**Bulk density ($g\ cm^{-3}$)**	**Thickness (nm)**	**Packing density (%)**	**Interface width (nm)**	**Topological roughness (nm)**	**Interdiffusion (nm)**
Al_2O_3	3.97	3 ± 4	125 ± 7	1.6 ± 1.4	0.4	1.5
Co	8.86	2 ± 4	91 ± 43	2.0 ± 5.9	0.4	1.9
MgO	3.60	2 ± 3	84 ± 9	1.2 ± 2.4	0.4	1.1
Co_3O_4	6.00	0 ± 3	53 ± 2	1.1 ± 4.9	0.4	1
Co	8.86	0.8 ± 0.6	100 (fixed)	1 ± 1	0.4	0.9
MgO	3.60	1.6 ± 0.9	109 ± 31	1 ± 1	0.4	0.9
Co_3O_4	6.00	0 ± 2	120 ± 65	1 ± 2	0.4	0.9
Co	8.86	1 ± 1	100 (fixed)	2 ± 7	0.4	1.9
MgO	3.60	2 ± 1	110 ± 5	1 ± 1	0.4	0.9
Co_3O_4	6.00	0 ± 2	150 ± 1	2 ± 3	0.4	1.6
Co	8.86	1 ± 2	100 (fixed)	2 ± 8	0.4	1.7
MgO	3.60	2 ± 2	94 ± 50	0.7 ± 0.1	0.4	0.6
Co_3O_4	6.00	0.3 ± 1.7	114 ± 27	2.0 ± 5.2	0.4	1.9
Co	8.86	0.8 ± 0.2	100 (fixed)	0.6 ± 0.3	0.4	0.4
MgO	3.60	2 ± 1	110 ± 45	0.7 ± 0.1	0.4	0.6
Co_3O_4	6.00	0 ± 2	51 ± 5	1 ± 3.1	0.4	0.9
Co	8.86	0.8 ± 0.4	100 (fixed)	1 ± 0.9	0.4	0.9
$Ni_{77}Fe_{14}Cu_5Mo_4$	8.900	20 (fixed)	102 (fixed)	0.4 ± 0.1	0.4	0.1
SiO_2	2.53	200 (fixed)	100 (fixed)	0.4 ± 0.1	0.4	0.0
Si	2.33	substrate	100 (fixed)	0.1 ± 0.1	0.1	0

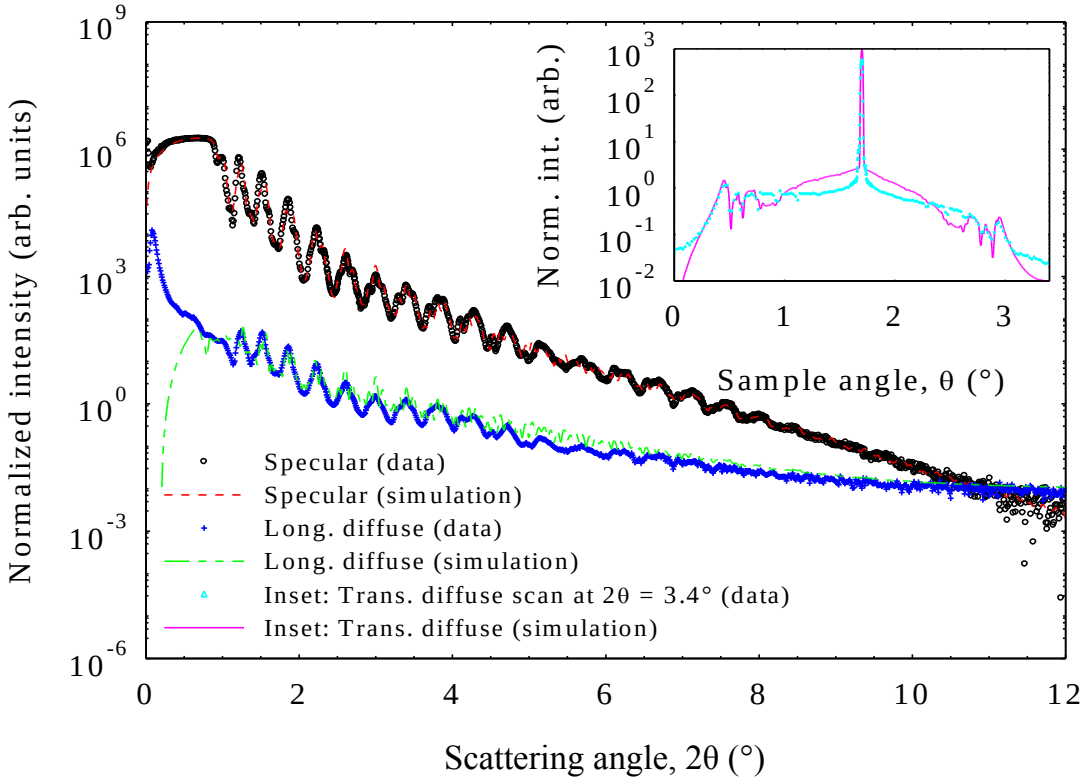

Figure 4-10. Specular and diffuse scatter from a structure nominally of the form Si / SiO_2 / $Ni_{77}Fe_{14}Cu_5Mo_4$ [20 nm] / (Co [10nm] / MgO [2 nm])×5 / Co [2.5 nm] / Al_2O_3 [1 nm] with pre-oxidation of the Co surface prior to MgO deposition. Inset: transverse diffuse scan and simulation. Simulation parameters are consistent for all scans in the figure.

Table 4-4. Fitted parameters for the specular, longitudinal and transverse diffuse measurements on the (Co/MgO)×5 multilayer with preoxidation, as shown in Figure 4-10. In the diffuse scatter fits, the in-plane correlation length = 7 nm, and the fractal exponent = 0.2.

MATERIAL PARAMETERS		**RECURSIVELY FITTED PARAMETERS**			**MANUALLY ADJUSTED PARAMETERS**	
Chemical composition	**Bulk density ($g\ cm^{-3}$)**	**Thickness (nm)**	**Packing density (%)**	**Interface width (nm)**	**Topological roughness (nm)**	**Interdiffusion (nm)**
Al_2O_3	3.97	2 ± 3	126 ± 1	2 ± 2	0.4	1.5
Co	8.86	3 ± 2	92 ± 21	2 ± 5	0.4	1.7
MgO	3.60	3 ± 1	78 ± 44	0.6 ± 0.1	0.4	0.4
Co_3O_4	6.00	0.5 ± 1	140 ± 3	1 ± 2	0.4	1.4
Co	8.86	2.0 ± 0.2	100 (fixed)	0 ± 1	0.02	0.0
MgO	3.60	3 ± 1	102 ± 22	0.7 ± 0.1	0.4	0.5
Co_3O_4	6.00	0.4 ± 1.9	126 ± 1	1 ± 1	0.4	1.0
Co	8.86	2 ± 2	100 (fixed)	1 ± 3	0.4	1.0
MgO	3.60	2.5 ± 0.6	70 ± 32	1.0 ± 0.7	0.4	1.0
Co_3O_4	6.00	0.5 ± 1.3	78 ± 27	1 ± 1	0.4	0.7
Co	8.86	1 ± 2	100 (fixed)	2 ± 5	0.4	1.7
MgO	3.60	2 ± 1	69 ± 1	2 ± 2	0.4	1.5
Co_3O_4	6.00	0 ± 1	150 ± 12	2 ± 4	0.4	2.0
Co	8.86	1.5 ± 0.2	100 (fixed)	0.5 ± 0.2	0.4	0.2
MgO	3.60	3 ± 1	110 ± 37	0.6 ± 0.1	0.4	0.5
Co_3O_4	6.00	0 ± 1	150 ± 8	2 ± 3	0.4	1.5
Co	8.86	2 ± 0	100 (fixed)	0.4 ± 0.1	0.4	0.1
$Ni_{77}Fe_{14}Cu_5Mo_4$	8.900	20 (fixed)	102 (fixed)	1 ± 2	0.4	0.9
SiO_2	2.53	200 (fixed)	100 (fixed)	0.4 ± 0.1	0.4	0
Si	2.33	substrate	100 (fixed)	0.1 ± 0.1	0.1	0

The specular reflectivity was fitted using the Parratt method (see section 3.3.5). Diffuse scans were then fitted within the distorted wave Born approximation (DWBA, section 3.4.6) by maintaining the layer compositions, thicknesses and interface widths, but by manually varying the balance of topology and interdiffusion and the in-plane correlation length and fractal parameter. The parameters used simultaneously to fit all these curves are provided in Table 4-3 (with preoxidation) and Table 4-4 (without preoxidation, in order to show that the key parameters cannot be adequately refined by fitting these data. Due to the number of free parameters required to achieve an acceptable fit, the uncertainties on each parameter are very large. Calculations show large covariances between fitted parameters, indicating strong correlations between many of the parameters. Despite this fact, an adequate fit cannot be found if the number of free parameters is reduced.

There are some, albeit limited conclusions which may reliably be drawn from these fits. There is no systematic, statistically significant difference between the fits for samples with and without preoxidation. The level of diffuse scatter is reproduced using a constant topological roughness 0.4 nm. In order to fit the longitudinal diffuse scatter, an in-plane correlation length of ξ = 10 nm is used with a fractal parameter of h = 0.2. This does not provide a good fit to the transverse diffuse scan for the preoxidized multilayer in Figure 4-10. One possibility is that additional layers may be necessary to generate an accurate model of the electron density profile.

Both scattering datasets shown in Figure 4-9 and Figure 4-10 were fitted using layer thicknesses close to their nominal values. Unlike comparative data taken from annealed [110] or preoxidized Al_2O_3 based tunnel junction structures [section 4.2], no statistically significant change in either the overall interface width (from the specular scatter) or the amplitude of the topological roughness was observed between the two types of specimen.

4.3.4. Born analysis of the transverse diffuse scatter

Transverse diffuse scans were performed on all the n = 3 and 5 samples with and without preoxidation at three different angles, as shown in Figure 4-11 (without preoxidation) and Figure 4-12 (with preoxidation).

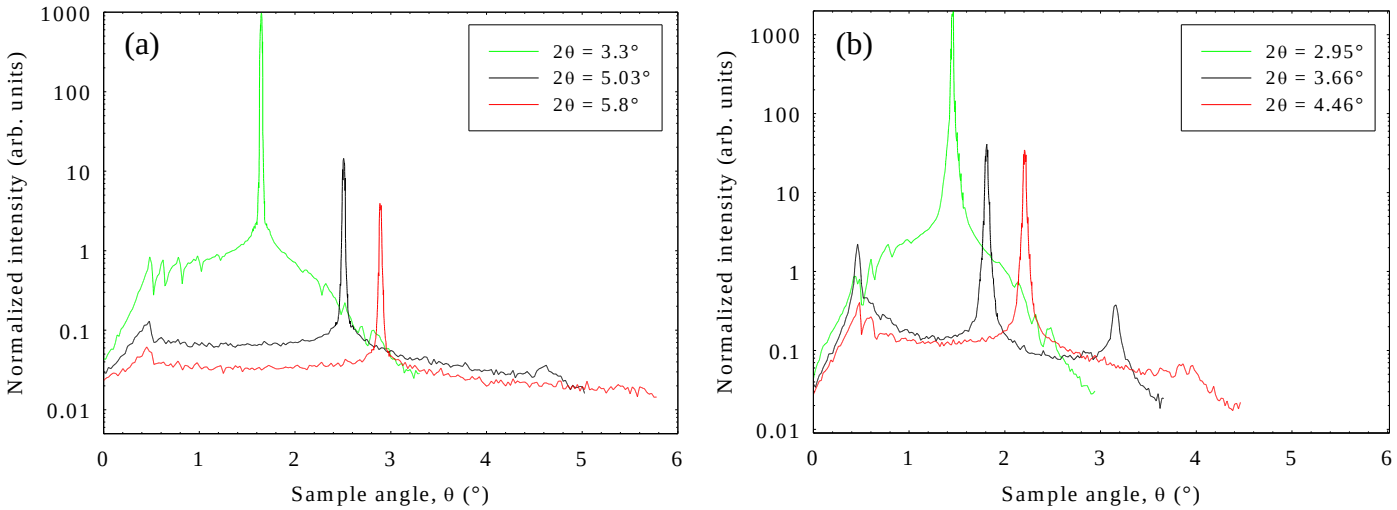

Figure 4-11. Transverse diffuse measurements from the multilayers without preoxidation (a) for n = 5, and (b) for n = 3. The specular intensity is fitted after subtracting the background diffuse level. The ratio of the integrated specular intensity to the integrated diffuse scatter is then used to estimate the topological roughness shown in Figure 4-13 and Table 4-5 using the Born approximation.

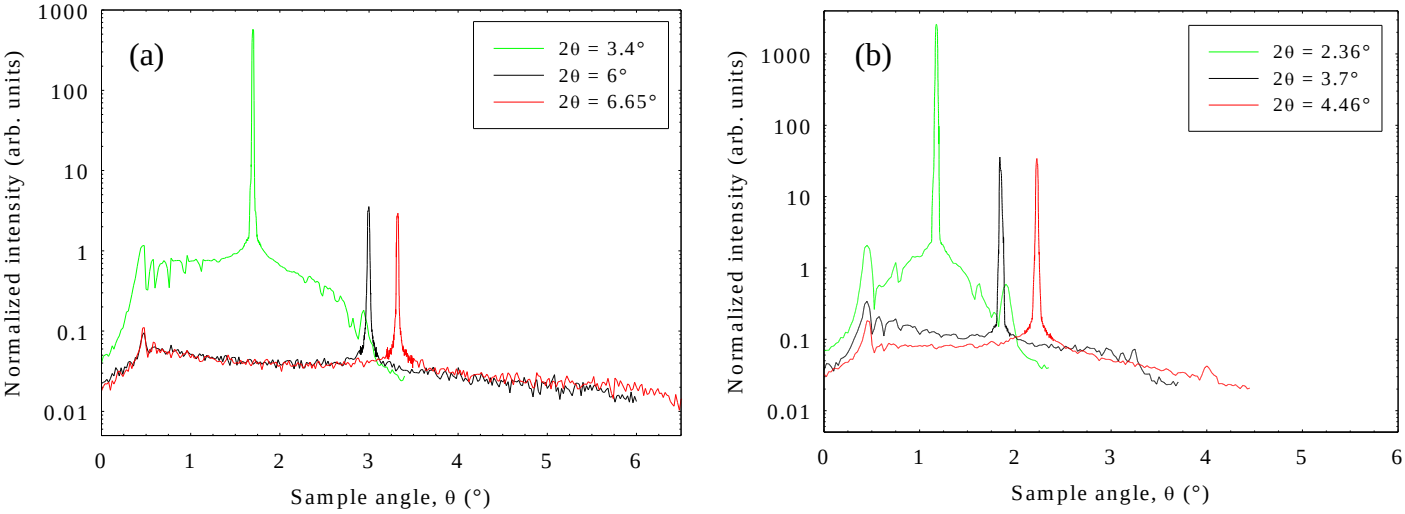

Figure 4-12. Transverse diffuse measurements from the multilayers with preoxidation (a) for n = 5, and (b) for n = 3.

The ratio of the integrated transverse diffuse scatter and the specular intensity can be interpreted within the Born approximation to estimate the topological roughness (as described in section 3.4.2). The resulting values are shown in Figure 4-13. Because the sample surface acts to restrict the range over which diffuse scatter can be collected, this slightly underestimates the true topological roughness. As the scan is performed at progressively higher fixed detector angles the geometrical restriction relaxes, and the estimated roughness asymptotes towards the true value.

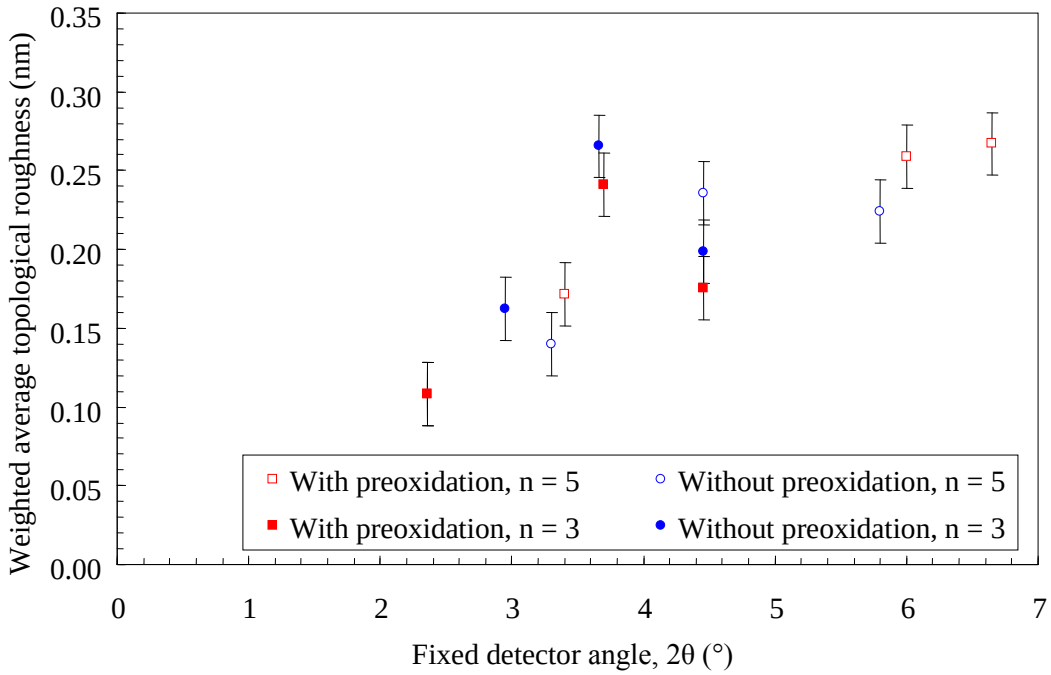

Figure 4-13. Topological roughness estimated from the ratio of the specular to diffuse scatter in a transverse diffuse scan. The dominant source of error is the discrimination of the specular intensity from the underlying diffuse scatter. Here the specular intensity is considered as accurate to ±10%.

Table 4-5. Weighted average topological roughnesses estimated using the Born approximation.

Number of repeats	**TOPOLOGICAL ROUGHNESS FROM BORN APPROXIMATION**			
	Without preoxidation		**With preoxidation**	
	Mean σ (nm)	**Standard error (nm)**	**Mean σ (nm)**	**Standard error (nm)**
3	2.0	0.5	1.6	0.6
5	2.0	0.5	2.3	0.5

The values obtained are shown in Table 4-5 and are weighted over all interfaces in the sample according to the contrast in refractive index at each interface, which in this case are predominantly the Co/MgO and Al_2O_3/air interfaces.

The resulting topological roughness of samples preoxidized and not preoxidized approaches a limiting value, $\sigma \rightarrow$ 0.3 nm. This is highly consistent with the 0.4 nm determined by fitting the longitudinal and transverse diffuse scans within the DWBA in section 4.3.3.

4.3.5. Grazing incidence small angle x-ray scattering

The plane of incidence is defined as the plane containing the incident beam and the surface normal of the sample. In reciprocal space (using the coordinate system specified in section 3.2.2), it is defined by $q_y = 0$. The x-ray reflectivity and diffuse measurements presented previously are all contained within this plane. It will now be shown that the diffuse scatter measured out of the plane of incidence was systematically different between samples using the technique commonly known as grazing incidence small angle x-ray scattering (GISAXS). A two dimensional Mar CCD detector was set at a distance 0.9 m from the sample, providing an angular resolution of 0.0057°.

Figure 4-14 shows the diffuse scatter image from a five repeat Co/MgO multilayer (a) without preoxidation, and (b) with preoxidation. Similarly, Figure 4-15 relates to the three repeat multilayer (a) without preoxidation, and (b) with preoxidation.

Each image was taken in a single exposure by a 2D detector with a count time of 60 seconds and an incidence angle of 1.038°. The central ridge at $q_y = 0$ intersects the specular reflection at a single point, which saturates the detector causing 'bleeding' to neighbouring CCD pixels (coloured white). For $|q_y| > 0$ the out-of-plane diffuse scatter is detected. The ridges extending into q_y are Bragg 'sheets' originating from coherent scatter from correlated interfaces through the multilayer stack. It is immediately apparent that in the preoxidized case these Bragg sheets are more restricted in the q_y direction than is the case without preoxidation.

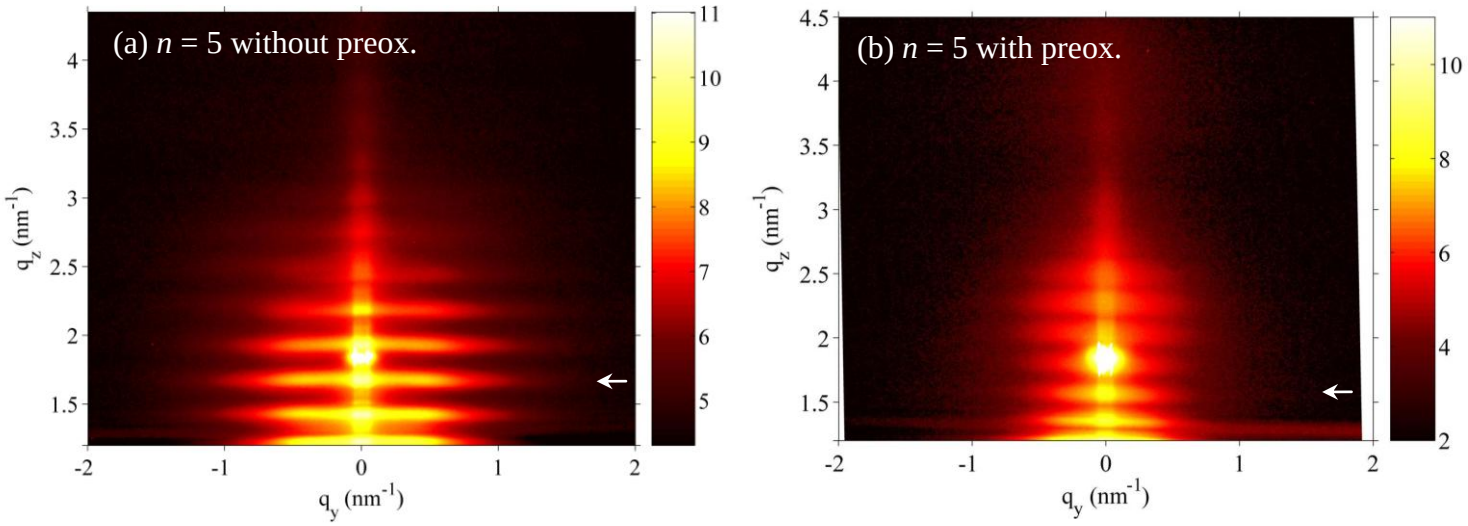

Figure 4-14. Diffuse scatter recorded with 2D CCD detector for the five repeat Co/MgO multilayer sample (a) without preoxidation and (b) with preoxidation. Colour scale is the natural logarithm of the counts per pixel over a sixty second integration period. Arrows indicate the Bragg sheet made subject to quantitative analysis.

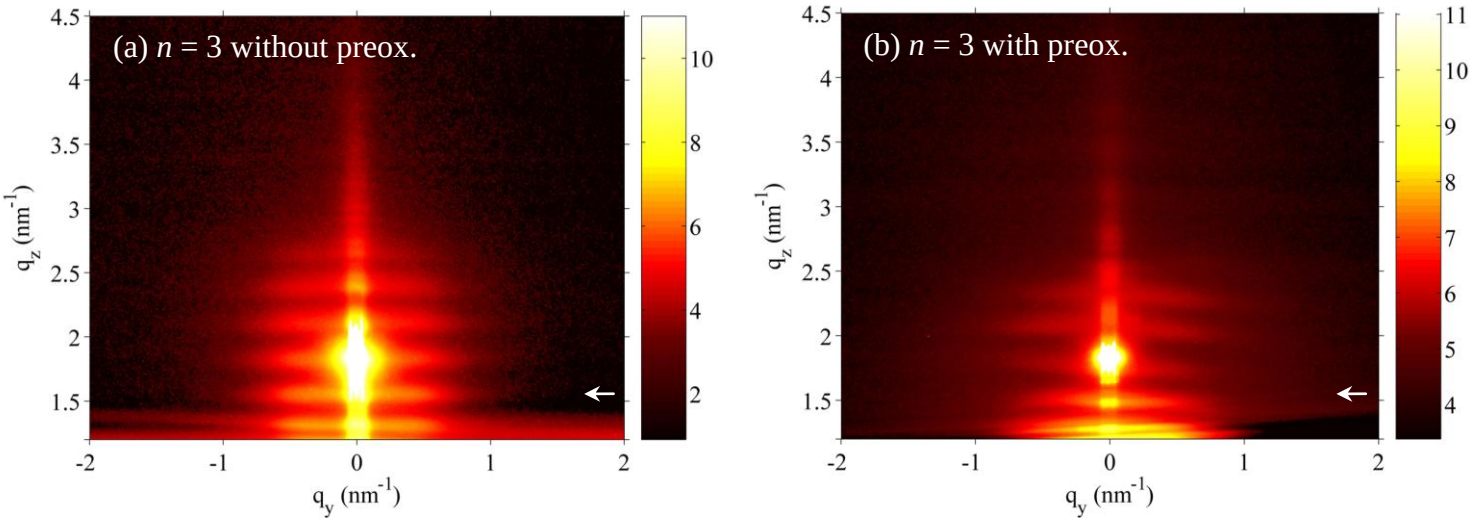

Figure 4-15. Diffuse scatter recorded with 2D CCD detector for the three repeat Co/MgO multilayer sample (a) without preoxidation and (b) with preoxidation. Colour scale is the natural logarithm of the counts per pixel over a sixty second integration period.

4.3.6. Method of quantitative analysis of GISAXS

These Bragg sheets are rich with information about the nature of the conformal topological roughness. The three key measurements obtained from the Bragg sheets are (i) the cut-off point in q_y, (ii) the power law by which they decay after this point, and (iii) how the width in q_z varies as a function of q_y.

In chapter 3, section 3.4, the theory of diffuse scattering was developed, and some relevant theory by Salditt *et al* [92] was discussed. Here, the application of this theory according to Paniago *et al* [93] is outlined

The in-plane correlation cut-off length, ξ relates to the length over which two points on a single interface are statistically correlated. The intensity of the Bragg sheet in q_y is often thought of as the Fourier transform of the height-height correlation function. The in-plane correlation cut-off length can therefore be related to the cut-off in q_y of the Bragg sheet by:

$$\xi = \frac{2\pi}{q_y^C} \tag{4.2}$$

Beyond this cut-off length, correlation drops according to a power-law of the form $q_y^{-\gamma}$. The exponent of this decay, γ is related to the Hurst fractal parameter [after eq. 3.7 of ref. 92] through:

$$\gamma = 2 + 2h - \left(\left|q_z\right|\sigma\right)^2 \tag{4.3}$$

In the weak roughness limit defined as $\left|q_z{}^{\sigma}\right| \ll 1$, h and γ are simply related:

$$h = \frac{\gamma - 1}{2} \tag{4.4}$$

Furthermore, because the width of the Bragg peaks depends on the coherence of the scattering from repeated interfaces in the multilayer, the full width at half maximum can be used to estimate an out-of plane coherence length ζ, by:

$$\zeta = \frac{2\pi}{\Delta q_z^{FWHM}} \tag{4.5}$$

This means that the full width at half maximum is inversely proportional to the out-of-plane coherence length.

In order to extract these parameters, the data captured in the two-dimensional CCD images was reduced by fitting Gaussian curves to the Bragg sheets at each value of q_y. The Gaussian line shape was chosen because this produced excellent fits to the data, and

because the Levenberg-Marquardt [111] fitting algorithm could robustly obtain best fits to the data. This was performed in the MATLAB environment using custom-written code. The raw data had initially been converted into an open data format using the Fit2D program written by Hammersley [112].

Bragg sheet analysis was performed after subtraction of a background level that varied as a function of q_z, and was assumed to originate from air scattering. This was estimated from the intensity measured at high q_y beyond the tails of the Bragg sheet.

4.3.7. Analysis of GISAXS images: integrated intensities

In Figure 4-16 and Figure 4-17 the first order Bragg peaks (labelled '←' in Figure 4-14 and Figure 4-15 respectively) are extracted from the CCD images and shown in a 3D representation. This peak was chosen in order best to satisfy the weak scattering limit $\left|q_z{}^{\sigma}\right| \ll 1$.

In the samples without preoxidation a constant saturation region at low q_y exists, corresponding to a constant height-height difference function equal to the interface width σ. This domain relates points on the surface separated by more than the correlation-cut off length, and therefore having uncorrelated heights. The location of the 'shoulder' defines the correlation cut-off frequency, q_y^C. For q_y above the cut-off frequency, there is a power law decay in the peak intensity, reflecting a drop in the expected height difference. This reflects the regime of close-together points on the surface whose heights are likely to be strongly correlated. The behaviour shown is typical of many other studies where the profiles of Bragg peaks in diffuse scatter from multilayers have been analysed [e.g. refs. 93, 113, 114, 115].

The change after preoxidation is stark: the shoulder shifts to lower q_y and is less pronounced. This is shown by both the n = 5 and n = 3 multilayers. A quantitative analysis is performed by fitting power law functions of the form $q_y^{-\gamma}$ to the saturation and decay regimes of the integrated peak intensity, as shown in Figure 4-18 (for n = 5), and Figure 4-19 (for n = 3).

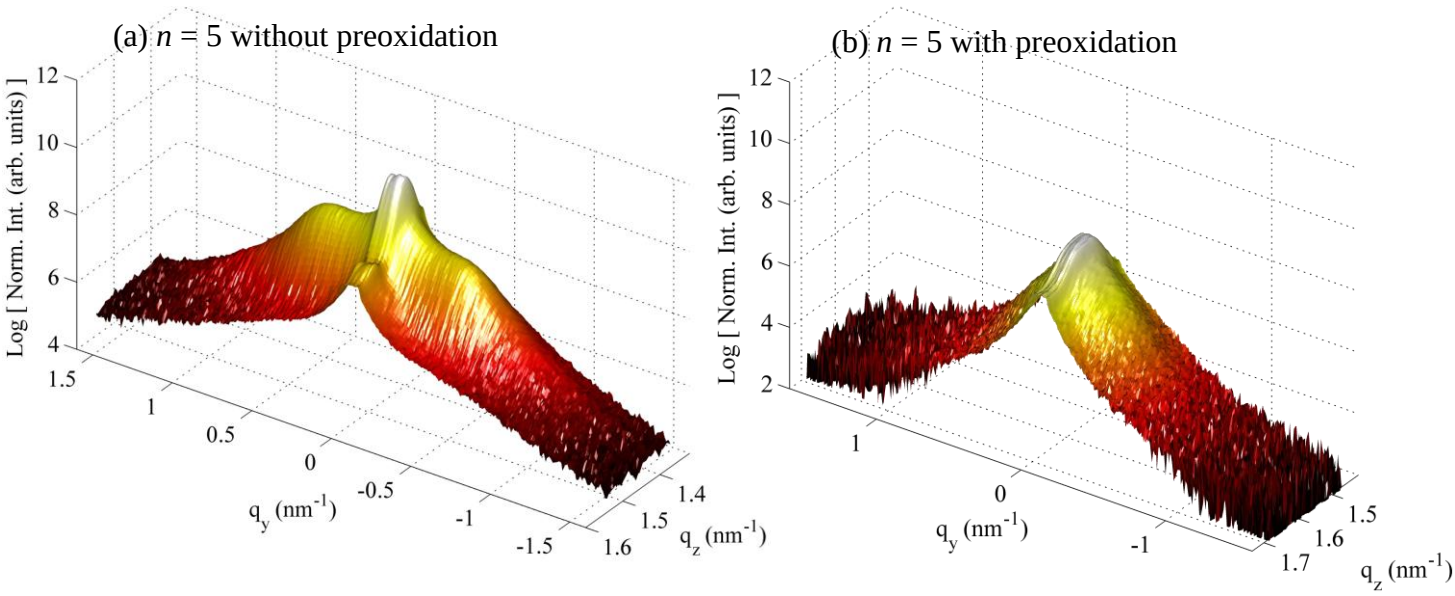

Figure 4-16. Three dimensional representation of the first order diffuse Bragg sheet for the five repeat multilayer Co/MgO (a) without pre-oxidation, showing power law decay above a characteristic cut-off wavevector, and (b) with pre-oxidation of the Co prior to MgO deposition.

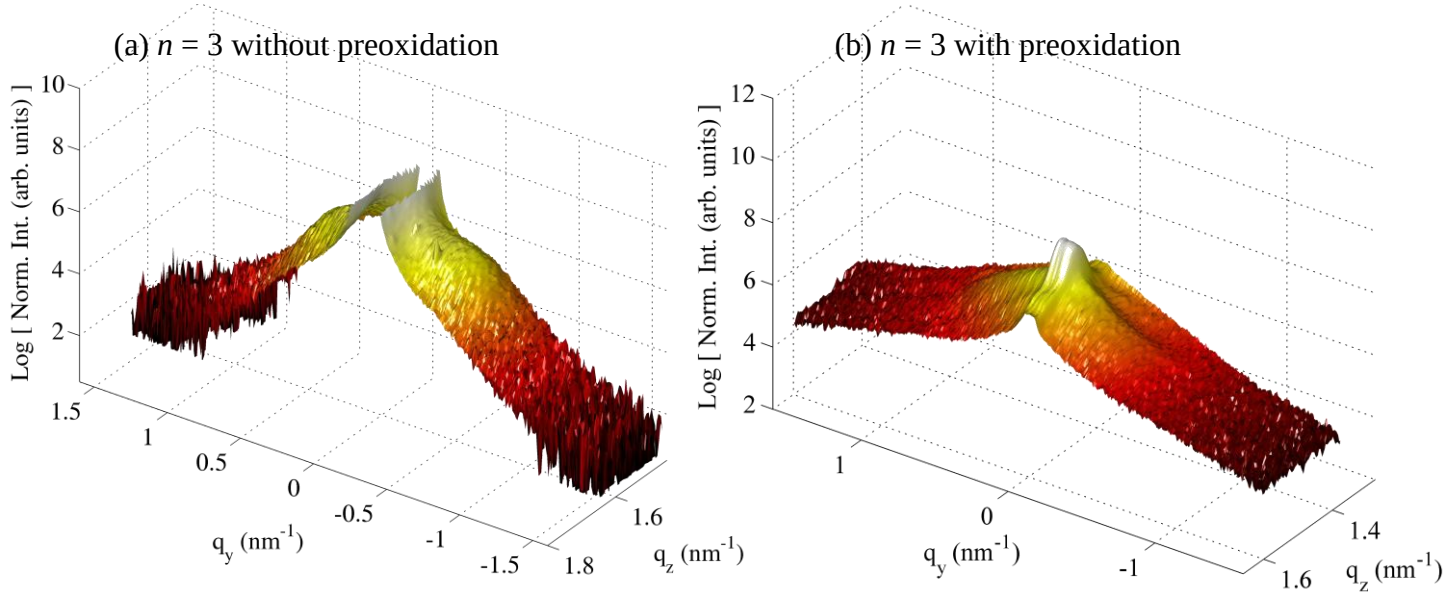

Figure 4-17. Three dimensional representation of the first order diffuse Bragg sheet for the three repeat multilayer (a) without pre-oxidation, and (b) with pre-oxidation.

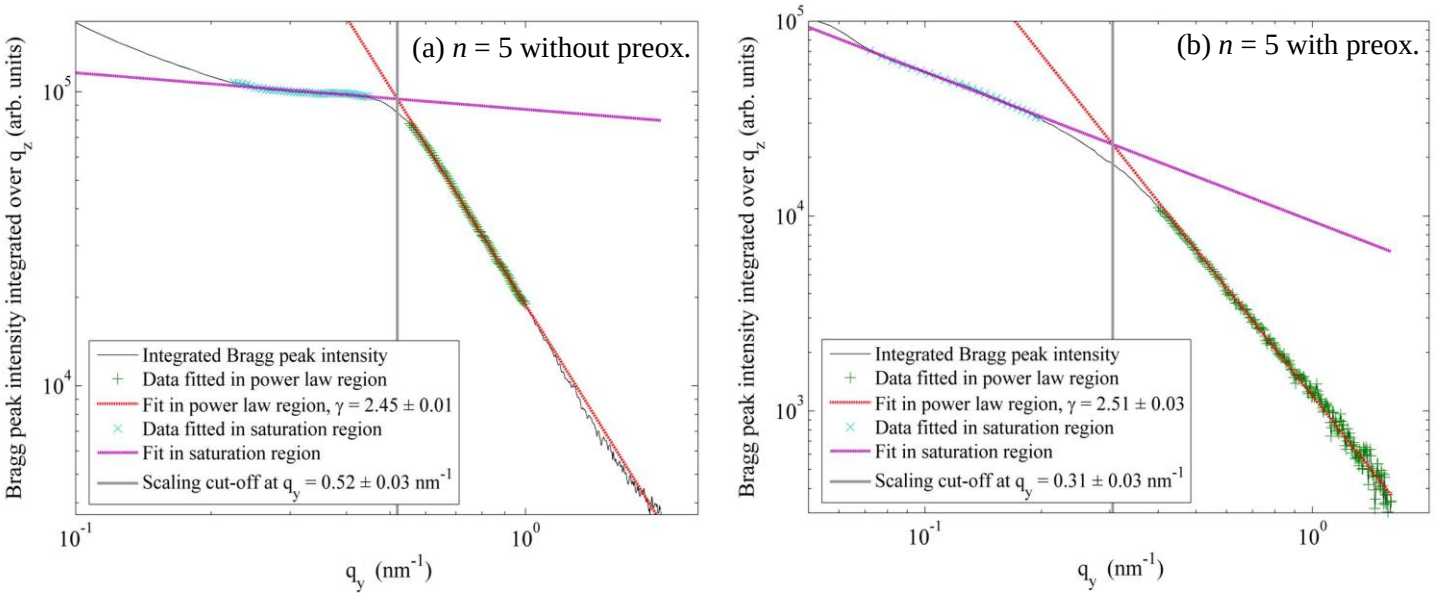

Figure 4-18. Integrated intensity of the first order Bragg peak of the five repeat Co/MgO multilayer (a) without preoxidation and (b) with preoxidation. Fits made after subtraction of a constant background, power law fits are applied in the low q_y 'saturation' region and the high q_y 'scaling' region in order to determine the point of cross-over between regimes.

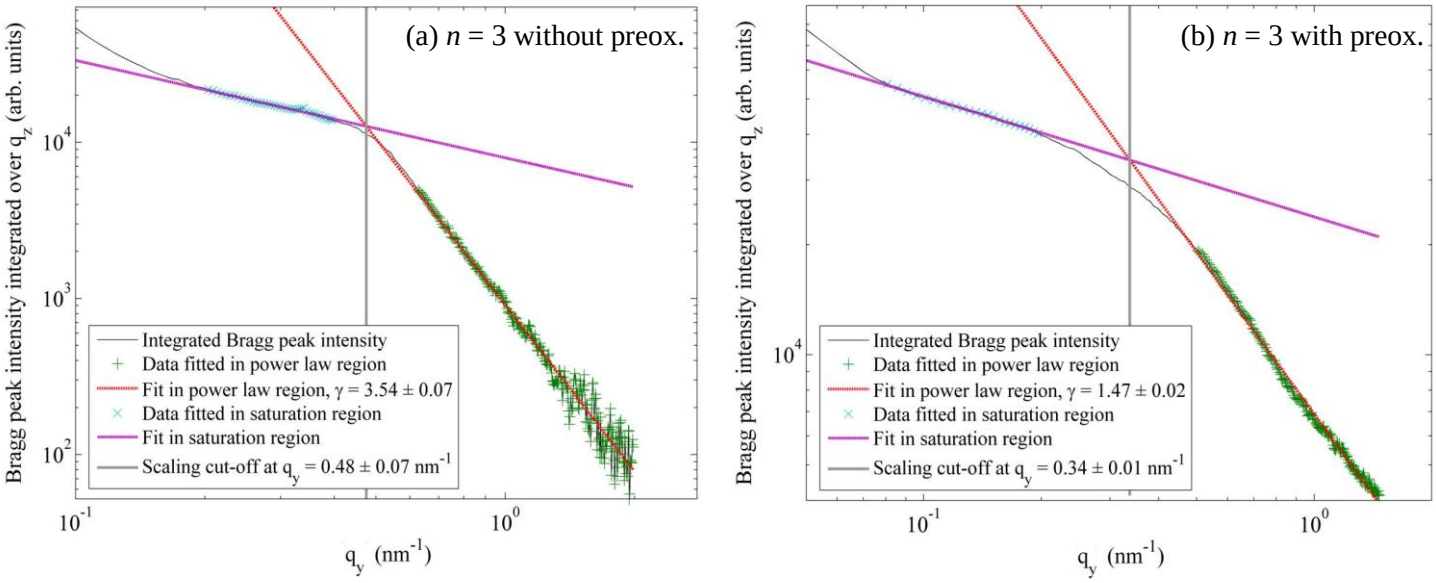

Figure 4-19. Integrated intensity of the first order Bragg peak for the three repeat Co/MgO multilayer (a) without preoxidation and (b) with preoxidation.

The cross-over points of the power law fits to the integrated intensity yield a correlation cut-off frequency q_y^C and therefore an in-plane correlation cut-off length. These are summarised in Table 4-6. There is a significant and consistent increase in the correlation cut-off length after preoxidation.

Table 4-6. Scaling parameters determined by power law fits to the integrated intensity of the first order diffuse Bragg sheets for Co/MgO multilayers, and from the fitted FWHMs. († the scaling parameter obtained for the n = 3 multilayer yields an unphysical fractal parameter.)

Number of repeats	**FITTED SCALING PARAMETERS**					
	Without preoxidation			**With preoxidation**		
	$\xi_{\parallel}$ **(nm)**	***h***	$\zeta_{\perp}^{max}$ **(nm)**	$\xi_{\parallel}$ **(nm)**	***h***	$\zeta_{\perp}^{max}$ **(nm)**
3	13 ± 1	0.77 ± 0.04 †	1000	19 ± 1	†	800
5	12 ± 1	0.23 ± 0.01	1300	20 ± 2	0.26 ± 0.02	1000

The fractal parameter obtained for the n = 5 multilayer is similar with and without preoxidation, and the value of $h \sim 0.2$ is typical for jagged, low repeat multilayer samples within the Kadar-Parisi-Zhang ballistic growth model [ref. 116, also ref. 117, chapter 6]. The h values obtained for the n = 3 multilayer are extremely large in comparison to the result for the n = 5 multilayer and results published elsewhere for low n multilayers [e.g. ref. 115]. Indeed, the value obtained using the n = 3 multilayer using relation (4.4) is greater than unity, and therefore outside the range of acceptable values. Coherent scattering from a three repeat multilayer is inherently much weaker than that from a five repeat multilayer. Without further measurements, preferably on multilayers with more repeats, the fractal exponent value for the n = 3 multilayer must be rejected as unphysical and indicative of low signal-to-noise in the data.

4.3.8. Analysis of GISAXS images: full widths at half maximum

The fitted full-widths at half maximum are plotted in Figure 4-20 (n = *5*) and Figure 4-21 (n = 3). As the spatial frequency becomes large, there is a point beyond which the out-of-plane coherence length drops.

Salditt *et al* apply a power law analysis to the peak widths in order to quantify the frequency dependence of roughness propagation [92, 113]. Unfortunately, the noisiness and nonlinearity of this data at high q_y prohibit such an interpretation here.

A qualitative comparison of the widths with and without preoxidation for n = 5 reveals that preoxidation broadens the Bragg sheet above a lower threshold frequency. In other words, preoxidation inhibits propagation of roughness for a wider range of frequency components. This is not reproduced in the three repeat multilayers, in which the samples with and without preoxidation begin to broaden at a similar q_y. One consistent trend for both n = 3 and n = 5 is that the preoxidized samples have a slightly

wider FWHM before they enter the broadening regime, indicating poorer out-of-plane coherence of roughness for all frequencies of roughness.

The three repeat multilayer displays an anomalous increase in FWHM for very low frequency components. This is unphysical, and can be attributed to saturation of the detector close to the specular point, as is visible in Figure 4-15. In order to gain a true measure of the out-of-plane coherence length, the fitted widths close to q_y = 0.03 nm^{-1} (at the minimum width) have been analysed.

The narrowest full width at half maximum gives a maximum value for the out-of-plane coherence length, $\zeta_\perp$. These lengths may appear large compared to the total sample thickness of ~ 350 nm, and the multilayer thickness of just ~ 10 nm. They are however valid, and indicate that roughness in the multilayer stack is highly conformal throughout the layers (albeit slightly less conformal after preoxidation.)

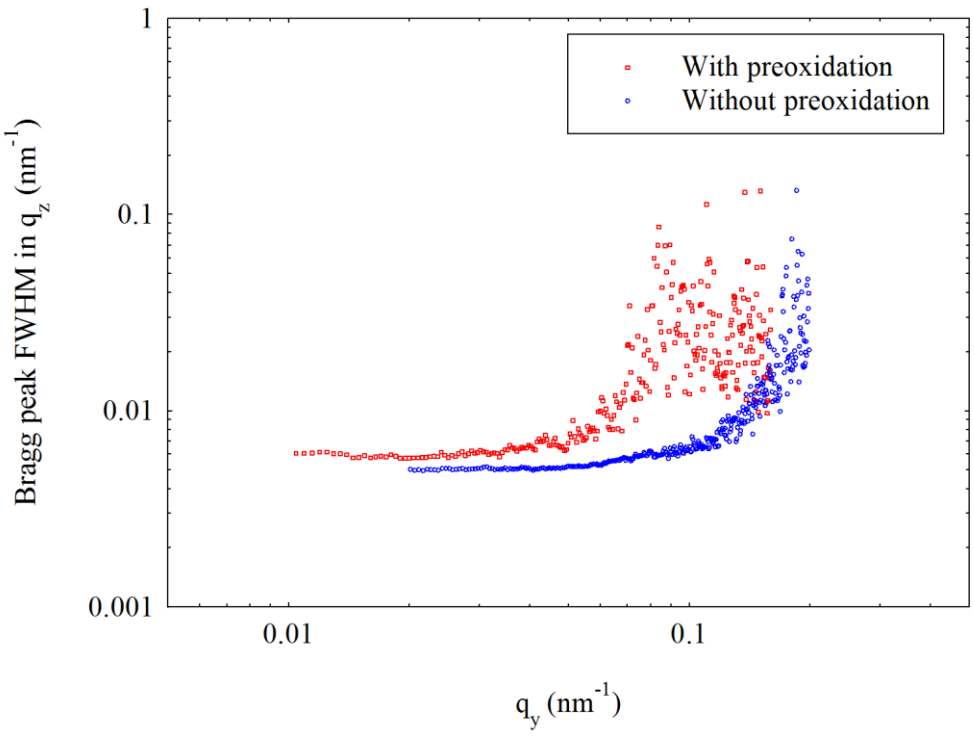

Figure 4-20. Fitted full width at half maximum of the first order Bragg peak for the five repeat Co/MgO multilayer without and with preoxidation.

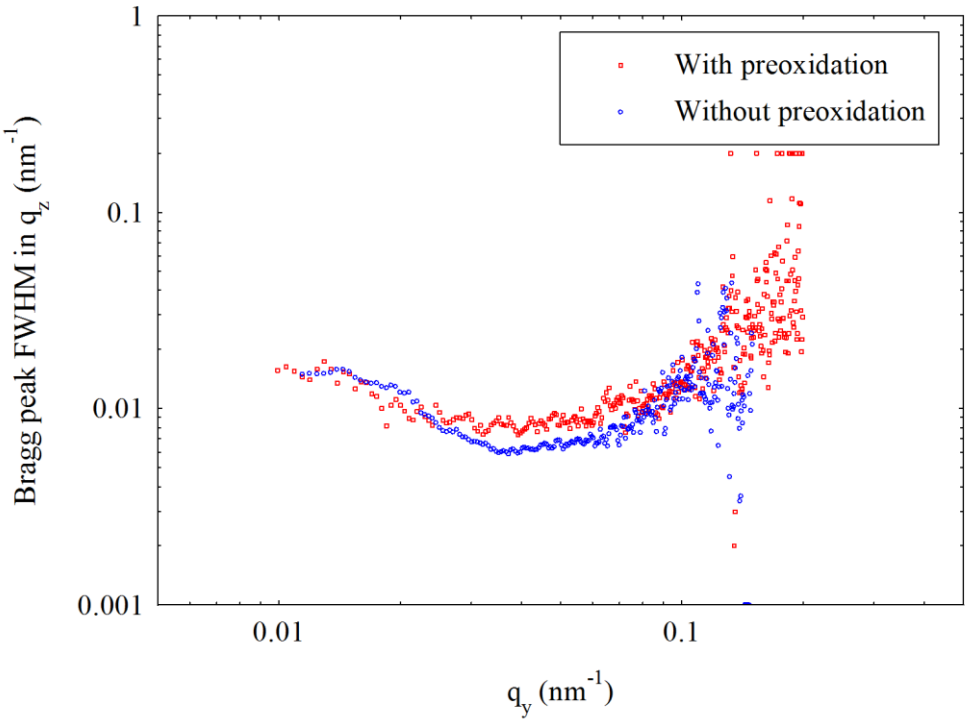

Figure 4-21. Fitted full width at half maximum of the first order Bragg peak for the three repeat Co/MgO multilayer without and with preoxidation. The rise in FWHM for $q_y < 0.03$ nm^{-1} is attributed to saturation 'bleeding' of the specular point to neighbouring CCD pixels, as can be seen in Figure 4-15.

4.3.9. Interpretation of results for Co/MgO multilayers

The topological roughness was estimated from the ratio of diffuse to specular intensity (using a Born analysis) to be approximately 0.3 nm irrespective of whether the sample was preoxidized or not. This is a systematic and direct measurement (rather than a parameter from a recursively fitted model) for both sets of multilayers.

The precise and confident fitting of the specular reflectivity is inhibited by the large number of interfaces present in the multilayer samples. There is no measured difference in the layer thicknesses or interface widths after preoxidation, but the diffuse scatter captured using a two-dimensional CCD camera gives strong evidence that the in-plane correlation length of the roughness increases. The consistent trends seen from the diffuse data are: (i) that preoxidation increases the in-plane correlation cut-off length, and (ii) that preoxidation decreases the out-of-plane correlation cut-off length.

The in-plane correlation length can be thought of as the typical extent of an expanding growth front during deposition as shown in Figure 4-22. According to the Tang, Alexander and Bruinsma (T.A.B.) model of film growth [118], initial layers in a multilayer stack can have short correlation lengths as many wavefronts are simultaneously nucleated, leading to high frequency components in the roughness

spectra. As additional layers are deposited, a Huygens wavefront propagation effect applies to the surface of each layer: short correlation length regions are subsumed into larger wavefronts, increasing the correlation length. The total interface amplitude, σ, is independent of the correlation length.

Within the T.A.B. growth model, the data shown here imply that preoxidation lowers the average correlated frequency component in the roughness, and decreases the out-of-plane distance over which all frequencies are propagated.

To understand the effect this would have on the Néel interlayer coupling, a fundamental connection must be made: that the in-plane correlation cut-off length found from diffuse x-ray scattering represents a characteristic wavelength in the surface topology. The correlation cut-off lengths in Table 4-6 are indeed similar to wavelength values reported by Schrag *et al* for Al_2O_3 tunnel junctions [119]. In reality, by describing the surface roughness using a self-affine fractal model there is an implicit acceptance that many wavelength components exist. This is important since Néel's simple model assumes a sinusoidal interface with a single characteristic wavelength. In reality, all wavelengths will contribute to some extent.

The results of Néel's model for different characteristic wavelengths and for varying barrier thicknesses are shown in Figure 4-23.

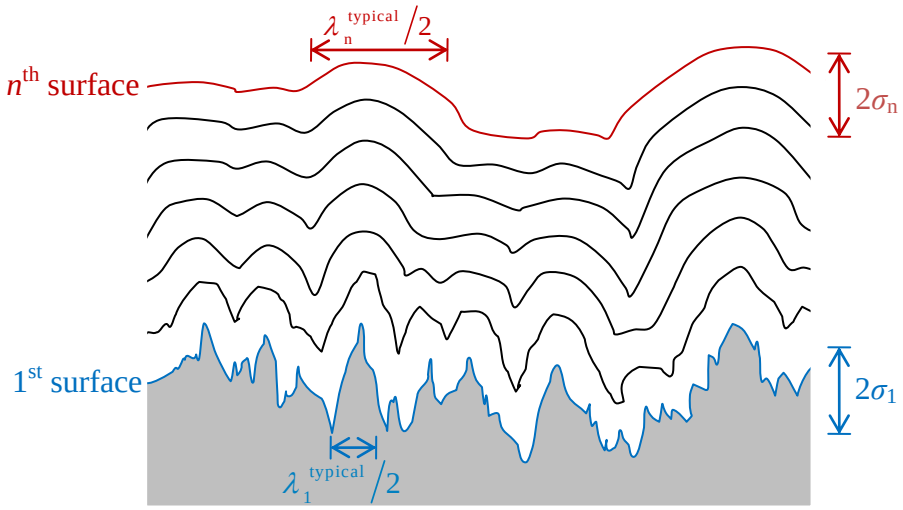

Figure 4-22. Schematic illustration of roughness propagation interpreted using Huygens' principle according to Tang, Alexander and Bruinsma [118].

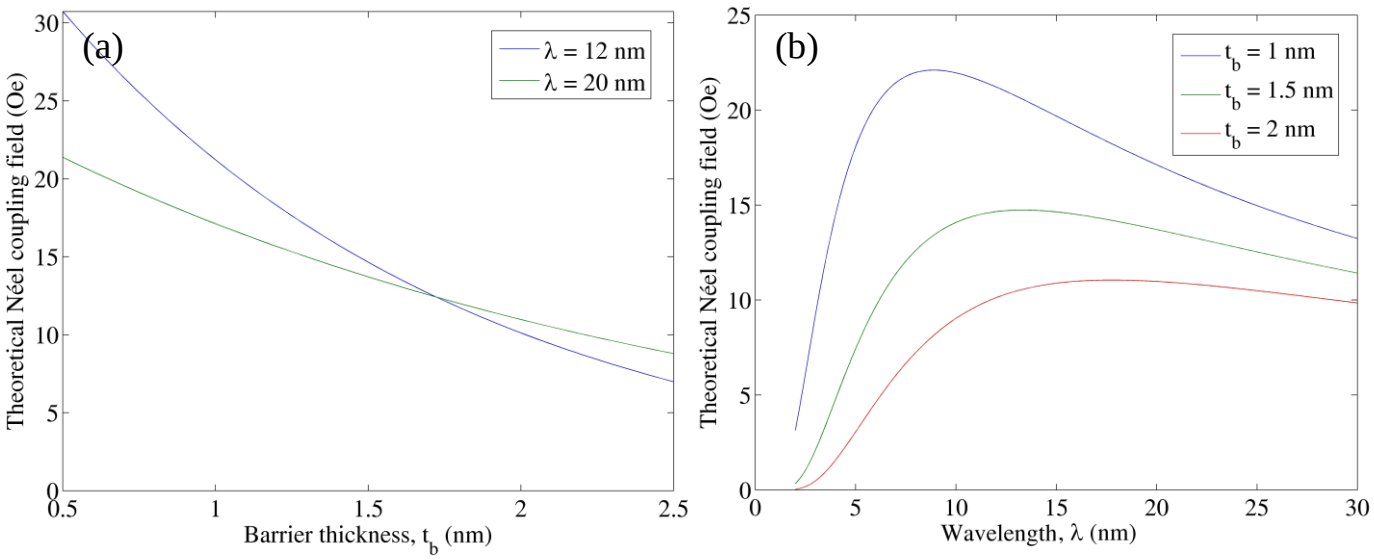

Figure 4-23. Theoretical Néel coupling fields in MTJ structures as a function of roughness wavelength and barrier thickness using the simple sinusoidal model of eq. (4.1). Material parameters used in the calculation are $M_s = 1.7 \times 10^6$ A m^{-1}, $t_f = 10$ nm, and $\sigma = 0.3$ nm.

These trends demonstrate the nonlinear dependencies of Néel coupling on barrier thickness and in-plane wavelength. For typical barrier layers less than 1.5 nm thick the shorter wavelength conformal roughness leads to a stronger Néel coupling.

A more rigorous simulation, incorporating multiple wavelength components and different fractal parameters could be obtained using a micromagnetic simulation. In this method a material is divided into a regular grid of microscopic magnetic moments. Through an iterative calculation of the interaction of each moment with the external field and with neighbouring moments, all the different physical interaction mechanisms may quantitatively be assessed. Unfortunately, this is beyond the scope of the current investigation.

4.4. Chapter conclusion

Preoxidation has been shown to cause significant and differing structural changes at Co/Al_2O_3 and Co/MgO interfaces. In aluminium oxide systems, evidence of reduced chemical intermixing at the interface has been obtained by fitting the specular reflectivity within the Parratt formalism and the diffuse scatter within the distorted wave Born approximation. The reduction in interdiffusion width has been estimated to be from 0.9 nm to 0.3 nm. The amplitude of the topological roughness is not seen to change, but the reproduction of Kiessig fringes in the diffuse scatter suggests that the topological roughness is highly conformal throughout the layers. It is proposed that preoxidation has the effect of creating a more uniformly oxidized tunnel barrier, which

is consistent with more reproducible magnetoresistance after preoxidation, as seen by Egelhoff *et al* [105].

Observations of in-plane structure seen both for samples with and without pre-oxidation are that:

a) a relatively small fractal parameter (h = 0.17) is required to fit the shape of the diffuse scatter, which is typical of very jagged layers in the early stages of T.A.B. type growth [118], and that
b) the in-plane correlation length (ξ = 7.5 nm) used to fit the same data is similar to the characteristic wavelength of topological roughness in Al_2O_3 tunnel junctions of ($\lambda = 10 \pm 1$) nm obtained by Schrag *et al* [119].

In measurements of Co/MgO three and five repeat multilayers no change in the layer thickness or interface widths upon preoxidation was found by fitting the specular reflectivity or coplanar diffuse scatter, although the precision of the fitted parameters was relatively poor. Two dimensional images showing the extent of Bragg sheets in the diffuse scatter showed that the in-plane correlation cut-off length of the roughness in the preoxidized samples was significant higher. The absolute values of the correlation length were similar to those found for the Al_2O_3 multilayers. When the assumption is made that this correlation length relates to a dominant wavelength in Néel's coupling model, an explanation for the decrease in interlayer coupling field becomes apparent.

Irrespective of preoxidation, the increase in full-width at half maximum of the Bragg peaks as the frequency component increases suggests that high frequency roughness does not propagate as well through the multilayers as low frequency roughness. Together with the small fractal parameter $h \approx 0.2$ found for the n = 5 multilayers, this indicates that the growth mechanism is well described by the TAB model [118]. With preoxidation, this effect is seen to occur (for the n = 5 multilayer only) over a greater frequency range than occurs without preoxidation.

In summary, these results for the out-of-plane scatter suggest that the reduction in coupling in MgO based tunnel junction devices arises primarily from the change in the in-plane spatial frequency of the roughness, rather than a reduction in the out-of-plane roughness amplitude.

There are some clear limitations to these conclusions caused by the quality of data presented and the fits obtained. In the case of the aluminium oxide barriers, measurements from complete electrode-barrier-electrode sequences may provide more clear-cut evidence of the uniformity of oxidation through the barrier. This would, however, complicate the modelling considerably since both an additional cobalt layer and a surface oxide layer would probably have to be incorporated into the model. No

comprehensive study has been found of the nature of in-plane correlation lengths in Co/Al_2O_3 multilayers. Such a study may prove enlightening.

In the case of the Co/MgO system, multilayers with more repeats would allow a more systematic characterization using the diffuse scatter image technique [similar, for example to ref. 93]. On the other hand, structures with a single Co/MgO interface may have been informative in a conventional x-ray reflectivity experiment.

This chapter highlights some of the difficulties in drawing conclusions from indirect, recursive fits to specular x-ray reflectivity in the study of thin film systems that cannot accurately be modelled using a limited number of free parameters. It also demonstrates the powerful insight that can be achieved when an interface is repeated in a multilayer structure to produce a coherent summation scatter from which direct measurements of key parameters can be made.

5. Structural changes during annealing in Fe/MgO/Fe and Fe/Au/MgO/Fe epitaxial thin films

Fully epitaxial tunnel junctions with lattice matching between electrodes and barrier offer the possibility of coherent electron tunnelling and enhanced tunnelling magnetoresistance.

Iron and magnesium (II) oxide grown along the [001] crystal direction have compatible lattice parameters, but the growth of these materials in sequential thin films provides a manufacturing challenge. The key material parameters are the degree of matching of the lattice dimensions and orientation, the topological roughness between layers, and the chemical sharpness across interfaces. In particular, the formation of iron (II) oxide destroys lattice matching and degrades electron tunnelling. The incorporation of a thin gold layer which is lattice matched to the iron and MgO has been proposed in order to reduce iron oxidation, and to enhance resonant tunnelling effects. The controlled epitaxial growth of gold on MgO is however, not well understood.

In situ characterization during deposition is commonly performed by reflection high-energy electron diffraction, but this is insensitive to changes in buried layers after further layer growth. In this chapter, measurements of the in- and out-of-plane structure of Fe/MgO/Fe and Fe/Au/MgO/Fe films grown on MgO (001) substrates by grazing-incidence x-ray diffraction and reflectivity, and high-angle diffraction measurements are presented. The consequences of post-deposition annealing are clarified.

5.1. Introduction

5.1.1. Motivation

The promise that highly crystalline tunnel junctions will deliver giant tunnelling magnetoresistance together with a low resistance-area product at room temperature has driven a major global research effort. Theoretical predictions have frequently preceded the realisation of improved device performance.

In 2001, Butler *et al* [44] and Mathon and Umerski [45] independently predicted the potential of Fe/MgO/Fe tunnel junctions using first-principle calculations of the spin-dependent tunnelling conductance. With these materials, for the first time a tunnel junction could be realistically modelled as a fully epitaxial structure, in which coherent tunnelling of conduction electrons through the barrier should occur and the in-plane momentum $k_{\|}$ be conserved. This simplification of the tunnelling process allowed a rigorous calculation of the conductance mechanisms by considering the density of states at the Fermi energy through the structure, and calculating the rate of decay of any potential Bloch modes through the barrier [44, 45].

The paper of Butler *et al* [44] considers an MgO barrier four or eight atomic layers thick, describing the majority conduction channel as Bloch electrons (with momenta largely perpendicular to the interface), whereas the minority channel electrons cannot tunnel in such simple Bloch states, but rely upon interface resonance states (introduced since the density of states is strongly modified by the presence of the interface). The majority channel Bloch electrons are found to tunnel through the insulating barrier with a decay rate dependent upon the symmetry between the Bloch states in the electrodes and the evanescent states in the barrier. As the barrier thickness increases, the majority channel becomes an increasingly dominant conductance process, and therefore the magnetoresistance increases with thickness. Since the minority conductance is dependent upon interface states, it is highly sensitive to interface imperfection. Butler *et al* went on to describe how interference states in the barrier could lead to the tunnelling current having a damped oscillatory dependence on the barrier thickness.

Mathon and Umerski [45] produced similar results using a slightly different calculation, and predicted specific values for the tunnelling magnetoresistance ratio at varying thicknesses of MgO barrier. In their idealised system with perfect lattice matching between layers and a perfectly sharp smooth interface, they calculated an optimistic TMR ratio which increased with barrier thickness up to 1000 % for twenty atomic planes.

5.1.2. The principle of lattice matched Fe/MgO films on MgO (001)

The physics of epitaxial thin film growth is complex and relies upon a series of compatible material properties. The growth mechanism must allow the formation of continuous, single-crystal films. Furthermore the crystal lattice of neighbouring layers must be congruent, allowing pseudomorphic growth of successive atomic layers. Creating a suitable thermodynamic environment for epitaxial growth has been a great technical challenge, and reports on this will be discussed in section 5.1.3. First the general principle of lattice matching in Fe/MgO will be outlined.

At room temperature, iron has the body centred cubic structure with the $IM\bar{3}M$ space group symmetry, whereas MgO, or magnesium (II) oxide, has the face centred cubic 'sodium chloride' structure with the $FM\bar{3}M$ symmetry. In bulk at room temperature, iron has a lattice parameter a_0 = 0.28664 nm and MgO has a lattice parameter of 0.42117 nm [120]. When growth is along the 'c'-axis of the two structures, a 45° rotation between the principal Fe [100] and MgO [100] axes reconciles the $\sqrt{2}$ difference in lattice parameters, and with a 3.9 % linear compression of the MgO in the [u v 0] plane the two crystals become perfectly lattice matched. The MgO $\{200\}$ planes are exactly equivalent to the Fe $\{110\}$ planes, as shown in Figure 5-1.

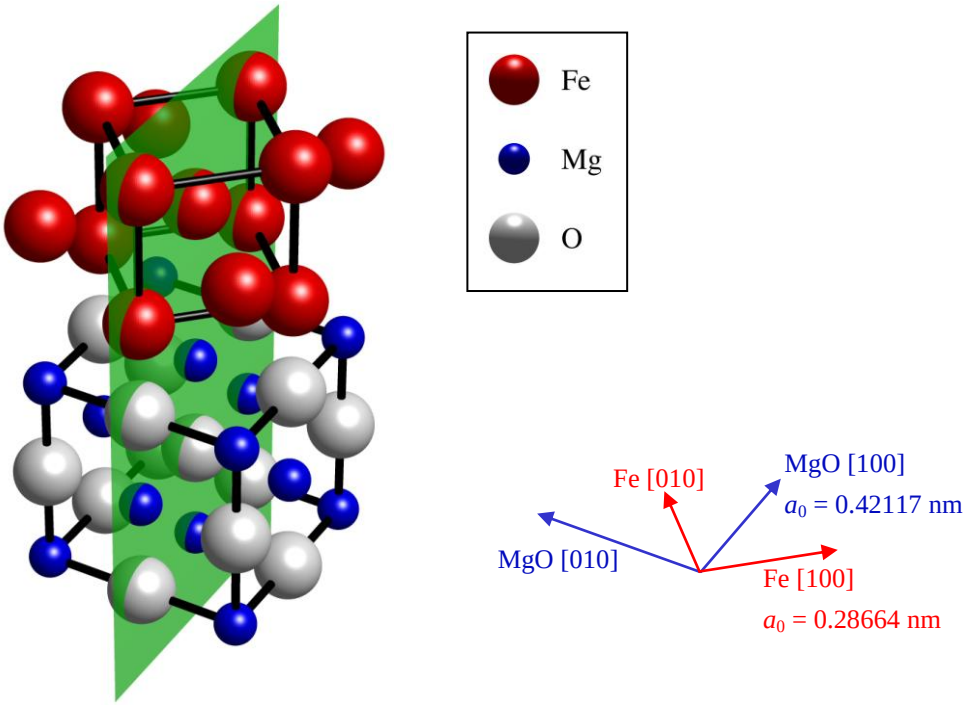

Figure 5-1. A 'ball-and-stick' representation of pseudomorphic lattice matching between the unit cells of body-centred cubic iron and face-centred cubic magnesium (II) oxide. The green plane is a member of the set of diffracting planes in the grazing-incidence diffraction experiment, containing the Fe (110) and the MgO (200) diffraction planes.

5.1.3. Previous reports of Fe/MgO thin film growth

In one of the earliest studies of the epitaxial deposition of iron on an MgO (001) substrate, Kanaji and Urano [121] observed by Auger electron spectroscopy (AES) that the bare substrate was highly contaminated by carbon after being cleaved in air. In order to eliminate the carbon Auger signal, the sample was heated to 527 K in a low pressure of O_2 gas at 1×10^{-3} Pa. Growth of the iron was then performed using resistive heating of a 7.5 mm diameter iron wire. Using low-energy electron diffraction they observed pseudomorphic growth of the iron atoms to the MgO lattice, and by obtaining I-V curves found that the iron sat directly above the oxygen sites on the substrate.

In 1996 Vassent *et al* [122] recorded reflection high-energy electron diffraction (RHEED) during the growth of thin layers of MgO on an iron (001) surface upon an MgO substrate for various temperatures. They observed pseudomorphic growth for MgO thicknesses up to a critical thickness of 4–5 monolayers (0.8-1.0 nm), beyond which the in-plane lattice parameter of the MgO relaxed towards the bulk through misfit dislocations. They interpreted the growth mode as two-dimensional Frank-van der Merwe mode, where magnesium and oxygen adsorb in perfect lattice registry onto the iron (001) surface before relaxation. This strong 'wetting' was attributed to the large difference in the surface free energy between the iron surface (2.9 J m^{-2}) and the MgO epilayer (1.16 J m^{-2}).

Vassent *et al* continued their study, and in 2000 published back-to-back papers which together provide a thermodynamical understanding of the MBE process. The first paper [123] analysed the composition of the beam emitted from an MgO target using mass spectrometry, and found that the constituent species were predominantly Mg (g) and O (g) with no detectable MgO (g) and a low level of O_2 (g) attributed to recombination at the UHV chamber walls. The subsequent article [124] examined the thermodynamics at the sample surface, and found that a stoichiometric excess of condensed magnesium would evaporate from the surface, whereas an excess of condensed O may lead to oxidation of the iron. Using low energy AES they did indeed detect iron oxide.

In 2002, surface x-ray diffraction was used by Meyerheim *et al* to observe a single FeO layer at the MgO/Fe interface [125]. This confirmed the findings of Vassent *et al*, and was significant in the light of later theoretical and experimental studies of the effect of interfacial structure on TMR.

More recently in 2008 Raanaei *et al* [126] studied magnetron-sputtered Fe/MgO superlattices using x-ray reflectometry, high-angle x-ray diffraction and transmission electron microscopy. They demonstrated the sensitivity to growth temperature for both

smooth and epitaxially matched Fe/MgO, with 438 K found as the optimal condition for a highly perfect crystal structure and reduced correlated topological roughness between layers.

Taken together, the published literature suggests that the stoichometric, epitaxial growth of MgO on Fe (001) is more difficult than the growth of iron on MgO (001) due to oxidation of the iron substrate by the free radical O· (g) species. The realisation of tunnel junction structures from these materials is now discussed.

5.1.4. Reports of giant TMR in Fe/MgO/Fe tunnel junctions

The first letters reporting giant room temperature tunnelling magnetoresistance in highly crystalline MgO based magnetic tunnel junctions were published in *Nature Materials* in 2004 by Parkin *et al* [53] and Yuasa *et al* [52]. Parkin *et al* used magnetron sputtering followed by annealing at 673 K and 1×10^{-10} Pa to produce polycrystalline but highly orientated tunnel junctions exhibiting room temperature TMR up to 220 % with both iron and cobalt-iron electrodes. Yuasa *et al* used molecular beam epitaxy followed by anneal at 623 K and 2×10^{-8} Pa to deposit Fe/MgO/Fe junctions. They deposited the MgO barrier at 0.01 nm s^{-1} in order to avoid oxidation of the lower iron electrode. Notably, Yuasa observed oscillations in the TMR with barrier thickness which did not coincide with the deposition of complete atomic monolayers. He attributed this to a coherent evanescent wave tunnelling through the barrier with a single, dominant wavevector, a theory which was further clarified in a later paper by the same group [127], and which was reconcilable with the earlier theory of Butler [44].

The 2007 paper of Mizuguchi *et al* [128] from the group of Yuasa provides a scanning tunnelling microscopy study of the surface morphology of MBE-grown Fe/MgO/Fe tunnel junctions, giving further technical details of their growth method. A sample was prepared with the deposition sequence: MgO (001) substrate, MgO (001) buffer layer at 638 K, 50 nm Fe (001) at 333 K followed by a 60 minute anneal at 573 K, 1.05 nm MgO (001) barrier layer followed by a 30 minute anneal at 573 K, and a final layer of Fe (001) a ‘few monolayers’ thick. They found the root-mean-square topological roughness of the structure to be 0.206 nm for the lower iron layer, 0.149 nm for the as deposited MgO decreasing to 0.126 nm after anneal, and 0.296 nm RMS roughness for the upper iron layer.

In 2006, Tusche *et al* [129] performed a systematic study of the growth of a complete Fe/MgO/Fe tunnel junction using surface x-ray diffraction at the BM32 beamline of the European Synchrotron Radiation Facility, Grenoble, France. Their method was to measure *in situ* four symmetry independent diffraction peaks during ion-beam assisted molecular beam epitaxy. This allowed the surface monolayer to be

characterized in relation to the previous layers. Interestingly, Tusche *et al* found the deposition of iron in UHV conditions did not preserve lattice registry, whereas deposition in an O_2 environment at 10^{-7} mbar (1.3×10^{-11} Pa) produced perfect lattice registry.

Despite some successful reports of tunnelling in Fe/MgO/Fe junctions, many research groups were unable to reproduce these results. This demanded theoretical considerations of the effect of disorder in the structures.

The effect of an iron oxide layer between the lower iron electrode and the barrier had earlier been calculated by Butler *et al* in 2003 [57]. Their work predicted a large drop in TMR due to Fe-O bonding. Later, in 2006, the effect of interfacial disorder in a Fe/MgO/Fe junction on the TMR was modelled by Mathon and Umerski [59]. They suggested that the discrepancy between their earlier theoretical TMR values and the 150 % TMR found in practice by Yuasa *et al* [52] was consistent with a 16 % intermixing of iron and magnesium atoms at the interface. A topical review of TMR through crystalline MgO (001) tunnel barriers is given by Yuasa and Djayaprawira [51].

5.1.5. Motivation for the incorporation of a gold layer

In 2005 Mathon and Umerski [130] published a theory of resonant tunnelling in a fully epitaxial Fe/Au/MgO/Au/Fe structure, where maximum TMR was predicted when the gold and MgO layers were each eight atomic planes thick. One key motivation for the incorporation of gold layers was that oxidation of the iron electrodes would be reduced. The calculations of Mathon and Umerski suggested that the magnetoresistance would survive because the tunnelling remains coherent and the two spin channels remain isolated. They predicted that giant TMR values would occur for eight atomic planes of MgO, and that the TMR would oscillate with gold thickness.

5.1.6. Previous reports of Fe/Au/MgO thin film growth

The epitaxial growth of gold on iron relies upon the near perfect bulk lattice matching between the body-centred cubic iron and the face-centred cubic gold when rotated through 45° about the [001] direction. In 1992 Fuß *et al* successfully grew epitaxial Fe / Au (8–24 monolayers) / Fe layers by e-gun evaporation onto a thick silver buffer, in order to establish the physical mechanism of oscillatory exchange coupling [131].

Harp and Parkin in 1996 successfully demonstrated the growth of epitaxial Au/Fe superlattices on an MgO substrate with an iron (100) buffer layer by high-temperature sputtering [8], a more commercially viable technique.

Later, in 2001 Dekadjevi *et al* [132] studied electron channelling in Fe/Au multilayers grown by MBE along the (001) orientation of MgO. Using grazing

incidence diffraction to confirm the sample quality they observed excellent crystallographic registration between the iron (100) and the gold (110). The root mean square roughness determined by diffuse x-ray scattering was (0.93 ± 0.03) nm, with negligible interdiffusion.

Cole *et al* [133] improved the epitaxial growth of iron and gold on an MgO (001) substrate by prior deposition of 3 nm of iron followed by an anneal at 450 K and the deposition of a 30 nm gold layer. In the gold and iron layers subsequently deposited, the roughness amplitude decreased and the in-plane correlation length increased when compared to layers deposited directly onto an MgO (001) substrate. Using grazing incidence x-ray scattering from MgO/Fe/Au samples, Cole *et al* measured a root-mean-square roughness of 0.1 nm. In multilayer repeats, they determined that the correlated RMS roughness through the twenty repeats was (0.16 ± 0.02) nm.

It is worth noting that in the studies by Dekadjevi *et al* and Cole *et al*, samples were produced in the group of Prof. B.J. Hickey at the University of Leeds, the origin of the samples analysed in this chapter.

Rickart *et al* [134] studied the growth of gold on MgO (001) with scanning tunnelling microscopy (STM), observing island growth as expected due to the high surface mobility of gold adatoms on MgO (001). By depositing a thin 1 nm layer of iron, they induced layer-by layer growth of the gold, resulting in improved epitaxial growth of the gold. STM revealed a RMS roughness of 0.26 nm. Their paper also discussed a method of reducing carbon contamination of the single crystal MgO substrates by low energy oxygen ion bombardment followed by heating, through which the Auger carbon signal could be eliminated and the surface roughness reduced to 0.1 nm. This is in good agreement with the work of Kanaji and Urano [121].

The growth of MgO on gold is less well reported in published literature, suggesting that there has been little success. The interface free energy considerations are similar to those for MgO on Fe. The converse epitaxial growth of gold on MgO is known to be more difficult since the difference in surface free energy causes the gold adatoms to be more strongly attracted to each other than to the substrate, and therefore exhibit island growth [135]. Nevertheless, the benefits of reduced electrode oxidation motivate the investigation of an Fe/Au/MgO layer sequence.

In summary, ultrasmooth iron epitaxial films have previously been grown on an MgO (001) substrate. A thin iron buffer layer is found to improve subsequent growth of gold and MgO independently. The incorporation of an MgO tunnel barrier within gold electrodes has not been reported in the literature, but is worthy of study.

5.2. Experimental method

5.2.1. Sample preparation

The samples considered in the current study were grown using molecular beam epitaxy (a technique described in section 2.3.2) in the Department of Physics at the University of Leeds by Dr Mannan Ali. A commercially produced MgO substrate with surface in the (001) plane and dimensions 10 mm × 10 mm × 0.5 mm was baked at 730 K for 60 minutes in order to eliminate hydrocarbon contamination. This bake reduced the chamber pressure from 4×10^{-10} mTorr to 2×10^{-10} mTorr. A buffer layer of 5 nm MgO and 3 nm iron was grown at 323 K and annealed at 373 K for 60 minutes. Successive layers were grown at 373 K, all at an approximate growth rate of 0.015 nm s^{-1}.

Schematic diagrams of the two sample structures are given in Figure 5-2 for the Fe/MgO/Fe layer sequence, and Figure 5-3 for the Fe/Au/MgO/Fe stack.

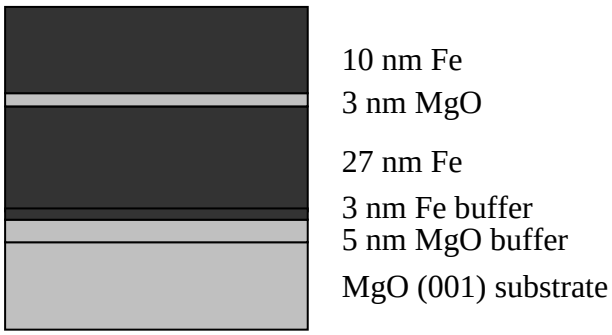

Figure 5-2. The structure of the Fe/MgO/Fe sample (not to scale).

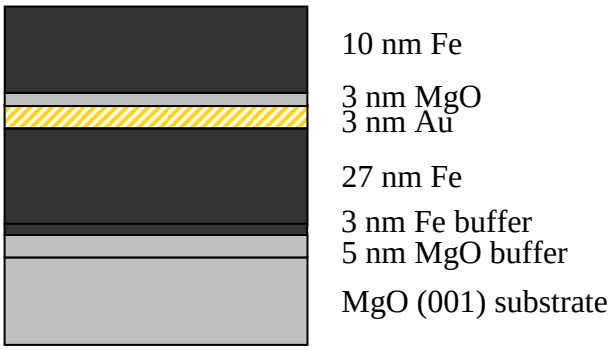

Figure 5-3. The structure of the Fe/Au/MgO/Fe sample (not to scale).

5.2.2. Experimental method for high-angle diffraction

The out-of-plane lattice and mosaic were measured after samples were annealed with *ex situ* high-angle geometry, at 298 K. Double axis diffraction (i.e. without an analysing crystal on the detector arm) was performed on a Bede D1 diffractometer using a 2.2 kW water-cooled copper anode x-ray tube operating at 1.9 kW. The beam from the x-ray tube was monochromated to Cu-K_α using a four-bounce monochromator constructed from two asymmetric Si (220) channel cut crystals, chosen for high intensity. This beam was defined by a 1 mm diameter circular aperture, and the detector resolution set with a 0.5 mm wide slit.

This geometry and intensity meant that thin films less than several nanometres thick were not expected to diffract strongly. In high-angle x-ray diffraction, a coupled θ–2θ scan was performed through the diffraction condition, with the Bragg angle θ set between atomic planes parallel to the sample surface and the source and detector, as in Figure 5-4.

In the case of symmetric high-angle geometry ($\theta_{incident} = \theta_{exit}$), the planes must be orientated parallel to the surface. For a substrate with a (001) surface, this means that only planes of the form (0 0 l) will meet the symmetrical scattering condition. In contrast, for the grazing incidence geometry, planes of the form (h k 0) will align in the symmetrical scattering condition, with the iron lattice by rotated 45° in the plane such that the iron [110] direction is parallel to MgO and gold [200].

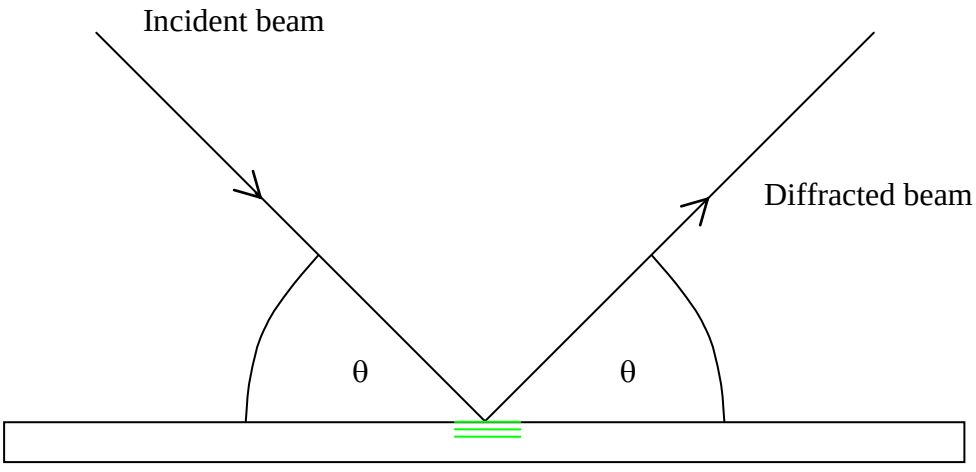

Figure 5-4. Geometry of a symmetric, coupled θ–2θ x-ray diffraction scan measuring the spacing of diffraction planes parallel to the sample surface.

Additionally, accessible reflections must be within the Ewald limiting sphere defined by the x-ray wavevector and the sample surface (as explained in section 3.2.2), and must provide an allowed reflection (as explained in section 3.5). For bulk iron, MgO and gold, the expected peak positions with a Cu-Kα x-ray source are given in Table 5-1.

In the case of the small lattice parameters of iron, gold and MgO, there are only four symmetrical diffraction conditions lying in the easily accessible range $0 < 2\theta < 120°$. This means that many peaks cannot be measured, so an analysis using the Williamson-Hall method to distinguish mosaic and micro-strain (known as twist and in-plane micro-strain respectively in the case of GIIXRD) is not possible.

In addition to the out-of-plane lattice measurements from the coupled θ–2θ scans, rocking curve measurements, (with the detector angle fixed at the scattering angle 2θ and the sample rocked about the diffraction condition) reveal in-plane details of sample mosaic and tilt of the epilayers grown onto the substrate.

Table 5-1. Peak positions expected for various bulk Fe, MgO and Au planes with a 2:1 weighted average of Cu-Kα_1 and Kα_2 x-rays in a symmetric diffraction geometry.

	CALCULATED BRAGG ANGLE, θ FOR BULK MATERIAL (°)		
Planes	**Fe**	**MgO**	**Au**
$\{110\}$	22.340	Forbidden	Forbidden
$\{200\}$	32.510	21.456	22.195
$\{220\}$	49.471	31.151	32.291
$\{400\}$	Geometrically unobtainable	47.017	49.070

5.2.3. Experimental method for grazing incidence scattering

The in-plane lattice parameters of iron and magnesium oxide epitaxial layers were measured at the I16 beamline of the Diamond Light Source, Didcot, using in-plane diffraction. The grazing incidence geometry (where the angle of the incident and detected x-ray beams to the surface was close to the critical angle) provided depth sensitivity to the measurements. All measurements were of the elastic scattering of (8.000 ± 0.001) keV radiation, with a low divergence and focussed at the sample to approximately 100 μm perpendicular to the sample surface.

5.2.4. Annealing process

Annealing was performed *in situ* on the beamline in a rough vacuum at 4×10^{-3} mbar (0.4 Pa), with a constant heating and cooling rate of five kelvins per minute controlled using a helium pumped closed-cycle cryostat heater controlled by a Lakeshore Model 340 controller with thermocouples mounted at sample.

The sample was incrementally annealed in 25 K steps, with grazing incidence diffraction scans at each increment. Although the anneal time was therefore approximately 300 minutes in total, the duration at the very high temperatures (T >500 K) commonly used in post-deposition annealing was approximately 60 minutes, and the time at the highest temperature, 600 K, only 30 minutes. The sample was realigned with respect to the incident beam after each increment to allow for thermal expansion of the sample mount.

The largest uncertainty in the temperature treatment of the samples originates from the tendency of the heating controller to overshoot the set point temperature by up to 3 K. This effect was managed by slowing the rate of the heating as the temperature neared the set point. Nevertheless, the temperatures quoted and shown on graphs should be assumed to be precise to ±3 K.

5.2.5. Measurement strategy

Three distinct measurements are made in this study. X-ray reflectivity measurements are sensitive to long-range morphology, and high-angle diffraction is sensitive to the out-of-plane lattice parameter of the layers. The key information, however, is provided by grazing-incidence in-plane diffraction.

The grazing incidence in-plane diffraction geometry is shown in Figure 5-5. The grazing angle of incidence is maintained throughout one diffraction scan, and is chosen to be at or close to the critical angle for the material. These critical angles are provided in Table 5-2.

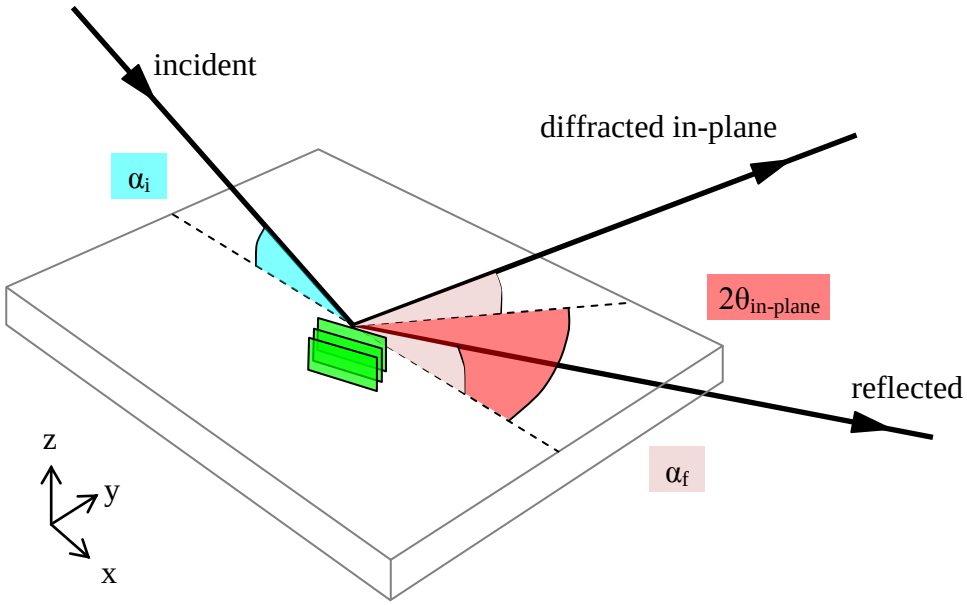

Figure 5-5. Diagram of the grazing incidence diffraction geometry. The grazing angles of incidence and exit, α_i and α_f , are equal and in the plane perpendicular to the sample surface, and the diffraction angle $2\theta_{in\text{-}plane}$ is in the plane of the sample surface. The sample is orientated such that a vertical (z-parallel) lattice plane is at the Bragg angle θ with both the source and detector, and the detector rotated about z to 2θ. For α_i and α_f much smaller than θ, the wavevector transfer on diffraction is considered to be entirely in-plane.

Table 5-2. Refractive indices and calculated critical angles at a vacuum-bulk interface for MgO, Fe and Au at 8 keV. Electron densities are derived from ref. [136], the refractive index from [78] and the critical angle derived using [78] and Eq. (3.26)

	REFRACTIVE INDICES AND CRITICAL ANGLES FOR IRON, MAGNESIUM OXIDE AND GOLD AT 8 keV.		
	Electron density (m^{-3}, to 3 s.f.)	**$n = 1 - \delta - i\beta$ (no units, to 3 s.f.)**	**α_c (°, to 3 s.f.)**
MgO	1.08×10^{30}	$1 - 1.16\times10^{-5} - i1.24 \times 10^{-7}$	0.276
Fe	2.21×10^{30}	$1 - 2.25\times10^{-5} - i2.92 \times 10^{-6}$	0.385
Au	4.66×10^{30}	$1 - 4.74\times10^{-5} - i4.89 \times 10^{-6}$	0.558

At each temperature increment, a coupled in-plane scan (where the θ–2θ 1:2 ratio is preserved) was made to measure the in-plane lattice parameter, and an azimuthal θ-only scan was made to determine the relative orientation of the layers and the twist mosaic.

5.2.6. Determination of the instrument resolution for in-plane diffraction

The instrumental resolution was determined from an in-plane (200) diffraction peak from the bare substrate, shown in Figure 5-6. This places a limit on the angular in-plane resolution due to the combined source beam size and divergence and the detector acceptance. The very narrow full-width at half maximum in in-plane θ of (0.0066 ± 0.0002)° suggests that the width of diffraction peaks is predominantly due to sample structure (the coherent scattering volume) rather than the instrument. (The minor peak below the fitted peak can be attributed to sample mosaic, i.e. diffraction from a slightly misorientated crystallite.)

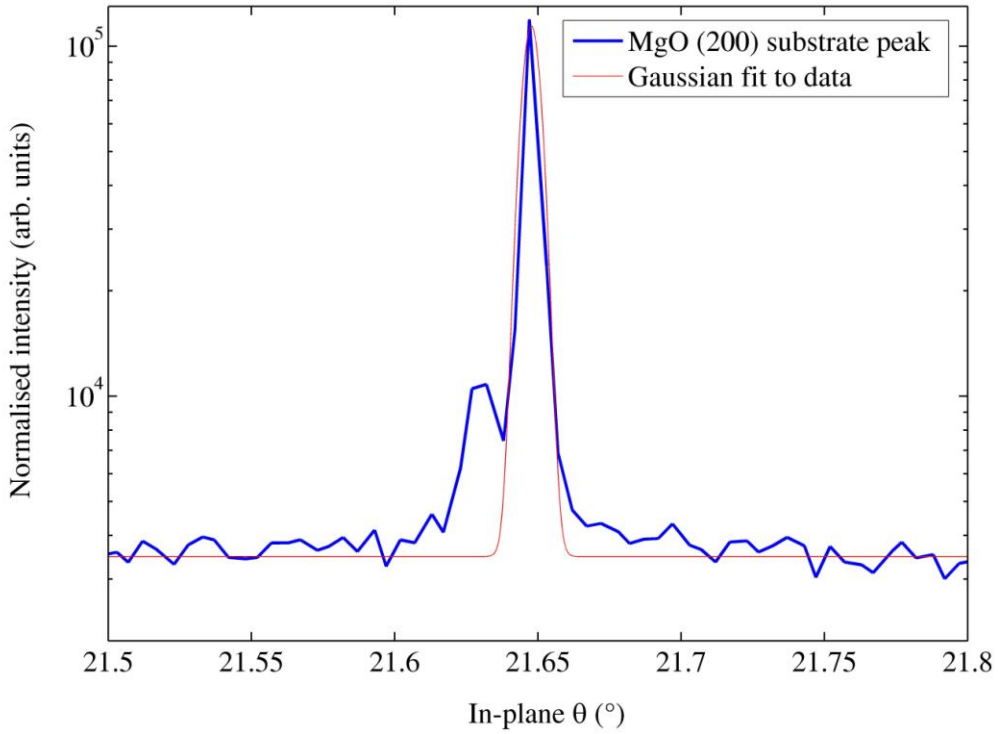

Figure 5-6. Evidence of the equipment resolution function from a 'rocking-curve' measurement of the in-plane diffraction peak from the MgO substrate. Grazing angle α_i = 0.44°. Width of fitted Gaussian is (0.0066 ± 0.0002°).

5.3. Simulation of the depth sensitivity of grazing incidence in-plane diffraction

The depth sensitivity of all grazing incidence x-ray measurements originates from the refractive index of the material being less than unity. This enables total reflection and refraction at an interface, which can be described by the Fresnel equations using the complex refractive index. The resulting Snell's law can be used to estimate the critical angle for a given interface (as explained in section 3.3.2). Estimated values for the materials in the current study are given in Table 5-2.

These critical angles are identified on Figure 5-7, which shows the 1/e penetration depths into bulk MgO, iron and gold. A sharp step-change in the penetration occurs when the critical angle is reached.

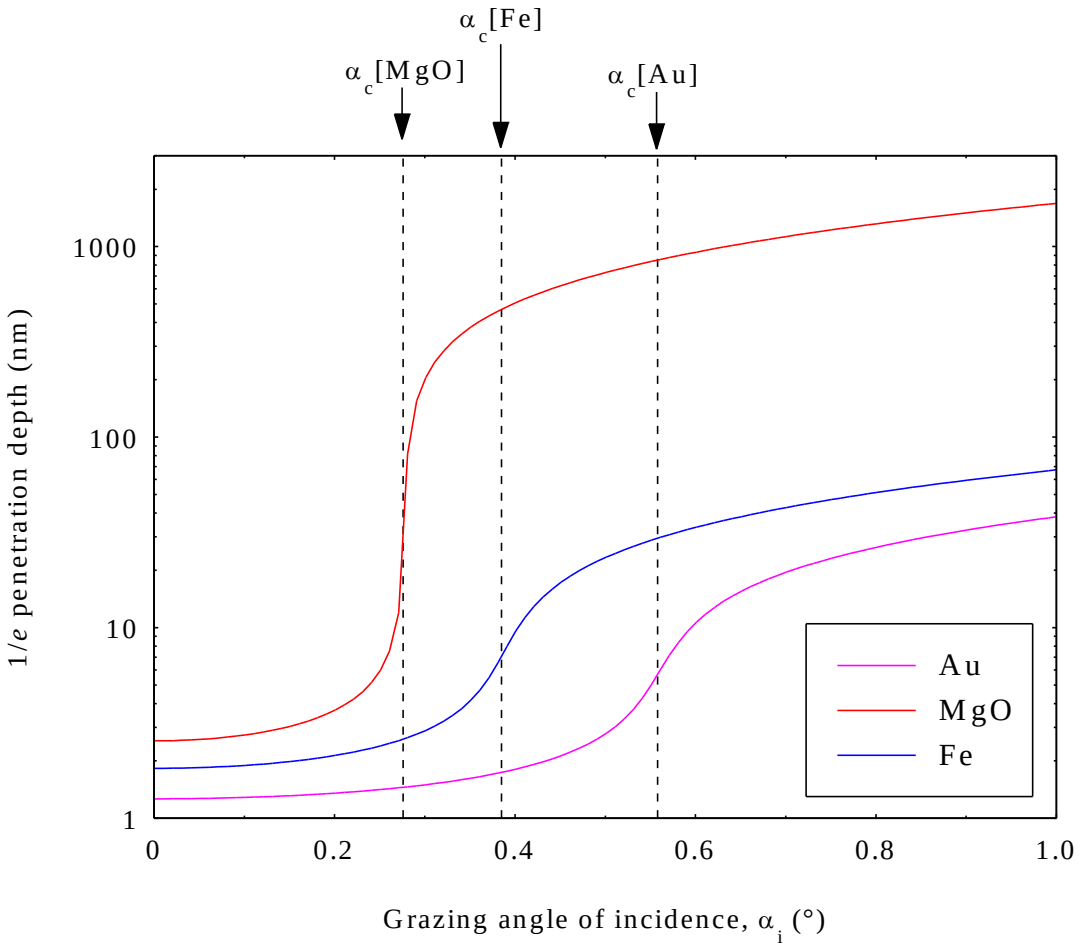

Figure 5-7. Penetration depth into the bulk material as a function of grazing incidence angle at 8 keV. The penetration depth is defined as the distance into the sample at which the intensity falls to 1/e from the value at the surface.

It is important to note that a determination of the probe depth in a stack of these layers is not a trivial combination of these data. To achieve strong in-plane diffraction, the grazing incidence angle, α_i is tuned so that the standing wave of the electric field reaches a maximum within the chosen layer. It was clear from the earlier description of specular reflectivity (in section 3.3) that both absorption and the refraction-reflection phenomena govern the electric field amplitude at a given depth. Both these factors were shown to vary with the grazing angle.

The discussion will now consider a method of predicting the sensitivity to different layers for varying grazing angle.

5.3.1. Simulation method

The scattering amplitude from a layer at a specific depth into the sample depends upon the local amplitude of the electric field, and the scattering strength of the material. More precisely, the diffracted intensity is proportional to the square of the product of the scattering factor and the electric field amplitude integrated over the path of the beam [137, 138].

A simple method for calculating the layer sensitivity of grazing incidence scattering is to simulate the x-ray fluorescence for an element-specific emission line [138] using comprehensively tested commercially available simulation software [84]. In order to predict the diffraction intensity from each layer, the simulated fluorescence must then be divided by the fluorescence yield of the layer, and multiplied by the scattering power.

Different layers with identical composition may be distinguished in simulations by artificially modifying the emission spectrum of the layer to be excluded, whilst maintaining its refractive index in order that the electric field remains undistorted.

Justification of this method requires some simplifying assumptions. Increased absorption along the exit path from deeper layers is ignored. Furthermore, the deviation from the exact diffraction condition caused by the tilting of the sample, and by refraction at interfaces is assumed to have the same effect for all layers.

5.3.2. Simulation of the layer sensitivity for MgO/Fe/MgO/Fe

Figure 5-8 shows the simulated diffracted intensity from a MgO / Fe (30 nm) / MgO (3 nm) / Fe (10 nm) structure, where an interface width of 0.5 nm was assumed between all layers. This is compared to a measurement of the Fe (110) peak.

The predicted intensity from the iron layers is much larger than the MgO signal (by two orders of magnitude). Importantly though, any small difference in lattice parameter would yield a distinct Bragg angle, allowing the MgO (200) peak to be seen despite the lower intensity.

At α = 0.22° the scattering is primarily sensitive to the uppermost iron layer, whereas at 0.44° there is equal sensitivity to both iron layers. The maximum sum of the two iron layers occurs at 0.4°. The magnesium oxide scattering intensity peaks at 0.39°, interestingly close to the critical angle of iron. This may imply that the MgO scatters most strongly when the incident beam is refracted along the interface between the iron and MgO (a waveguide-like effect). Importantly, it is predicted that the MgO diffraction peak will originate almost entirely from the barrier MgO rather than the substrate for all grazing angles below 0.5°.

Also shown on Figure 5-8 is a measurement of the iron peak amplitude, which is similar to the simulated trend for the combined iron layers. For angles above this maximum, the more rapid decrease in intensity may be attributed to increased absorption along the exit path, and to the deviation from the diffraction condition.

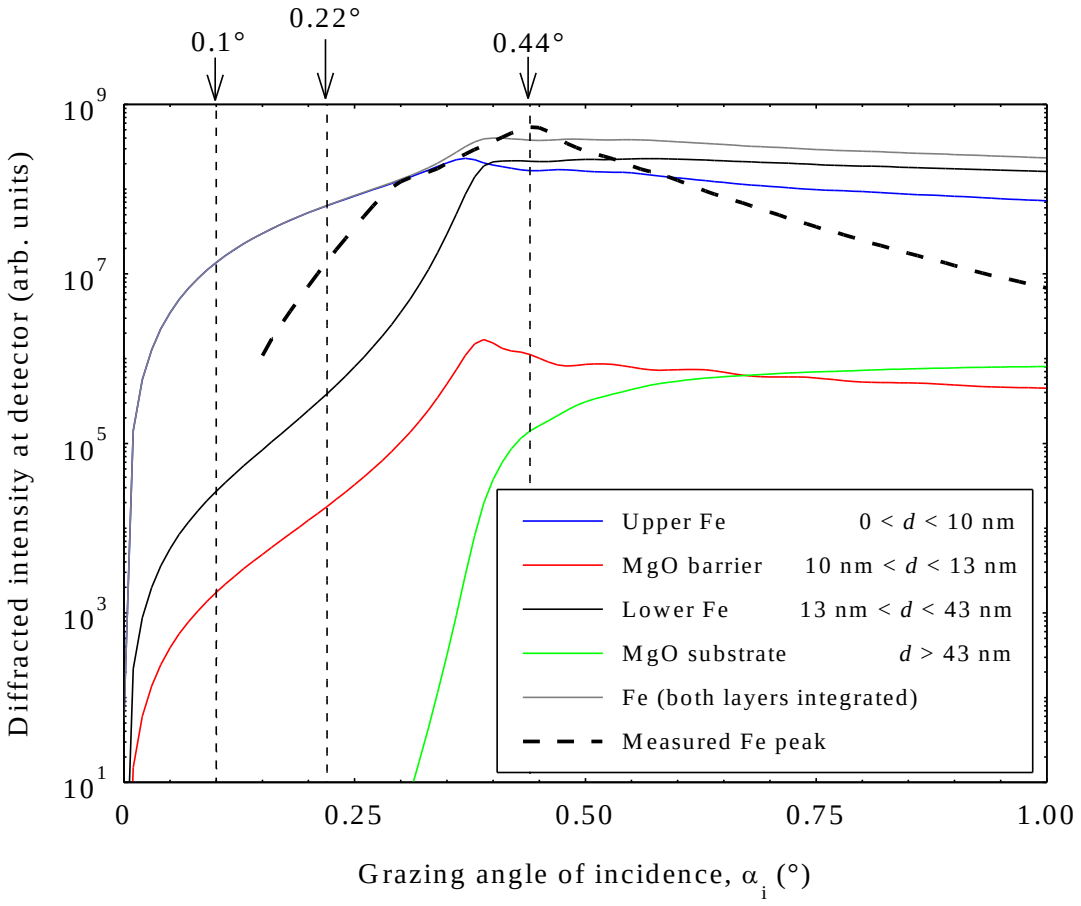

Figure 5-8. Simulation of the scattered intensity from each layer of the stack: MgO (substrate) / Fe (30 nm) / MgO (3 nm) / Fe (10 nm), together with a measured amplitude of the iron diffraction peak.

5.3.3. Simulation of the layer sensitivity for MgO/Fe/Au/MgO/Fe

Similar simulations on a sample with a 3 nm gold layer separating the lower iron electrodes and the barrier MgO are shown in Figure 5-9. Sensitivity to the top iron layer remains dominant at low grazing angles. However, the gold layer (coloured pink) scatters strongly, and limits scatter from layers buried deeper in the sample.

It is apparent that at $\alpha = 0.44°$ the iron and gold will scatter approximately equally, but that at shallower angles, the iron diffraction should be much the stronger. Therefore a mechanism for distinguishing between the iron and gold is suggested (which are expected to scatter at much more similar Bragg angles than the iron and MgO).

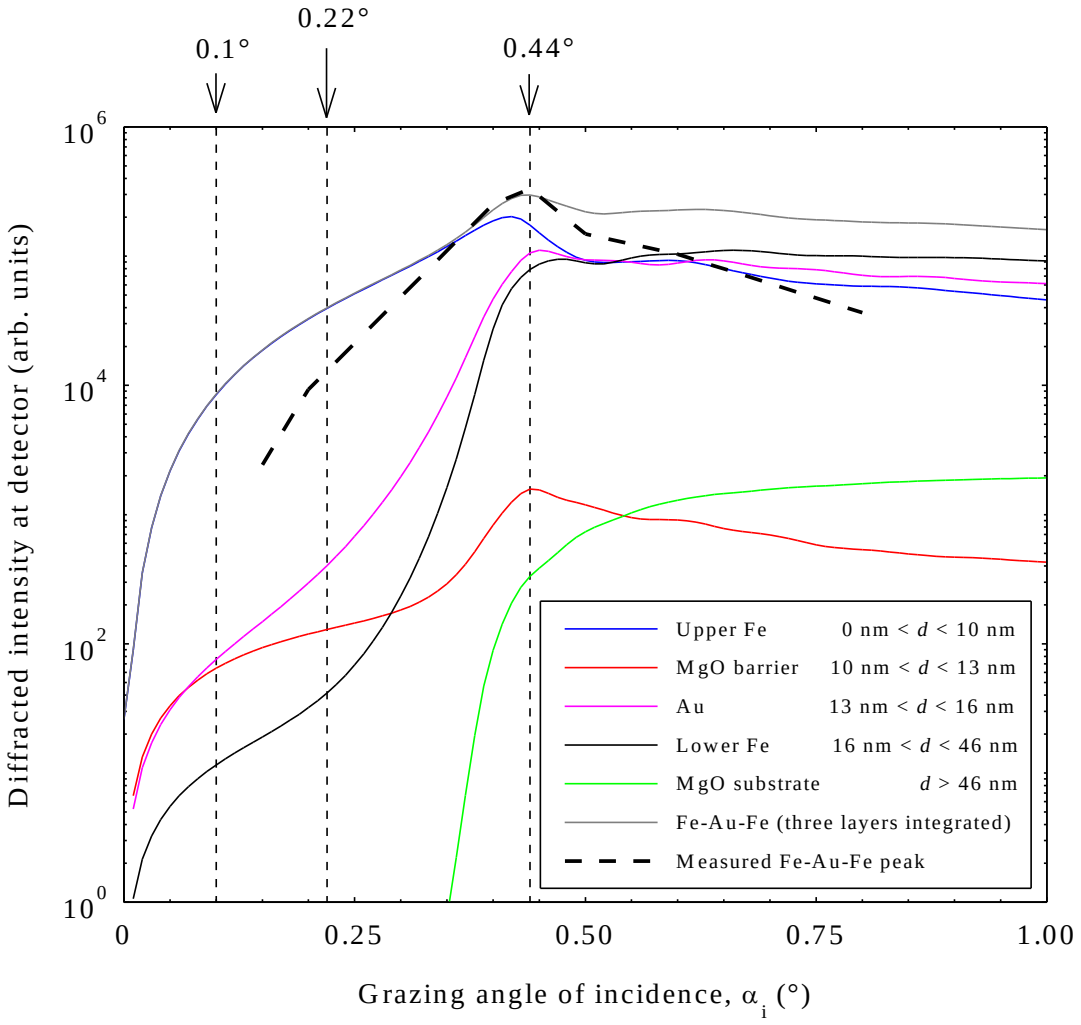

Figure 5-9. Simulation of the scattered intensity from each layer of the stack: MgO (001) / Fe (30 nm) / Au (3 nm) / MgO (3 nm) / Fe (10 nm), together with a measured amplitude of the iron/gold diffraction peak.

To summarize the sensitivity simulation, the angle of grazing incidence provides a way to tune the relative proportion of a single diffraction peak due to each layer. For the case of layers with identical interplanar spacing this is essential in order to compare and contrast layers. When different layers are lattice mismatched, in-plane diffraction peaks will occur at different Bragg angles, and the different materials may be identifiable by their implied lattice parameter.

5.4. Characterization of Fe/MgO/Fe on MgO (001) during annealing

Measurements of the x-ray reflectivity and grazing incidence diffuse scattering can show changes in the interface morphology on the scale of 10 nm – 1 μm; this is a very different length scale to the crystal lattice seen in diffraction measurements, but is of fundamental importance in the growth of thin film materials and is the starting point in this investigation.

5.4.1. X-ray reflectivity and diffuse scatter from Fe/MgO/Fe

The specular reflectivity scans shown in Figure 5-10 do not change during the annealing process. This is evidence that the averaged out-of-plane structure of the sample (the layer thickness and interfacial widths) does not change upon annealing.

Despite a variety of parameter sets and fitting strategies being employed, the specular reflectivity could not be fitted by the process described in section 3.3.5. Without such a layer width model, modelling of the frequency distribution in the in-plane roughness is not possible. This may imply that the interface widths are greater than the range for which the assumptions made within the Parratt formalism are valid. This is clarified by the analysis of the transmission electron microscopy images in the following section.

The ratio of the integrated transverse diffuse scatter and the specular intensity can be interpreted within the Born approximation to provide an estimation of the topological roughness (see section 3.4.2). Because of the limited validity of the Born approximation, and the geometrical restriction of the range over which diffuse scatter may be collected, the absolute measurements are likely to underestimate slightly the topological component of interface widths. Therefore, this analysis is most reliable as a comparative method.

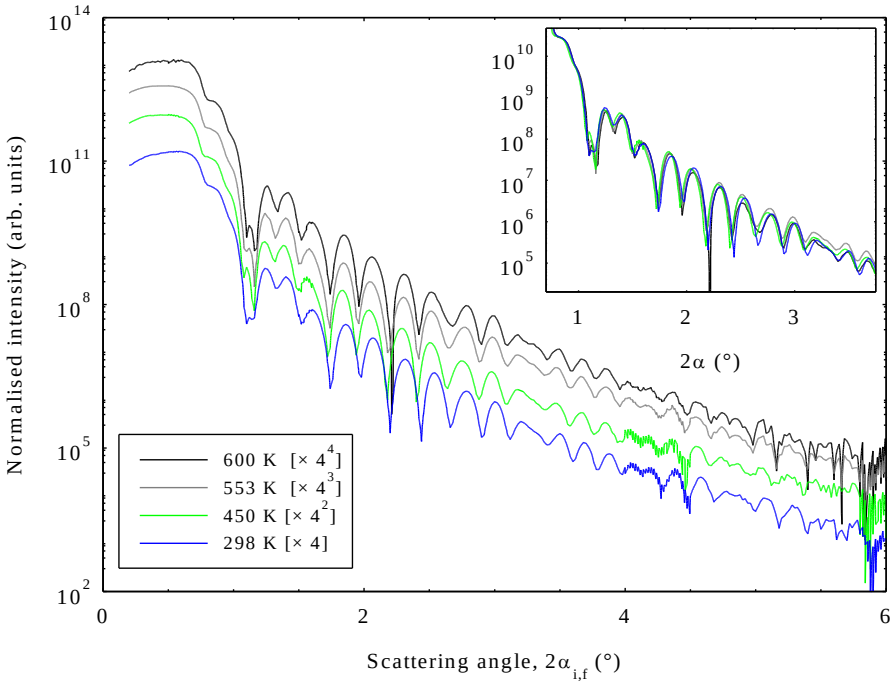

Figure 5-10. True specular reflectivity from sample structure MgO / MgO (5 nm) / Fe (30 nm) / MgO (3 nm) / Fe (10 nm). Successive scans are offset by powers of four for clarity. Inset: close-up of the low-angle region with curves overlaid for comparison.

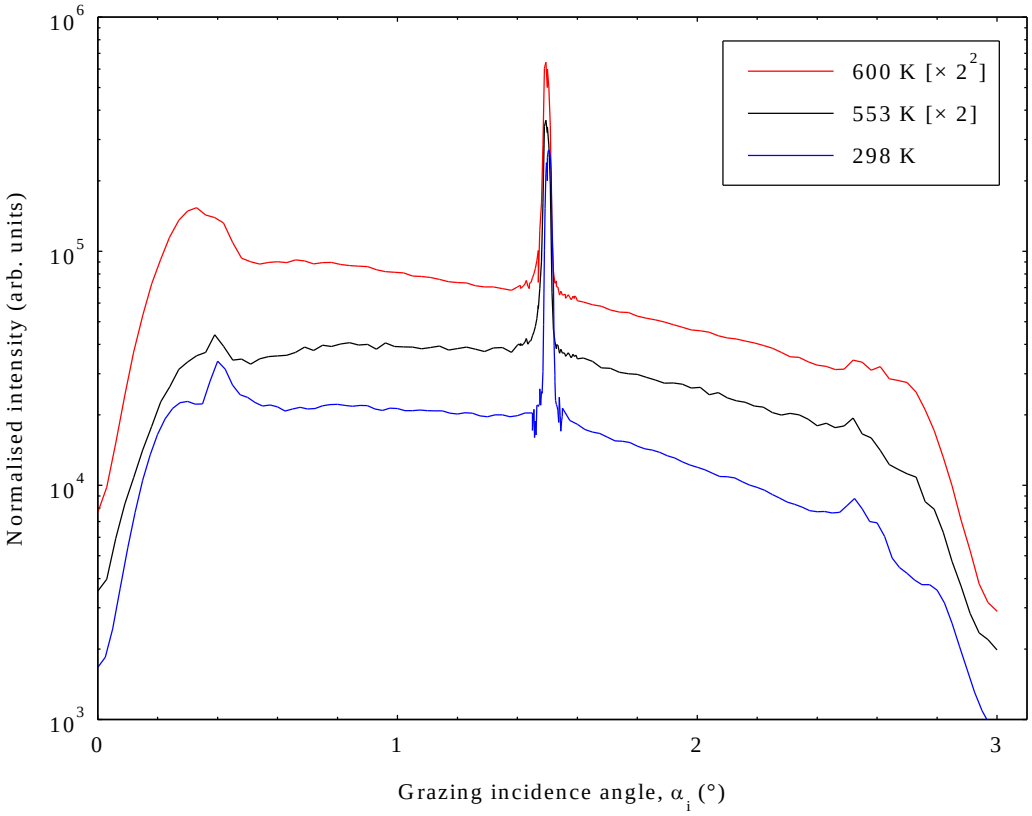

Figure 5-11. Transverse diffuse reflectivity with a detector angle of 3°. Successive scans are offset by powers of two for clarity.

Table 5-3. Topological roughness as deduced from the ratio of the specular to integrated diffuse scatter at a detector angle of 3°, where q_z is constant at 2.12 nm^{-1}.

Temperature (K)	**BORN ANALYSIS OF TRANSVERSE SCAN**	
	$\frac{I_{diffuse}}{I_{specular}}$ **(no units, to 2 sig. figs.)**	**Deduced topological roughness, $\sigma_{topological}$ (nm, to 2 sig. figs.)**
298	6.5	0.67
553	7.2	0.68
600	9.2	0.72

5.4.2. Transmission electron microscopy cross-sections of Fe/MgO/Fe

Transmission electron microscopy (TEM) cross-sections were obtained by Dr. D. McGrouther in the Department of Physics and Astronomy at the University of Glasgow. The samples were prepared in the Department of Physics at the University of Leeds, were nominally identical to those used in the separate x-ray investigation, and had been annealed post-deposition at 550 K for 60 minutes. Hence, they provide finalised, post-anneal images of the tunnel junction structure.

TEM is a complementary technique to grazing incidence x-ray scattering: it provides real space atomic resolution images of small regions of the sample, but it is a destructive technique and is incompatible with *in situ* annealing. X-ray scattering on the other hand is non-destructive and provides statistical long-range information with sub-atomic resolution. For further information on the technique of TEM the reader is directed towards reference [139].

Figure 5-12 shows a cross-section image of the entire structure, from the MgO substrate and buffer layer down through the Fe/MgO/Fe junction to the surface of iron oxide with the amorphous adhesive layer used to bond the sample to the holder. The buffer layer–lower iron layer interface appears particularly topologically rough, and the electrode-barrier interfaces also appear rough. The thicknesses labelled indicate the measured range of thicknesses in the field of view.

A higher magnification image is required to inspect the crystallinity of the individual layers, and is provided in Figure 5-14 which shows the substrate-buffer-lower iron layer region.

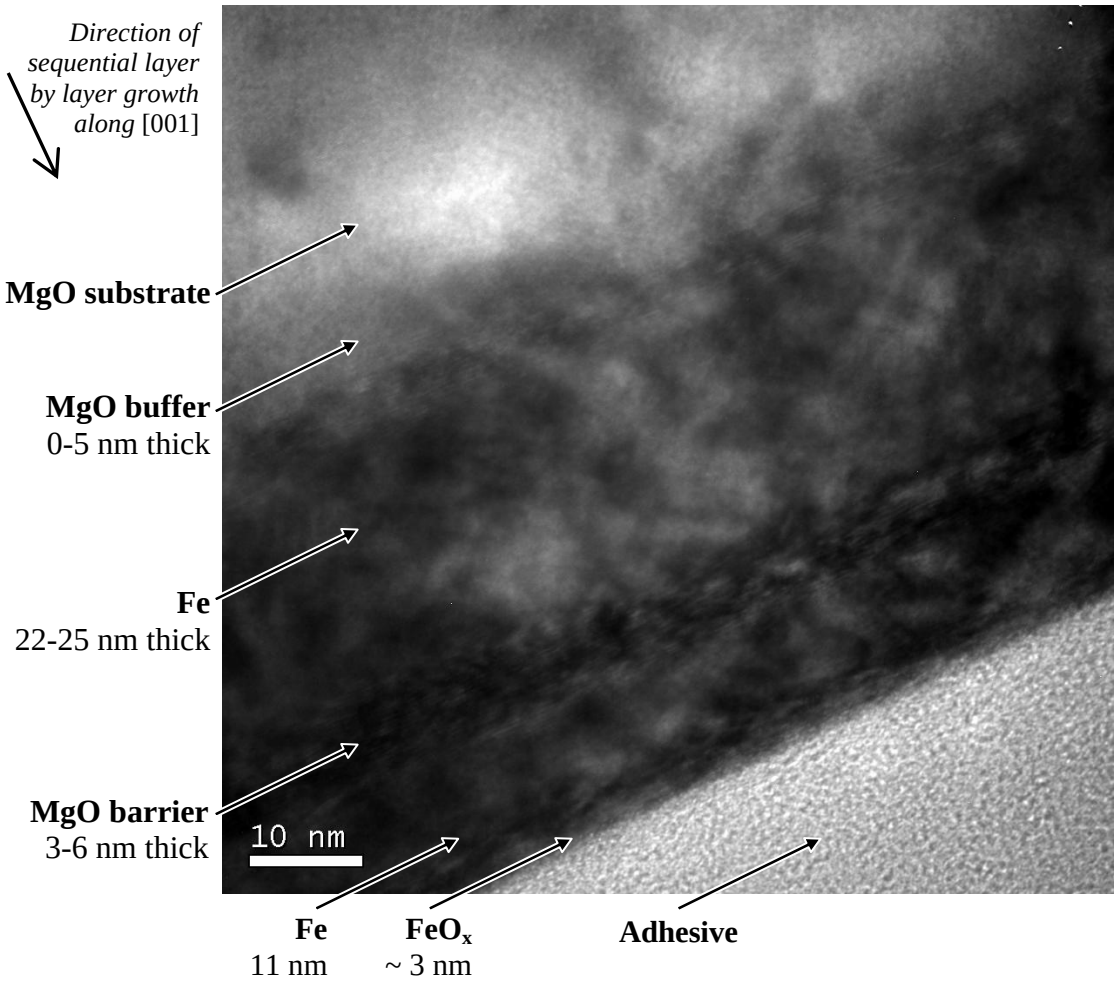

Figure 5-12. TEM cross-section of an Fe/MgO/Fe layer sequence on an MgO (001) substrate prepared with a MgO buffer layer. 195,000× magnification. Image by D. McGrouther, University of Glasgow [140].

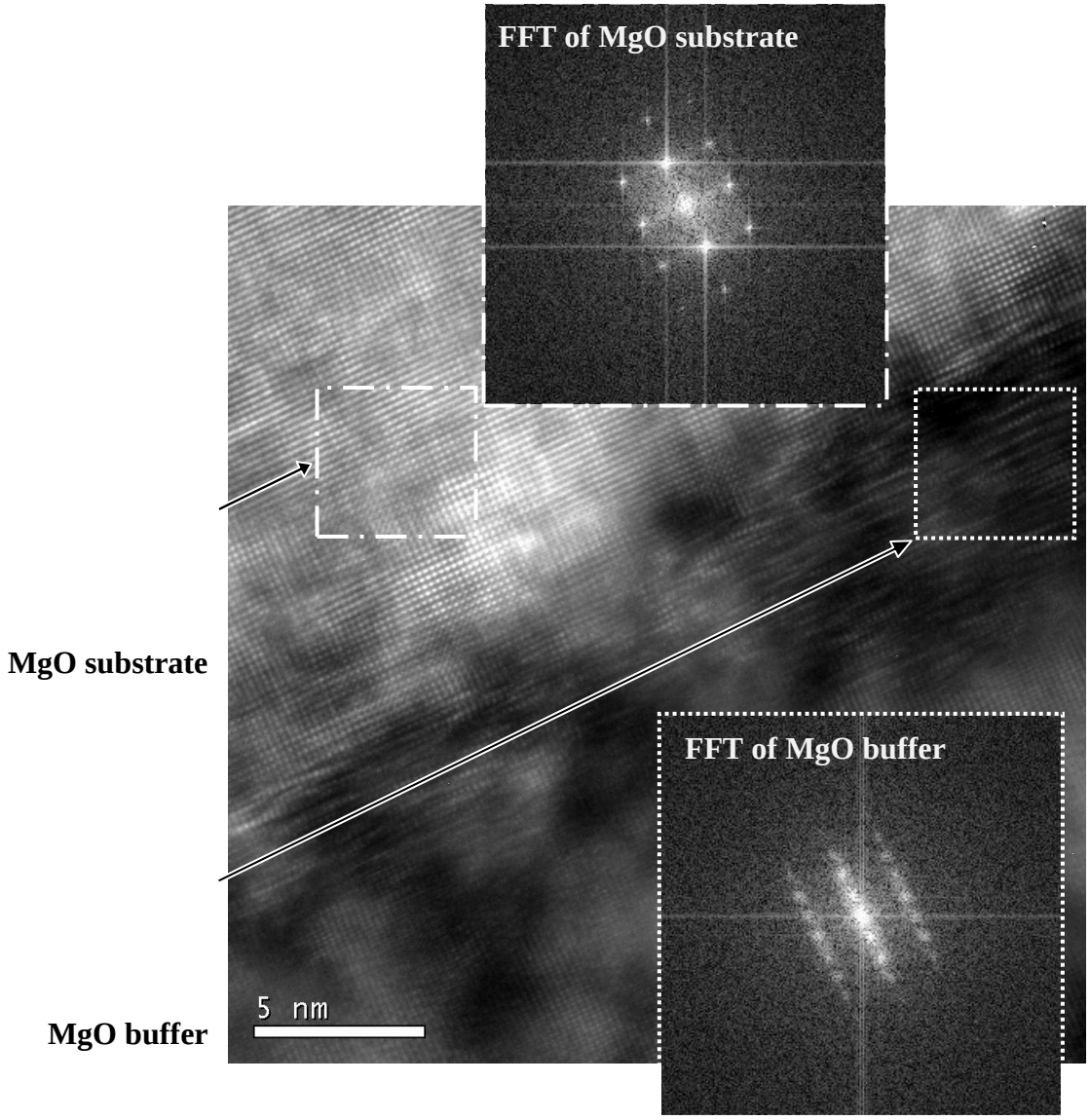

Figure 5-13 (above). TEM cross-section of the MgO substrate / MgO buffer / Fe region. Insets: two-dimensional Fast Fourier transforms of the labelled substrate and buffer regions. Image and FFTs by D. McGrouther, University of Glasgow [140].

The bulk of the substrate is highly single crystal: this can be observed from the square lattice in the image, and from the analysis of spatial frequencies shown fast Fourier transform (FFT) of the substrate. This shows the same lattice period both in and perpendicular to the direction of growth [001].

This is contrasted with the FFT of the buffer MgO, which has the same lattice period perpendicular to the [001] growth direction as the bulk, but approximately half that period in the [001] direction. This indicates that one atomic layer grows at atom sites determined by the previous atomic layer, but that there is no coordination of magnesium and oxygen atoms with the previous layer. The electrode-barrier-electrode region is shown in Figure 5-13.

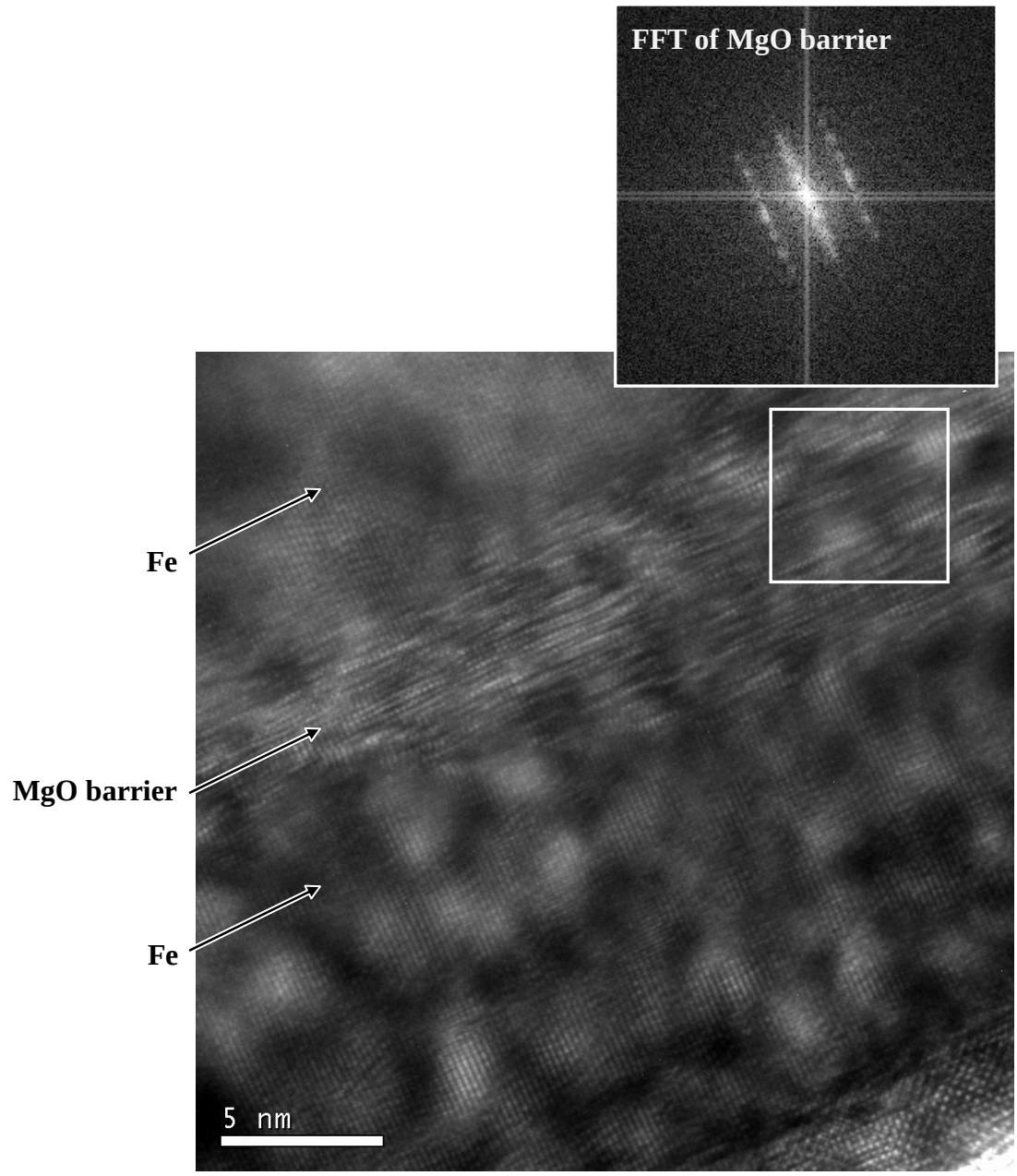

Figure 5-14. TEM cross-section of an Fe/MgO/Fe structure on an MgO (001) substrate prepared with a MgO buffer layer. Inset: two-dimensional Fast Fourier transform of the labelled barrier region. Image and FFT by D. McGrouther, University of Glasgow [140].

The [001] growth of both iron layers and the MgO barrier is clear. A fast Fourier transform of the barrier region (inset) reveals identical growth to the MgO buffer seen in the previous figure: the growth of one layer has a coherent sodium chloride like lattice, but between successive layers the epitaxy is poor.

This image shows that the barrier varies considerably in thickness from approximately 3 nm on the left to 6 nm on the right.

In summary, the TEM cross-sections illustrate that the substrate-buffer and electrode-barrier interfaces are very rough (or equivalently that the layer thicknesses vary greatly). This explains why the specular reflectivity could not be fitted in the Parratt formulation. It also shows that the epitaxy between the MgO atomic layers is poor in comparison with samples exhibiting giant TMR [52, 53].

The amplitude of the topological roughness obtained from the TEM images is much higher than the estimate from the Born analysis of the diffuse scatter. The labels on Figure 5-12 show a variation of approximately three nanometres through most of the layers, whereas the diffuse x-ray scatter gives an interface topology $2\sigma_{\text{topological}} \approx 1.4$ nm. This discrepancy may be attributed to the limitations of the simple Born analysis: firstly, the approximation breaks down for strong scattering which may be the case with rough but highly conformal undulations. Secondly, the Born analysis is primarily sensitive to the uppermost surface of the sample, which may be smoothed by the presence of iron oxide.

5.4.3. High-angle diffraction from the out-of-plane lattice

Shown in Figure 5-15, the MgO substrate provides two intense diffraction peaks relating to the (200) and (400) reflections. The iron (220) peak is just visible above the noise level of the measurement. From the peak positions it is possible to determine the out-of-plane lattice parameter of the substrate and iron layers, as given in Table 5-4, but the MgO barrier layer is not distinguishable. The iron parameter coincides with a standard reference value, whereas the MgO measurement is significantly larger (by 0.6%). This is unexpected, since the quasi-bulk substrate should not be strained significantly by the subsequent growth of thin surface epilayers. The highly disordered MgO buffer is too thin to diffract strongly in the high angle geometry. A possible explanation is that the substrate was flexed, causing distension of the lattice close to the surface. The full-width at half maximum of the iron peak is (0.45 ± 0.21)°; this value will later be compared to the width of the in-plane iron diffraction peak.

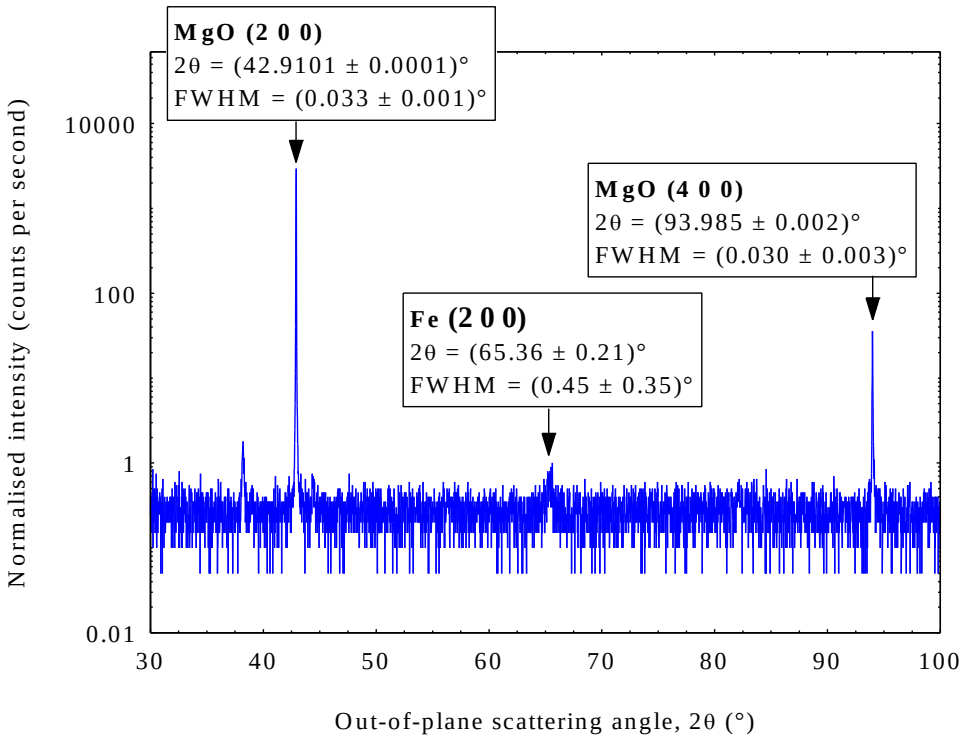

Figure 5-15. Out-of-plane (high-angle) coupled axis diffraction scan measured in the laboratory, after the annealing process. Measured with an integrated count time of 30 seconds per point.

Table 5-4. Out-of-plane lattice parameters determined from high-angle diffraction measurement of Bragg peak positions, together with reference values for the bulk material [136]. Uncertainty on average MgO parameter determined by standard deviation of the two independent measurements.

	LATTICE PARAMETER (nm)	
	Measured	**Reference bulk value**
Fe	0.287 ± 0.002	0.28664
MgO deduced from (200)	0.423694 ± 0.000002	0.42117
MgO deduced from (400)	0.423855 ± 0.000002	
MgO average of (200) and (400)	0.4237 ± 0.0001	

5.4.4. Grazing incidence in-plane diffraction from Fe/MgO/Fe

As has been discussed previously, depth sensitivity is determined by the grazing angle. Figure 5-16 shows the effect of α on the amplitude of the Fe (110) diffraction peak. The maximum amplitude is seen for α = 0.44°, where there is greatest sensitivity to the iron lattice. Orthogonal to the series of θ-2θ scans is overlaid an additional coupled scan of α_i and α_f sat at the diffraction condition.

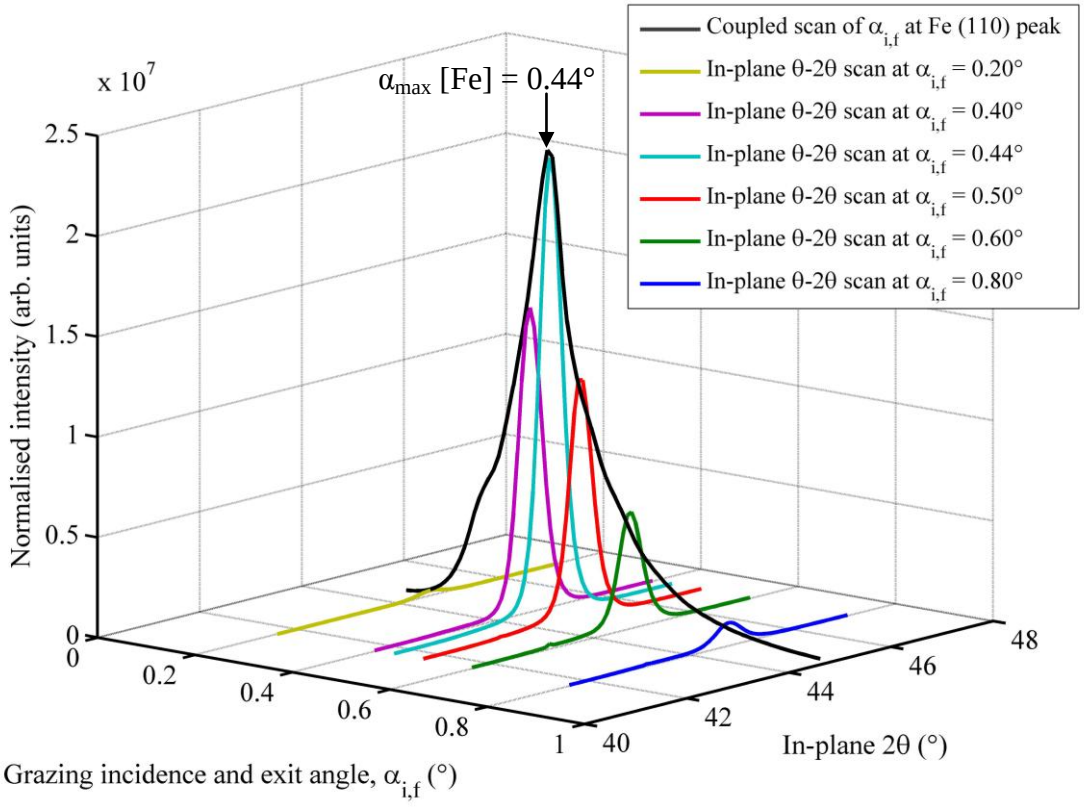

Figure 5-16. Measurements of the Fe (110) in-plane θ-2θ peak for various grazing incidence and exit angles, shown in relation to the variation of the Fe (110) peak amplitude with grazing angle. The peak at α = 0.44° is the critical angle for iron at 8 keV. Sample structure: MgO / MgO (5 nm) / Fe (30 nm) / MgO (3 nm) / Fe (10 nm) at ambient temperature, prior to annealing.

The following measurements for the Fe / MgO / Fe sample were all performed at a grazing angle of 0.44°, where the maximum in the diffracted intensity occurs. This angle is nominally sensitive to both iron layers equally, and to the MgO barrier but not the substrate (as was shown in section 5.3).

The changes in the in-plane diffraction peaks during annealing are presented in Figure 5-17. Higher curves relate to the time progression of the experiment; each 25K increment relates to an offset by a power of two for clarity. The iron peak intensity dominates the MgO peak due to the iron layers being thicker and having higher scattering power.

The iron (110) peak is seen to shift linearly with temperature due to thermal expansion, before returning to the original position after cooling. A significant change is seen to occur in the MgO (200) peak, which becomes much more distinct from the iron peak, shifts to lower angles and becomes sharper. These changes are quantified in the following section.

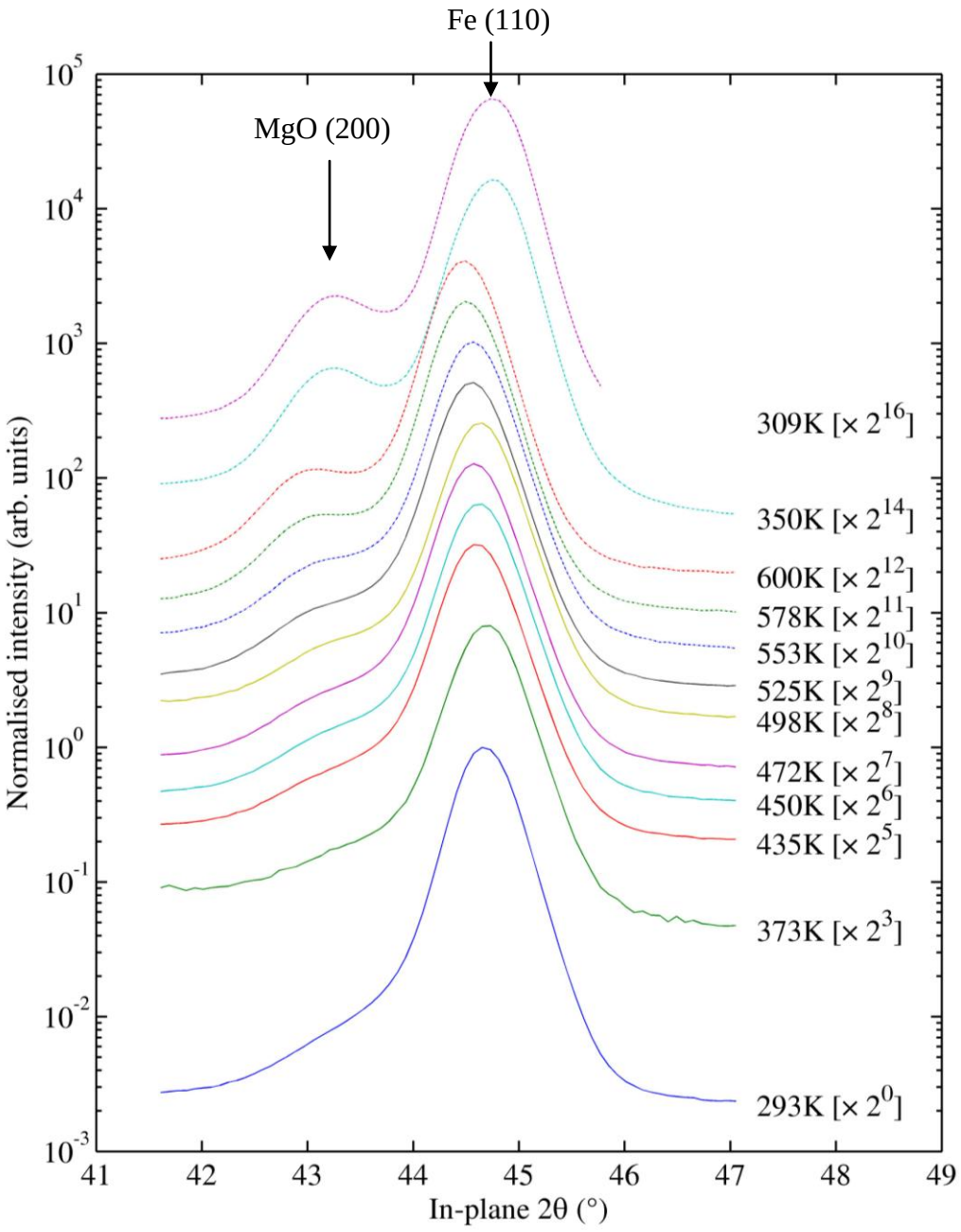

Figure 5-17. Evolution of the magnesium oxide peak during sample anneal to 600 K and cooling to 300 K. Sample structure: MgO / MgO (5 nm) / Fe (30 nm) / MgO (3 nm) / Fe (10 nm). Measurements are offset by powers of two for clarity, with higher curves corresponding to later measurements. The uppermost curves at 350 K and 309 K are during and after cooling of the sample to room temperature.

5.4.5. Method of peak analysis

To analyse the coupled in-plane diffraction scans, a least-squares method was used simultaneously to fit three components: an asymmetric Pearson VII lineshape (with six free parameters), to the Fe (110) peak, a Pearson VII lineshape (four free parameters) to the MgO (200) peak, and an exponential background (two free parameters).

The Pearson VII function is defined as:

$$y = \frac{c_0}{\left[1 + \left(\frac{x - c_1}{c_2}\right)^2 \left(2^{-c_3} - 1\right)\right]^{c_3}} \tag{5.1}$$

Here c_1 is the peak centre, c_2 is a parameter related to peak width, and c_3 is a shape defining parameter.

An exemplary fit to the data from one scan is shown in Figure 5-18 (a) on a logarithmic scale, and (b) on a linear scale.

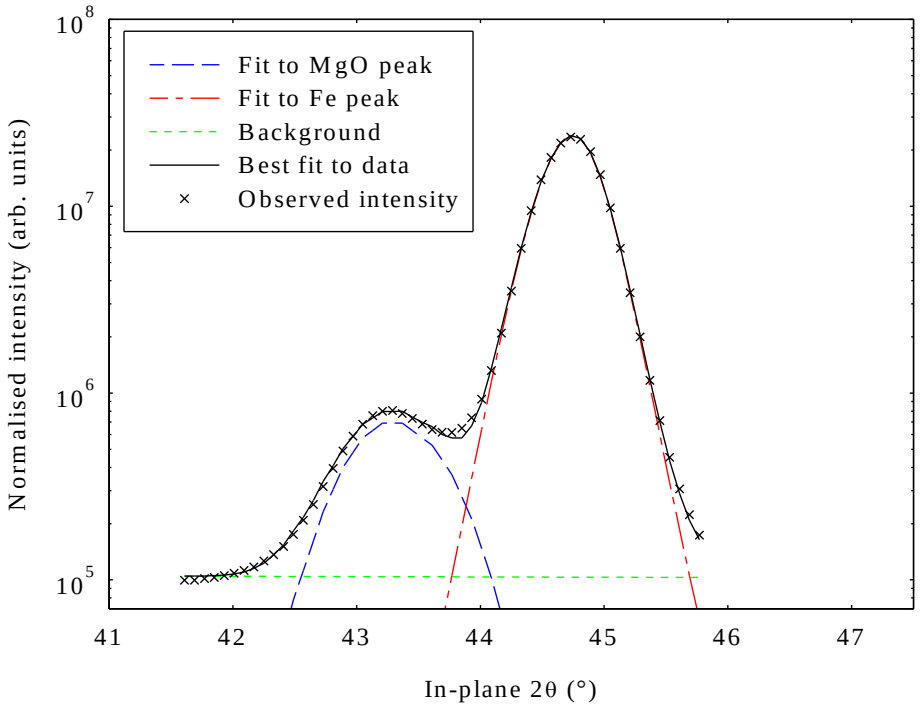

Figure 5-18(a). Exemplary fit at T = 309K. Sample structure: MgO / MgO (5 nm) / Fe (30 nm) / MgO (3 nm) / Fe (10 nm).

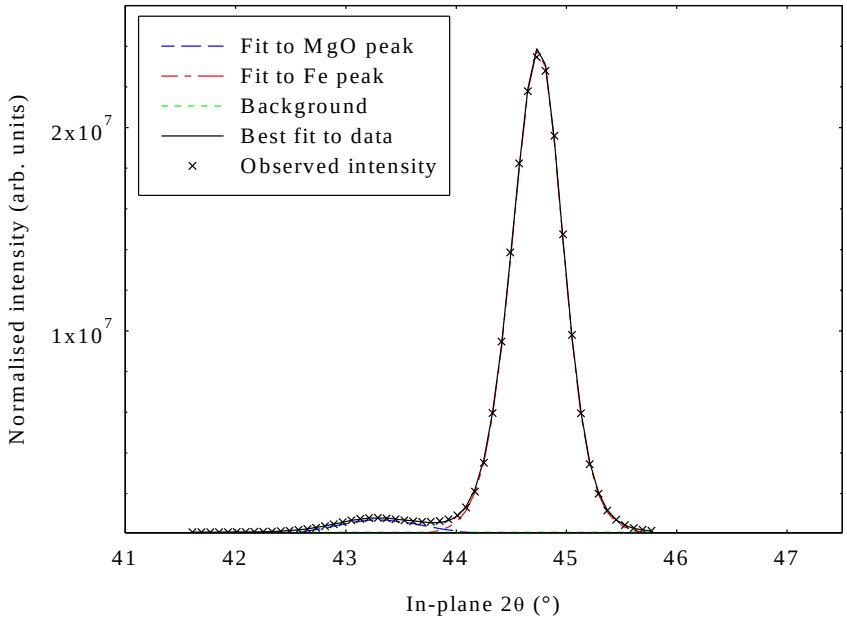

Figure 5-18(b). As Figure 5-18(a), plotted on a linear intensity scale.

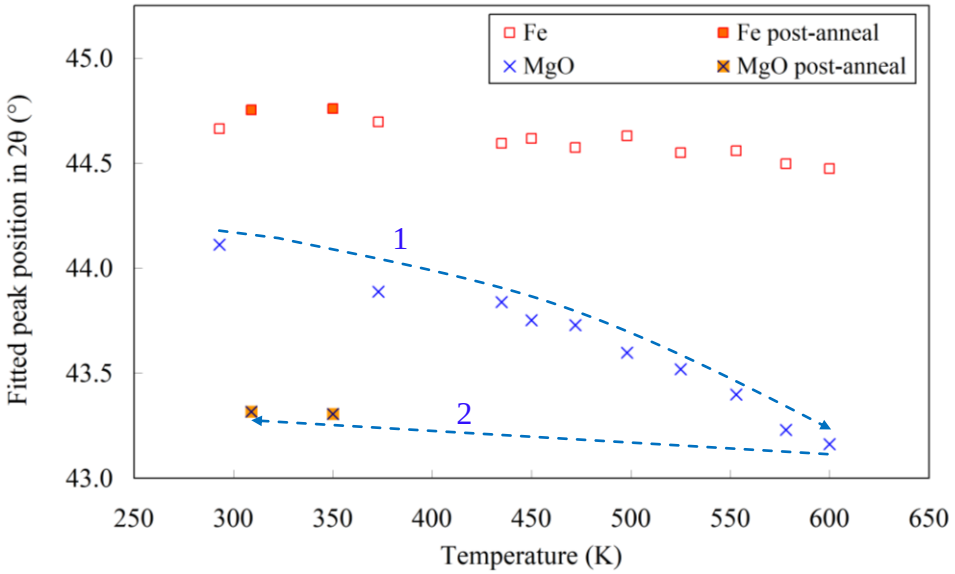

Figure 5-19. Fitted peak position for Fe and MgO. Sample structure: MgO / MgO (5 nm) / Fe (30 nm) / MgO (3 nm) / Fe (10 nm). Blue arrows show the sequence of (1) annealing and (2) cooling. Error bars are less than 0.05° in 2θ, and less than 0.5 K in temperature, contained within the data markers shown.

From these fits to all the in-plane scans, it was possible to extract peak positions and widths. Figure 5-19 shows the fitted peak positions as a function of the annealing and cooling cycle. These values are converted into interplanar *d*-spacings using Bragg's law.

Azimuthal-only scans, where the detector is fixed at the diffraction angle and the sample rotated about the surface normal were also performed, in order to measure the degree of preferred in-plane orientation of the deposited layers. These were fitted to a single Pearson VII line shape.

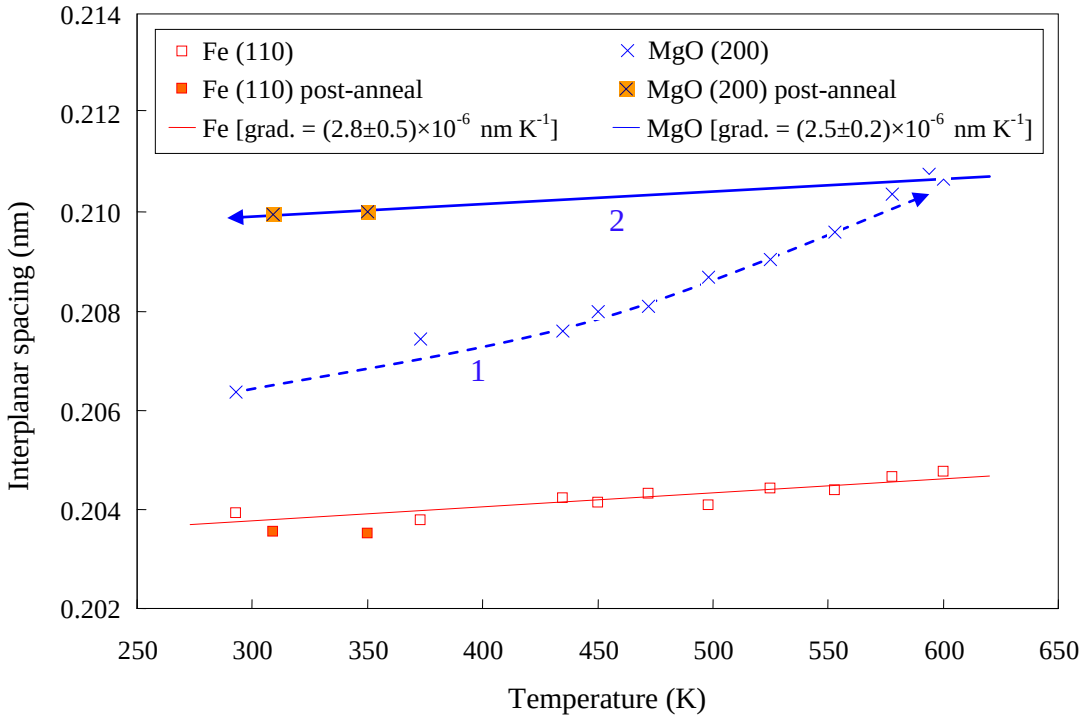

Figure 5-20. Fitted interplanar spacing as a function of temperature (1) during anneal and (2) after cooling. Blue arrows show the sequence of annealing and cooling, and the dashed line is a guide to the eye. Sample structure: MgO / MgO (5 nm) / Fe (30 nm) / MgO (3 nm) / Fe (10 nm). Error bars are less than 0.00025 nm in interplanar spacing, and less than 0.5 K in temperature, both contained within the data markers shown.

It is apparent that the iron layers expand reversibly along the Fe (110) direction, whereas the MgO layer undergoes an irreversible relaxation.

The linear thermal expansion coefficient, is defined by Eq. (5.2), where L_0 is the initial length.

$$\bar{\alpha} = \frac{1}{L_0}\left(\frac{\Delta L}{\Delta T}\right) \tag{5.2}$$

From the gradient of the straight line fit to the interplanar spacing shown in Figure 5-20, the mean linear thermal expansion coefficient of iron is obtained as $(14.0 \pm 2.5) \times 10^{-6}$ K^{-1}, in close agreement with the standard reference values [120] given in Table 5-5.

A similar determination is made for the MgO barrier; in this case, a linear contraction is assumed, from the highest temperature measurement down through to the points after cooling. The measured thermal expansion is $(11.9 \pm 1.0) \times 10^{-6}$ K^{-1}, agreeing reasonably well with the reference data.

In this analysis of thermal expansivity it is assumed that the layers expand and contract independently of one another. Since the MgO barrier contracts more slowly than the iron layers, misfit dislocations must be introduced at the interface between these layers.

The interplanar spacings are converted into lattice parameters by assuming in-plane isotropy, and the results given in Table 5-6. These data provide evidence that the iron layer matches the expected bulk value. The MgO barrier layer is initially strained towards the iron by 1.94% and relaxes towards the bulk value for MgO after anneal so that it is strained by only 0.28%.

The iron layers, being thicker, appear to have relaxed close to the bulk value prior to the annealing measurement. It has been reported [e.g. ref. 122] that this relaxation occurs soon after deposition.

Table 5-5. A comparison of the measured in-plane thermal expansion coefficient of iron and MgO to reference values for the bulk material [120]. Sample structure: MgO / MgO (5 nm) / Fe (30 nm) / MgO (3 nm) / Fe (10 nm).

	THERMAL EXPANSION COEFFICIENTS		
	Determined value $\bar{\alpha}$ **[× 10^{-6} K^{-1}]**	**Reference value for bulk** $\alpha(T=298\ K)$ **[× 10^{-6} K^{-1}]**	**Reference value for bulk** $\alpha(T=500\ K)$ **[× 10^{-6} K^{-1}]**
Fe	14.0 ± 2.5	11.8	13.9
MgO	11.9 ± 1.0	10.8	Unavailable

Table 5-6. A comparison of measured in-plane and reference [136] bulk lattice parameters of iron and magnesium oxide layers. Sample structure: MgO / MgO (5 nm) / Fe (30 nm) / MgO (3 nm) / Fe (10 nm).

	LATTICE PARAMETER OF IRON AND MAGNESIUM OXIDE		
	Pre-anneal measurement at 298 K (nm)	**Post-anneal measurement at 309 K (nm)**	**Reference value for bulk at 293 K (nm)**
Fe	0.288 ± 0.001	0.287 ± 0.001	0.28664
MgO	0.413 ± 0.001	0.420 ± 0.001	0.42117

The fitted widths of the peaks are presented in Figure 5-21. The iron peak width undergoes no significant and systematic variation during heating, whereas the MgO peak becomes significantly narrower; this is indicative of either a reduction in micro-strain, or a reduction of twist mosaicity. With the evidence from specular x-ray reflectivity measurements suggesting that there is no significant change in interface morphology, the most plausible mechanism is a reduction in micro-strains.

The average iron peak full width at half maximum in in-plane 2θ is (0.524 ± 0.014)°. This is identical (within the margin of uncertainty) to the value obtained for the out-of-plane high-angle diffraction peak. If the width is attributed to localised strain dispersion (micro-strain) this implies similar strains in and out-of-plane.

By making the assumption that the atomic layers form a single, perfectly orientated crystal (allowing the use of Eq. 3.85), the peak width of the iron can be attributed to a local strain dispersion $\Delta\varepsilon_{in\text{-}plane}$ = (0.0112 ± 0.0003). For the out-of-plane width found in section 5.4.3, the value was $\Delta\varepsilon_{out\text{-}of\text{-}plane}$ = (0.010 ±0.005). This value for the FWHM compares with 0.2° measured by Dekadjevi *et al* [132] in similar measurements on an Fe/Au bilayer grown on MgO (001), suggesting that their films contained lower microstrain. The MgO peak width and therefore strain dispersion reduces markedly (as shown in Figure 5-22). From an initial figure of (0.0371 ± 0.0004) it reduces to (0.0205 ± 0.0001). This relief of local micro-strains supports the hypothesis of overall layer strain relief by dislocation formation.

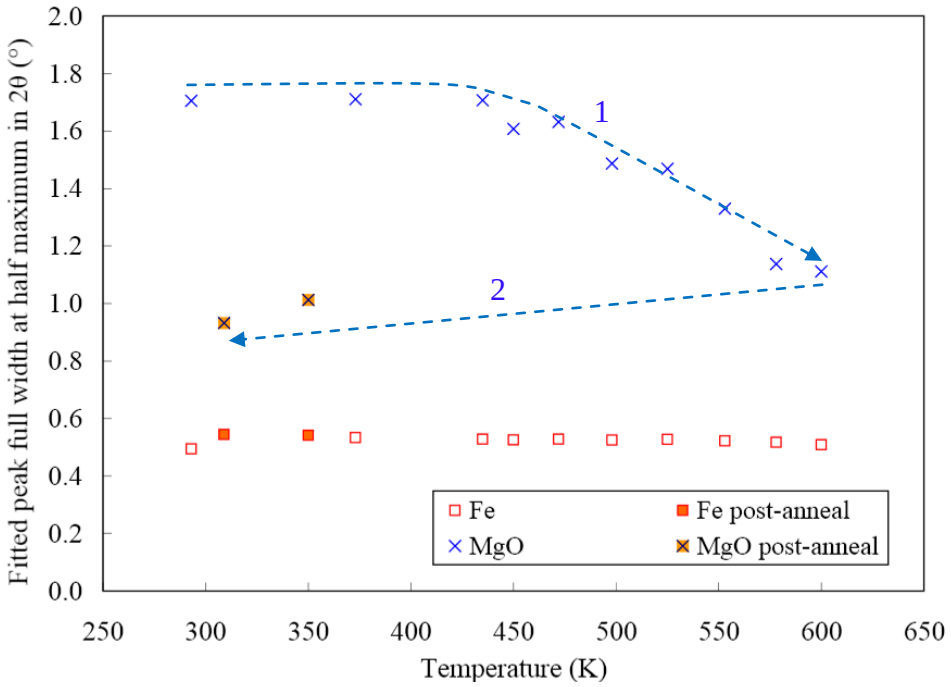

Figure 5-21. Full-width at half maximum of the peaks of in-plane θ-2θ. Error bars within data points.

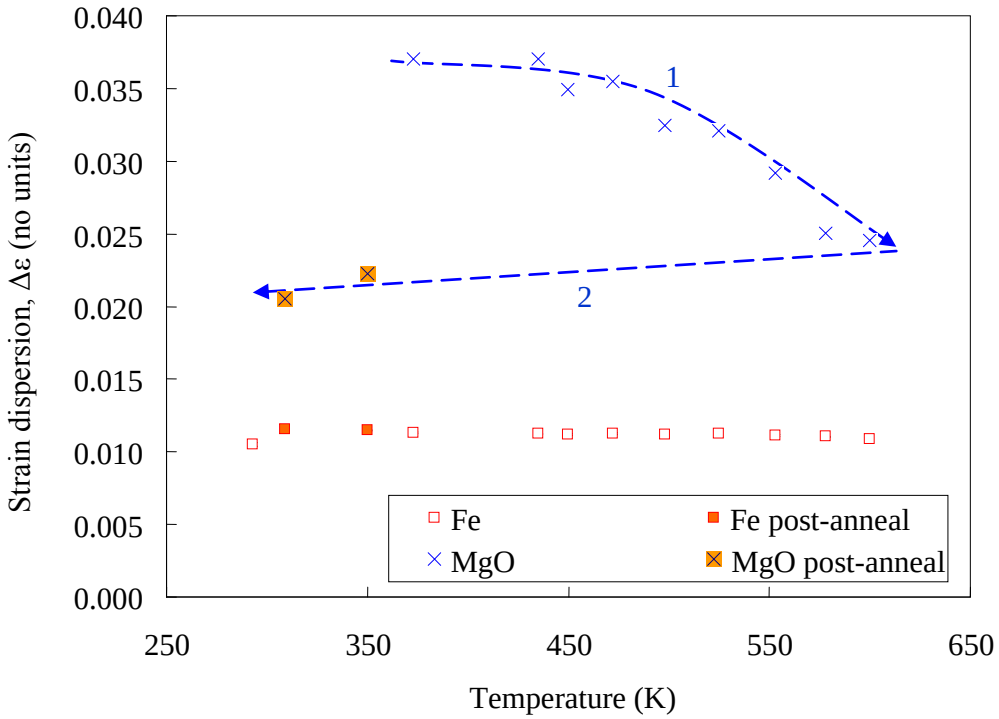

Figure 5-22. Strain dispersion during (1) the annealing and (2) the cooling processes. Error bars are contained within data points, and the dashed lines serve as a guide to the eye.

Figure 5-23 presents the MgO peak width with the azimuthal angle of the sample θ only, which can be interpreted as an in-plane rocking curve. The constancy of this peak is evidence that the MgO (200) is highly orientated in the plane, as would be expected for epitaxial growth.

Similarly, Figure 5-24 shows the azimuthal scans with the detector fixed at the Bragg 2θ angle for iron. The fitted rocking curve widths for both iron and MgO are plotted in Figure 5-25, and show negligible variance; there is no significant and systematic change in peak widths either on annealing or between the iron and MgO. Together, the peak positions and widths would indicate that the Fe/MgO/Fe system has the same degree of in-plane misorientation of crystallites (twist) throughout the sequence of layers, and that annealing has little effect on either the angle or the distribution of their in-plane orientation. Dekadjevi *et al* [132] measured an azimuthal FWHM of (0.25 ± 0.06)°, implying a higher degree of preferred in-plane orientation than seen here.

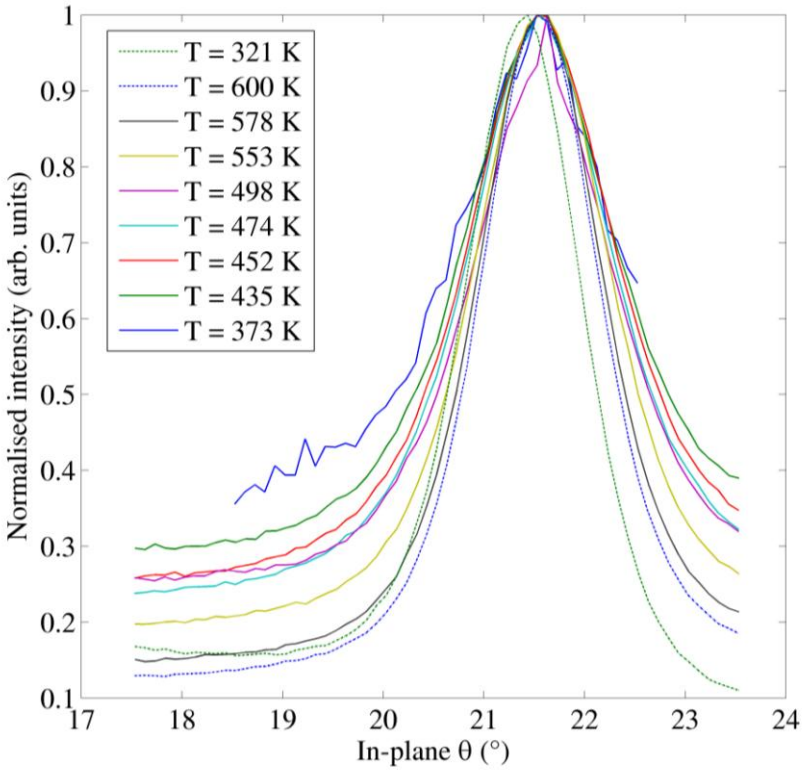

Figure 5-23. In-plane azimuthal (sample-only) scans through the MgO (200) peak.

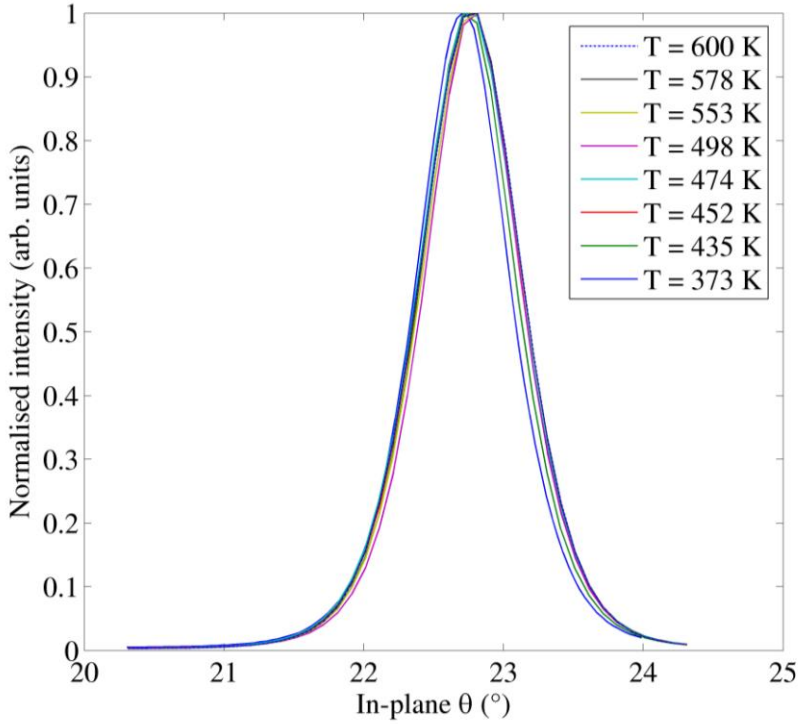

Figure 5-24. In-plane azimuthal (sample-only) scans through the Fe (110) peak.

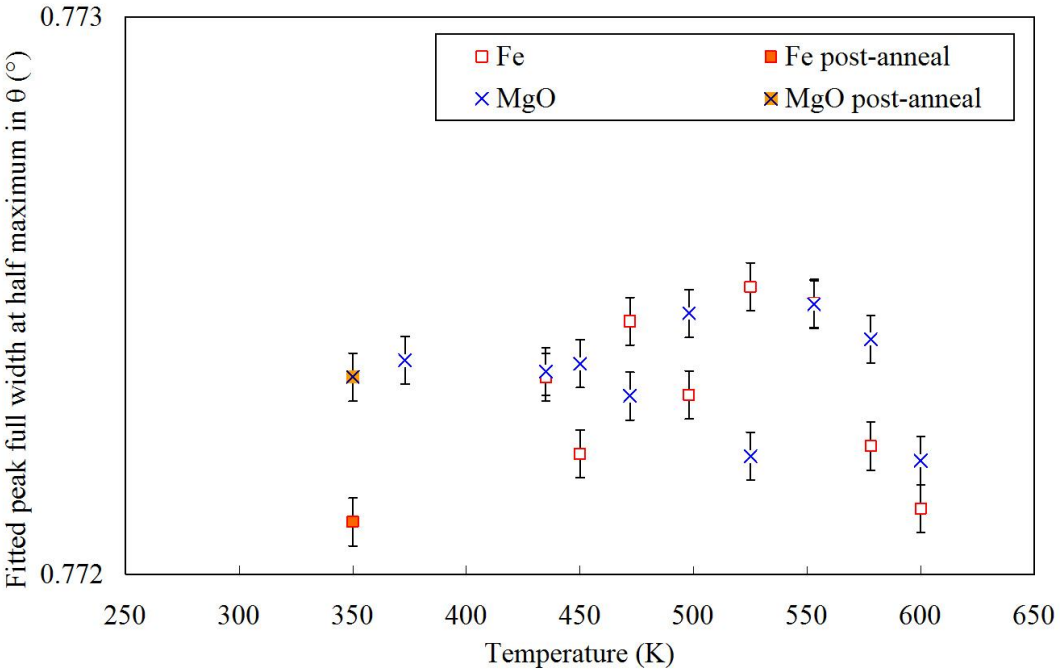

Figure 5-25. Fitted full-widths at half maximum for the rocking curves through the iron and MgO peaks. Error bars relate to precision of the fitting algorithm.

5.4.6. Method for an Arrhenius interpretation of lattice relaxation

The empirical Arrhenius equation is a general relationship describing the effect of temperature on the rate of a thermally induced process [see, for example, ref. 141]. It was proposed by van t' Hoff in 1884 and physically justified by Arrhenius in 1889, and allows the activation energy, E_a to be estimated for a process. The assumption is made that the lattice dislocations at the interface between iron and MgO layers act as diffusive particles. The simplest form of an Arrhenius law is given in Equation (5.3).

$$D = D_0 \exp\left(\frac{-E_a}{k_B T}\right) \tag{5.3}$$

Here, D is the diffusion coefficient, D_0 is a temperature-independent constant term and k_B is the Boltzmann constant. By rearranging (5.3) into a linear form (5.4), the activation energy can be estimated from the gradient of a plot of the natural logarithm of the diffusion against the inverse of the temperature (Figure 5-26).

$$\ln D = \ln D_0 - \frac{E_a}{k_B T} \tag{5.4}$$

This linear form applies when temperature is the sole rate determining factor during a process.

Relaxation acts to minimize the total film energy, which is a balance of the chemical bonding energy across the interface with the strain energy within the film. Thermal fluctuations act upon this potential energy landscape to increase the relaxation rate, but temperature is not the only rate limiting factor. If the potential energy terms also vary, for example as the relaxation decreases the strain energy, it may be necessary to introduce a variable prefactor into the Arrhenius law description. Alexander and Haasen [142] proposed the modified form:

$$D = C_0 \tau^n \exp\left(\frac{-E_a}{k_B T}\right) \tag{5.5}$$

Where τ is the effective stress in the film during the relaxation process and n is some exponent in the range $1 \leq n \leq 2$ which may, in general, be temperature dependent.

5.4.7. Arrhenius interpretation of the lattice relaxation in Fe/MgO/Fe

Figure 5-26 shows an Arrhenius plot of the rate of change in the MgO interplanar spacing as a function of temperature over the range 472 K – 600 K. This rate is assumed to be proportional to the rate of dislocation diffusion, meaning that the gradient provides a measure of the activation energy for the relaxation process.

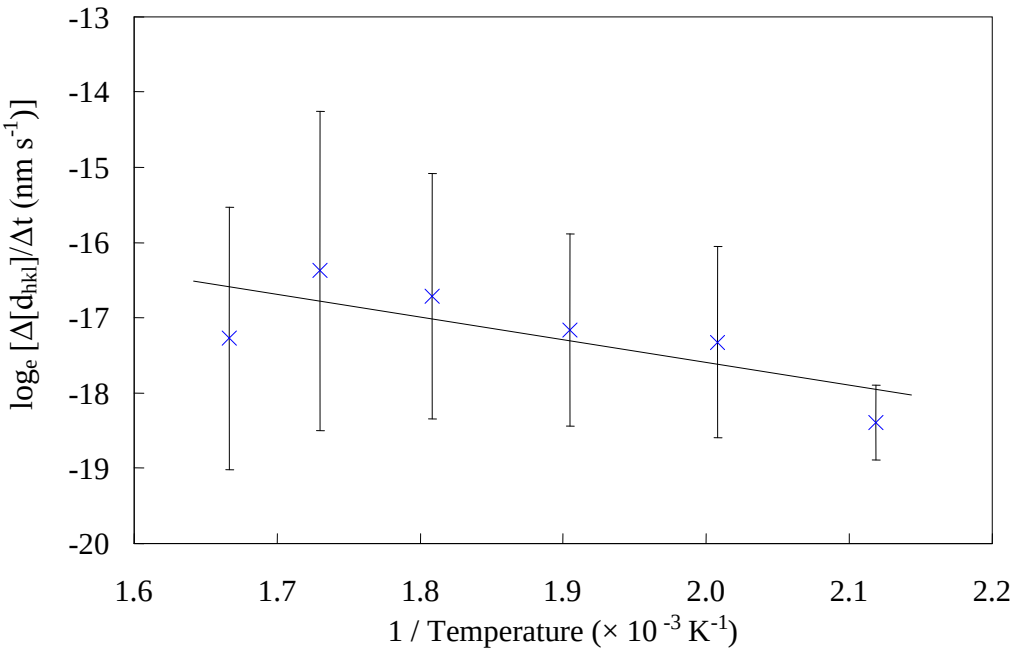

Figure 5-26. Arrhenius plot of the rate of change in MgO interplanar spacing within an Fe/MgO/Fe structure as a function of temperature between 472 K and 600 K. The line of best fit was fitted by least squares, with a gradient of (-3000 ± 1300) = - E_a / k_B.

The gradient of the fitted trendline is (-3000 ± 1300) kelvins, which provides an activation energy of (0.3 ± 0.1) eV for the initiation of a dislocation. This is lower than the lattice energy of FeO, which is 39 eV [136], a fact which indicates that strain and localized strain concentrations provide the dominant contributions to the dislocation process, whereas thermal vibrations simply destabilize the equilibrium between chemical bonding and strain.

It is a reasonable assumption that the effective (microscopic) strains decrease during the relaxation process. The simple form of the Arrhenius law (5.3) is does not account for varying strain. If the data were more precise and complete, this additional consideration may be required for a satisfactory fit to an Arrhenius law.

5.4.8. Summary for Fe/MgO/Fe epitaxial structures

In summary, it is found that the MgO in-plane diffraction peak sharpens and shifts to a lower angle during annealing. This corresponds to a relaxation of the magnesium oxide barrier layer, which is initially strained (from the bulk value) by 1.94 % towards the iron lattice upon which it is grown. A proposed mechanism for this relief – the creation and movement of dislocations at the barrier interface – is consistent with observed relief of strain dispersion, and of the temperature dependence of the relaxation. The state after annealing is strained by only 0.28 %, much closer to fully relaxed bulk value.

The position of the iron peak shifts during annealing solely due to thermal expansion, and contracts equally during cooling. The value for the in-plane linear thermal expansion coefficient is consistent with reported values for the bulk. The measured in-plane iron lattice parameter is consistent with the expected bulk value.

These measurements of small changes in the lattice may be somewhat surprising when the rough topological nature of the layers is considered. Both TEM and diffuse x-ray scattering indicate relatively poor epitaxy of the MgO buffer and barrier with respect to the MgO substrate and iron, since there is a relatively high interfacial roughness and layer thickness variation. There does appear to be strong orientation of the MgO barrier in the plane of the sample, suggesting that the nucleation and layer-by-layer growth does indeed follow the underlying lattice.

5.5. Characterization of Fe/Au/MgO/Fe during annealing

Corresponding measurements to those presented above were made on a sample with a three nanometre gold layer separating the lower iron electrode and the barrier MgO.

5.5.1. X-ray reflectivity and diffuse scatter from Fe/Au/MgO/Fe

The first measurements to be considered are the x-ray reflectivity presented in Figure 5-27, and the diffuse scatter in Figure 5-28. There is little change on annealing or after cooling, suggesting that the layer thicknesses and interface widths are invariant. The specular data could not be fitted within the Parratt formulation, possibly because the topological roughness was greater than a few nanometres.

There is some change visible in the transverse diffuse scatter close to the critical angle, as shown in the inset to Figure 5-28. The scattered intensity at this location is extremely sensitive to the air-sample surface, and relatively insensitive to the buried interfaces. These changes may be attributed to surface damage or oxidation due to exposure to a high intensity beam. The Born analysis obtained from the ratio of the integrated specular intensity to the integrated diffuse intensity shows negligible change in the topological roughness (shown in Table 5-7).

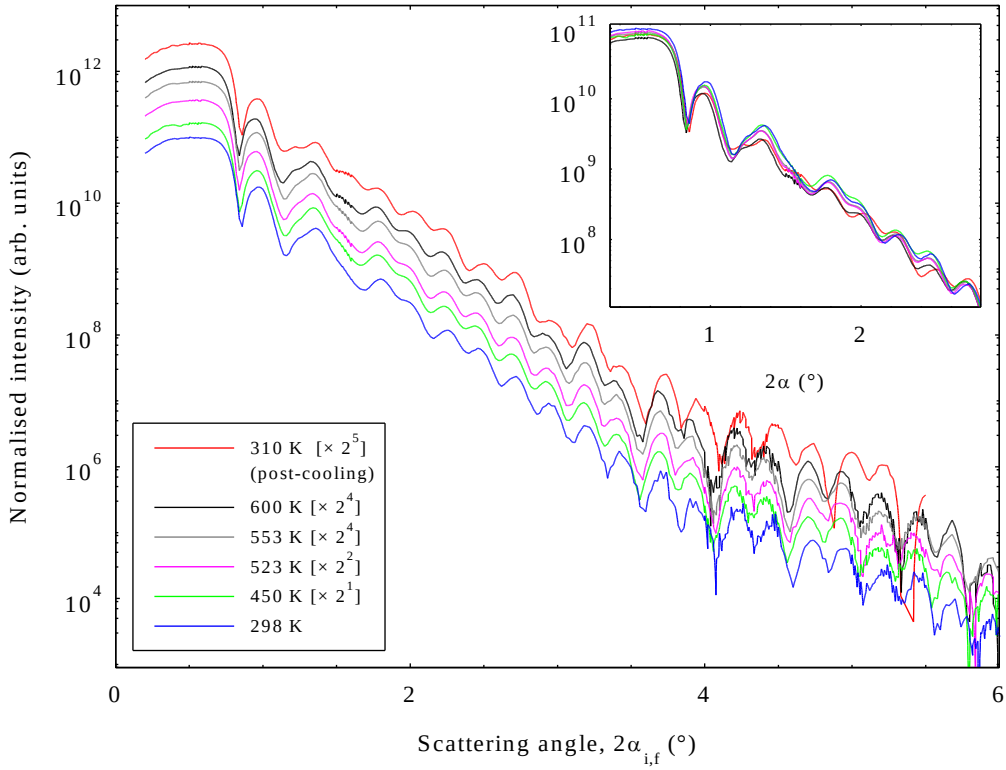

Figure 5-27. True specular reflectivity from sample of the form MgO (001) / MgO (5 nm) / Fe (3 nm) / Au (3 nm) / MgO (3 nm) / Fe (10 nm). Successive scans are offset by powers of two for clarity. Inset: close-up of the low-angle region with curves overlaid for comparison.

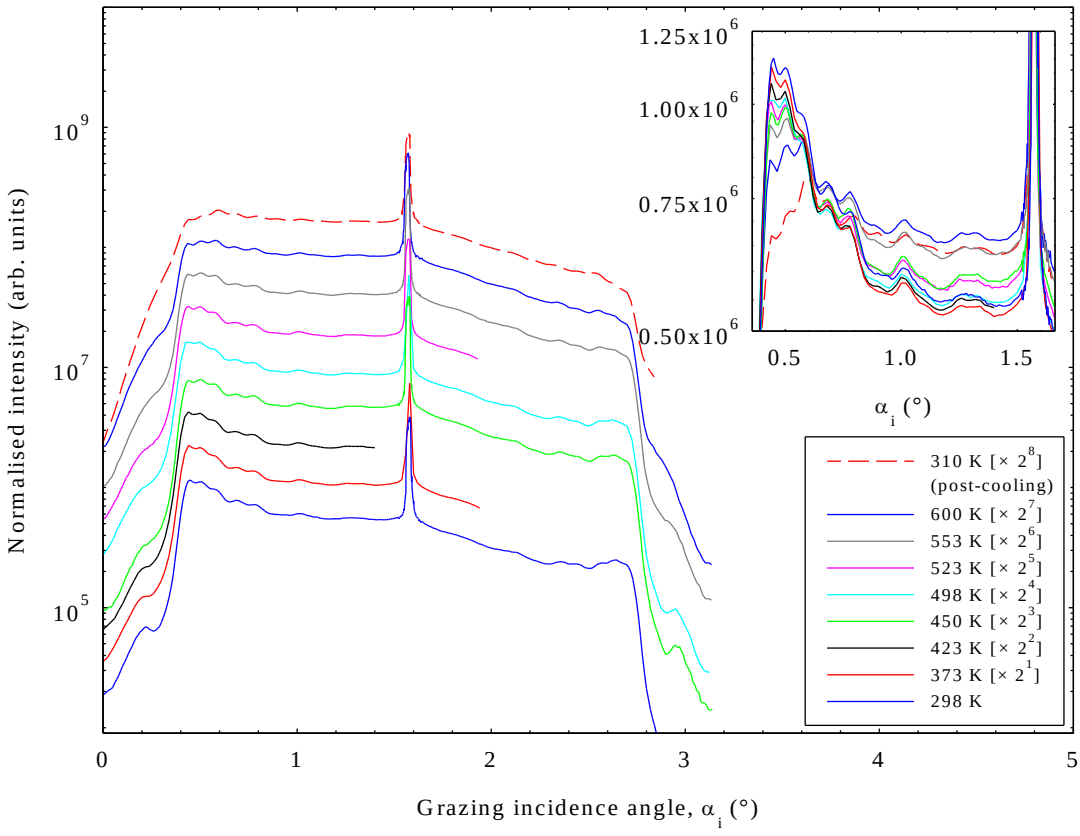

Figure 5-28. Transverse diffuse reflectivity from Fe/Au/MgO/Fe sample with a detector angle of 3.14°. Scans at higher temperatures offset by powers of two for clarity. Inset: close-up of the low angle Yoneda wing with scans overlaid for comparison.

Table 5-7. Topological roughness as deduced from the ratio of the specular to integrated diffuse intensities at a detector angle of 3.14°, where q_z is constant at 2.22 nm^{-1}.

Temperature (K)	**BORN ANALYSIS OF TRANSVERSE SCAN**	
	$\frac{I_{diffuse}}{I_{specular}}$ **(no units, to 2 sig. figs.)**	**Deduced topological roughness, $\sigma_{topological}$ (nm, to 2 sig. figs.)**
298	11	0.71
450	9.1	0.68
498	9.7	0.69
600	11	0.71
310	11	0.71

5.5.2. Transmission electron microscopy cross-sections of Fe/Au/MgO/Fe

A nominally identical sample to that used in the x-ray study was examined using high-resolution transmission electron microscopy by Dr D. McGrouther at the University of Glasgow. Figure 5-29 shows a cross-section TEM through the entire structure.

In this image the high topological roughness of the substrate-buffer interface is clearer than in the previous Fe/MgO/Fe sample. The upper surface of the buffer layer also undulates, but (within the limited field of view) appears to have lower amplitude roughness than the substrate. The gold appears to fill in the troughs in the thick iron layer, creating a smoother surface prior to the barrier deposition. This means that the gold thickness ranges from zero to approximately six nanometres.

A higher magnification view of the tunnel junction is given in Figure 5-30. From this, the barrier thickness can be measured as 2 – 3 nm, and the image displays an improved degree of epitaxy than the Fe/MgO/Fe sample. This may be linked to the smoother surface of the gold upon which it is grown.

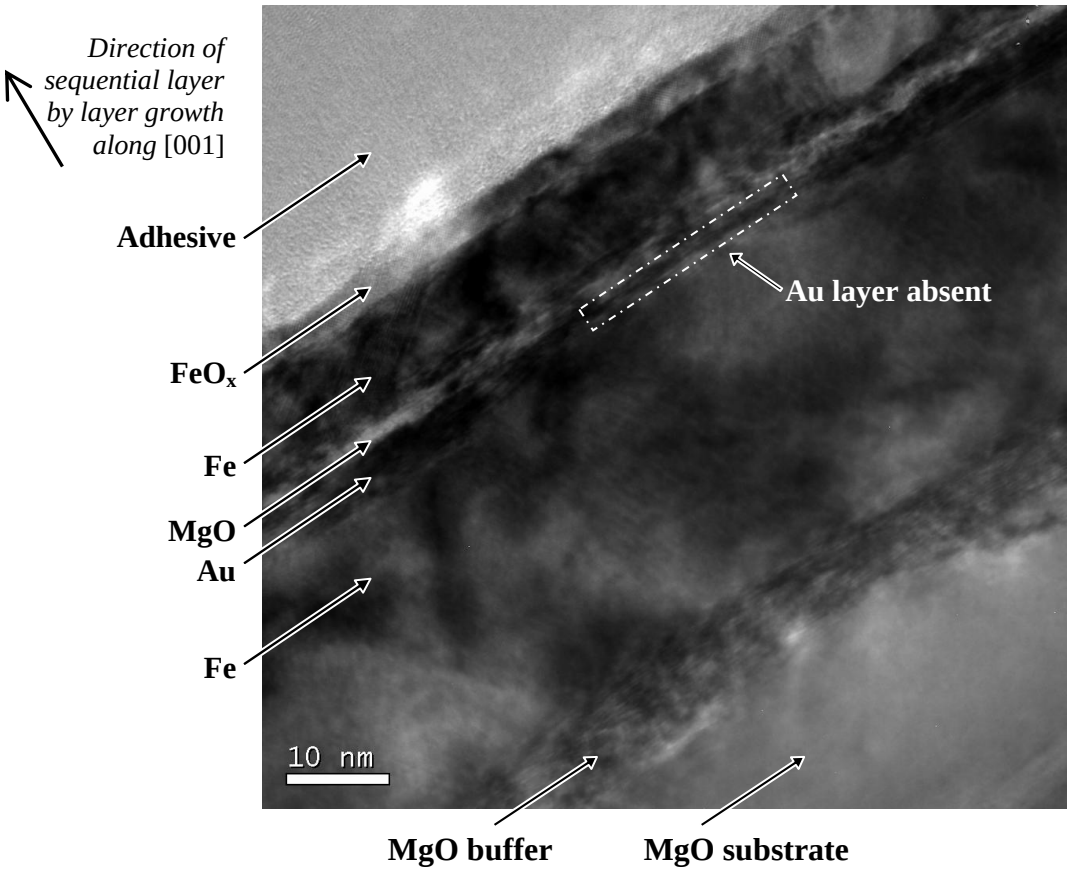

Figure 5-29. TEM cross-section of an Fe/Au/MgO/Fe structure on an MgO (001) substrate prepared with a MgO buffer layer. Image by D. McGrouther, University of Glasgow [140].

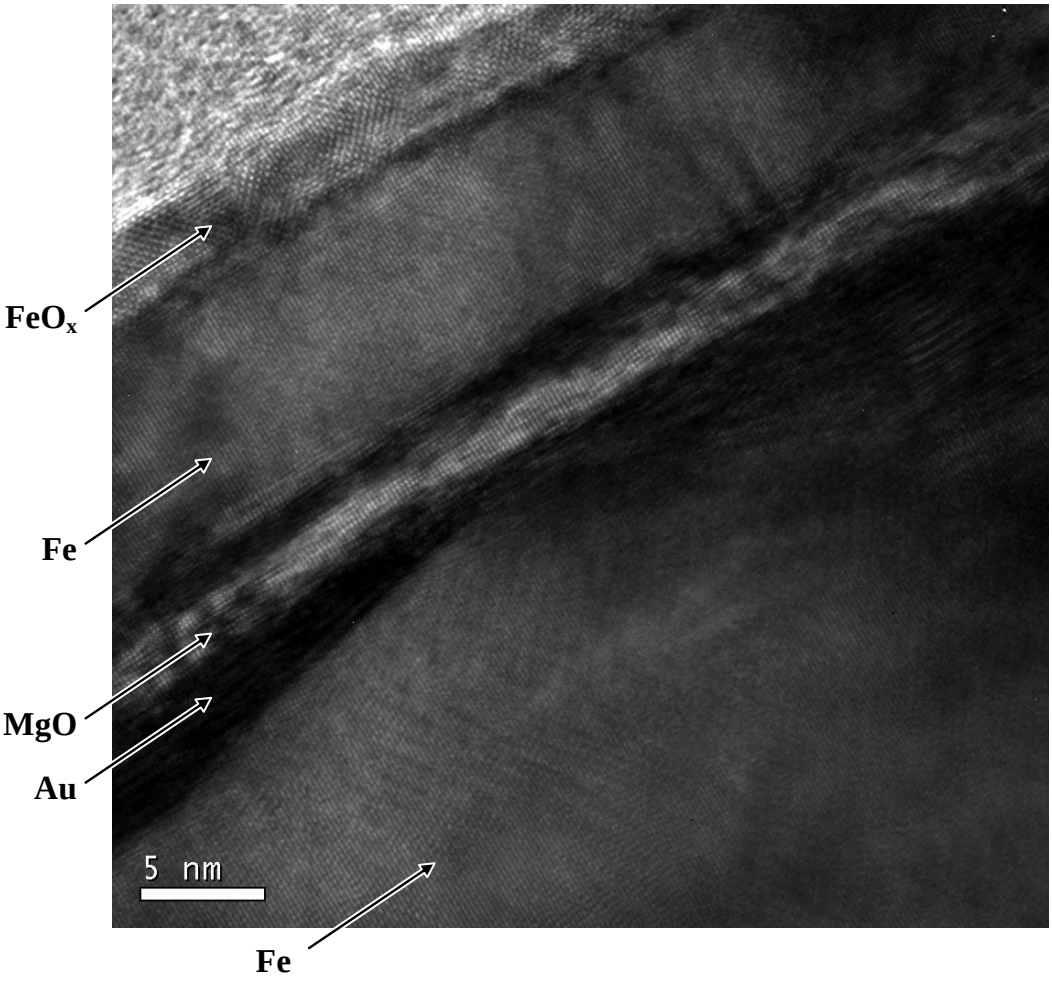

Figure 5-30. TEM section of the Fe/Au/MgO/Fe region. Image by D. McGrouther, University of Glasgow [140].

In summary, the TEM images of the Fe/Au/MgO/Fe stack shows a marginally improved degree of epitaxy in comparison with the Fe/MgO/Fe sample, but possess a large amount of topological undulation which extends from the MgO buffer to the gold electrode. This peak-to-peak roughness value propagating through the upper Au/MgO/Fe layers is approximately 2 nm by inspection of Figure 5-29, which is in reasonable agreement with the Born analysis value obtained for 2σ obtained from the diffuse scatter.

5.5.3. High-angle diffraction from the out-of-plane lattice

The measurements of the out-of-plane lattice parameters of the MgO substrate and iron layers can be determined from the high-angle diffraction measurement in Figure 5-31. The data set is similar to that for the Fe/MgO/Fe structure; the peak positions are extremely consistent. The iron/gold bilayer is relaxed to the bulk value, whereas the MgO substrate appears to have a small strain away from the bulk value, as was seen with the corresponding measurement for the Fe/MgO/Fe sample.

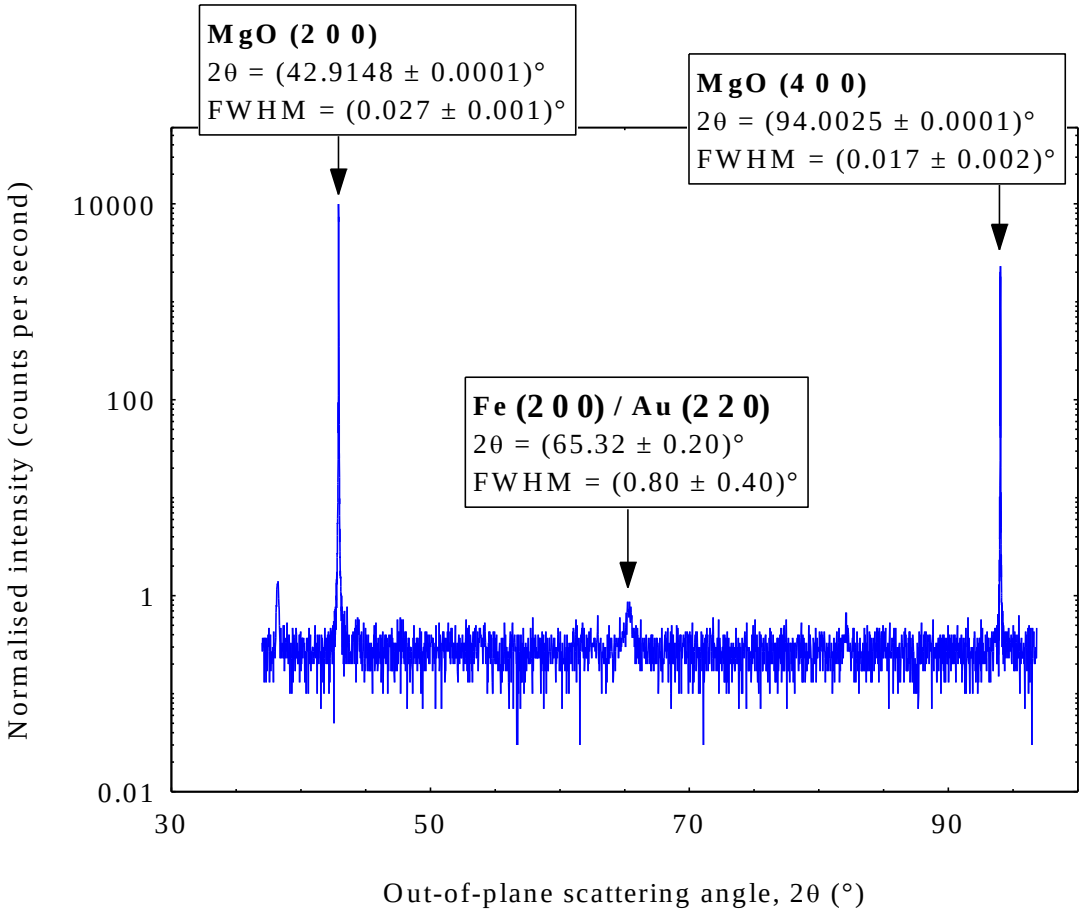

Figure 5-31. Out-of-plane (high-angle) coupled axis diffraction scan. Measured with an integrated count time of 30 seconds per point.

Table 5-8. Out-of-plane lattice parameters determined from high-angle diffraction measurement of Bragg peak positions, compared to reference values for the bulk [136]. Uncertainty on average MgO determined by standard deviation of the two independent measurements.

	LATTICE PARAMETER (nm)	
	Measured	**Reference for bulk**
Fe	0.287 ± 0.002	0.28664
Au	0.406 ± 0.003	0.40782
MgO deduced from (200)	0.423649 ± 0.000002	0.42117
MgO deduced from (400)	0.423794 ± 0.000002	
MgO average of (200) and (400)	0.4237 ± 0.0001	

5.5.4. Grazing incidence diffraction from Fe/Au/MgO/Fe

A key experimental consideration is that the gold has a much higher critical angle than iron or MgO (as shown in Table 5-2), which should have a waveguide-like effect, preventing penetration of the x-ray beam into the lower iron layer. Despite this, the peak amplitude of the in-plane diffraction peak still occurs at 0.44°, which suggests that in all the grazing incidence in-plane diffraction measurements the iron peak originates most strongly from the uppermost iron layer.

Scans corresponding to the in-plane diffraction peaks at different grazing angles are shown in Figure 5-32. With this sample, complete in-plane diffraction peaks were measured systematically at three different grazing incidence angles (α = 0.1°, 0.22° and 0.44°) in order to enhance sensitivity to the different layers in the structure.

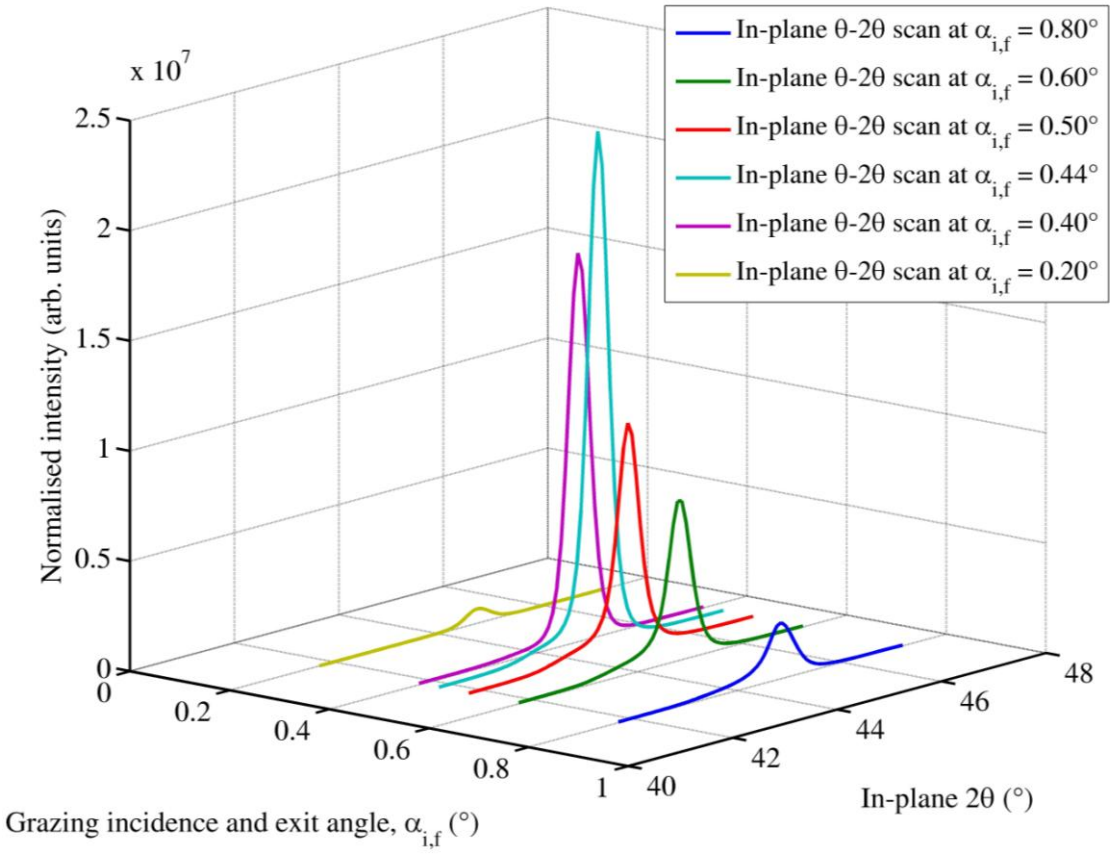

Figure 5-32. Coupled in-plane scans through the Fe (110) / Au (200) and MgO (200) peaks for varying grazing incidence angles. Taken at T = 293 K prior to annealing.

5.5.5. Grazing incidence diffraction at α = 0.44°

Scans at a grazing angle of 0.44° (in Figure 5-33) are made in the same geometry as those on the Fe/MgO/Fe system. Here, the iron and gold peaks are indistinguishable due to their near perfect natural lattice matching.

A similar overall trend is seen as previously: the MgO peak becomes sharper and shifts to lower angle. In comparison with Figure 5-17 however, the Fe/Au peak is much more dominant than the MgO peak because gold (atomic number 79) scatters much more strongly than iron (atomic number 26) due to an electron density.

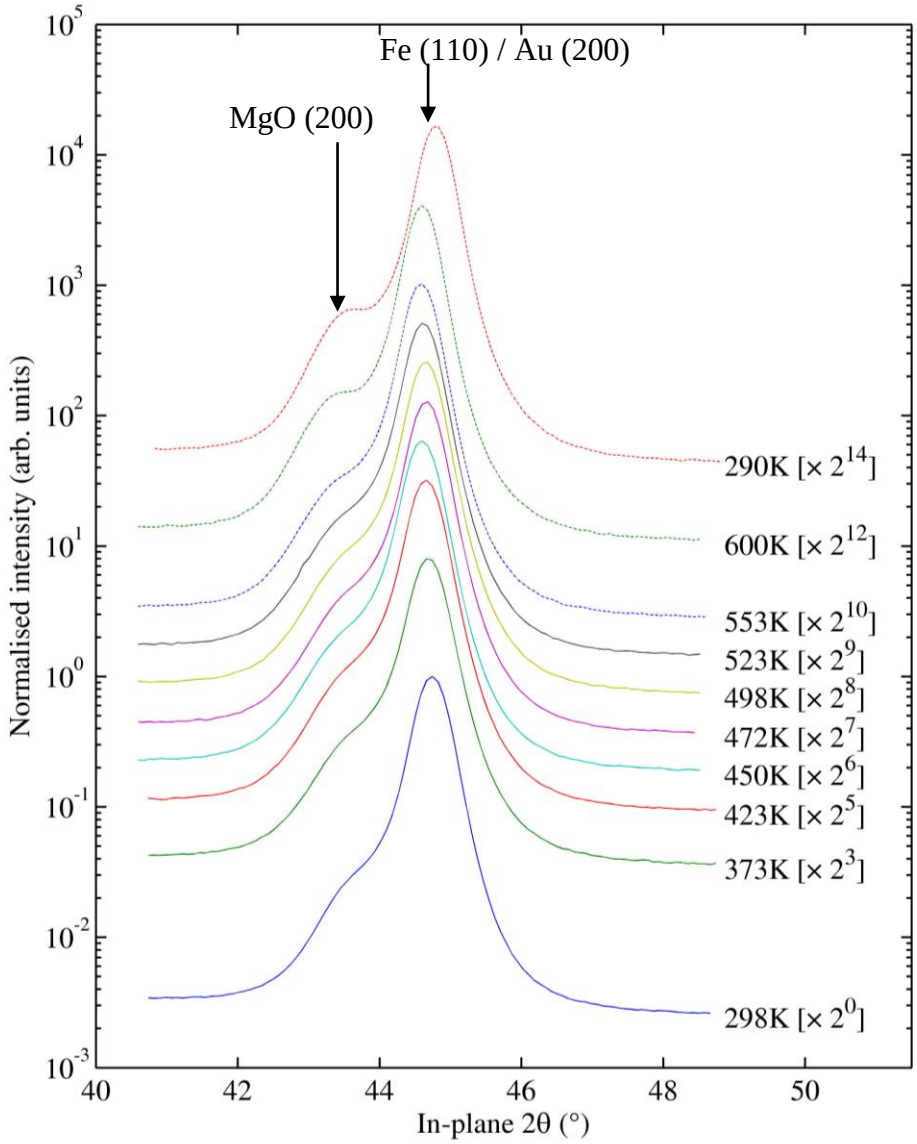

Figure 5-33. Evolution of the magnesium oxide peak during sample anneal to 600 K and cooling to 290K, seen at a grazing incidence and exit angle of 0.44°. Sample structure: MgO / MgO (5 nm) / Fe (30 nm) / Au (3nm) / MgO (3 nm) / Fe (10 nm). Measurements are offset by powers of two for clarity, with higher curves corresponding to later measurements. The uppermost curve at 290 K is after cooling of the sample to room temperature.

The in-plane peak positions are fitted and analysed in Figure 5-34 and Figure 5-35, showing a similar trend to that for the Fe/MgO/Fe structure. It can be seen in Table 5-9 that there is a significant relaxation of the MgO as the sample is annealed to 600K. The MgO is initially strained by 2.4% from its bulk value towards the gold lattice, but relaxes to a strain of 1.0% after anneal and cooling.

The deduced lattice parameters quantify the degree of relaxation that the magnesium oxide is observed to undergo during annealing. The values for iron and gold are both deduced from a single diffraction peak, and differ by a factor of $\sqrt{2}$ due to the relative orientation of their unit cells. The iron and gold measurements are identical to standard reference values for the bulk and are not significantly changed by annealing.

The gradients of the linear expansion/contraction of the interplanar spacing provide values for the linear thermal expansivity, given in Table 5-10. The determined values are marginally lower than reference bulk values.

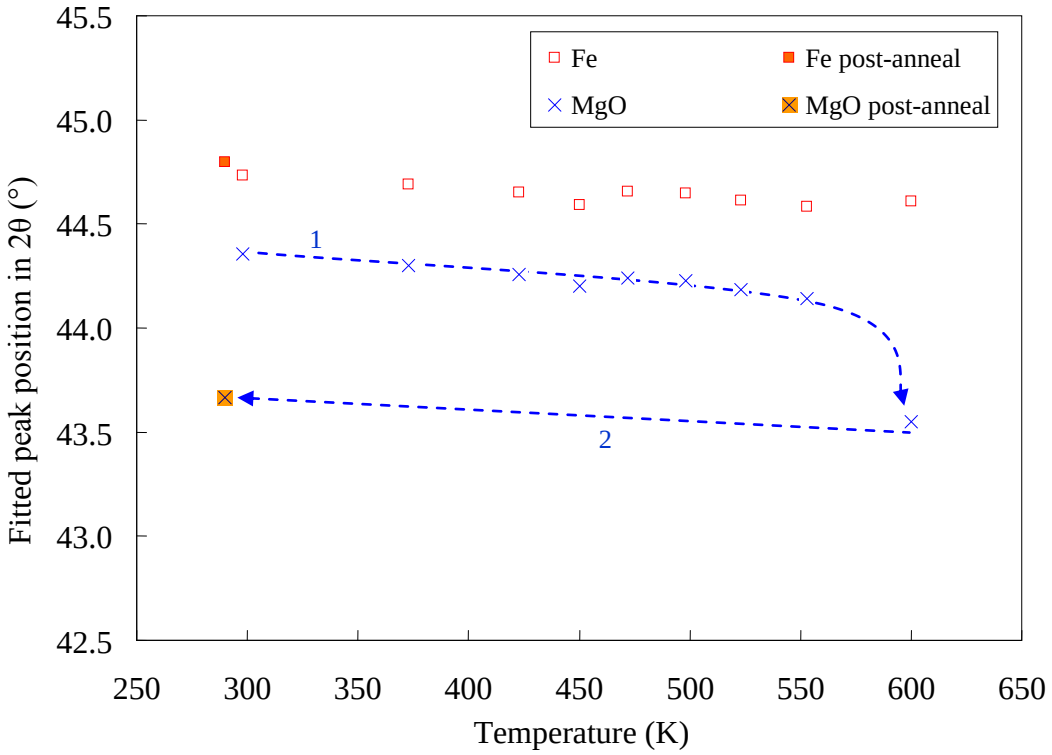

Figure 5-34. Centre of fitted peak position for Fe-Au and MgO. Sample structure: MgO / MgO (5 nm) / Fe (30 nm) / Au (3nm) / MgO (3 nm) / Fe (10 nm) , seen at a grazing incidence and exit angle of 0.44°. Blue arrows show the sequence of annealing and cooling, and act as a guide to the eye. Error bars are less than 0.05° in 2θ, and less than 0.5 K in temperature, both contained within the data markers shown.

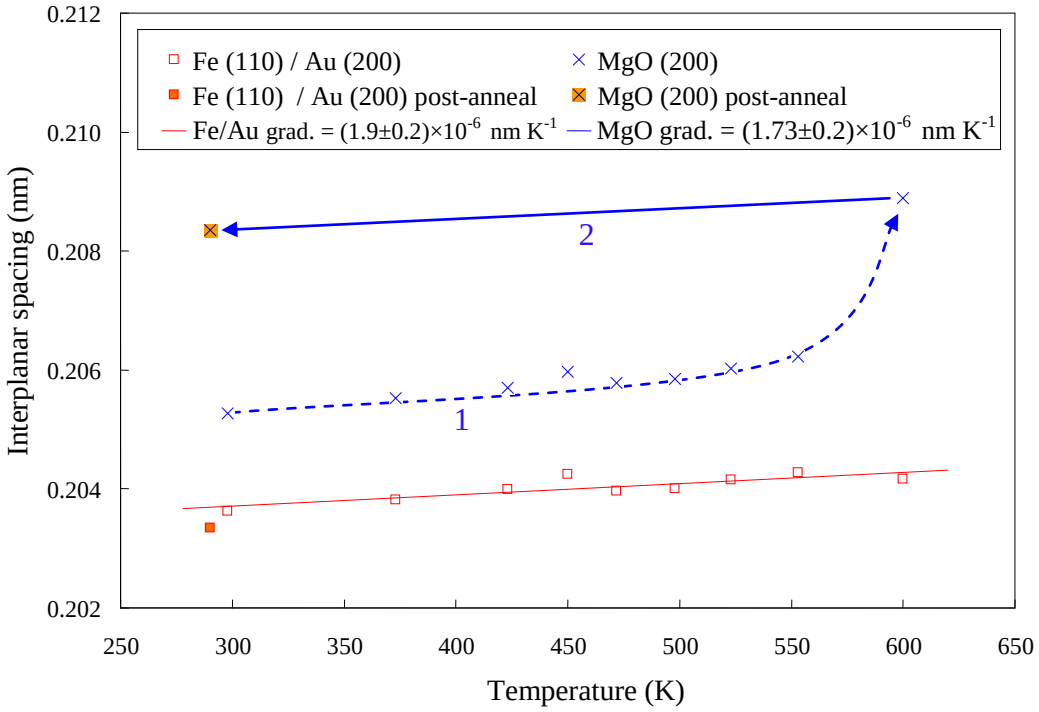

Figure 5-35. Fitted interplanar spacing as a function of temperature (1) during anneal and (2) after cooling. Sample structure: MgO / MgO (5 nm) / Fe (30 nm) / Au (3nm) / MgO (3 nm) / Fe (10 nm), seen at a grazing incidence and exit angle of 0.44°. Blue arrows show the sequence of annealing (1) and cooling (2), and the dashed line is a guide to the eye. Error bars are less than 0.00025 nm in interplanar spacing, and less than 0.5 K in temperature, both contained within the data markers shown.

Table 5-9. A comparison of the measured in-plane lattice parameters of an iron/gold bilayer and magnesium oxide layer to reference values [136]. Sample structure: MgO / MgO (5 nm) / Fe (30 nm) / Au (3nm) / MgO (3 nm) / Fe (10 nm) at a grazing angle of incidence and exit of 0.44°.

	LATTICE PARAMETER OF IRON, GOLD AND MAGNESIUM OXIDE		
	Pre-anneal measurement at 298 K (nm)	**Post-anneal measurement at 290 K (nm)**	**Reference value for bulk at 293 K (nm)**
Fe	0.288 ± 0.001	0.288 ± 0.001	0.28664
Au	0.407 ± 0.001	0.407 ± 0.001	0.40782
MgO	0.411 ± 0.001	0.417 ± 0.001	0.42117

Table 5-10. A comparison of the measured in-plane thermal expansion coefficient of an iron/gold bilayer average over the range 300 – 600 K to reference values for bulk iron and gold [120]. Sample structure: MgO / MgO (5 nm) / Fe (30 nm) / Au (3nm) / MgO (3 nm) / Fe (10 nm) at a grazing angle of incidence and exit of 0.44°.

	THERMAL EXPANSION COEFFICIENTS		
	Determined value $\bar{\alpha}$ **[× 10^{-6} K^{-1}]**	**Reference value for bulk** $\alpha(T=298\ K)$ **[× 10^{-6} K^{-1}]**	**Reference value for bulk** $\alpha(T=500\ K)$ **[× 10^{-6} K^{-1}]**
Fe	9.0 ± 1.0	11.8	13.9
Au		14.2	15.4
MgO	8.1 ± 1.0	10.8	Unavailable

The fitted full widths at half-maximum are plotted in Figure 5-36. The fitted full width at half maximum of the MgO decreases from a value at 450 K prior to annealing of (1.698 ± 0.001)° to (1.087 ± 0.002)° after annealing. The iron peak width remains constant across the range of annealing temperatures at 0.44° with a standard deviation of 0.02°.

The fact that the iron/gold peak is narrower than the barrier MgO peak reflects the increased thicknesses of the iron layer (10 nm compared to 3nm for the MgO), and hence the increased coherent scattering volume. It may also indicate that the iron layer has uniform strain, whereas the MgO initially contains localised in-plane micro-strains. With only a single diffraction peak, it is not possible to distinguish the scattering volume and micro-strain contributions to peak broadening by a Williamson-Hall analysis. The micro-strain hypothesis is supported by measurements made during annealing, where the MgO peak width narrows with no indication from the x-ray reflectivity (section 5.5.1) that the layer thickness changes. This suggests that in-plane micro-strain is relieved upon annealing, as well as the long-range overall strain.

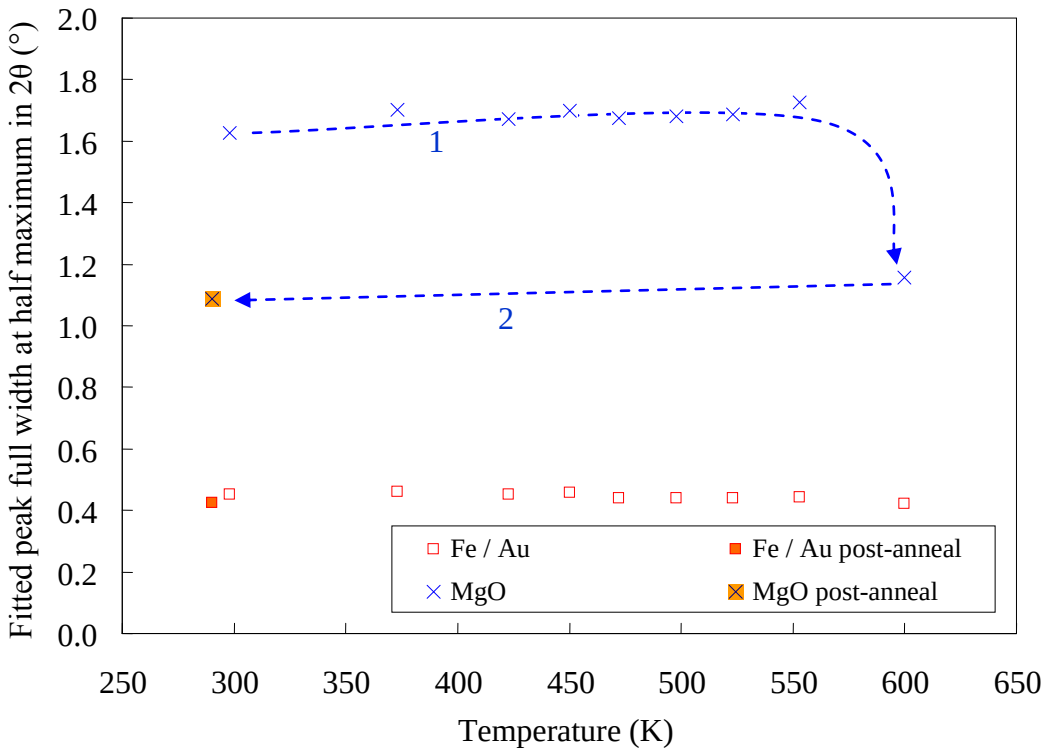

Figure 5-36. Full-width at half maximum of the fitted peaks in θ-2θ.Error bars are within data points.

5.5.6. *Grazing incidence diffraction at α < 0.44*

Similar measurements were made at shallower grazing angles as a test of the depth sensitivity of the technique. Figure 5-37 shows the evolution of the peaks at α = 0.22° and α = 0.1°.

As previously, the peak shapes can be fitted and converted into interplanar spacings, in Figure 5-38 and Table 5-11 for α = 0.22° and Figure 5-39 and Table 5-12 for α = 0.1°. The magnesium oxide lattice parameter follows the same general relaxation of strain as seen at α = 0.44°.

The results are identical for all grazing angles within experimental uncertainty, although the uncertainty on fitting of the MgO peak position prior to anneal for α = 0.1° is notably higher due to the noisiness of the data. The gradient of the linear shift in interplanar spacing provides a measure of the linear thermal expansivity which is closer to standard bulk values than those for the higher grazing angle, as shown in Table 5-13 and Table 5-14.

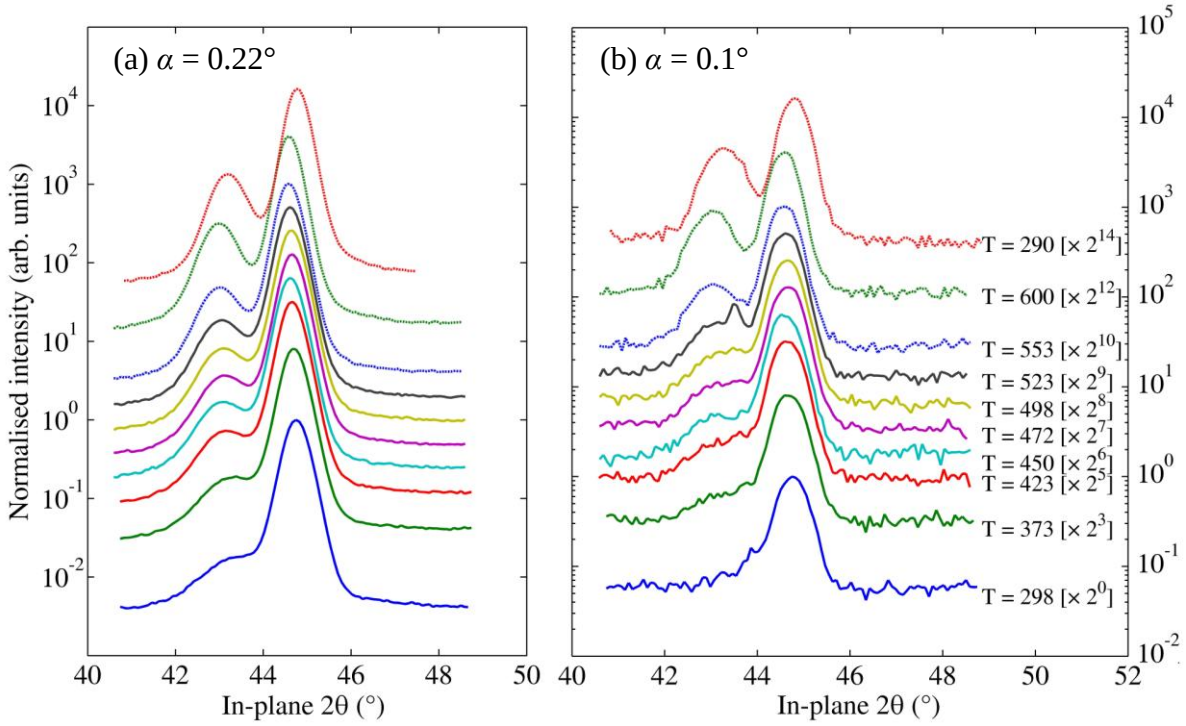

Figure 5-37. Grazing incidence diffraction scans taken at α = 0.22° (a, left) and 0.1° (b, right). Sample structure: MgO / MgO (5 nm) / Fe (30 nm) / Au (3nm) / MgO (3 nm) / Fe (10 nm). Measurements are offset by powers of two for clarity, with higher curves corresponding to later measurements. The uppermost curve at 290 K is after cooling of the sample to room temperature.

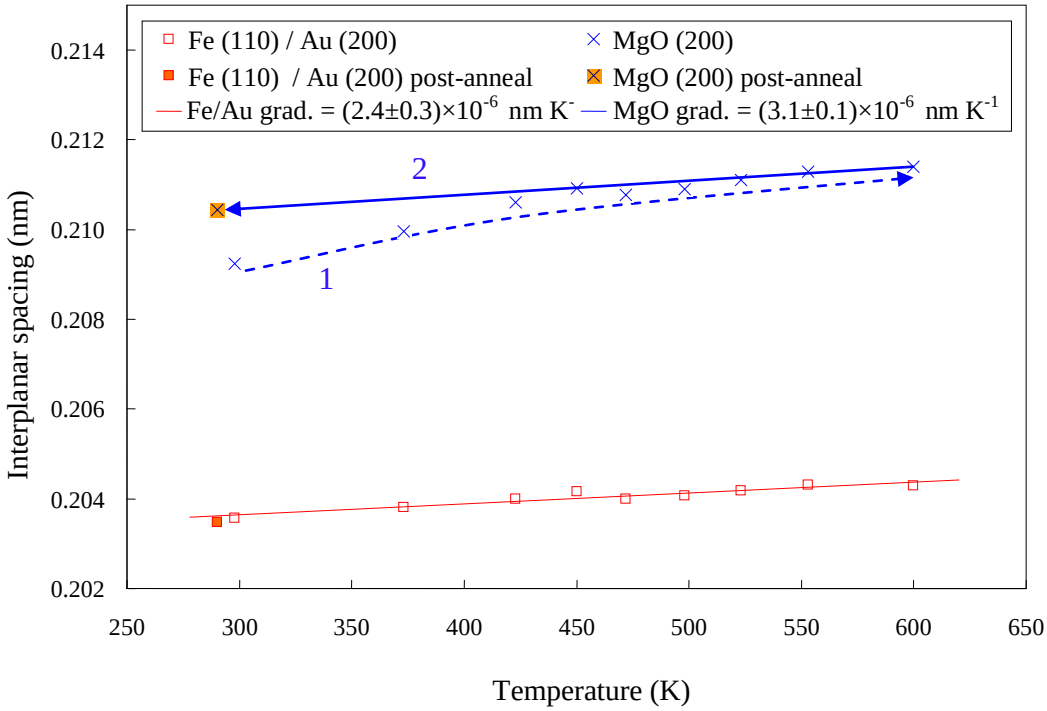

Figure 5-38. Fitted interplanar spacing as a function of temperature, seen at α = 0.22°. Sample structure: MgO / MgO (5 nm) / Fe (30 nm) / Au (3nm) / MgO (3 nm) / Fe (10 nm). Blue arrows show the sequence of annealing (1) and cooling (2), and the dashed line is a guide to the eye. Error bars are less than 0.00025 nm in interplanar spacing, and less than 0.5 K in temperature, both contained within the data markers shown.

Table 5-11. A comparison of the measured in-plane lattice parameters seen at α = 0.22° of an iron/gold bilayer and magnesium oxide layer to reference values [136]. Sample structure: MgO / MgO (5 nm) / Fe (30 nm) / Au (3nm) / MgO (3 nm) / Fe (10 nm).

	LATTICE PARAMETER OF IRON, GOLD AND MAGNESIUM OXIDE		
	Pre-anneal measurement at 298 K (nm)	**Post-anneal measurement at 290 K (nm)**	**Reference value for bulk at 293 K (nm)**
Fe	0.288 ± 0.001	0.287 ± 0.001	0.28664
Au	0.407 ± 0.001	0.407 ± 0.001	0.40782
MgO	0.413 ± 0.001	0.420 ± 0.001	0.42117

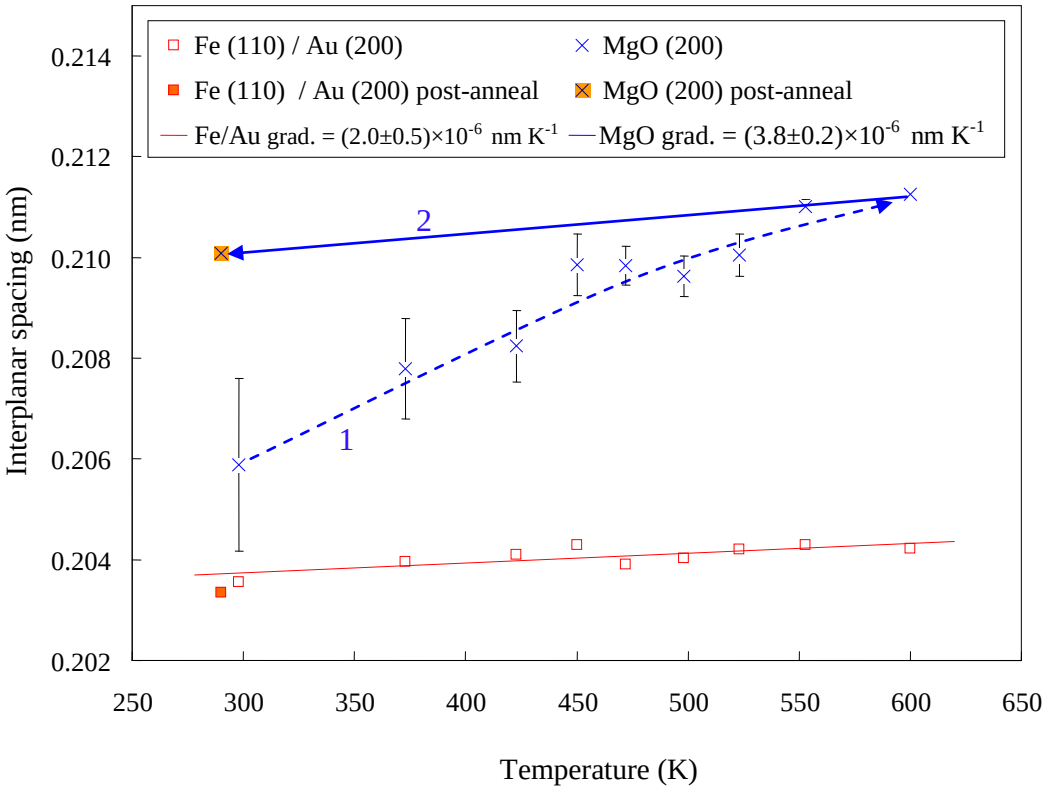

Figure 5-39. Fitted interplanar spacing as a function of temperature, seen at a grazing incidence and exit angle of 0.1°. Sample structure: MgO / MgO (5 nm) / Fe (30 nm) / Au (3nm) / MgO (3 nm) / Fe (10 nm). Blue arrows show the sequence of annealing (1) and cooling (2), and the dashed line is a guide to the eye. Error bars are less than 0.00025 nm in interplanar spacing for Fe and contained within the data markers shown.

Table 5-12. A comparison of the measured in-plane lattice parameters seen at α = 0.1° of an iron/gold bilayer and magnesium oxide layer to reference values [136].

	LATTICE PARAMETER OF IRON, GOLD AND MAGNESIUM OXIDE		
	Pre-anneal measurement at 298 K (nm)	**Post-anneal measurement at 290 K (nm)**	**Reference value for bulk at 293 K (nm)**
Fe	0.288 ± 0.001	0.288 ± 0.001	0.28664
Au	0.407 ± 0.001	0.407 ± 0.001	0.40782
MgO	0.41 ± 0.01	0.420 ± 0.001	0.42117

Table 5-13. A comparison of the measured in-plane thermal expansion coefficient of an iron/gold bilayer average over the range 300 – 600 K to reference values for bulk iron and gold [120] obtained at a grazing angle of 0.22°.

	THERMAL EXPANSION COEFFICIENTS		
	Determined value $\bar{\alpha}$ **[× 10^{-6} K^{-1}]**	**Reference value for bulk** $\alpha(T=298\ K)$ **[× 10^{-6} K^{-1}]**	**Reference value for bulk** $\alpha(T=500\ K)$ **[× 10^{-6} K^{-1}]**
Fe	11.4 ± 1.4	11.8	13.9
Au		14.2	15.4
MgO	15	10.8	Unavailable

Table 5-14. A comparison of the measured in-plane thermal expansion coefficient of an iron/gold bilayer average over the range 300 – 600 K to reference values for bulk iron and gold [120]. Obtained at a grazing angle of 0.1°.

	THERMAL EXPANSION COEFFICIENTS		
	Determined value $\bar{\alpha}$ **[× 10^{-6} K^{-1}]**	**Reference value for bulk** $\alpha(T=298\ K)$ **[× 10^{-6} K^{-1}]**	**Reference value for bulk** $\alpha(T=500\ K)$ **[× 10^{-6} K^{-1}]**
Fe	10.0 ± 2.5	11.8	13.9
Au		14.2	15.4
MgO	18 ± 1.4	10.8	Unavailable

5.5.7. Arrhenius interpretation of the lattice relaxation in Fe/Au/MgO/Fe

As for the Fe/MgO/Fe sample, an Arrhenius analysis (shown in Figure 5-40) can yield an approximate value for the activation energy of the relaxation process.

In this case, the value obtained is E_a = (0.9 ± 0.2) eV. The steeper gradient reflects the later onset of the relaxation process apparent in Figure 5-35. The initial level of strain in this sample is not significantly different from that in the previous sample, so the increased value found for the activation energy may reflect stronger chemical bonding of the barrier MgO to the gold surface.

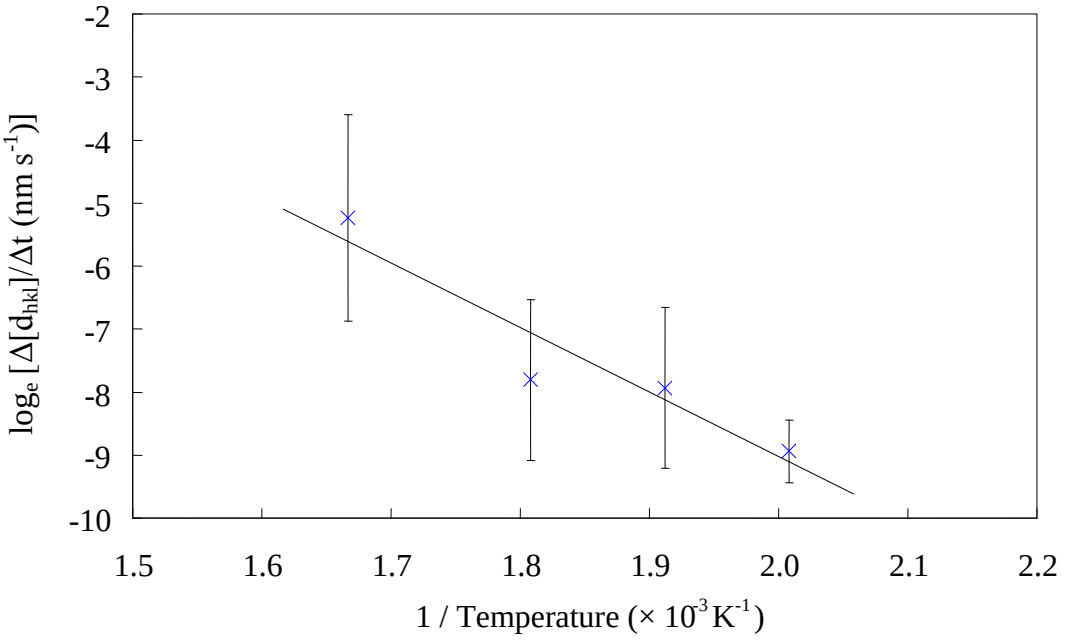

Figure 5-40. Arrhenius plot of the rate of change in MgO interplanar spacing within an Fe/Au/MgO/Fe structure measured at α = 0.44° as a function of temperature between 498 K and 600 K. The line of best fit was fitted by least squares, with a gradient of (-10000 ± 2400) = - E_a / k_B.

5.6. Chapter conclusion

In this chapter, measurements on the in- and out-of-plane lattice structure of Fe/MgO/Fe and Fe/Au/MgO/Fe MBE-deposited epitaxial thin films have been presented.

In both the pre-annealed and post-annealed states at 298 K, both systems have been shown to be highly epitaxial, though without perfect lattice registry between layers. There is an unusually high topological roughness at layer interfaces, and a large variation in layer thickness when compared to other experimental studies [e.g. refs. 128, 132]. The grazing incidence diffraction measurements have been sensitive to the in-plane structure of the two iron electrodes and the MgO tunnel barrier.

The growth process for an Fe/MgO/Fe structure can be deduced as follows. The lower iron layer grows epitaxially on the MgO substrate but relaxes to a value typical for bulk iron measured as 0.288 ± 0.001 nm in-plane (seen from grazing-incidence diffraction measurements) with a consistent value seen out-of-plane after annealing. The barrier MgO layer then grows epitaxially on the iron layer with the [100] direction rotated at 45° to the iron [100] (seen from azimuthal-only scans), but with a lattice parameter intermediate between the iron surface sites and what would be expected for bulk MgO. Prior to anneal, the MgO is strained by 1.94%. Diffuse x-ray scattering and TEM show that the deposition of MgO (both as buffer and barrier layers) is far from the thermodynamic equilibrium necessary for ultrasmooth epitaxial films. The second iron layer grows epitaxially on the MgO barrier, but relaxes fully to a bulk lattice parameter during growth.

During the post-deposition anneal to 600 K, the MgO relaxes towards a bulk value, but retains a residual strain of 0.28%. Both MgO and iron are seen to expand thermally; the thermal expansion coefficient of the iron layers is $(14.0 \pm 2.5) \times 10^{-6}\ K^{-1}$, in close agreement with standard reference values for bulk iron. The strain dispersion of the iron is measured as (0.0112 ± 0.0003) in-plane (invariant during annealing and cooling) and (0.010 ±0.005) out-of-plane after post-anneal. In addition to the strain reduction during anneal in the MgO, the strain dispersion also decreases markedly from an initial figure of (0.0371 ± 0.0004) to (0.0205 ± 0.0001).

X-ray reflectivity measurements suggest that the layer thicknesses and interface widths do not change during annealing, meaning that the relaxation occurs purely in the plane, with no increase of terracing or other rippling of the interface. The nucleation of misfit dislocations at the interfaces which then extend throughout the MgO layer is proposed as a mechanism consistent with all the above observations. A dislocation activation energy of (0.3 ± 0.1) eV is obtained from an Arrhenius law analysis of the rate of relaxation. The relaxation process is outlined in Figure 5-41.

It should be noted that the out-of-plane lattice parameter of the barrier MgO has not successfully been measured due to the small coherent scattering volume caused by this geometry.

(a) Perfect lattice matching (ideal epitaxy)

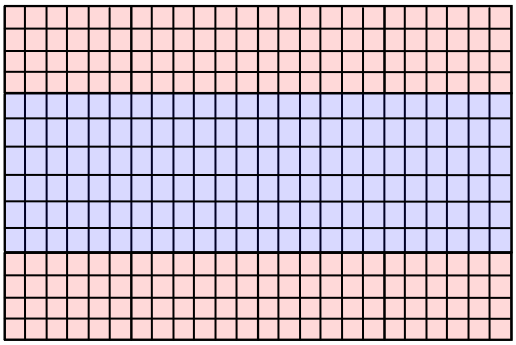

Fe: bulk lattice

MgO: fully strained to Fe

Fe: bulk lattice

(b) Partial relaxation of MgO

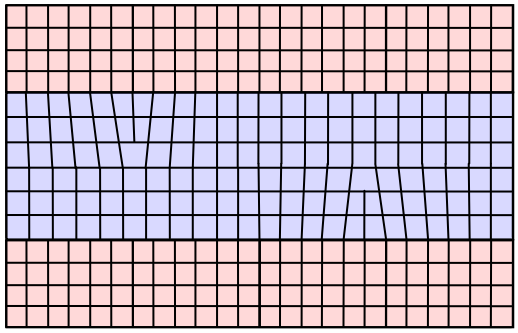

Fe: bulk lattice

MgO: partially relaxed: high strain dispersion. Some dislocation at interfaces.

Fe: bulk lattice

(c) High relaxation of MgO, close to bulk lattice parameters

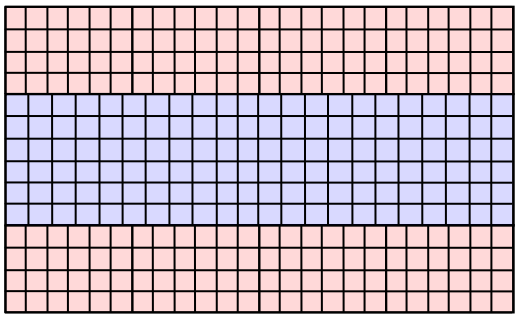

Fe: bulk lattice

MgO: highly relaxed, low strain dispersion

Fe: bulk lattice

Figure 5-41. Schematic diagram of lattice planes explaining the changes in strain and strain dispersion seen before and after annealing as viewed in cross-section, (a) represents a hypothetical single crystal structure with perfect registry throughout the layers, (b) the partial relaxation of the MgO barrier measured after deposition, before annealing, (c) the fuller relief of strain and strain dispersion after anneal to 600 K.

In the measurement of a structure of the form MgO (001) / Au (3 nm) / Fe (30 nm) / MgO (3 nm) / Fe (10 nm) very similar results were obtained, and an accordant analysis holds. The incorporation of a 3 nm gold layer creates no new in-plane or out-of-plane diffraction peaks. From this it is interpreted that the gold in-plane lattice planes sit commensurately with the underlying iron lattice planes. The dislocation-relaxation process in the MgO barrier is found to have an activation energy of (0.9 ± 0.2) eV.

The small lattice parameter limits the number of accessible diffraction peaks in symmetric diffraction from a single crystal sample, meaning that generally only single peaks for each material could be measured. A more consistent peak width analysis may be obtainable by exploring asymmetric reflections to generate multiple peaks, but the analysis of such measurements would be nontrivial since the depth sensitivity may vary.

On longer length scales, a more fundamental issue is the smoothness and epitaxial quality of these samples in comparison to previously studied systems. The substrate surface is shown by TEM to be rough, and the deposition of the buffer and barrier MgO has clearly not enhanced the layer smoothness. This contrasts starkly with the work of Yuasa *et al* [52, 128] on Fe/MgO/Fe tunnel junctions, and the work of Dekadjevi *et al* [132] and Cole *et al* [133] on Fe/Au systems on MgO (001) substrates. Given the roughness amplitudes found here of approximately 0.7 nm (from diffuse x-ray scattering) and similar measurements from TEM, it is unsurprising that samples grown in the same set as those presented here do not exhibit tunnelling magnetoresistance. Pinholes in such a variable tunnel barrier material are likely to short-circuit any electron tunnelling. Even if pinholes were absent, it is known that TMR falls significantly as the RMS roughness rises [143].

In overview of this chapter, the epitaxial growth of Fe/MgO/Fe and Fe/Au/MgO/Fe on MgO (001) by MBE epitaxy has been confirmed, and the post-deposition relief of strain has been clarified. The thermal expansion of all three materials in thin film form is similar to that of the bulk material, and after annealing the lattice parameter is also close to values expected for the bulk. The relief of strain in these structures and the subsequent removal of defects within the barrier layer may be of importance to the reproducibility of high room temperature TMR in these systems, although the effect of strain on the electronic tunnelling wavevectors and TMR therefore is complex to predict theoretically. Although the development of Fe/Au/MgO/Au/Fe structures remains limited by the growth kinetics of gold onto MgO, this work provides an important insight into the MBE deposition of the component materials.

6. Grazing incidence x-ray scattering from periodic nanostructures

In this final experimental chapter the coherent interference of x-rays scattered at grazing incidence from periodic surface nanostructures is examined, both experimentally and using a semi-kinematical numerical simulation. A series of case studies corresponding to different forms of nanoscale patterning are presented in which key structural parameters such as periodicity, element shape, ordering coherence length and dispersion are quantified through a comparison of observations with theory. The validity of the assumptions made during the formulation of the simulation algorithm give an understanding of the scattering processes occurring when periodic nanostructures are illuminated at grazing incidence.

6.1. Introduction

X-ray metrology has many diverse applications in the characterization of continuous thin films, and can resolve structural features below the thickness of a single plane of atoms [72]. The theory presented in chapter 3 combines the principles of Fresnel reflectivity from perfectly smooth interfaces with nonspecular scattering models for random rough interfaces. Both these descriptions have analogies in visible light scattering, and indeed can be considered as an extreme case of Fourier optics; the fundamental difference is the wavelength of the radiation being scattered. X-rays have two key advantages over visible light for the study of thin films:

(i) since their refractive index is less than unity, the penetration depth of the x-rays at grazing incidence can be varied from just a few nanometres at zero incidence angle to several microns at normal incidence, and

(ii) the wavelength of x-rays allows structures separated only by nanometres to be resolved as independent scatterers.

The first condition allows surface, near-surface and bulk-sensitive measurements to be made. The second condition permits the interference of scattering from crystal lattices, thin films and nanoscale patterning to be observed. Optical diffraction grating

periods can range from a few microns to a hundred microns. X-ray interference can be seen from structures possessing nanometre and submicron periodicity, encompassing the length scales of many important nanotechnologies including patterned magnetic recording media [144] and MRAM arrays [145], and in the future may include arrays of other devices such as spin torque oscillators [19].

Aside from spintronics devices, periodic nanostructures have important applications when designed for use as x-ray optical components. In synchrotron beamlines specialising in hard x-ray diffraction (considered as $E > 1$ keV equivalent to $\lambda < 1.2$ nm), monochromation of the white polychromatic beam can be performed using a single crystal monochromator (typically silicon or germanium) to diffract a single component of the spectrum. In the soft x-ray regime, the wavelength of the radiation becomes very large in comparison with the lattice spacing, so an artificial nanoscale grating can be used to monochromate the beam [e.g. ref. 146].

Another application in x-ray optics is the grating interferometer used for phase contrast imaging. In this apparatus a series of two or three sub-micron gratings are used to determine the refractive index (both the absorption and phase delay terms) of an object placed in the beam path. As described by Weitkamp *et al* [ref. 147], by adjusting the relative lateral offsets between the gratings a "phase stepping" effect allows the deflection and retardation caused by the object to be converted into an intensity modulation over an area detector. Images taken in multiple directions can be reconstructed tomographically to provide a three-dimensional reconstruction of the object. In both these x-ray optical applications highly engineered structures must possess perfect and precise periodicity to optimise the diffracted intensity.

A contrasting extreme of perfection in periodic nanostructures can be seen with self-assembled materials. As discussed in chapter 2, section 2.5.2, these are considered promising materials in a wide range of applications because of their relative low-cost and rapid production processes. Self-assembly can occur through a variety of mechanisms including chemical synthesis, ion bombardment and raft assembly. They are however prone to poor long-range ordering (coherence) if the assembly process does not permit extensive reordering of component units until the energy of the system is fully minimised.

A rapid, non-destructive and statistical technique for the extraction of key structural parameters from such nanoscale patterned materials is of great utility. Important parameters to obtain include the array periodicity in different orientations, coherence, preferential orientation and details on the size and shape of the constituent elements.

6.2. A background to x-ray scattering from periodic structures

6.2.1. Kinematical and dynamical scattering theories

X-ray scattering theories can be classified as either kinematical or dynamical. In the kinematical approximation scattering is assumed weak, so that the electric field throughout the sample is equal and parallel to the incident wavefield. When the kinematical approximation is combined with far-field observation conditions (so that the scattered waves are also parallel) the diffracted amplitude is proportional to the Fourier transform of the function describing the diffracting potential. This greatly simplifies the mathematical modelling of the scattering, and for regular one-dimensional diffraction gratings an analytical expression is readily obtainable (as was shown in chapter 3, section 3.7 of this thesis after the work of Morrison [97]). The one-dimensional grating is clearly the simplest of periodic structures, and many of the nanoscale devices in development will have final implementations as two-dimensional arrays of structures each with their own internal two- or three-dimensional structure

A dynamical theory is required when the scattered amplitude is strong in comparison to the incident wavefield and therefore significantly modifies the electric field in the sample. The dynamical theory given by Pietsch, Holý and Baumbach [ref. 70, chapter 6] involves the solution of the scalar wave equation for one or more pervasive wavefields which differ from the incident field. In the case of x-ray reflectivity, the solution obtained is the Fresnel reflectivity, and was given in section 3.3 of chapter 3. For reflectivity the electric field inside the crystal is assumed to be a single, parallel wavefront modified only by refraction at the interface. This is referred to as the single-beam case.

The dynamical theory of diffraction from the crystal lattice demands consideration of both the transmitted wave in the crystal and one or more diffracted waves originating after scattering. For a semi-infinite crystal, a two-beam solution is generally satisfactory, but for a thin film where the diffracted wave may experience repeated internal reflection within layers, many further wavefields must be superimposed to calculate the effective electric field amplitude throughout the crystal. Such a dynamical scattering theory becomes extremely complicated when nanoscale patterning is superimposed on the crystalline structure.

6.2.2. Previously reported scattering theories for periodic structures

There is an extensive library of literature concerning scattering from submicron and nanoscale structures. Two contrasting theoretical descriptions have been developed by

Tolan *et al* and Baumbach *et al*, both in works primarily modelling crystalline semiconductor grating structures.

Tolan *et al* [71, 96, 148, 149] have presented x-ray scattering measurements from gallium arsenide diffraction gratings, together with a corresponding dynamical calculation of the scatter. Their samples were prepared by acid etching through a photoresist after exposure to a laser interference pattern and chemical development, and typically had micron and sub-micron periods and etch-depths of more than 100 nm. Using a rotating anode laboratory-based diffractometer in a three-crystal arrangement they were able to obtain sufficient scattering signal from their single-crystal sample. Their measurement strategy was to select an order of diffraction from the grating and to perform a coupled scan of the incident and exit angles. For the $n = 0$ diffraction order, this measurement was conventional specular x-ray reflectivity. For $n \neq 0$, it is an offset coupled θ-2θ scan with a varying offset (such that the scan runs vertically on Figure 3-5 on p. 37, at constant q_x). Tolan's theoretical approach involved combining the Fresnel equations with a kinematical diffraction theory. The resulting model was integrated successfully in recursive fitting to obtain parameters including grating period, width and surface roughness.

Another prolific author in the field of study is Baumbach, who with various colleagues has considered the modulation of the small angle scattering pattern from semiconductor crystalline grating structures [150, 151] and more recently self-organized nanostructures resulting from Stranski-Krastanow growth [ref. 70, chapter 14]. Their general theoretical analysis is evaluated in both the kinematical and a semi-kinematical approximation. They include a term called the 'lateral geometrical factor' describing the correlation function between neighbouring nanostructures. This is one approach for the study of randomised structures.

6.3. A semi-kinematical theory for the characterization of periodic nanostructures by grazing incidence x-ray scattering

In section 3.7 an existing theory of scattering from a reflection grating was outlined, with particular citation of the work of Morrison [97]. A grating is an example of a surface periodic in only one dimension. The aim of the following section is to develop a theory applicable to thin films periodic in two dimensions.

One important difference between the systems considered here and those previously reported by Tolan *et al* and Baumbach *et al* is the thickness of the elements. These previous studies consider structures with deeply etched gratings such that scattering from the crystal lattice over a range of depths into the sample must be considered. In the

study of films of just a few nanometres in thickness, a much simpler theory can be developed as follows.

6.3.1. Outline theory

The theory is constructed in a semi-kinematical framework. Scattering is composed of two components:

(i) The kinematical diffraction pattern due to interference originating from the periodic surface structure. This describes scatter close to scattering vectors at which strong constructive scattering occurs. The diffraction pattern is the focus of the developments presented in the following sections.

(ii) The dynamical solution of the wave equation to a single, smooth surface given by the Fresnel equations. In reality, the refractive index of this surface is determined by the in-plane average of the electron density. This term describes scattering away from strong coherent scattering vectors, and is at its most intense close to the critical angles (at angles determined by the refractive index, with amplitude determined by the refractive index and surface roughness), and around the specular reflection (with width and amplitude determined by the in-plane correlation length and fractal parameter).

The Fresnel reflectivity was comprehensively discussed in chapter 3, section 3.4, and will not be developed any further in this chapter, other than to say that the refractive index used in modelling is the average value at the uppermost surface, which is weighted according to the area of each material at the surface. A single film of patterned material on a semi-infinite substrate with a different refractive index is modelled.

Importantly the two components are considered independently; the approximation is made that constructive interference dominates at specific scattering vectors, and is negligible elsewhere, and that the Fresnel reflectivity determines the underlying level of diffuse scatter. Dynamical effects in the diffraction pattern, most significantly those close to the critical angle, are ignored. This means that multiple scattering events resulting in coherent interference between different array elements are ignored.

The formulation describes scattering in a transverse scan at constant q_z and for q_x varying as the grazing angle α_i is rocked from zero to the fixed detector angle. The detector acceptance range in q_y is effectively infinite. The general function used to simulate the coherent scatter from an array of periodic nanostructures is:

$$I(q_x) = I_0 \left\{ A I_{diffracted}(q_x) + [1 - A] I_{\substack{substrate \\ specular}}(q_x) \right\} \otimes D(q_x) \tag{6.1}$$

where A is the fraction of the surface area covered by periodic nanostructures, and $[1 - A]$ is the remaining area covered by the substrate. $D(q_x)$ is the resolution function, and varies with the detector angle such that the resolution is finer at higher (positive) q_x than at lower (negative) q_x. This relation sums the intensities of scatter from the diffracted and underlying substrate rather than the amplitudes. The approximation is valid only when there is a very large difference between the two intensities. In this model the assumption is that at any q_x relating to the diffraction condition, the diffracted intensity is much greater than the substrate scatter. At q_x away from the diffraction condition, the Fresnel reflectivity is the only component of scatter.

6.3.2. The coherence of x-rays scattered at grazing angles

If the wavelength of the radiation sets a lower limit on the separation of structures that can be seen to diffract constructively, the coherence volume of the radiation sets an upper limit. Beyond the coherence volume scattering centres do not scatter in phase and interference does not sum constructively. In the case of synchrotron x-rays at grazing incidence, the coherent footprint on the sample surface can extend over to hundreds of microns, sufficient to sample several hundreds or thousands of nanometre sized elements.

The coherence of an x-ray beam is defined both spatially (perpendicularly to the propagation direction) which depends primarily upon the angular divergence of the x-ray source, and temporally (along the direction of propagation) which is often limited by the degree of monochromation. The coherence length can be quantified as the distance over which the phase of the wavefront varies by 2π, as is given by Schmidbauer [ref. 76, p. 73] for the spatial and temporal directions respectively as:

$$L_{\perp} = \frac{2\pi}{k\Delta\theta} = \frac{\lambda}{\Delta\theta} \tag{6.2}$$

$$L_{\parallel} = \frac{\lambda^2}{2\Delta\lambda} \tag{6.3}$$

Here $\Delta\theta$ is the angular divergence (in radians) and $\Delta\lambda$ is the wavelength spread.

When this coherence volume is projected onto the surface of a thin film at grazing angle α, the coherent footprint is given by:

$$L_{\perp}^{proj} = \frac{L_{\perp}}{\sin\alpha} \tag{6.4}$$

For typical divergence angles (for a synchrotron bending magnet) of $\Delta\theta = 0.005°$ and a wavelength of 0.15 nm the spatial coherence length $L_{\perp}$ is 1700 nm. At an incidence angle of 1° the coherent footprint is therefore 10 µm.

6.3.3. The diffracted intensity

In the kinematical approximation when Fraunhofer observation conditions apply the diffracted field is approximated to the Fourier transform of the scattering potential:

$$E_{diffr}(\mathbf{q}) \propto \Im\left[Z(\mathbf{x})\right] = E_0 \int Z(\mathbf{x}) \exp(-i\mathbf{x}.\mathbf{q})\, d\mathbf{x} \tag{6.5}$$

For the case of a regular diffraction grating, an analytical solution is readily obtainable, as was shown in chapter 3 section 3.7. For the case of an irregular diffracting structure or an array of diffracting structures on a similar scale to the coherence length, analytical solutions become increasingly complicated. Even when an analytical solution is obtainable for a specific structure, a more general numerical method can be informative.

The parameters of a cross-section through the grating structure are defined as in Figure 6-1. The discrete Fourier transform, in an algorithm known as the Fast Fourier Transform (FFT) is used to generate the diffraction pattern, and for the simple rectangular grating given in Figure 6-1 with d = 1280 nm and w = 780 nm, the algebraic and numerical Fourier transforms are shown in Figure 6-2. The FFT algorithm gives an excellent approximation to the algebraic transform.

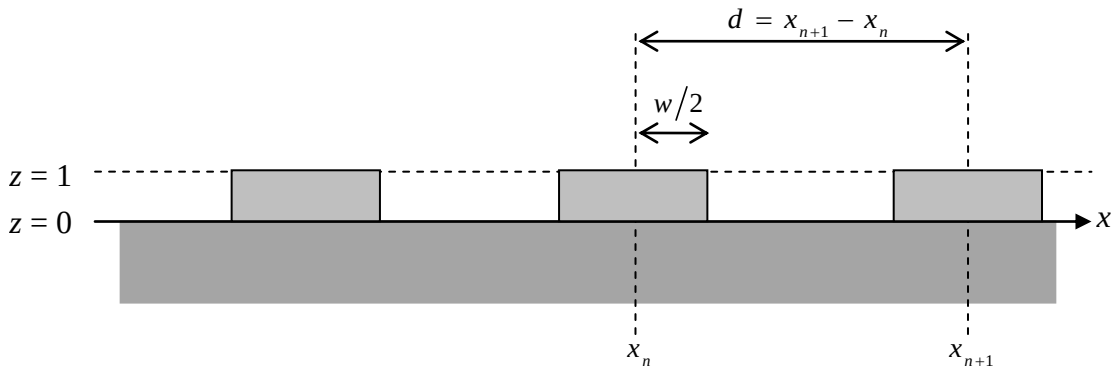

Figure 6-1. A schematic diagram showing the definitions used for a rectangular grating structure.

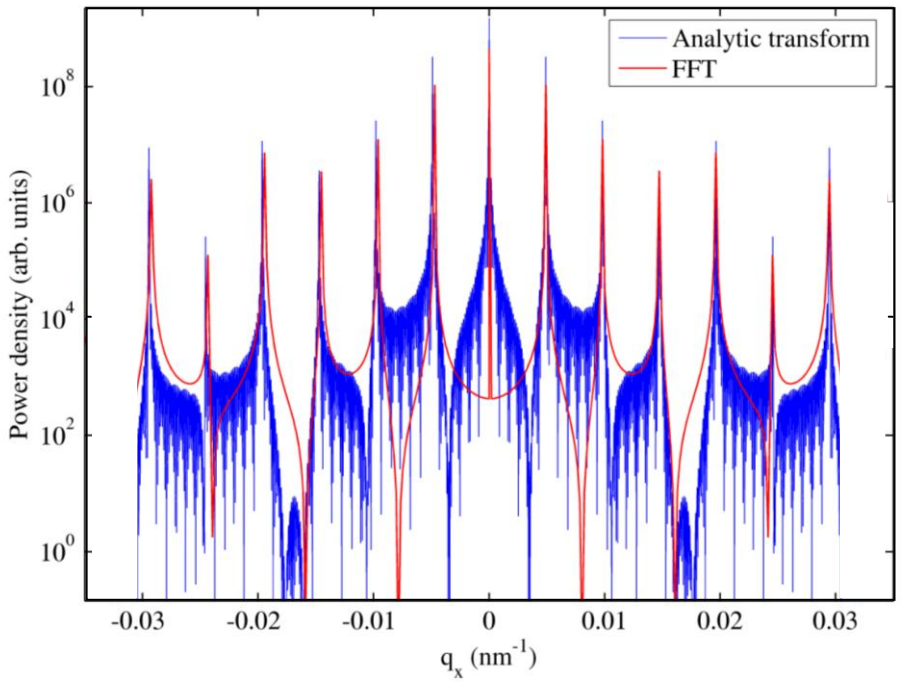

Figure 6-2. A comparison of the analytical and numerical Fourier transform of a rectangular grating structure with periodicity d = 1280 nm, element width w = 780 nm, and coherent scattering volume 250 μm. The FFT was performed for a structure with 16 nm resolution describing the profile Z(x), and with a minimum frequency resolution given by 2π / (250 μm) = 0.025 μm^{-1}. The q_x domain is limited by the sample surface when 2θ = 2° and the incident energy E = 7 keV.

Whilst the analytical transform is the more mathematically correct transform for a regular grating structure, for periodic structures with irregular periods, or for two-dimensional structures in which the coherence length of the radiation on the surface needs to be considered, the numerical method yields more rapid and flexible diffraction patterns.

A two-dimensional map representative of the beam footprint on the sample must be input into the Fourier transform algorithm. This ‘slice’ of surface structure information will possess spatial frequencies which vary with the azimuthal orientation of the sample, as can be appreciated by considering Figure 6-3 on which part of a representative footprint is highlighted. Here the azimuthal angle is defined in the sample surface from the axis of highest symmetry (the [1 0] axis).

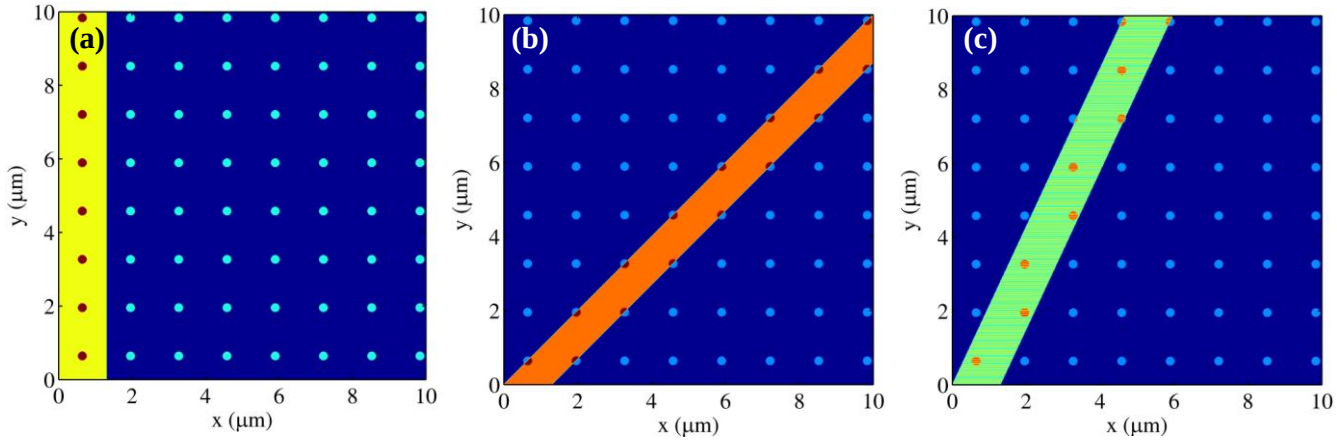

Figure 6-3. A limited extent of the representative coherent scattering footprint (the actual length of the footprint considered is ~ 100 μm) shown for various azimuthal orientations: (a) ϕ = 0° (i.e. along the [1 0] axis), (b) ϕ = 45° (i.e. along the [1 1]), and (c) at a low-symmetry axis at ϕ = 25°. The spatial frequencies present vary with the azimuthal orientation angle ϕ.

The length of the input structure is determined by the coherence length of the scattering. This is determined by the shorter of the coherence of the radiation, or the coherence of the periodic structures, defined as the length beyond which there is a phase change of 2π.

The powerful potential of this simplified process should not be underestimated. By exploiting such a numerical routine it is possible to simulate a range of spatial frequencies present in a surface away from the principle axes of symmetry, including surfaces with simulated element dispersion, element incongruity and element shape asymmetry.

6.3.4. The detector resolution function

The convolution in equation (6.1) is conventionally performed by applying the convolution theorem:

$$A = B \otimes C \Rightarrow \Im(A) = \Im(B) \times \Im(C) \tag{6.6}$$

where $\Im(Y)$ represents the Fourier transform of Y. The numerical calculation of two discrete Fourier transforms followed by the inverse transform of their product is computationally intensive. A more rapid calculation can be made by preparing a detector function matrix $D_M(q_x)$ to represent the detector acceptance for the discrete values of q_x at which the intensity is measured. This can then simply be multiplied with the diffraction pattern to determine the measured intensity:

$$I(q_x) = I_0 \left\{ AI_{diffracted}(q_x) + [1-A] I_{\substack{substrate \\ specular}}(q_x) \right\} \times D_M\left(q_x^{\,nominal}, q_x^{\,accept}\right) \tag{6.7}$$

The matrix $D_M\left(q_x^{\,nominal}, q_x^{\,accept}\right)$ is calculated as a Gaussian function with width parameter *C* that varies in a manner dependent upon the detector acceptance.

$$D_M\left(q_x^{\,nominal}, q_x^{\,accept}\right) = C\left(q_x^{\,nominal}\right) \exp\left\{ -\frac{\left(q_x^{\,nominal} - q_x^{\,accept}\right)^2}{\left[C\left(q_x^{\,accept}\right)\right]^2} \right\} \tag{6.8}$$

Here $q_x^{\,nominal}$ represents the in-plane vector probed at the centre of the detector aperture, and $q_x^{\,accept}$ represents the entire range of in-plane scattering vectors over which the detector integrates scatter. The result of (6.8) is a series of Gaussian functions for all $q_x^{\,nominal}$ with a varying width and amplitude, but constant area.

The detector acceptance $C(q_x)$ is calculated using the angular definition of q_x written as:

$$q_x = k(\cos\alpha_r - \cos\alpha_i) \tag{6.9}$$

If there are uncertainties in α_r and α_i due to the width of the incident beam and the detector acceptance, the total uncertainty in q_x is found by the sum in quadrature of the uncertainties on the individual terms in (6.9):

$$C(q_x) = \Delta q_x = k\sqrt{\sin^2\alpha_r(\Delta\alpha_r)^2 + \sin^2\alpha_i(\Delta\alpha_i)^2} \tag{6.10}$$

This defines the width of the Gaussian detector function for all $q_x^{\,nominal}$.

6.3.5. Implementation of the theory for computer simulation

The numerical simulation was written in the MATLAB programming environment, and was intended to run on an ordinary personal computer. The computer code developed for all the simulations in this chapter is included in Appendix B for reference.

The best fits to the data were optimised by manual variation parameters and graphical fitting by eye, starting with values close to the nominal structure. Uncertainties on periodicity were estimated as the increment required to shift the satellite peak by one half width at half maximum at the extreme range of q_x. Uncertainties in parameters such as element shape and coherence length are more difficult to quantify rigorously, and the best estimation from repeated fitting of the data was ± 10% on each value.

The integration of the simulation with a recursive fitting algorithm is feasible, and would eliminate human perception from the process. It would allow a statistical quantification of the uncertainty on each fit parameter, for example by the variation required to increase the χ^2 measure of correlation by one. Such a fitting routine is however beyond the scope of the work presented here.

6.4. Experimental method

All data presented in this chapter were collected at the XMaS beamline of the European Synchrotron in Grenoble, France. The beamline and diffractometer specifications were reported by Brown *et al* in 2001 [107]. The energy of the incident and measured scattered radiation was 7 keV. The nominally parallel incident beam was limited by slits to a height (approximately in the *z*-direction) of 100 µm and a width (in *y*) of 500 µm. The sample was mounted on a goniometer stage which had previously been centred by the use of x-ray sensitive paper so that the patterned region on the sample was close to the centre of the beam width when first mounted. The detector aperture was set at 200 µm high and 4 mm wide, and the grazing incidence scatter detected using an avalanche photodiode detector.

The detector angle was set in the range 2–3°, whilst the sample angle θ was rocked from zero to the detector angle in a transverse scan over which the in-plane scattering vector q_x varied. Transverse scans were performed for different orientations of the sample about the surface normal, labelled as ϕ and named the azimuthal angle. This allowed the in-plane symmetry and structural periodicity of the array to be determined.

6.5. Studies of highly periodic arrays defined by e-beam lithography

6.5.1. Sample preparation

A series of samples were prepared by electron beam lithography in Durham using the process described in section 2.5.1.

Commercially produced thermally oxidized silicon (100) wafer chips approximately 5 mm × 5 mm in size were cleaned using acetone in an ultrasonic bath followed by rinsing with isopropanol. The cleaned substrates were then spin coated with polymethylmethacrylate (PMMA of molar mass 495 kg) at 3000 r.p.m. for 30 seconds, and heated at 180 ºC for one minute. The periodic pattern was exposed using a Scanning Electron Microscope (SEM) equipped with a Raith 150 lithography system which enabled computer controlled rastering of the beam position. The electron beam was

produced by an electron gun operating at 30 kV and was calculated to provide a current dose of 360 μA s cm^{-2}.

The exposed sample was developed in one part 4-methyl-2-pentanone (MIBK) to three parts isopropanol at 20 ºC for 30 seconds, followed by rinsing in isopropanol for 30 seconds. 10 nm Permalloy ($Ni_{81}Fe_{19}$) was deposited by thermal evaporation, and the remaining PMMA (capped with unwanted Permalloy) was removed, using acetone as a solvent, by soaking for one hour and finally being agitated in an ultrasonic bath for thirty seconds.

The extent of the arrays patterned by this technique were between 400 μm × 400 μm and 600 μm × 600 μm. This area was limited by the time required for electron beam exposure, which was typically 24 hours per sample.

6.5.2. Results and simulated GIXS from a square array of circular elements

Figure 6-4 shows scanning electron microscope (SEM) images of the first sample presented, a highly regular, square array of rough circular elements. X-ray scattering measurements from this one sample have been previously presented in reference [1]. The measurements and simulations shown here have been published in reference [152].

From repeated measurements of the array periodicity in the [0 1] direction on these SEM images (and other images not shown here), a mean and corresponding standard error of d = (1320 ± 10) nm is obtained. The element diameters were measured (averaged in all directions) as w = (580 ± 30) nm. The arrays extended over $(500\ \mu m)^2$.

A map of the measured transverse scatter as a function of azimuthal angle of rotation is given in Figure 6-5(a). These measurements were made with a detector angle $2\theta = 2°$. The square symmetry of the array is apparent from the 90° angular recurrence of the satellite peaks with the widest separation, corresponding to the [0 1] and [1 0] array directions. A simulation generated using the semi-kinematical theory is shown in Figure 6-5(b). The satellite peak period gives an extremely precise measurement of the array period, as d = 1260 ± 10 nm. The uncertainty in this value relates to the half-width at half maximum of the satellite peaks.

The element width (or conversely the element-element separation along the <1 0> directions) is more indirectly obtained. This modifies the relative amplitudes of the satellite peaks. A selection of simulations along [1 0] for different values of element diameter w are given in Figure 6-6. Graph (a) corresponds to the nominal element size, but the peak amplitudes do not match well. The best fit to the amplitudes is obtained at w = 490 nm, corresponding to an element-to-element separation of 890 nm. An uncertainty on this value is difficult to quantify, but by comparison of the different plots

in Figure 6-6 it can be estimated at approximately 50 nm, the precision to which *w* can be optimised in successive fits.

Whilst this fitted element width parameter is difficult to quantify precisely, it is smaller than the nominal measurement determined by SEM, (580 ± 30) nm. This difference can be attributed to the random edge roughness present: (490 ± 50) nm may represent the entirely coherent region of the element, whereas the outermost element 'border' may be intermittently present due to random edge roughness.

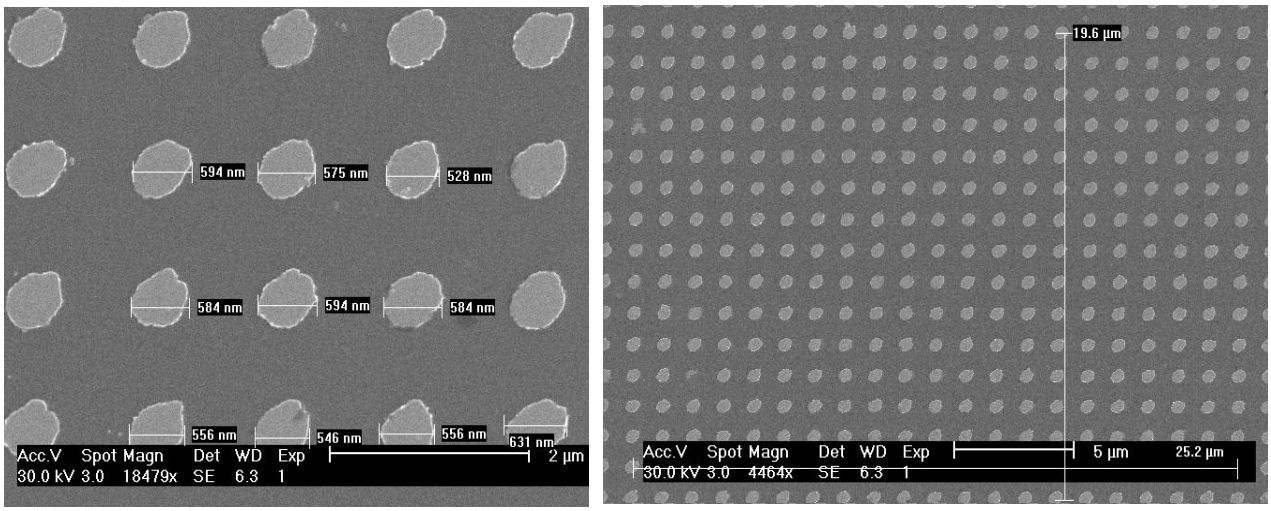

Figure 6-4. Scanning electron microscope image of the array of Permalloy 'nanodots' fabricated by electron beam lithography.

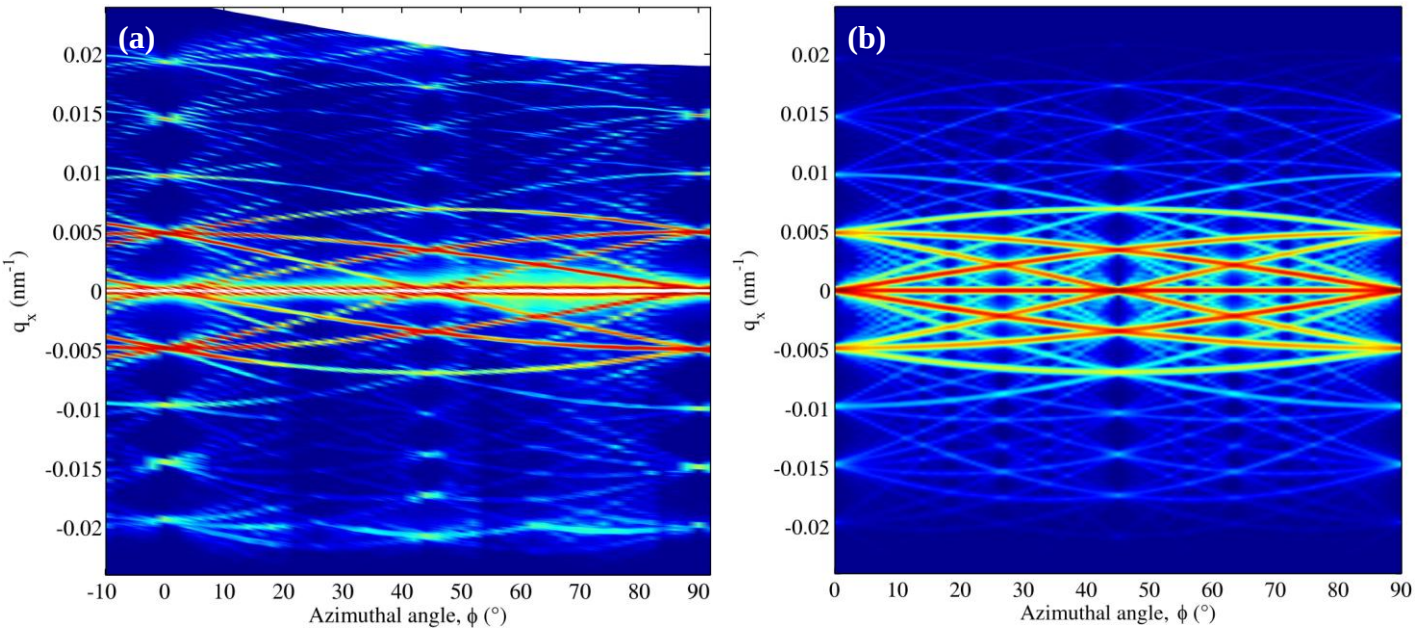

Figure 6-5. Grazing incidence scatter from a square array as a function of the angle of azimuthal rotation. (a) experimental, and (b) simulated. Simulation parameters are given in the body text.

Both Figure 6-5 and Figure 6-6 show how the change in the resolution function can be observed: for more negative q_x the resolution is lower, and the satellite peaks broader. At more positive q_x the resolution becomes finer, as described by the variable width resolution function given in (6.10). In Figure 6-7 the effect of decreasing the number of coherently scattering elements is shown. For small N, the satellite widths increase significantly beyond what is expected from the instrument resolution. For $N = 80$, the simulated peaks are too sharp. The best fit is found to occur at $N = 42$, corresponding to a coherent length on the sample of 75 μm. This is a reasonable value for the coherence length of a bending magnet synchrotron source (earlier calculated to be ~ 10 μm, although these measurements have not established that the coherence of the array is not the cause of this limitation. This series of graphs demonstrate that the peak width is a combination of the number of coherently scattering elements and the instrument resolution.

At this point is should be noted that in principle N is not constant during a single transverse scan: the coherently illuminated footprint on the sample is, in general, dependent upon the angle. However, for the samples discussed in this chapter the patterned area is relatively small (less than one millimetre in extent), meaning that at shallow grazing angles the change in N can be assumed to be negligible.

Finally, Figure 6-8 shows the measured and simulated scatter (using the optimised parameters) at an angle of 30° from the [1 0] axis, i.e. a low-symmetry orientation. The positions and amplitudes of the strongest satellite peaks are well reproduced, providing further evidence of the accuracy and power of the simulation method.

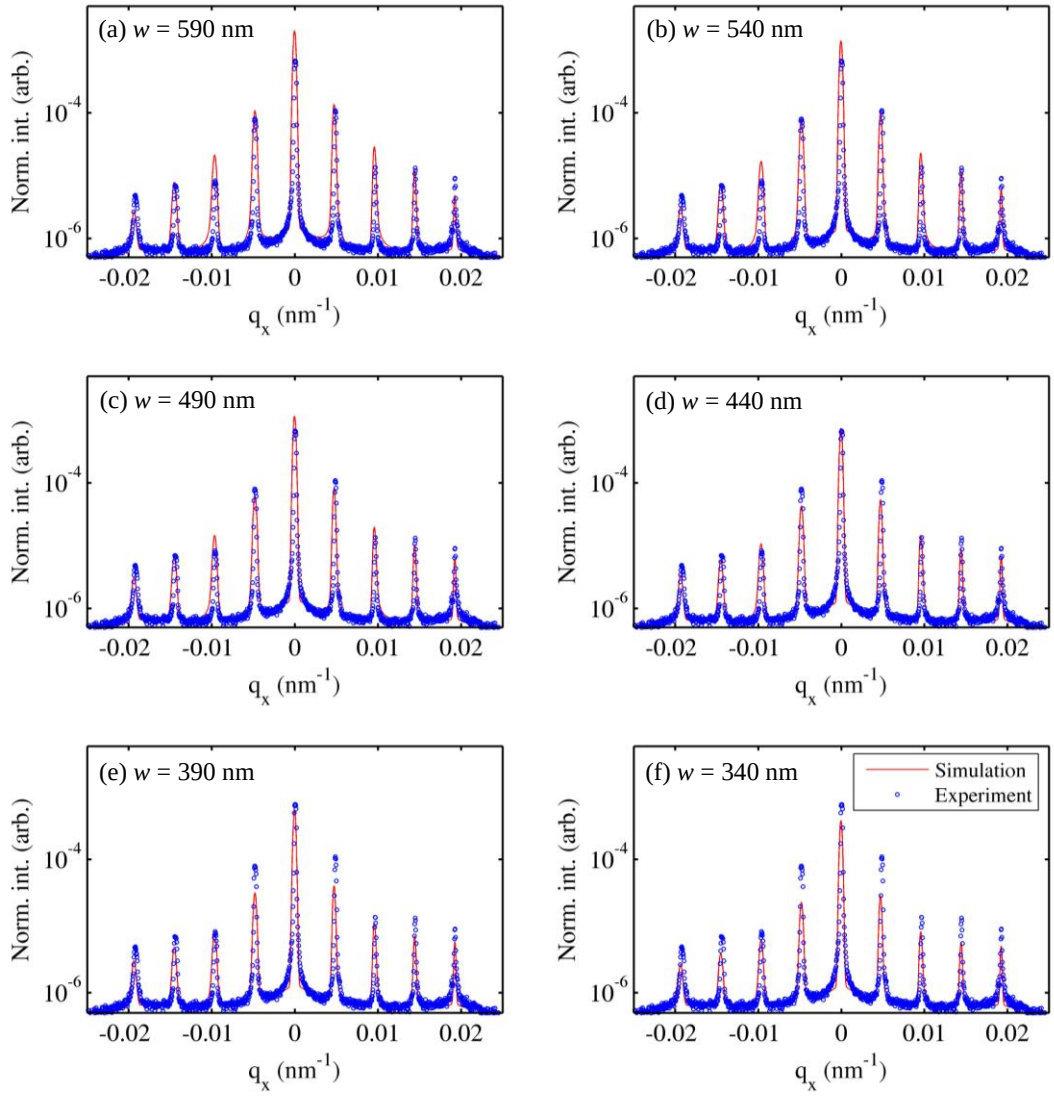

Figure 6-6. Experimental transverse scatter from a square grating of circular structures orientated along [0 1], with simulations for varying element diameter w. The modelled array periodicity is d = 1320 nm, and the number of coherently scattering elements is N = 42.

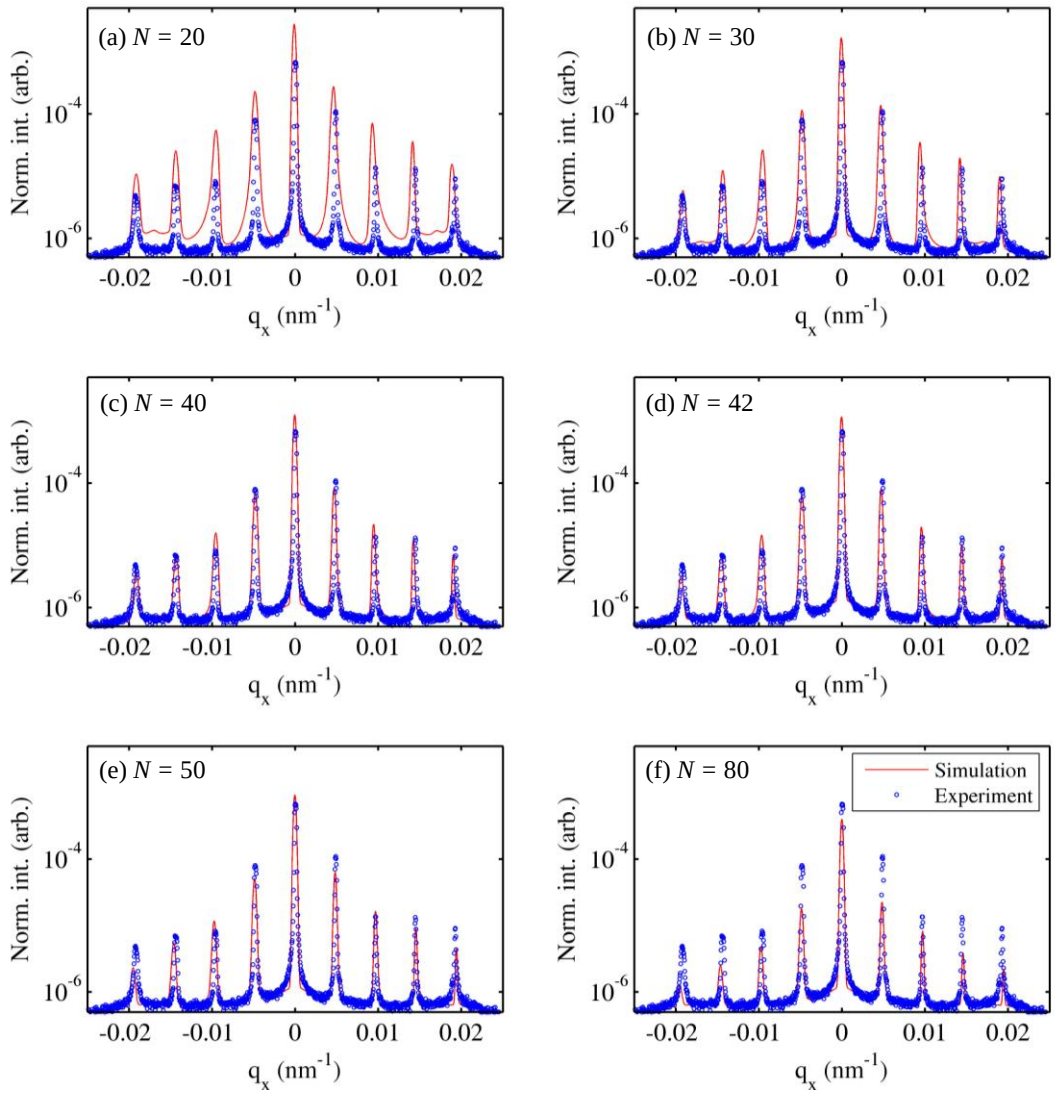

Figure 6-7. Experimental grazing incidence scatter with simulations for different numbers of coherently scattering elements, N. The array is described by the parameters d = 1320 nm, w = 490 nm.

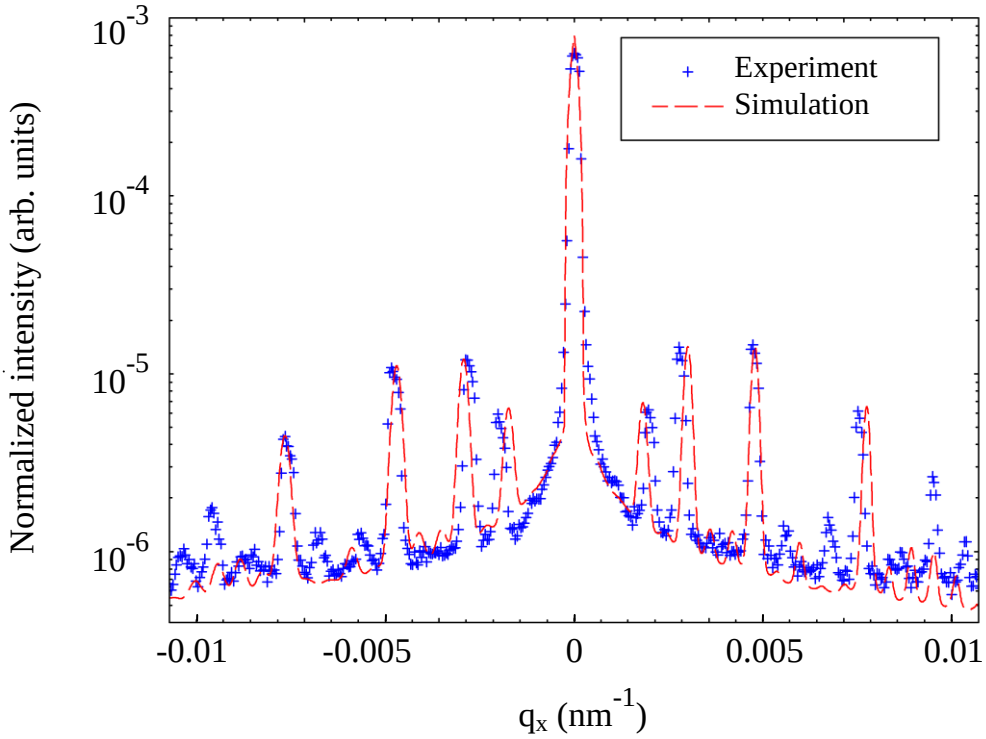

Figure 6-8. Experimental grazing incidence scatter and corresponding simulation at an azimuthal angle of 30° to the [0 1] direction. The array is described by the parameters d = 1320 nm, w = 490 nm.

6.5.3. Results and simulated GIXS from a rectangular array of nanostructures

Extended chains of closely-spaced Permalloy nanomagnetic elements were fabricated by electron beam lithography, and were made the subject of a structural characterization by x-rays in the grazing incidence geometry.

The shape of the element was elongated parallel to the chains, originally intended to induce a shape anisotropy preferring magnetization along the axis of the chain. As shown in the SEM images shown in Figure 6-9 the chains had very large inter-element separations perpendicular to the chain (~4 μm), and very small separations along the chain axis (90 ± 10 nm).

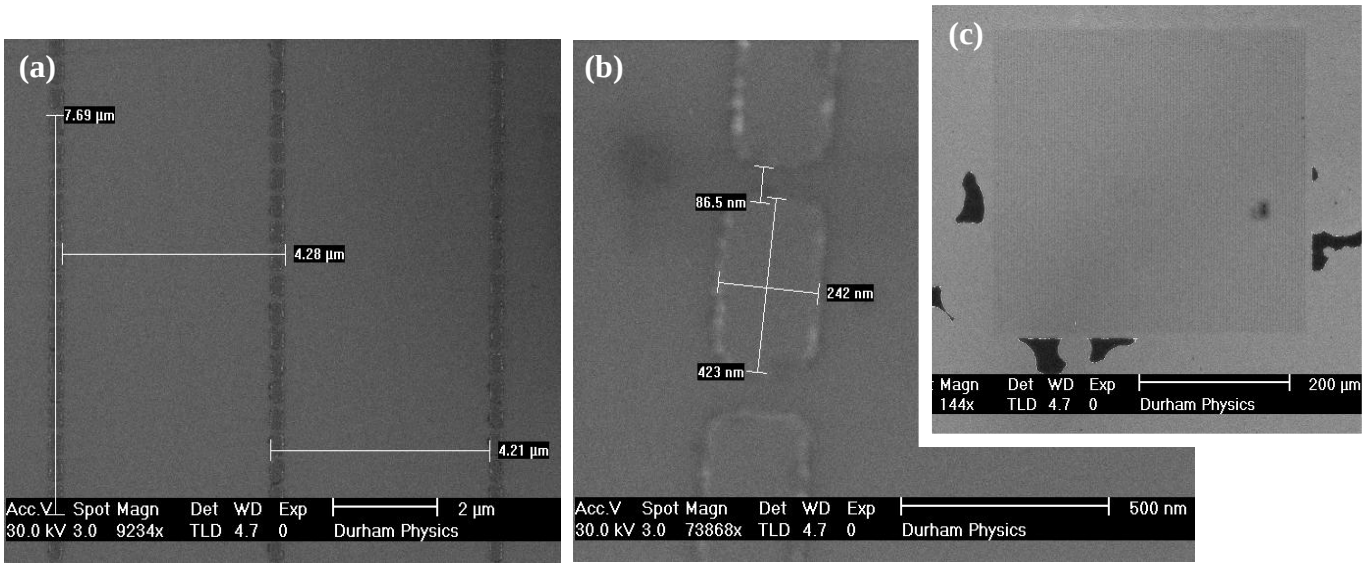

Figure 6-9. Scanning electron microscope images of magnetic chains fabricated in Durham by electron beam lithography. Indicating: (a) the periodicity of the chains, (b) the typical size and proximity of elements in a chain, and (c) the extent of the array: 400 × 400 µm^2.

The grazing incidence scattering was measured with the detector angle fixed at 2θ =2.5° (higher than the previous sample in order to expand the measurement domain in q_x), with incident x-ray energy of 7 keV.

An azimuthal rotation map of the transverse grazing incidence scatter is shown in Figure 6-10 (a) for the measured scatter at 2.5°, and (b) for the corresponding simulated scatter. The parameters used for the simulated scatter are chosen to reproduce the scatter along and perpendicular to the chain lengths.

The change in symmetry is stark: at ϕ = 0°, the satellite peaks are very closely spaced (replotted in Figure 6-11), relating to the scattering plane being perpendicular to the chain lengths when the spatial frequency of the surface is low. At ϕ = 90° the scattering plane is along the chain length and the satellite peaks occur at higher reciprocal space vectors (replotted in Figure 6-12).

Perhaps these data in particular demonstrate most clearly that constructive interference occurs well away from axes of high symmetry. Each scattering element in these nanoscale arrays has dimensions of the same magnitude as the grating periodicity, leading to strong off-axis interference. This is well reproduced in the simulation.

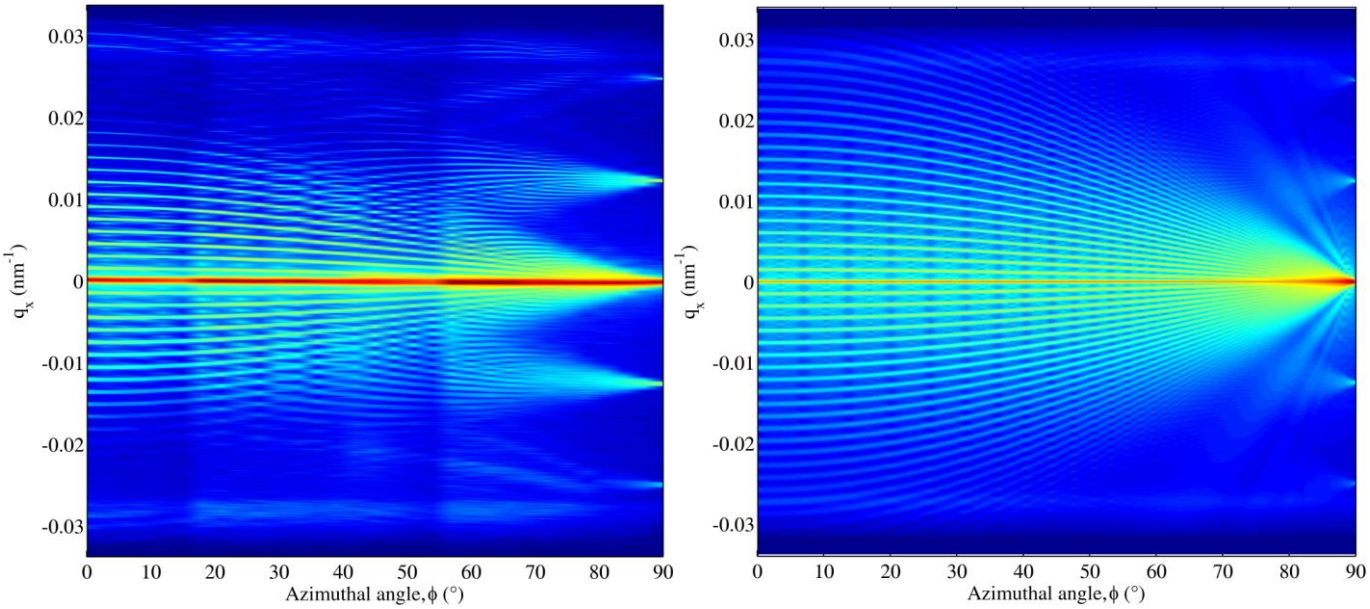

Figure 6-10. (a) Experimental grazing incidence scattering from the array of magnetic chains as a function of azimuthal angle. Zero azimuthal angle is perpendicular to the chains, 90° is along the chains. (b) The corresponding best-fit simulation of scatter.

Table 6-1. Nominal and determined values for the structure of the sample of nanoscale magnetic chains. Mean values and standard error on SEM image measurements are obtained by repeated measurement of regions over the whole extent of the patterned array. Values and uncertainties on GIXS best fit periodicities are established by matching of the simulation and experimental data, and the deviation from the model periodicity required to offset the satellite peaks by one half-width at half-maximum for the satellite at the largest discernible $|q_x|$.

Parameter	**Nominal value (nm)**	**SEM image measurement (nm)**	**Best fit value to GIXS (nm)**
Major period	4000	4200 ± 100	4150 ± 50
Minor period	500	495 ± 10	505 ± 50
Element length	400	425 ± 20	405 ± 100
Element width	250	240 ± 10	150 ± 100
Coherence length	Not applicable	Not measurable	20 000

The measurement in Figure 6-11 shows enhanced amplitude of the satellite peaks around the critical angle. Close to the critical angle there is strong constructive interference of the incident and scattered wave; the kinematical approximation is no longer valid, and a dynamical model is required to describe the enhanced scatter. A second factor causing the mismatch at the critical angles may be that in the experiment an unpatterned area of the substrate is also illuminated, and is contributing a strong Fresnel reflectivity.

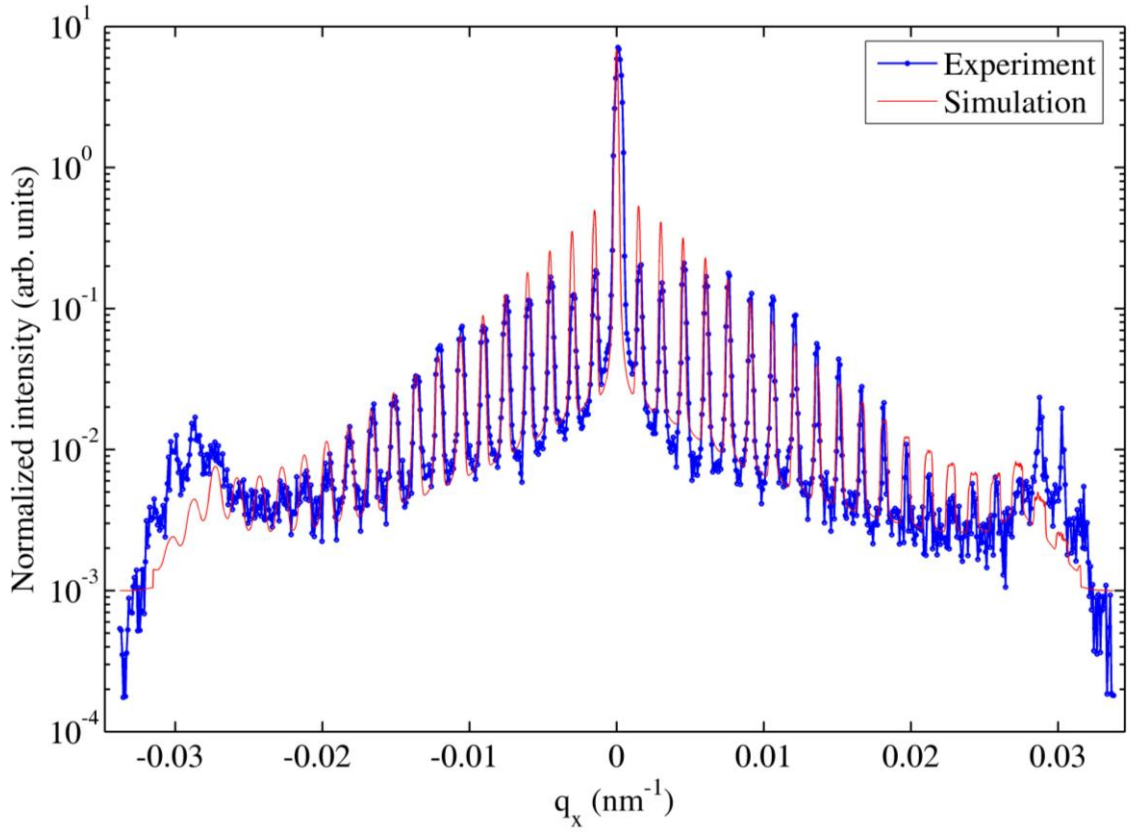

Figure 6-11. Experimental and simulated grazing incidence scatter perpendicular to the magnetic chains. Detector angle fixed at $2\theta = 2.5°$.

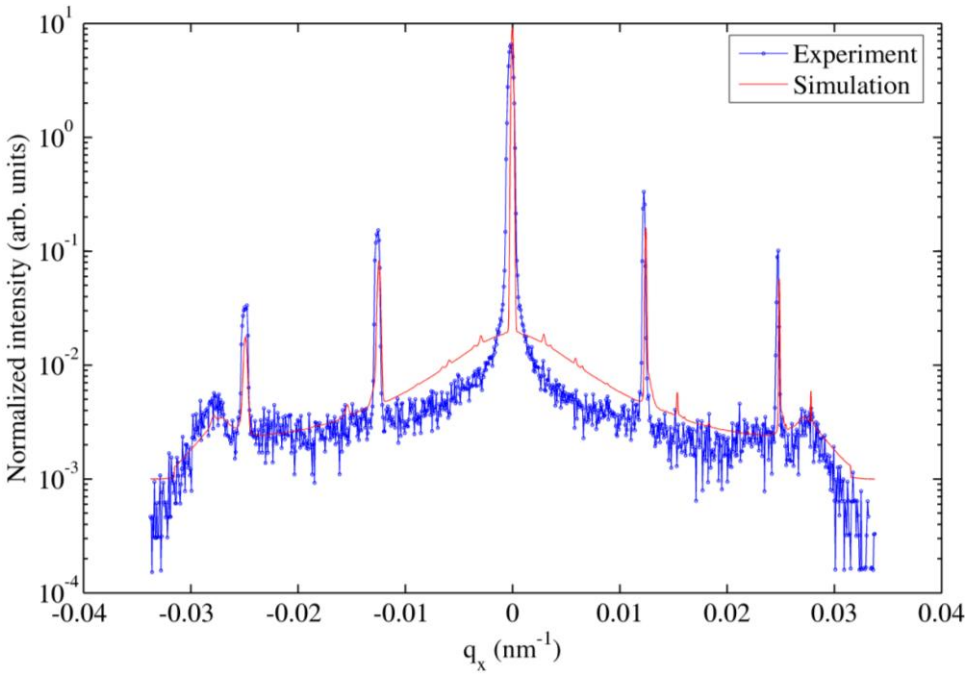

Figure 6-12. Experimental and simulated grazing incidence scattering along the length of the magnetic chains. Detector angle $2\theta = 2.5°$.

6.6. Studies of disordered patterned arrays

Electron beam lithography is a serial process: the focussed electron beam traces out each element one after another in an electron sensitive resist (section 2.5.1). The position of the e-beam is precisely controlled by beam deflectors in the electron gun, and the resulting exposure pattern can be extremely regular across its full extent. The resulting array is highly coherent, but the processing time is slow (typically 1 mm^2 takes at least 24 hours to pattern), and therefore unsuitable for patterning very large areas on many samples. Self-assembly may be an attractive alternative. One example of a self-assembled array of SiO_2 spheres with nominal diameter 500 nm and capped with a Co/Pd multilayer was structurally characterized using grazing incidence x-rays.

6.6.1. Sample preparation

The self-assembled arrays presented in section 6.6.2 were prepared at the Universität Konstanz in Germany by M. Albrecht and co-workers, in the process reviewed in section 2.5.2 and originally provided in references [29, 30]. A monolayer of SiO_2 spheres were assembled onto a silicon substrate and capped with a Co/Pd multilayer [Co (0.3 nm)/Pd (0.8 nm)]$_{\times 8}$ stack deposited on a 3-nm-thick Pd buffer layer (a structure illustrated in Figure 6-13). This multilayer was deposited for another study of perpendicular magnetic anisotropy by Albrecht *et al*, but the measurements presented in this thesis could not resolve the multilayer structure.

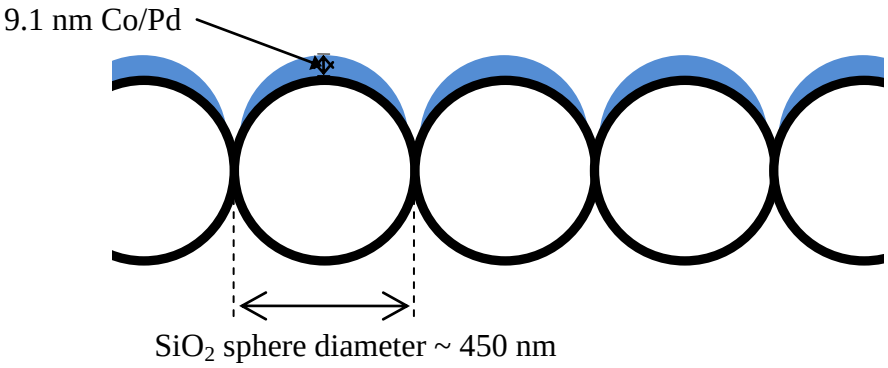

Figure 6-13. Schematic diagram of a cross-section of the self-assembled sphere array. Adapted from figure 1(a) of reference [29].

It should be noted from Figure 6-13 that the capping layers are not necessarily flat thin films, but rather curved 'caps' sitting upon the sphere surface.

6.6.2. Results and simulated GIXS from a self-assembled array of spheres

The arrays supplied were imperfect, since very long-range ordering was inhibited by a rapid evaporation of the solvent. Microscope images of the sample are shown in Figure 6-14 (optical) and Figure 6-15 (SEM). These images show the excellent short-range ordering with domains of hexagonal arrangement. The packing density is similar for all domains. There is no long-range preferential orientation of domains. From the electron microscope images in Figure 6-15(a) the size of the coherent domains can be estimated at approximately ten spheres. From Figure 6-15(b) the diameter of the spheres is measured as 455 ± 5 nm. It can be seen that there is some separation between the spheres, which may be due to the spheres shrinking as they are heating during film deposition.

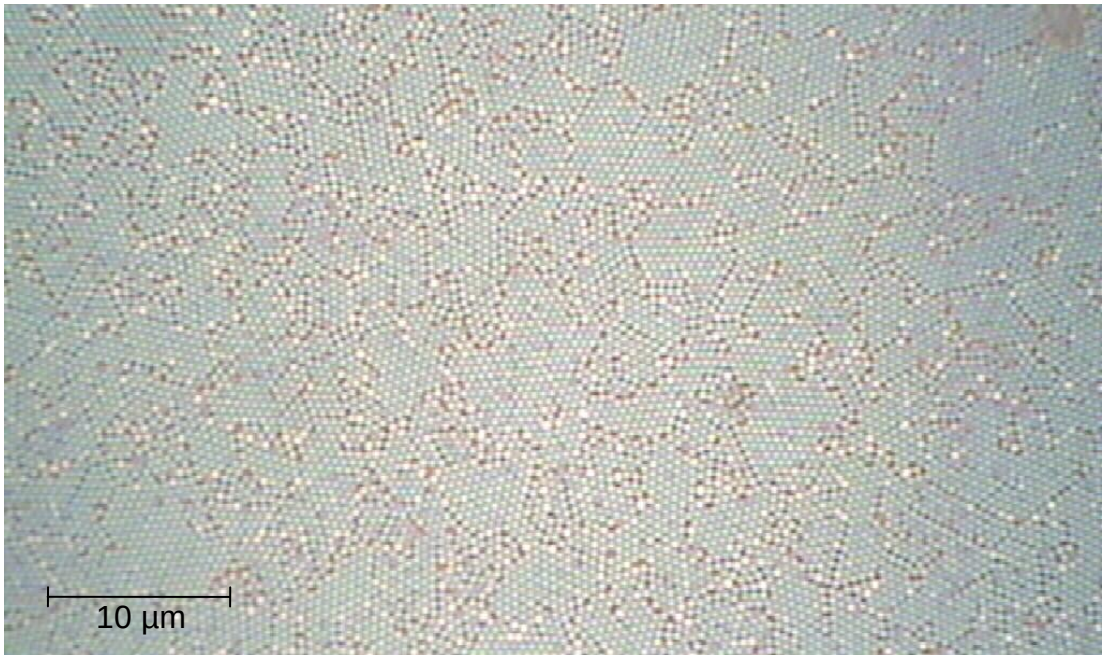

Figure 6-14. Optical image of the self-assembled silica spheres array supplied by M. Albrecht at the Universität Konstanz. Image obtained in Durham by the author, showing the long-range isotropy of grains (i.e. there is no preferred orientation.)

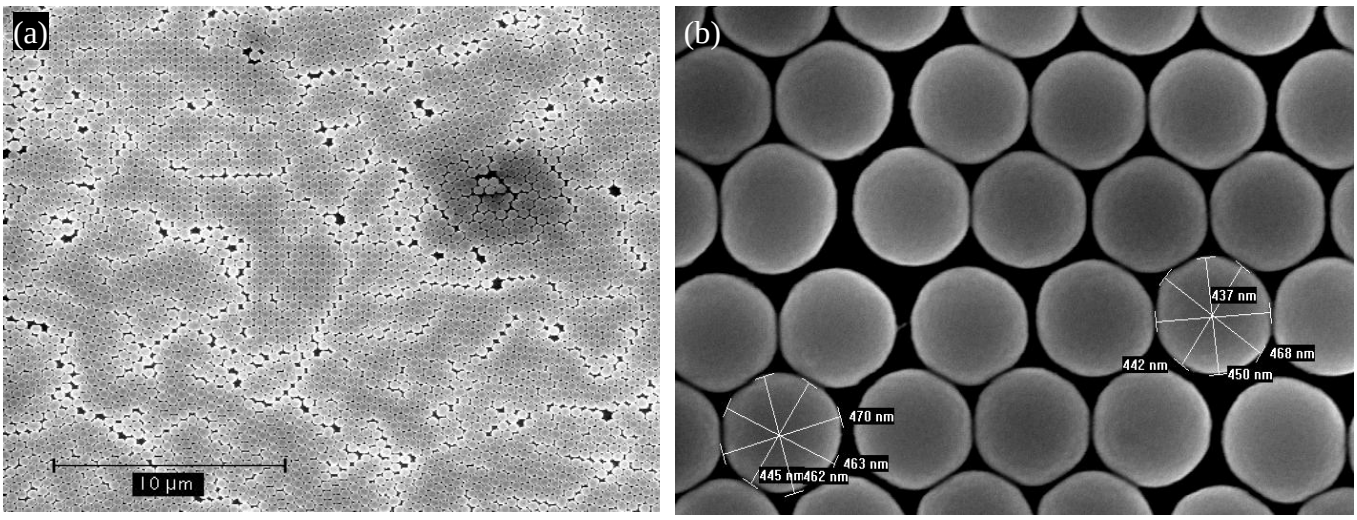

Figure 6-15. Scanning electron microscope images of the self-assembled silica sphere array fabricated by M. Albrecht at the Universität Konstanz (a) showing the distinctive 'grains' of coherent ordering, and (b) showing the shape, dimensions and consistency of the spheres. Images obtained in Durham by the author.

The measured transverse scans from the sample at various detector angles are shown in Figure 6-16. For lower detector angles, the extent of the scan in q_x is more limited, and the positions of the critical angles vary with detector angle. There are shoulders present at scattering vectors which do not depend upon the detector angle, and which therefore must originate from the sample structure rather than being a facet of the experiment. The locations of these shoulders correspond to a structural periodicity of approximately 450 nm.

It should be noted that the scans shown in Figure 6-16 represent an average of domains at all azimuthal orientations. Figure 6-17 shows a series of scans taken whilst the sample is azimuthally rotated at 15° increments over 90°. There is little change upon rotation, indicating no preferred in-plane orientation (i.e. the sample is isotropic). There is a small change in the width of the peak around the specular scatter, but these q_x values relate to very long in-plane correlation lengths. This variation may be due to a region of unpatterned substrate being exposed more at some orientations, providing a stronger specular reflection relative to the scatter from the spheres. (If the specular reflection had originated from the spheres, which are known to have a curved surface, then the specular peak would be spread more broadly. The sharpness of the measured specular peak suggests that this originates largely from the relatively smooth, flat silicon substrate.)

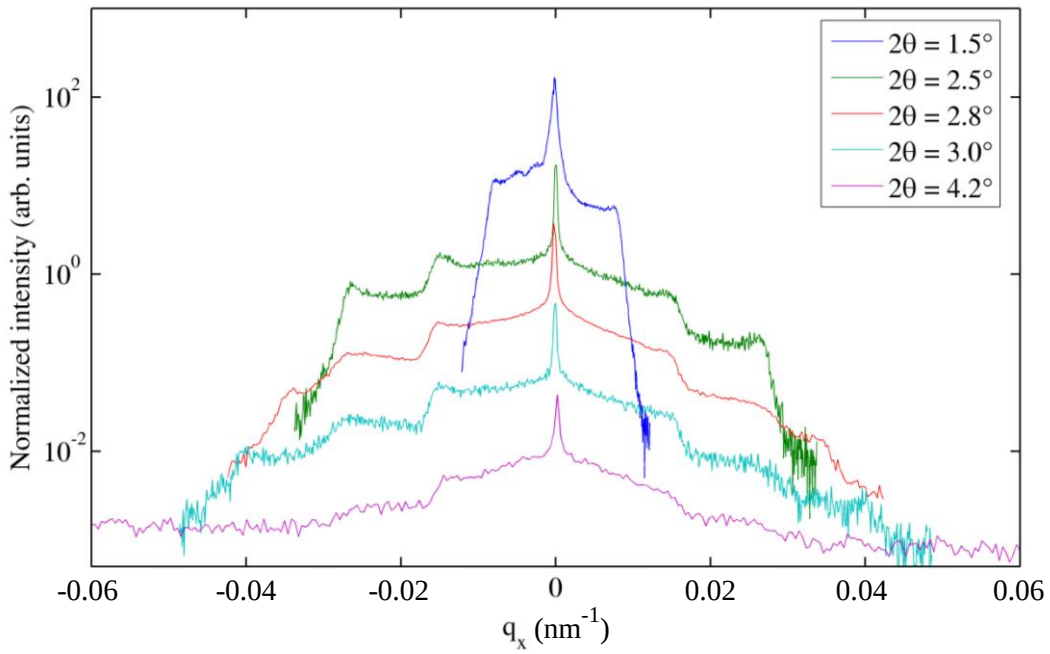

Figure 6-16. Transverse diffuse scatter from a self-assembled sphere array at varying detector angles. Note the constant position of the shoulders at q_x = 0.014 nm^{-1}, indicating that these steps are sample-dependent, not a facet of the limited measurement range.

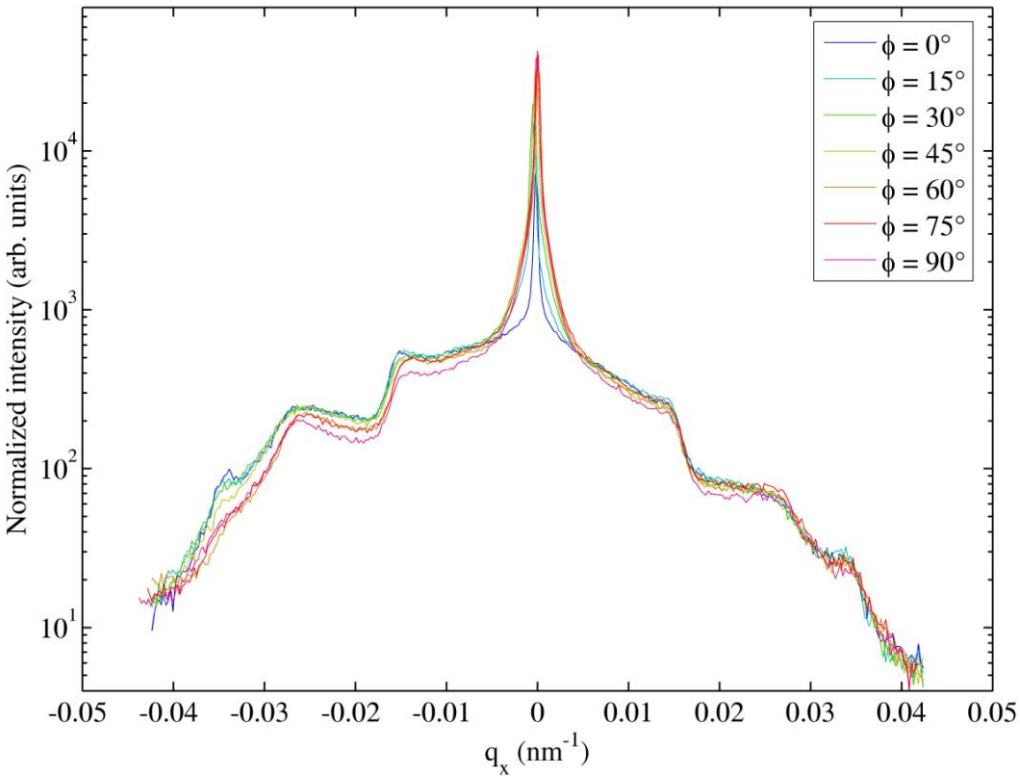

Figure 6-17. Experimental transverse diffuse scans at varying azimuthal rotation angles for the self-assembled array of silicon dioxide spheres.

Simulations were made assuming that the spheres scattered as flat circular discs in a hexagonal lattice with a limited structural coherence length. The computed scatter is shown in Figure 6-18 for different numbers of coherently scattering elements.

The simulations in Figure 6-18 suggest that for large domain sizes (more than twenty elements) sharp peaks begin to appear in the diffuse scatter despite a lack of any preferred grain orientation. These are principally located at the <1 0> reciprocal space amplitude, where the coherence length will contain the highest number of coherently scattering elements.

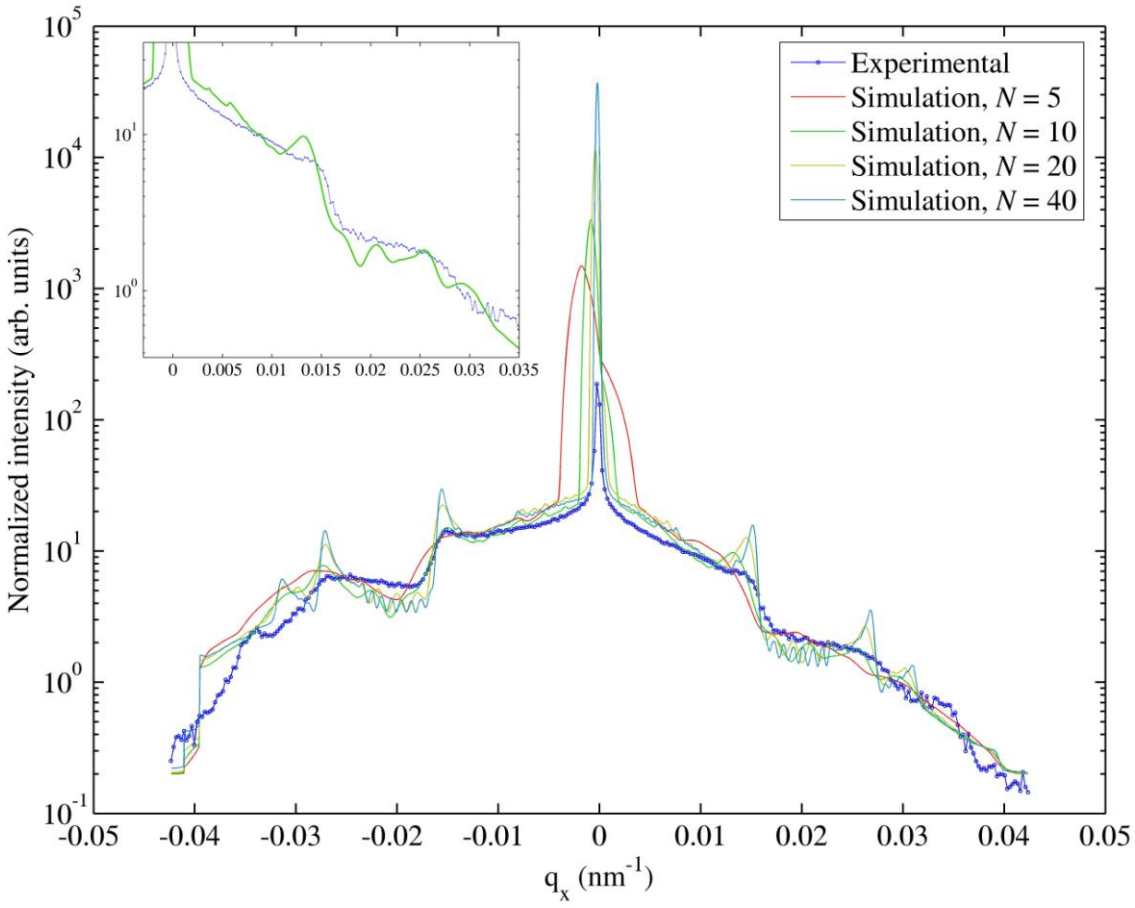

Figure 6-18. Simulations of diffuse scatter from an anisotropic array of 410 nm diameter circular elements with an edge-to-edge separation of 50 nm and a coherence length equivalent to N interplanar spacings along <1 0>, where N = 5, 10, 20 and 40. Simulations plotted together with experimental data. Inset: close-in of experimental data and N = 10 best-fit simulation.

In order to understand better the origins of the steps in these transverse scans, it is helpful to consider a hypothetical simulation of the scatter from a single ten-element diameter hexagonal domain, as shown in Figure 6-19(a), which represents the scattering by individual domains orientated at different azimuthal angles ϕ. The average over ϕ of this map is shown in part (b) of the Figure, which represents the best fit (N = 10) simulation from Figure 6-18. When the scatter is averaged over the full azimuthal range, the distinct steps in intensity are reproduced.

In contrast to the azimuthal maps generated for the lithographically designed samples, the coherent 'satellite' peaks are broad due to the short coherence length. There is also less continuity in the positions of the peaks as the domain orientation is rotated. This originates from the large size of the elements compared to the periodicity, meaning that the condition for strong coherent scattering from ten elements is maintained over several degrees of rotation.

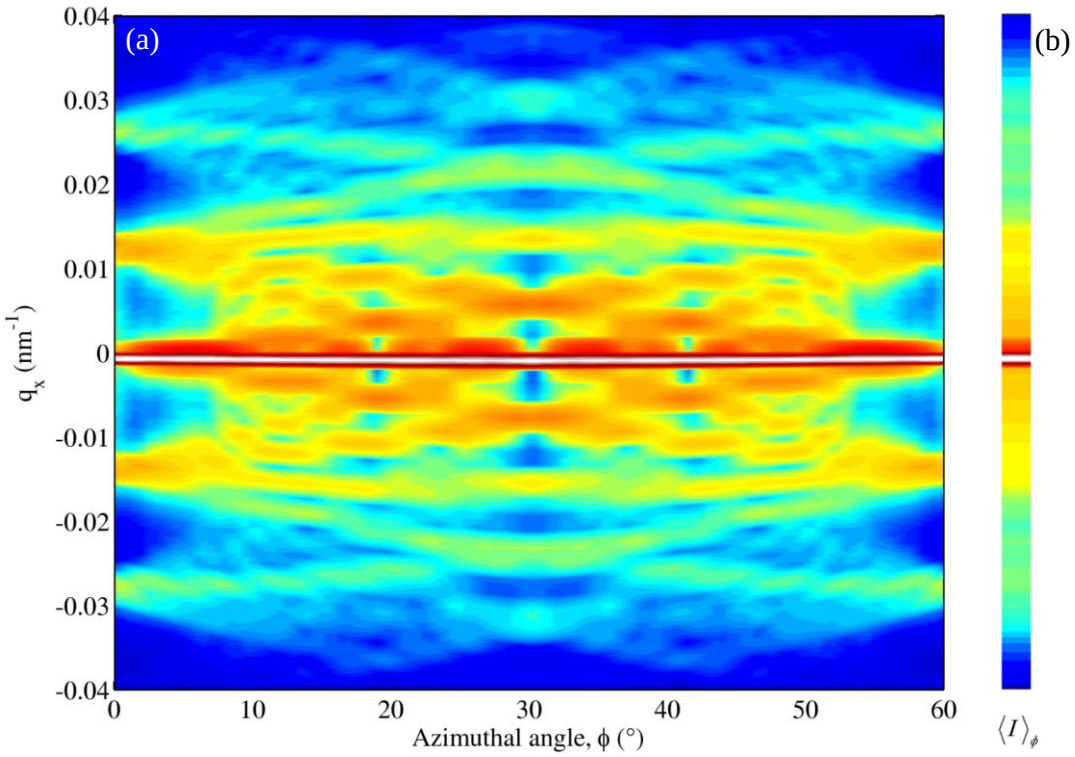

Figure 6-19(a). A simulation of the transverse grazing incidence scatter from a hypothetical perfectly orientated hexagonal close-packed array of 410 nm diameter circular elements with an edge-to-edge separation of 50 nm and a coherent scattering length equivalent to ten elements. (b) The average intensity over all azimuthal orientations, $\langle I \rangle_\phi$, which provides the simulation of scatter from an isotropic array in Figure 6-18.

Due to the superposition of scattering from domains of all orientations, a direct estimation of the array periodicity is difficult to establish. The assumption that the scattering surfaces of the spheres are flat discs is also limited.

From these transverse measurements on self-assembled sphere arrays it is possible to establish a good statistical estimate of the domain size. The best-fit simulation used a value of ten elements.

6.6.3. Simulated GIXS from randomly displaced structures

A contrasting form of disorder occurs when the array coherence is highly perfect, but there is random displacement of each element in the array independent of its neighbours. In this case there is a long coherence length, but the constructive interference is less focussed upon specific scattering vectors.

Using the same nominal structure parameters as in 6.5.2, but introducing random displacements from the perfect square array, it is possible to predict the sensitivity of grazing incidence scattering to such array disorder. The simulated arrays (shown in

Figure 6-20) have a varying root-mean-square displacement κ in a random direction from the nodes of the square array.

The result is shown in Figure 6-21. The effect of dispersion is twofold. First, the sharp satellite peaks subside as κ increases until there are no peaks characteristic of the lattice structure. (They do not, however, appear to broaden.) Meanwhile, the underlying shape of what may be termed the incoherent background scatter rises.

This random displacement is analogous to the Debye-Waller temperature factors used to describe the thermal diffuse scatter from vibrating atoms in a crystal lattice [see for example ref. 68, p. 139].

The controlled engineering of such structures is difficult, since the random displacements are often associated with a reduction in coherence. Such deliberate and precise randomness can however be controllably produced in arrays designed by electron beam lithography. Examples of such a structure are shown in Figure 6-22. The Fortran code custom-written to generate coordinate files of such structures for input into the Raith lithography software is included in Appendix C to this thesis.

Unfortunately, no experimental beamtime has yet been available to test the validity of the predicted grazing incidence scattering from these arrays.

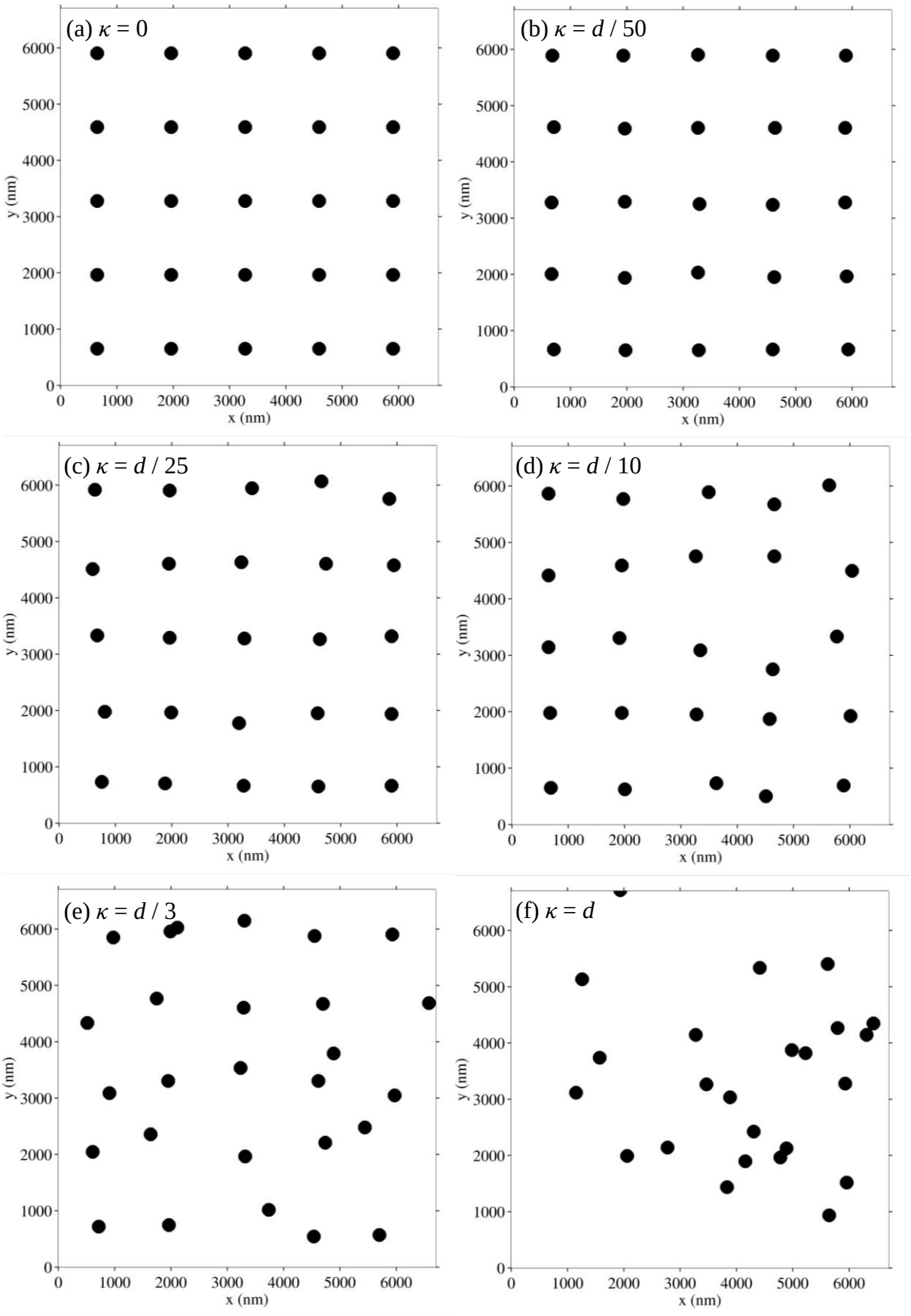

Figure 6-20. Sections of the simulated square array with varying root-mean-square deviations from the nodes of a perfect square array with period d = 1320 nm.

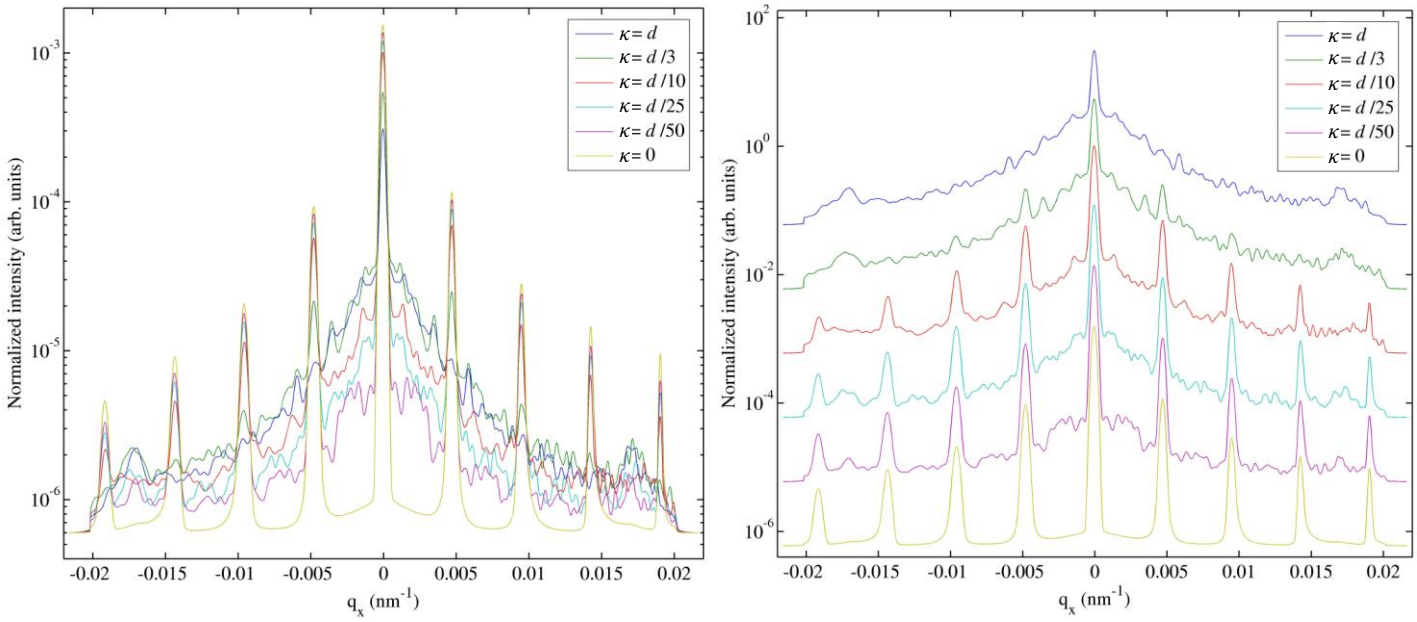

Figure 6-21. Simulated transverse grazing incidence scatter from a square array with varying degrees of random displacement from the square array, relating to the arrays structures simulated in Figure 6-20(a)-(f). Transverse scans along the [0 1] direction. (a) overlaid on the same intensity scale, and (b) sequentially offset by integer orders of magnitude.

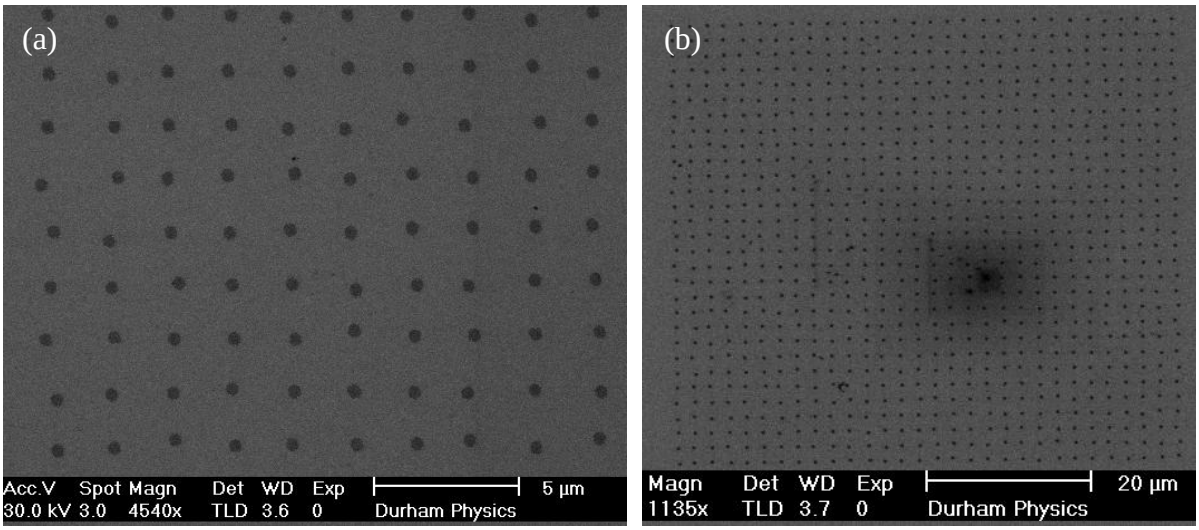

Figure 6-22. Scanning electron microscope images of a controllably disordered yet highly coherent array, with κ = d / 20, and a periodicity d = 2 µm. Structures fabricated in Durham using electron beam lithography.

6.7. Chapter conclusion

The simulation formulation presented here provides a simple and physically intuitive method of determining the grazing incidence scattering measured in a transverse scan when submicron periodic structures are illuminated by coherent radiation.

Direct interpretations of the satellite peaks can reveal the periodicity of the array when scans are made along the simplest <1 0> axes of the array, but when higher order axes are considered, the relatively large size of the elements means that the location of 'satellite peaks' is not trivially related to the array structure. At such orientations, and for arrays where there is a large degree of disorder, a numerical simulation of the transverse scan allows a rapid interpretation of experimental data.

By comparing the experimental data with the simulations the array period can be determined to a high degree of accuracy and precision on length scales ranging from 100 nm to several microns. Additionally, the array symmetry, coherently organised domain size, preferred domain orientation and random element dispersion can be inferred. The element shape can be quantified, although the precision for its measurement is poorer than real-space measurements from microscopy.

In the case of a two-dimensional array, the scattering profile varies as a function of the azimuthal orientation of the surface in the scattering plane. The orientation changes both the reciprocal array vectors probed in the sample surface, and the coherently illuminated footprint on the sample. Both these factors are easily taken into account by the semi-kinematical method developed in this chapter.

There are pre-existing theoretical constructions for the description of diffuse scatter, the most general of which is the dynamical solution of the scalar wave equation presented by Baumbach *et al*. This is valid for truly three-dimensional nanostructures, but the evaluation of such a theory is nontrivial. For periodic nanostructures patterned into thin films where the film thickness is only a few nanometres but the in-plane size is ~100 nm, the work presented in this chapter has shown that an exact dynamical solution is unnecessarily complex.

The measurements presented in this chapter have relied upon the high brilliance of synchrotron radiation. Tolan *et al* successfully used a rotating anode laboratory source to make measurements from single crystal grating structures, but with relatively small arrays of magnetic thin film elements as studied here, the noise levels using in-house x-ray reflectivity apparatus may well conceal the satellite peaks. The work of Tolan *et al* does show that sufficient scattering resolution can be obtained in the laboratory with an x-ray tube and suitable optics. If material applications of periodic nanoscale patterning arise where the patterned surface is of the order of centimetres squared rather than

millimetres squared, the scattered intensity may well be sufficient to allow quantitative measurements of nanoscale array properties to be made using grazing incidence scattering.

Whilst the simplicity of the semi-kinematical theoretical construction presented here provides important advantages in terms of the speed and applicability to imperfect arrays, the conclusions must be carefully qualified. If there is strong scattering, including at critical angles (which is probable in ultrasmooth repeat multilayer structures), a dynamical theory is required to describe the multiple scattering events.

Metrology is most appropriate when it is applied as a comparative science, when the sample of interest is compared to other samples in a series or to a well-characterized reference sample. Using such an experimental process the simple theoretical developments and implementation presented here may be of use in the quality control of nanoscale device arrays.

7. Conclusions and proposals for further study

Synchrotron radiation, scattered at grazing incidence from thin film magnetic and magnetoresistive materials, has been measured and interpreted within a variety of scattering theories in order to extract important structural parameters. Specular reflectivity has been fitted by Parratt's method [80] to obtain layer thicknesses and out-of-plane interface widths. Diffuse x-ray scattering has been interpreted in the Born approximation to establish the topological roughness amplitude, and within the distorted wave Born approximation to characterize the in-plane frequency spectrum of the roughness in the self-affine fractal model developed by Sinha [86]. Grazing incidence in-plane x-ray diffraction has been measured to establish how the in-plane lattice parameter changes due to a combination of thermal expansion and strain relaxation during annealing. Finally, the grazing incidence x-ray interference pattern created by nanoscale and submicron arrays has been modelled within a novel semi-kinematical formulation in order to characterize the degree of array periodicity element dispersion.

Chapter 4 examined the structural modifications of magnetron sputtered Co/Al_2O_3 and Co/MgO interfaces when the cobalt is exposed to oxygen gas before deposition of the metal oxide layer. The quality of these interfaces is fundamental in determining the degree of interlayer magnetostatic coupling and electron tunnelling in magnetic tunnel junctions.

By fitting the specular x-ray reflectivity and transverse diffuse scatter, it was shown that preoxidation reduces chemical intermixing at the Co/Al_2O_3 interface, but that there is no observed change in the amplitude of topological roughness. The conclusion drawn is that preoxidation creates a more uniformly oxidized tunnel barrier, an interpretation consistent with the improved reproducibility of magnetoresistance reported elsewhere [105].

Similar x-ray reflectivity measurements were performed on Co/MgO multilayer thin films, but no discernible change in the interface interdiffusion was found. Further investigations focussed upon the in-plane nature of the conformal topological roughness by analyzing the diffuse scatter measured using a two-dimensional CCD detector in a GISAXS geometry. From these measurements, preoxidation was seen to inhibit the propagation of high-frequency conformal roughness up through the stack of layers. This

implies that by eliminating adjacent short wavelength undulations on either side of the tunnel barrier, the number of strongly interacting dipoles is reduced, and therefore the interlayer magnetostatic coupling is lowered. This interpretation is valid within Néel's sinusoidal coupling [100], and helps explain the important observations of Egelhoff *et al* [102, 105] with reference to linear low-field magnetoresistive sensors.

Whilst these results provide a self-consistent analysis, the inability to precisely fit the specular reflectivity from the Co/MgO multilayer (attributed to variation in thicknesses of the repeated layers) limits the confidence that a complete characterization has been obtained. The possibility of variations in the barrier thickness caused by preoxidation has not been entirely excluded.

Further x-ray reflectivity measurements on carefully designed thin films could detect any layer thickness or morphology changes occur due to preoxidation. The choice of single Co/MgO structures, or of Co/MgO/Co trilayers with a minimum number of underlying buffer layers would enable more direct fitting of the specular reflectivity. By attempting to simplify the structure there is the danger that samples no longer represent realistic device materials. A complementary method would use cross-section transmission electron microscopy to examine realistic device structures. This would give a short-range real-space characterization specifically from the preoxidized interfaces. Since the GISAXS analysis presented here indicates that preoxidation modifies roughness on length scales below twenty nanometres, the restricted field of view in TEM should be inconsequential.

Chapter 5 presented a systematic study of changes during annealing in epitaxial Fe/MgO/Fe and Fe/Au/MgO/Fe surface layers grown in the [001] orientation on an MgO (001) substrate, making use of a range of grazing incidence x-ray techniques.

Inspection of specular reflectivity and grazing incidence diffuse scatter scans during annealing of both samples revealed no perceptible structural changes. The inability to fit the reflectivity within the Parratt formalism was explained by transmission electron microscopy, which showed that high roughness amplitude exceeded the limits of the Parratt model. The topological roughness (estimated as approximately 0.7 nm by Born analysis of the total diffuse scatter and consistent with the TEM) is large compared to Fe/MgO/Fe junctions in other studies which do exhibit coherent tunnelling [128]. Large surface roughness is known to inhibit tunnelling magnetoresistance [143] and in the extreme case can generate 'pinholes' through the tunnel barrier which nullify tunnelling entirely.

Despite this high amplitude roughness, grazing incidence in-plane diffraction revealed that growth of the layers was highly epitaxial, with strong preferred orientation

inherited from the MgO substrate. During annealing to 600 K, relaxation in the in-plane lattice of the thin MgO barrier layer from the iron lattice towards a typical bulk value was observed. Prior to annealing, the as-deposited Fe/MgO/Fe system contained a 3 nm MgO barrier strained by 1.94%; after controlled heating to 600 K, the MgO barrier had a residual strain of 0.28 %, which remained after cooling to 298 K.

The strain dispersion also decreased after annealing, as demonstrated by an analysis of the diffraction peak widths. This is interpreted as the formation of misfit dislocations at the Fe/MgO interface (some of which are present in the highly-strained as-deposited state), which during annealing propagate throughout the MgO barrier. This reduces both strain and strain dispersion.

Very similar results were seen in the Fe/Au/MgO/Fe sample. A reduction of the MgO strain from 2.4% to 1.0% was seen after annealing. The 3 nm gold layer was interpreted as being perfectly commensurate with the underlying iron lattice sites, as would be expected from the very close inherent lattice matching of these two materials. In TEM cross-sections, the gold interlayers appeared to have a smoothing effect on the roughness introduced from the substrate, providing a second important advantage in addition to the likely inhibition of oxidation of the lower iron layer.

The slow, controlled MBE deposition used to produce these samples permitted highly epitaxial films despite the high degree of topological roughness. Annealing has the effect of permanently relieving strain in the barrier MgO, whilst the iron layers expand and contract thermally. The values for the thermal expansivity for the iron, and the values for the MgO deduced from the thermal contraction after annealing are in agreement with previously reported values.

The grazing incidence experimental methods applied in this study could be extremely informative with ultrasmooth epitaxial films; these techniques have the sensitivity to correlate very small structural modifications under controlled deposition conditions with the resulting TMR performance. Unfortunately, at the time of writing it has been impossible to obtain genuinely ultrasmooth Fe/MgO/Fe structures. A systematic comparison of tunnelling performance with in-plane lattice structure would demonstrate the validity that the tunnelling theories which assume perfect lattice registry have to realistic TMR structures.

Chapter 6 showed the development and exploitation of a physically intuitive semi-kinematical model describing grazing incidence x-ray scattering from thin films with periodic patterned surfaces. The model is valid in the weak scattering approximation, and combined the kinematical interference pattern expected from a periodic array with the Fresnel reflectivity characteristic of the material.

A series of examples representing a progression from highly coherent lithographic arrays to disordered self-assembled arrays demonstrated the range of validity of the semi-kinematical theory and its numerical implementation over a range of technologically important length scales and degrees of ordering. Whilst surface periodicity and element dispersion can be measured to a high degree of precision using real-space probe measurements and microscopy techniques, reciprocal space grazing incidence x-ray scattering uniquely combines rapid data collection with intrinsically statistical measurements.

The limitations to the semi-kinematical model must be clarified: firstly, the model is only valid when scattering is weak in comparison with the intensity of the incident wave. It would not describe scattering from periodic multilayer structures due to the strong reinforcement of scattering by repeated layers. Secondly, the model describes only a single thin film. Whilst this simplifies the theoretical description, the corollary is that no metrological information on the layers can be extracted by fitting data with this model. It is clear from simulations of transverse diffuse scatter within the distorted wave Born approximation that the layer structure does indeed influence the diffuse scatter, although the layer structure cannot easily be fitted to diffuse data due to the complexity of the calculations. Specular reflectivity from an unpatterned continuous film could be fitted using the Parratt formalism to provide sensitivity to the layer structure, with the diffuse scatter from a patterned sample providing information of the periodic surface patterning.

Collectively these findings form a thesis showing the strengths and weaknesses of grazing incidence scattering applied to the structural characterization of magnetic thin film materials. The statistical analysis provided by reciprocal space scattering techniques is best used in conjunction with real-space imaging of localized sample regions in order to understand the critical physical processes occurring during fabrication.

A drawback in the recursive fitting of x-ray reflectivity is that the large number of independent material parameters in a many-layer model can be difficult to fit with precision. Therefore, the design of samples optimized for structural sensitivity in measurements is critical. This judgement must find a compromise between samples that are simple enough to analyse, yet realistically similar to device materials.

It is the conclusion of this author that when grazing incidence x-ray scattering is carefully applied to magnetic thin film materials possessing nanometre thicknesses and low surface roughness, an unrivalled precision and range of structural measurements can be obtained.

References

[1] Eastwood, D.S., *X-ray Scattering from Patterned Nanostructures*, M.Sci. Project, University of Durham, Durham (2005).

[2] Herman, M.A. and Sitter, H., *Molecular beam epitaxy: fundamentals and current status*, 2nd edition, Springer Series in Materials Science, Vol. 7, Springer, Berlin (1996).

[3] Chikazumi, S. and shin, 'Ferromagnetic Properties and Superlattice Formation of Iron Nickel Alloys (I)', *Journal of the Physical Society of Japan* **5** (1950) 327-332.

[4] Chikazumi, S. and shin, 'Ferromagnetic Properties and Superlattice Formation of Iron Nickel Alloys (II)', *Journal of the Physical Society of Japan* **5** (1950) 333-338.

[5] Kelly, P.J. and Arnell, R.D., 'Magnetron sputtering: a review of recent developments and applications', *Vacuum* **56** (2000) 159-172.

[6] Gallagher, W.J. and Parkin, S.S.P., 'Development of the magnetic tunnel junction MRAM at IBM: From first junctions to a 16-Mb MRAM demonstrator chip', *IBM Journal of Research and Development* **50** (2006) 5-23.

[7] Harp, G.R. and Parkin, S.S.P., 'Seeded epitaxy of metals by sputter deposition', *Applied Physics Letters* **65** (1994) 3063-3065.

[8] Harp, G.R. and Parkin, S.S.P., 'Epitaxial growth of metals by sputter deposition', *Thin Solid Films* **288** (1996) 315-324.

[9] Bauer, E., 'Phaenomenologische theorie der kristallabscheidung an oberflachen I [Phenomenological theory of thin film crystal deposition I]', *Zeitschrift fur Kristallographie* **110** (1958) 372-394.

[10] Bauer, E. and van der Merwe, J.H., 'Structure and growth of crystalline superlattices: From monolayer to superlattice', *Physical Review B* **33** (1986) 3657-3671.

[11] Freund, L.B. and Suresh, S., *Thin film materials: stress, defect formation and surface evolution*, Cambridge University Press, Cambridge (2003).

[12] Frank, F.C. and van der Merwe, J.H., 'One-dimensional dislocations: I. Static theory', *Proceedings of the Royal Society of London* **A198** (1949) 205-216.

[13] Frank, F.C. and van der Merwe, J.H., 'One-dimensional dislocations: II. Misfitting monolayers and orientated growth', *Proceedings of the Royal Society of London* **A198** (1949) 216-225.

[14] Ball, C.A.B. and van der Merwe, J.H., 'The growth of dislocation-free layers' in *Dislocations in Solids*, vol. 6, Nabarro, F.R.N. (Ed.), North-Holland, Amsterdam (1983).

[15] Palasantzas, G., 'Roughness spectrum and surface width of self-affine fractal surfaces via the K-correlation model', *Physical Review B* **48** (1993) 14472.

[16] Sen, S. and Kouklin, N.A., 'Nanofabrication based upon self-assembled alumina templates' in *Nanofabrication*, Tseng, A.A. (Ed.), World Scientific, Singapore (2008), chapter 3, p. 166.

[17] Ross, C., 'Patterned magnetic recording media', *Annual Review of Materials Research* **31** (2001) 203-235.

[18] Cowburn, R.P. and Welland, M.E., 'Room Temperature Magnetic Quantum Cellular Automata', *Science* **287** (2000) 1466-1468.

[19] Kiselev, S.I., Sankey, J.C., Krivorotov, I.N., Emley, N.C., Schoelkopf, R.J., Buhrman, R.A., and Ralph, D.C., 'Microwave oscillations of a nanomagnet driven by a spin-polarized current', *Nature* **425** (2003) 380-383.

[20] Bert, T., Utke, I., Gaillard, C., and Hoffmann, P., 'Periodic structure formation by focussed electron-beam-induced deposition', *Journal of Vacuum Science & Technology B* **22** (2004) 2504-2510.

[21] Yamazaki, K., 'Electron beam direct writing' in *Nanofabrication*, Tseng, A.A. (Ed.), World Scientific, Singapore (2008), chapter 7.

[22] Yamazaki, K. and Namatsu, H., '5 nm order electron-beam lithography for nanodevice fabrication', *Japanese Journal of Applied Physics* **43** (2004) 3767-3771.

[23] Owen, H. and Rissman, P., 'Proximity effect correction for electron beam lithography by equalization of background dose ', *Journal of Applied Physics* **54** (1983) 3573-3581.

[24] Parikh, M., 'Self-consistent proximity effect correction technique for resist exposure', *Journal of Vacuum Science & Technology* **15** (1978) 931-933.

[25] Atkinson, D., 'Patterning nanostructures to study magnetization processes', *Journal of Physics: Conference Series* **17** (2005) 33-39.

[26] Denkov, N.D., Velev, D., Kralchevsky, P.A., Ivanov, I.B., Yoshimura, H., and Nagayamat, K., 'Mechanism of Formation of Two-Dimensional Crystals from Latex Particles on Substrates', *Langmuir* **8** (1992) 3183-3190.

[27] Micheletto, R., Fukuda, H., and Ohtsu, M., 'A Simple Method for the Production of a Two-Dimensional, Ordered Array of Small Latex Particles', *Langmuir* **11** (1995) 3333-3336.

[28] Weekes, S.M., Ogrin, F.Y., Murray, W.A., and Keatley, P.S., 'Macroscopic Arrays of Magnetic Nanostructures from Self-Assembled Nanosphere Templates', *Langmuir* **23** (2007) 1057-1060.

[29] Albrecht, M., Hu, G., Guhr, I.L., Ulbrich, T.C., Boneberg, J., Leiderer, P., and Schatz, G., 'Magnetic multilayers on nanospheres', *Nature Materials* **4** (2005) 203-206.

[30] Makarov, D., Brombacher, C., Liscio, F., Maret, M., Parlinska, M., Meier, S., Kappenberger, P., and Albrecht, M., 'FePt films on self-assembled SiO_2 particle arrays', *Journal of Applied Physics* **103** (2008), art. no. 053903.

[31] Thomson, W., 'On the Electro-dynamic Qualities of Metals: Effects of Magnetization on the Electric Conductivity of Nickel and Iron', *Proceedings of the Royal Society of London* **8** (1856-1857) 546-550.

[32] Mott, N.F., 'The electrical conductivity of transition metals', *Proceedings of the Royal Society of London - Series A* **153** (1936) 699-726.

[33] Tumanski, S., *Thin film magnetoresistive sensors*, Institute of Physics Publishing, Bristol (2001), pp. 263-265.

[34] Binasch, G., Grünberg, P., Saurenbach, F., and Zinn, W., 'Enhanced magnetoresistance in layered magnetic-structures with antiferromagnetic interlayer exchange', *Physical Review B* **39** (1989) 4828-4830.

[35] Baibich, M.N., Broto, J.M., Fert, A., Vandau, F.N., Petroff, F., Eitenne, P., Creuzet, G., Friederich, A., and Chazelas, J., 'Giant magnetoresistance of (001) Fe / (001) Cr magnetic superlattices', *Physical Review Letters* **61** (1988) 2472-2475.

[36] Thompson, S.M., 'The discovery, development and future of GMR: The Nobel Prize 2007', *Journal of Physics D: Applied Physics* **41** (2008), art. no. 093001.

[37] Grünberg, P., Schreiber, R., Pang, Y., Brodsky, M.B., and Sowers, H., 'Layered magnetic structures: evidence for antiferromagnetic coupling of Fe layers across Cr interlayer', *Physical Review Letters* **57** (1986) 2442-2445.

[38] Parkin, S.S.P., 'Systematic variation of the strength and oscillation period of indirect magnetic exchange coupling through the 3d, 4d and 5d transition metals', *Physical Review Letters* **67** (1991) 3598-3601.

[39] Bruno, P. and Chappert, C., 'Ruderman-Kittel theory of oscillatory interlayer exchange coupling', *Physical Review B* **46** (1992) 261-270.

[40] Dieny, B., Speriosu, V.S., Metin, S., Parkin, S.S.P., Guerney, B.A., Baumgart, P., and Wilhoit, D.R., 'Magnetotransport properties of magnetically soft spin-valve structures', *Journal of Applied Physics* **69** (1991) 4774-4779.

[41] Freitas, P.P., Ferreira, R., Cardoso, S., and Cardoso, F., 'Magnetoresistive sensors', *Journal of Physics: Condensed Matter* **19** (2007), art. no. 165221.

[42] Parkin, S.S.P., 'Origin of enhanced magnetoresistance of magnetic multilayers: Spin-dependent scattering from magnetic interface states', *Physical Review Letters* **71** (1993) 1641.

[43] Parkin, S.S.P., Li, Z.G., and Smith, D.J., 'Giant Magnetoresistance in antiferromagnetic Co/Cu multilayers', *Applied Physics Letters* **58** (1991) 2710-2712.

[44] Butler, W.H., Zhang, X.G., Schulthess, T.C., and MacLaren, J.M., 'Spin-dependent tunneling conductance of Fe | MgO | Fe sandwiches', *Physical Review B* **63** (2001), art. no. 054416.

[45] Mathon, J. and Umerski, A., 'Theory of tunneling magnetoresistance of an epitaxial Fe/MgO/Fe(001) junction', *Physical Review B* **63** (2001), art. no. 220403.

[46] Jullière, M., 'Tunneling between ferromagnetic films', *Physics Letters A* **54** (1975) 225-226.

[47] Moodera, J.S., Kinder, L.R., Wong, T.M., and Meservey, R., 'Large magnetoresistance at room temperature in ferromagnetic thin film tunnel junction', *Physical Review Letters* **74** (1995) 3272-3276.

[48] Miyazaki, T. and Tezuka, N., 'Giant Magnetic Tunneling Effect in $Fe/Al_2O_3/Fe$ Junction', *Journal of Magnetism and Magnetic Materials* **139** (1995) L231-L234.

[49] Parkin, S.S.P., Yang, H., Yang, S.-H., and Hayashi, M., 'Magnetic tunnel junctions' in *Handbook of magnetism and advanced magnetic materials*, vol. 5, Parkin, S.S.P. and Kronmüller, H. (Eds.), John Wiley & Sons, Chichester (2007), pp. 2571-2591.

[50] Meservey, R. and Tedrow, P.M., 'Spin-polarized electron tunneling', *Physics Reports* **238** (1994) 173-243.

[51] Yuasa, S. and Djayaprawira, D.D., 'Giant tunnel magnetoresistance in magnetic tunnel junctions with a crystalline MgO(0 0 1) barrier', *Journal of Physics D: Applied Physics* (2007) R337.

[52] Yuasa, S., Nagahama, T., Fukushima, A., Suzuki, Y., and Ando, K., 'Giant room-temperature magnetoresistance in single-crystal Fe/MgO/Fe magnetic tunnel junctions', *Nature Materials* **3** (2004) 868-871.

[53] Parkin, S.S.P., Kaiser, C., Panchula, A., Rice, P.M., Hughes, B., Samant, M., and Yang, S.-H., 'Giant tunnelling magnetoresistance at room temperature with MgO (100) tunnel barriers', *Nature Materials* **3** (2004) 862-867.

[54] Djayaprawira, D.D., Tsunekawa, K., Nagai, M., Maehara, H., Yamagata, S., Watanabe, N., Yuasa, S., Suzuki, Y., and Ando, K., '230% room-temperature magnetoresistance in CoFeB/MgO/CoFeB magnetic tunnel junctions', *Applied Physics Letters* **86** (2005), art. no. 092502.

[55] Yuasa, S., Suzuki, Y., Katayama, T., and Ando, K., 'Characterization of growth and crystallization processes in CoFeB/MgO/CoFeB magnetic tunnel junction structure by reflective high-energy electron diffraction', *Applied Physics Letters* **87** (2005), art. no. 242503.

[56] Meyerheim, H.L., Popescu, R., Kirschner, J., Jedrecy, N., Sauvage-Simkin, M., Heinrich, B., and Pinchaux, R., 'Geometrical and Compositional Structure at Metal-Oxide Interfaces: MgO on Fe(001)', *Physical Review Letters* **87** (2001) 076102.

[57] Zhang, X.G., Butler, W.H., and Bandyopadhyay, A., 'Effects of the iron oxide layer in Fe-FeO-MgO-Fe tunnel barriers', *Physical Review B* **68** (2003), art. no. 092402.

[58] Tsymbal, E.Y. and Pettifor, D.G., 'The influence of spin-independent disorder on giant magnetoresistance', *Journal of Physics: Condensed Matter* **8** (1996) L569-L575.

[59] Mathon, J. and Umerski, A., 'Theory of tunneling magnetoresistance in a disordered Fe/MgO/Fe(001) junction', *Physical Review B* **74** (2006), art. no. 140404.

[60] Atkinson, D., Eastwood, D.S., and Bogart, L.K., 'Controlling domain wall pinning in planar nanowires by selecting domain wall type and its application in a memory concept', *Applied Physics Letters* **92** (2008), art. no. 022510.

[61] Röntgen, W.C., 'On a new kind of radiation', *Nature* **53** (1896) 274-276.

[62] Friedrich, W., Knipping, P., and von Laue, M., 'Interferenz Erscheinungen bei Röntgenstrahlen [Appearances of interference in X-rays]', *Proceedings of the Bavarian Academy of Sciences* (1912) 303-322.

[63] Bragg, W.L., 'The Structure of Some Crystals as Indicated by Their Diffraction of X-rays', *Proceedings of the Royal Society of London - Series A* **89** (1913) 248-277.

[64] Laue, M., 'Eine quantitative Prüfung der Theorie für die Interferenzerscheinungen bei Röntgenstrahlen [A quantitative examination of the theory for interference features with X-rays]', *Proceedings of the Bavarian Academy of Sciences* (1912) 363-373.

[65] Ewald, P.P., 'Zur Begründung der Kristalloptik. III. Die Kristalloptik der Röntgenstrahlen [Understanding crystal optics III: The crystal optics of the X-ray]', *Annalen der Physik (Leipzig)* **54** (1917) 519-597.

[66] Compton, A.H., 'The total reflection of X-rays', *Philosophical Magazine* **45** (1923) 1121-31.

[67] Born, M. and Wolf, E., *Principles of optics*, 7th edition, Cambridge University Press, Cambridge (2003).

[68] Als-Nielsen, J. and McMorrow, D., *Elements of modern x-ray physics*, Wiley, Chichester (2001).

[69] Birkholz, M., *Thin film analysis by X-ray scattering*, Wiley-VCH, Weinheim (2006).

[70] Pietsch, U., Holý, V., and Baumbach, T., *High-resolution X-ray scattering: from thin films to nanostructures*, 2nd edition, Springer Tracts in Modern Physics, Vol. 149, Springer, Berlin (2004).

[71] Tolan, M., *X-ray scattering from soft-matter thin films*, Springer Tracts in Modern Physics, Vol. 148, Springer, Berlin (1999).

[72] Bowen, D.K. and Tanner, B.K., *X-ray Metrology in Semiconductor Manufacturing*, Taylor and Francis, London (2006).

[73] Robinson, I.K. and Tweet, D.J., 'Surface X-ray diffraction', *Reports on Progress in Physics* (1992) 599-651.

[74] Stoev, K.N. and Sakurai, K., 'Review on grazing incidence X-ray spectrometry and reflectometry', *Spectrochimica Acta Part B: Atomic Spectroscopy* **54** (1999) 41-82.

[75] Stangl, J., Holý, V., and Bauer, G., 'Structural properties of self-organized semiconductor nanostructures', *Reviews of Modern Physics* **76** (2004) 725-783.

[76] Schmidbauer, M., *X-ray diffuse scattering from self-organized mesoscopic semiconductor structures*, Springer Tracts in Modern Physics, Vol. 199, Springer, Berlin (2004).

[77] Maslen, E.N., Fox, A.G., and O'Keefe, M.A., 'X-ray Scattering' in *International Tables for Crystallography, Volume C*, Prince, E. (Ed.), Kluwer Academic, Dordrecht (2004), p. 554.

[78] 'X-ray interactions with matter calculator' (website, accessed 25th October 2008), Center for X-ray Optics, Lawrence Berkeley National Laboratory, Berkeley; available from: http://www.cxro.msd.lbl.gov/.

[79] Kiessig, H., 'Interferenz von Röntgenstrahlen an dünnen Schichten [Interference of X-rays in thin layers]', *Annalen der Physik* **402** (1931) 715-725 & 769-788.

[80] Parratt, L.G., 'Surface Studies of Solids by Total Reflection of X-Rays', *Physical Review* **95** (1954) 359-369.

[81] Névot, L. and Croce, P., 'Characterization of surfaces by grazing x-ray reflection - application to study of polishing of some silicate glasses', *Revue de Physique Appliquée* (1980) 761-779.

[82] de Boer, D.K.G., 'Influence of the roughness profile on the specular reflectivity of x-rays and neutrons', *Physical Review B* **49** (1994) 5917-5820.

[83] Wormington, M., Panaccione, C., Matney, K.M., and Bowen, D.K., 'Characterization of structures from X-ray scattering data using genetic algorithms', *Philosophical Transactions of the Royal Society of London - Series A* **357** (1999) 2827-2848.

[84] *Bede REFS (version 4.5): User Manual*, Bede plc, Durham (2007).

[85] Björck, M. and Andersson, G., 'GenX: an extensible X-ray reflectivity refinement program utilizing differential evolution', *Journal of Applied Crystallography* **40** (2007) 1174-1178.

[86] Sinha, S.K., Sirota, E.B., Garoff, S., and Stanley, H.B., 'X-ray and neutron scattering from rough surfaces', *Physical Review B* **38** (1988) 2297-2311.

[87] 'Electromagnetic Wave MATLAB Library: Rsgenf.m function' (website, accessed 20th December 2008); available from: http://www.emwave.com/.

[88] Yoneda, Y., 'Anomalous Surface Reflection of X Rays', *Physical Review* **131** (1963) 2010-2013.

[89] Wormington, M., Pape, I., Hase, T.P.A., Tanner, B.K., and Bowen, D.K., 'Evidence for an electron density gradient at polished surfaces from grazing-incidence X-ray scattering', *Philosophical Magazine Letters* **74** (1996) 211-216.

[90] Holý, V. and Baumbach, T., 'Nonspecular x-ray reflection from rough multilayers', *Physical Review B* **49** (1994) 10668-10676.

[91] Holý, V., 'Diffuse X-ray scattering from non-ideal periodical crystalline multilayers', *Applied Physics A: Materials Science & Processing* **58** (1994) 173-180.

[92] Salditt, T., Metzger, T.H., Brandt, C., Klemradt, U., and Peisl, J., 'Determination of the static scaling exponent of self-affine interfaces by nonspecular x-ray scattering', *Physical Review B* **51** (1995) 5617-5627.

[93] Paniago, R., Forrest, R., Chow, P.C., Moss, S.C., Parkin, S.S.P., and Cookson, D., 'Growth mode and asymptotic smoothing of sputtered Fe/Au multilayers studied by diffuse x-ray scattering', *Physical Review B* **56** (1997) 13442-13454.

[94] Marra, W.C., Eisenberger, P., and Cho, A.Y., 'X-ray total external reflection – Bragg diffraction: A structural study of the GaAs-Al interface', *Journal of Applied Physics* **50** (1979) 6927-6933.

[95] Doerner, M.F. and Brennan, S., 'Strain distribution in thin aluminum films using x-ray depth profiling', *Journal of Applied Physics* **63** (1988) 126-131.

[96] Gibaud, A., Wang, J., Tolan, M., Vignaud, G., and Sinha, S.K., 'An X-ray Scattering Study of Laterally Modulated Structures: Investigation of Coherence and Resolution Effects with a Grating', *Journal de Physique I* **6** (1996) 1085-1094.

[97] Morrison, G.R., 'Diffractive X-ray Optics' in *X-ray Science and Technology*, Michette, A.G. and Buckley, C.J. (Eds.), Institute of Physics Publishing, Bristol (1993), chapter 8.

[98] Clarke, J., *X-ray scattering from thin films and interfaces*, PhD Thesis, University of Durham (1999), chapter 7.

[99] Tanner, B.K., Hase, T.P.A., Clarke, J., Pape, I., Li-Bassi, A., and Fulthorpe, B.D., 'High resolution X-ray scattering from nanotechnology materials', *Applied Surface Science* (2001) 202-208.

[100] Néel, L., 'Magnetisme - sur un nouveau mode de couplage entre les aimantations de deux couches minces ferromagnetiques [Magnetism - on a new mode of coupling between the magnetizations of two ferromagnetic thin layers]', *Comptes Rendus Hebdomadaires Des Seances De L' Academie Des Sciences* **255** (1962) 1676.

[101] Kools, J.C.S., Kula, W., Mauri, D., and Lin, T., 'Effect of finite magnetic film thickness on Néel coupling in spin valves', *Journal of Applied Physics* **85** (1999) 4466-4468.

[102] Egelhoff Jr., W.F., McMichael, R.D., Dennis, C.L., Stiles, M.D., Shapiro, A.J., Maranville, B.B., and Powell, C.J., 'Preoxidation as a general approach to suppressing orange-peel coupling in magnetic tunnel junctions', *IEEE Transactions on Magnetics* **42** (2006) 2664-2666.

[103] Egelhoff Jr., W.F., Chen, P.J., Powell, C.J., Stiles, M.D., McMichael, R.D., Judy, J.H., Takano, K., and Berkowitz, A.E., 'Oxygen as a surfactant in the

growth of giant magnetoresistance spin valves', *Journal of Applied Physics* **82** (1997) 6142-6151.

[104] Schrag, B.D., Anguelouch, A., Gang, X., Trouilloud, P., Yu, L., Gallagher, W.J., and Parkin, S.S.P., 'Magnetization reversal and interlayer coupling in magnetic tunneling junctions', **87** (2000) 4682-4684.

[105] Egelhoff Jr., W.F., McMichael, R.D., Dennis, C.L., Stiles, M.D., Shapiro, A.J., Maranville, B.B., and Powell, C.J., 'Suppression of orange-peel coupling in magnetic tunnel junctions by preoxidation', *Applied Physics Letters* **88** (2006), art. no. 162508.

[106] Egelhoff Jr., W.F., McMichael, R.D., Dennis, C.L., Stiles, M.D., Johnson, F., Shapiro, A.J., Maranville, B.B., and Powell, C.J., 'Soft magnetic layers for low-field-detection magnetic sensors', *Thin Solid Films* **505** (2006) 90-92.

[107] Brown, S.D., Bouchenoire, L., Bowyer, D., Kervin, J., Laundy, D., Longfield, M.J., Mannix, D., Paul, D.F., Stunault, A., Thompson, P., Cooper, M.J., Lucas, C.A., and Stirling, W.G., 'The XMaS beamline at ESRF: instrumental developments and high resolution diffraction studies', *Journal of Synchrotron Radiation* **8** (2001) 1172-1181.

[108] Buchanan, J.D.R., Hase, T.P.A., Tanner, B.K., Chen, P.J., Gan, L., Powell, C.J., and Egelhoff Jr., W.F., 'Anomalously large intermixing in aluminum–transition-metal bilayers', *Physical Review B* **66** (2002), art. no. 104427.

[109] Phang, Y.H., Savage, D.E., Kariotis, R., and Lagally, M.G., 'X-ray diffraction measurement of partially correlated interfacial roughness in multilayers', *Journal of Applied Physics* **74** (1993) 3181-3188.

[110] Pym, A.T.G., Lamperti, A., Tanner, B.K., Dimopoulos, T., Ruhrig, M., and Wecker, J., 'Interface sharpening in CoFeB magnetic tunnel junctions', *Applied Physics Letters* **88** (2006), art. no. 162505.

[111] Marquardt, D., 'An Algorithm for Least-Squares Estimation of Nonlinear Parameters', *SIAM Journal of Applied Mathematics* **11** (1963) 431-441.

[112] Hammersley, A.P., *FIT2D: An Introduction and Overview*, E.S.R.F. Internal Report ESRF97HA02T, Grenoble (1997). Accessed (on 14th January 2009) online at www.esrf.eu/computing/scientific/FIT2D/.

[113] Salditt, T., Metzger, T.H., and Peisl, J., 'Kinetic Roughness of Amorphous Multilayers Studied by Diffuse-X-Ray Scattering', *Physical Review Letters* **73** (1994) 2228-2231.

[114] Salditt, T., Lott, D., Metzger, T.H., Peisl, J., Vignaud, G., Legrand, J.F., Grübel, G., Høghøi, P., and Schärpf, O., 'Characterization of interface roughness in W/Si multilayers by high resolution diffuse X-ray scattering', *Physica B* **221** (1996) 13-17.

[115] Pym, A.T.G., Rozatian, A.S.H., Marrows, C.H., Brown, S.D., Bouchenoire, L., Hase, T.P.A., and Tanner, B.K., 'The in-plane length scale of the conformal interface roughness as a function of bilayer repeat number in Co/Pd multilayers', *Journal of Physics D: Applied Physics* **38** (2005) A190-A194.

[116] Kadar, M., Parisi, G., and Zhang, Y.-C., 'Dynamic scaling of growing interfaces', *Physical Review Letters* **56** (1986) 889-892.

[117] Barabási, A.-L. and Stanley, H.E., *Fractal concepts in surface growth*, Cambridge University Press, Cambridge (1995).

[118] Tang, C., Alexander, S., and Bruinsma, R., 'Scaling theory for the growth of amorphous films', *Physical Review Letters* **64** (1990) 772-775.

[119] Schrag, B.D., Anguelouch, A., Ingvarsson, S., Gang, X., Yu, L., Trouilloud, P.L., Gupta, A., Wanner, R.A., Gallagher, W.J., Rice, P.M., and Parkin, S.S.P., 'Néel "orange-peel" coupling in magnetic tunneling junction devices', *Applied Physics Letters* **77** (2000) 2373-2375.

[120] Kaye, G.W.C. and Laby, T.H., (original authors), *Tables of physical and chemical constants*, 16th edition, Noyes, J.G., Phillips, G.F., Jones, O., and Asher, J. (Eds.), Longman, London (1995).

[121] Kanaji, T. and Urano, T., 'Atomic and Electronic Structure of Ultrathin Iron Film on MgO(001) Surface', *Journal of the Physical Society of Japan* **57** (1988) 3403-3410.

[122] Vassent, J.L., Dynna, M., Marty, A., Gilles, B., and Patrat, G., 'A study of growth and the relaxation of elastic strain in MgO on Fe(001)', *Journal of Applied Physics* **80** (1996) 5727-5735.

[123] Vassent, J.L., Marty, A., Gilles, B., and Chatillon, C., 'Thermodynamic analysis of molecular beam epitaxy of MgO(s) I. MgO vaporization by electron bombardment', *Journal of Crystal Growth* **219** (2000) 434-443.

[124] Vassent, J.L., Marty, A., Gilles, B., and Chatillon, C., 'Thermodynamic analysis of molecular beam epitaxy of MgO(s) II. Epitaxial growth of MgO layers on Fe(0 0 1) substrates', *Journal of Crystal Growth* **219** (2000) 444-450.

[125] Meyerheim, H.L., Popescu, R., Jedrecy, N., Vedpathak, M., Sauvage-Simkin, M., Pinchaux, R., Heinrich, B., and Kirschner, J., 'Surface X-ray diffraction analysis of the MgO/Fe(001) interface: Evidence for an FeO layer', *Physical Review B* **65** (2002), art. no. 144433.

[126] Raanaei, H., Lidbaum, H., Liebig, A., Leifer, K., and Hjörvarsson, B., 'Structural coherence and layer perfection in Fe/MgO multilayers', *Journal of Physics: Condensed Matter* **20** (2008), art. no. 055212.

[127] Matsumoto, R., Fukushima, A., Nagahama, T., Suzuki, Y., Ando, K., and Yuasa, S., 'Oscillation of giant tunneling magnetoresistance with respect to tunneling barrier thickness in fully epitaxial Fe/MgO/Fe magnetic tunnel junctions', *Applied Physics Letters* **90** (2007), art. no. 252506.

[128] Mizuguchi, M., Suzuki, Y., Nagahama, T., and Yuasa, S., 'Surface morphology of epitaxial magnetic tunnel junctions', *Journal of Nanoscience and Nanotechnology* **7** (2007) 255-258.

[129] Tusche, C., Meyerheim, H.L., Jedrecy, N., Renaud, G., and Kirschner, J., 'Growth sequence and interface formation in the Fe/MgO/Fe(001) tunnel junction analyzed by surface x-ray diffraction', *Physical Review B* **74** (2006), art. no. 195422.

[130] Mathon, J. and Umerski, A., 'Theory of resonant tunneling in an epitaxial Fe/Au/MgO/Au/Fe(001) junction', *Physical Review B* **71** (2005), art. no. 220402.

[131] Fuß, A., Demokritov, S., Grunberg, P., and Zinn, W., 'Short- and long period oscillations in the exchange coupling of Fe across epitaxially grown Al- and Au-interlayers', *Journal of Magnetism and Magnetic Materials* **103** (1992) L221-L227.

[132] Dekadjevi, D.T., Ryan, P.A., Hickey, B.J., Fulthorpe, B.D., and Tanner, B.K., 'Experimental Evidence for Electron Channeling in Fe/Au (100) Superlattices', *Physical Review Letters* **86** (2001) 5787.

[133] Cole, A., Hickey, B.J., Hase, T.P.A., Buchanan, J.D.R., and Tanner, B.K., 'Influence of the interfacial roughness on electron channelling in Fe/Au(001) multilayers', *Journal of Physics: Condensed Matter* **16** (2004) 1197-1209.

[134] Rickart, M., Roos, B.F.P., Mewes, T., Jorzick, J., Demokritov, S.O., and Hillebrands, B., 'Morphology of epitaxial metallic layers on MgO substrates: influence of submonolayer carbon contamination', *Surface Science* **495** (2001) 68-76.

[135] Ali, M. (2008), in private correspondence.

[136] *CRC Handbook of Chemistry and Physics*, 77th edition, Lide, D.R. (Ed.) CRC Press, Boca Raton (1996).

[137] Weisbrod, U., Gutschke, R., Knoth, J., and Schwenke, H., 'Total reflection X-ray fluorescence spectrometry for quantitative surface and layer analysis', *Applied Physics A: Materials Science & Processing* **53** (1991) 449-456.

[138] Buchanan, J.D.R., Hase, T.P.A., Tanner, B.K., Powell, C.J., and Egelhoff Jr., W.F., 'Interface intermixing and in-plane grain size in aluminum transition-metal bilayers', *Journal of Applied Physics* **96** (2004) 7278-7282.

[139] Williams, D.B. and Carter, C.B., *Transmission Electron Microscopy: A Textbook for Materials Science*, Kluwer Academic, New York (1996).

[140] McGrouther, D. (2008), in private correspondence.

[141] Tiley, R.J.D., *Understanding Solids: The Science of Materials*, John Wiley and Sons, Chichester (2004), pp. 208-212.

[142] Alexander, H. and Haasen, P., 'Dislocations and plastic flow in the diamond structure', *Solid State Physics* **22** (1968) 27-158.

[143] Shen, W., Mazumdar, D., Zou, X., Liu, X., Schrag, B.D., and Xiao, G., 'Effect of film roughness in MgO-based magnetic tunnel junctions', *Applied Physics Letters* **88** (2006), art. no. 182508.

[144] White, R.L., Newt, R.M.H., and Pease, R.F.W., 'Patterned media: a viable route to 50 Gbit/in^2 and up for magnetic recording?' *I.E.E.E. Transactions on Magnetics* **33** (1997) 990-995.

[145] Nordquist, K., Pendharkar, S., Durlam, M., Resnick, D., Tehrani, S., Mancini, D., Zhu, T., and Shi, J., 'Process development of sub-0.5 μm nonvolatile

magnetoresistive random access memory arrays', *Journal of Vacuum Science and Technology B* **15** (1997) 2274-2278.

[146] Reininger, R. and Saile, V., 'A soft X-ray grating monochromator for undulator radiation', *Nuclear Instruments and Methods in Physics Research Section A: Accelerators, Spectrometers, Detectors and Associated Equipment* **288** (1990) 343-348.

[147] Weitkamp, T., Diaz, A., David, C., Pfeiffer, F., Stampanoni, M., Cloetens, P., and Ziegler, E., 'X-ray phase imaging with a grating interferometer', *Optics Express* **13** (2005) 6296 - 6304.

[148] Tolan, M., König, G., Brügemann, L., Press, W., Brinkop, F., and Kotthaus, J.P., 'X-Ray Diffraction from Laterally Structured Surfaces: Total External Reflection and Grating Truncation Rods', *Europhysics Letters* **20** (1992) 223-228.

[149] Tolan, M., Press, W., Brinkop, F., and Kotthaus, J.P., 'X-ray diffraction from laterally structured surfaces: Total external reflection', *Physical Review B* **51** (1995) 2239-2251.

[150] Baumbach, T. and Lübbert, D., 'Grazing incidence diffraction by laterally patterned semicondctor nanostructures', *Journal of Physics D: Applied Physics* **32** (1999) 726-740.

[151] Baumbach, T., Lübbert, D., and Gailhanou, M., 'Strain and shape analysis of multilayer surface gratings by coplanar and by grazing-incidence diffraction', *Journal of Applied Physics* **87** (2000) 3744-3758.

[152] Eastwood, D.S., Hase, T.P.A., van Kampen, M., Bručas, R., Hjörvarsson, B., Atkinson, D., and Tanner, B.K., 'X-ray scattering from two-dimensionally patterned magnetic thin film nanoscale arrays', *Superlattices and Microstructures* **41** (2007) 163-167.

Appendices

Appendix A. MATLAB code for the analytical simulation of transverse diffuse scatter from a rough surface

A.1 transfunc.m

```
%Script to provide an analytical calculation of the transverse diffuse scatter

clear

transfunc_specs                                 %load material parameters from a script

ac_rad=sqrt(2*delta)
ac_deg=ac_rad/pi*180;
p_plus=sqrt(0.5*(sqrt((ai_rad.^2-ac_rad^2).^2+4*beta^2)+(ai_rad.^2-ac_rad^2)));
                                                %real part of complex transmission angle
p_minus=sqrt(0.5*(sqrt((ai_rad.^2-ac_rad^2).^2+4*beta^2)-(ai_rad.^2-ac_rad^2)));
                                                %imag part of complex transmission angle

Rf_simple=((ai_rad-p_plus).^2+p_minus.^2)./((ai_rad+p_plus).^2+p_minus.^2);

rs=(kiz-ktz)./(kiz+ktz);                        % independent of polarisation
ts=(2*kiz)./(kiz+ktz);                          % ... for angles << Brewster angle

conj(rs);
Tf=ts.*conj(ts);

S0=1; W=0.001

S_prefactor=(k^2*(1-n)^2).*conj(k^2*(1-n)^2)/16*pi;
S_lorentzian=W./(qx.^2+(W/2)^2*qz.^4);

S1=S0*S_prefactor*S_lorentzian;
I0=1

source_z_slit=0.5
source_y_slit=0.5
    source_beam_area=source_z_slit*source_y_slit
det_z_slit=0.5
det_y_slit=0.5
det_dist=1
    det_solid_angle=det_z_slit*det_y_slit/det_dist
sample_x=5
sample_y=5
    sample_area=sample_x*sample_y

    geometry_factor=det_solid_angle./source_beam_area*sample_area./sin(ai_rad);

Ilor=I0*S1.*Tf.*fliplr(Tf).*geometry_factor;

figure(1); clf; plot(kiz, Tf); title('Transmission coefficient'); xlabel('k_f_,_z}');
ylabel('Transmission')

figure(2); clf; plot(ai_deg, Ilor); legend(['lorentzian']); title('Resulting total
intensity'); xlabel('a_i (°)'); ylabel('Norm. Int.'); set(gca, 'yscale','log');
ylim([max(Ilor)/1e7 max(Ilor)])
```

A.2 transfunc_specs.m

```
%Script containing the material and experimental parameters for a transverse simulation

ai_deg=0:0.001:2;

ai_rad=ai_deg/180*pi;

delta=2.99120929E-05; beta=2.2081831E-06
n=1-delta-i*beta

k=1

kiz=k*sin(ai_rad);                              %incident wavevector in z
ktz=k*(n^2-(cos(ai_rad)).^2).^0.5;              %transmitted wavevector in z

tth=2
    tth_rad=tth/180*pi;
af_deg=tth-ai_deg;                              %set specular condition

    af_rad=af_deg/180*pi;

kfz=k*sin(af_rad);
qz=kiz+kfz;

kix=k*cos(ai_rad);
kfx=k*cos(af_rad);

qx=kfx-kix;
```

Appendix B. MATLAB code for the numerical simulation of GIXS from periodic nanostructured surfaces

B.1 numerical_array_master.m

```
% Master script to calculate GIXS pattern from an array of elements using FFT of a numerical cross-section
% David S. Eastwood, Durham University 2009

az_deg_list=[0]                                                         %List of azimuthal angles to simulate
                                                                        %Load specifications for simulation
[d, g, N, points, ai_deg, ai_rad, qx, qz, delta, beta, k, kiz, ktz, n, const_bg,...
    resolution_width,var_res_lower, var_res_upper, I_0, I_lor_mult, I_lor_add, W]=numerical_specs();

[ac_rad, ac_deg, Rf_simple, rs, ts, Rf, Tf, S_lorentzian, geometry_factor, Ilor]...
                                =transfunc(delta, beta, k, kiz, ktz, n, qx, qz, ai_rad, ai_deg, W);
%Calculate Fresnel reflectivity

qx_plot_lower_lim=min(qx); qx_plot_upper_lim=max(qx);                   %Sets plotting range
f_interp=linspace(qx_plot_lower_lim,qx_plot_upper_lim,points);          %Interpolation range for final plot

for i=1:length(az_deg_list)                     %Simulate coherently illuminated track on sample surface
    disp(['Calculating coherently illuminated track on array at azimuthal angle = ',num2str(az_deg_list(i))])
    [sampleataz_xy_matrix(:,:,i),
sampleataz_z_matrix(:,:,i)]=prepare_circular_array(d,g,points,N,az_deg_list(i));
%[sampleataz_xy_matrix(:,:,i),sampleataz_z_matrix(:,:,i)]=prepare_eb100_array(d,g,points,N,az_deg_list(i));
%[sampleataz_xy_matrix(:,:,i),sampleataz_z_matrix(:,:,i)]=prepare_hex_array(d,g,points,N,az_deg_list(i));
end

for i=1:length(az_deg_list)                     %Calculate diffraction pattern for each azimuthal angle
    disp(['Calculating profile and Fourier transform at azimuthal angle = ',num2str(az_deg_list(i))])
    for j=1:length(sampleataz_z_matrix(1,:,i))  %Calculate FFT and diffraction pattern for each pixel line
        sampleataz_xy_matrix_j_i=sampleataz_xy_matrix(:,j,i);
        sampleataz_z_matrix_j_i=sampleataz_z_matrix(:,j,i);                     %Select pixel line
        [fraw_j_i,Pyy_j_i,Ay_j_i,xp1,xm,Xs]=fft_simple(sampleataz_xy_matrix_j_i',sampleataz_z_matrix_j_i);
                                                                                %FFT pixel line
        clear sampleataz_xy_matrix_j_i sampleataz_z_matrix_j_i                  %Clear redundant variables
        [P_i(:,j),f_i(:,j)]=fft_to_diff(Pyy_j_i,fraw_j_i);  %Flip Fourier output into a diffraction profile
        f_i(ceil(length(f_i)/2)+1,j)=mean([f_i(ceil(length(f_i)/2),j),f_i(ceil(length(f_i)/2)+2,j)]);
                                                                                %Avoid duplicate at f=0
        clear fraw_j_i Pyy_j_i Ay_j_i                                           %Clear redundant variables
    end

    disp(['Calculate total scattered intensity at azimuthal angle = ',num2str(az_deg_list(i))])
    P_sum_over_beam_width_i=sum(P_i(:,:),2);        %Sum intensity over all pixel lines in illuminated track
    [sampleataz_length,sampleataz_width,sampleataz_depth]=size(sampleataz_z_matrix); %Calculate array size
    f_beam_width_single_i=f_i(:,ceil(sampleataz_width/2));                          %Pick qx coord. list

    Ilor_interp_i=interp1(qx, Ilor, f_beam_width_single_i);
                                %Interpolate Fresnel reflectivity at points of diffraction simulation

    I_fft_lor_i=Ilor_interp_i.*P_sum_over_beam_width_i+I_lor_add*Ilor_interp_i;
                                %Multiply and add Fresnel reflectivity and diffraction simulation

    intensity_interp_i=interp1(f_beam_width_single_i, I_fft_lor_i, f_interp);
    geometry_factor_interp_i=ones(size(intensity_interp_i));   %Calculate varying beam footprint on sample

    disp(['Starting var res func at azim. ang. = ',num2str(az_deg_list(i))])
    simulated_intensity(:,i)=I_0*variable_resfunc(f_interp, intensity_interp_i, geometry_factor_interp_i,...
        var_res_lower, var_res_upper)+const_bg;
    disp(['Finished var res func at azim. ang. = ',num2str(az_deg_list(i))])
    clear Ivr_i geometry_factor_interp_i P_sum_over_beam_width_i   %Clear redundant variables
end

figure(2); hold all; plot(f_interp, simulated_intensity); set(gca, 'yscale','log')
```

B.2 numerical_specs.m

```
function [d,g,N,points,ai_deg,ai_rad,qx,qz,delta,beta,k,kiz,ktz,n,const_bg,resolution_width,var_res_lower, ...
    var_res_upper,I_0,I_lor_mult,I_lor_add,W]=numerical_specs()

    E_kev=7; lambda_nm=1.2398/E_kev; k=2*pi/lambda_nm;

    d=1320; g=830;                                  %periodicity and separation of array
    N=42;                                           %number of coherently scattering elements
    points=2^11;                                    %number of points in simulation

    delta=2.99120929E-05/4; beta=2.2081831E-06/4; %refractive index terms for Permalloy
    n=1-delta-i*beta;

    tth=2;

    ai_deg=linspace(0, tth, points);
        ai_rad=ai_deg/180*pi;

    kiz=k*sin(ai_rad);                              %incident wavevector in z
    ktz=k*(n^2-(cos(ai_rad)).^2).^0.5;              %transmitted wavevector in z

        tth_rad=tth/180*pi;
    af_deg=tth-ai_deg;                              %set specular condition
        af_rad=af_deg/180*pi;

    kfz=k*sin(af_rad);
    qz=kiz+kfz;

    kix=k*cos(ai_rad); kfx=k*cos(af_rad);
    qx=kfx-kix;

    resolution_width=0.00001;                       %an optional constant resolution width
    var_res_lower=0.0000001;                        %a minimum width for a variable resolution function
    var_res_upper=0.00025;                          %a maximum width for a variable resolution function

    const_bg=6e-11;
    I_lor_add=0.00003;                              %Lorentzian component specular reflection describing...
    I_lor_mult=1;                                   %                    ... long-range correlated roughness
    I_0=8e6;

    W=0.003                                        %Lorentzian component width
return
```

B.3 transfunc.m

```
%Function calculating Fresnel reflectivity

function [ac_rad, ac_deg, Rf_simple, rs, ts, Rf, Tf, S_lorentzian, geometry_factor, Ilor]...
                                                    =transfunc(delta, beta, k, kiz, ktz, n, qx, qz, ai_rad, ai_deg, W)

    ac_rad=sqrt(2*delta);
    ac_deg=ac_rad/pi*180;
    p_plus=sqrt(0.5*(sqrt((ai_rad.^2-ac_rad^2).^2+4*beta^2)+(ai_rad.^2-ac_rad^2)));  %real part of complex transmission angle
    p_minus=sqrt(0.5*(sqrt((ai_rad.^2-ac_rad^2).^2+4*beta^2)-(ai_rad.^2-ac_rad^2))); %imag part of complex transmission angle

    Rf_simple=((ai_rad-p_plus).^2+p_minus.^2)./((ai_rad+p_plus).^2+p_minus.^2);

    rs=(kiz-ktz)./(kiz+ktz);                         %for angles << Brewster angle, these are independent of polarisation
    ts=(2*kiz)./(kiz+ktz);

    Rf=rs.*conj(rs);
    Tf=ts.*conj(ts);

    S_prefactor=(k^2*(1-n)^2).*conj(k^2*(1-n)^2)/16*pi;
    S_lorentzian=W./(qx.^2+(W/2)^2*qz.^4);

    W_Si=0.0001; S_silicon_specular=W_Si./(qx.^2+(W_Si/2)^2*qz.^4);
    S1=S_prefactor*(S_lorentzian+0.2*S_silicon_specular); %0.05

    [geometry_factor]=geometry_calc(ai_rad);

    Ilor=S1.*Tf.*fliplr(Tf).*geometry_factor;

return
```

B.4 prepare_circular_array.m

```
%Function to calculate an the profile of an array based upon input parameters

function [sampleataz_xy_interp, sampleataz_z_interp]=prepare_circular_array(d,g,real_steps,periods,az_deg)

    az=az_deg/180*pi;
    x_range=d*periods;

    sample_plot_range_periods=8; %extent of array in optional plot
    sample_plot_range_steps=3000;

    [sample_x, sample_y, sample_z, sample_plot_range_steps]...
                    =create_circular_array(real_steps, x_range, d, periods, g, sample_plot_range_periods);
    sample_x_to_plot=sample_x(1:sample_plot_range_steps); sample_y_to_plot=sample_y(1:sample_plot_range_steps);
        sample_z_to_plot=sample_z(1:sample_plot_range_steps,1:sample_plot_range_steps);

    [sampleataz_z, sampleataz_xy, sample_z_marked, sampleataz_x, sampleataz_y]...
                    =extract_cross_section(sample_x, sample_y, sample_z, az, real_steps, periods);
    figure(1); clf; contourf(sample_x(1:1000)/1000, sample_y(1:1000)/1000, sample_z_marked(1:1000,1:1000));
        shading flat; axis equal; xlim([0 10000]/1000); ylim([0 10000]/1000); xlabel('x (\mum)'), ylabel('y (\mum)')

    [az_array_length, az_array_width]=size(sampleataz_z);

    for j=1:az_array_width
         sampleataz_xy_interp(:,j)=linspace(min(sampleataz_xy(:,j)), max(sampleataz_xy(:,j)), 2*az_array_length);
         sampleataz_z_interp(:,j)=interp1(sampleataz_xy(:,j), sampleataz_z(:,j), sampleataz_xy_interp(:,j));
    end

return
```

B.5 geometry_calc.m

```
%Function to calculate how illuminated footprint varies with angle

function [geometry_factor]=geometry_calc(ai_rad);

    source_z_slit=0.5;
    source_y_slit=0.5;
        source_beam_area=source_z_slit*source_y_slit;
    det_z_slit=0.5;
    det_y_slit=0.5;
    det_dist=1;
        det_solid_angle=det_z_slit*det_y_slit/det_dist;
    sample_x=5;
    sample_y=5;
        sample_area=sample_x*sample_y;
        geometry_factor=det_solid_angle./source_beam_area*sample_area./sin(ai_rad);
        geometry_factor(1:ceil(length(ai_rad)/30))=geometry_factor(ceil(length(ai_rad)/30))/8;

return
```

B.6 create_circular_array.m

```
%Function to extract the profile of an illuminated footprint on a regular array

function [sample_x, sample_y, sample_z, sample_plot_range_steps]...
                =create_circular_array(real_steps, x_range, d, periods, g, sample_plot_range_periods);
            element_radius=(d-g)/2;

            sample_size_steps=real_steps;
            sample_size=x_range;

            sample_x=linspace(0, sample_size, real_steps);
            sample_y=linspace(0, sample_size, real_steps);

            element_size_steps=floor(sample_size_steps/periods);
            element_size=d;

            single_element_z(element_size_steps,element_size_steps)=0;
            sample_z(ceil(sample_size_steps),ceil(sample_size_steps))=0;

            element_radius_steps=element_radius/element_size*element_size_steps;

            element_midpoint_steps=element_size_steps/2;

            for i=1:element_size_steps
                for j=1:element_size_steps
                    if element_radius_steps>sqrt((element_midpoint_steps-i)^2+(element_midpoint_steps-j)^2)
                        single_element_z(i, j)=1;
                        for n=0:periods+1
                            for m=0:periods+1
                                sample_z(n*element_size_steps+i, m*element_size_steps+j)=1;
                            end
                        end
                    else
                        single_element_z(i, j)=0;
                    end
                end
            end

            sample_plot_range_steps=sample_plot_range_periods*element_size_steps;

  return
```

B.7 fft_simple.m

```
%Function to calculate a Fast Fourier transform

function [f,Pyy, Ay, xp1, xm, Xs]=fft_simple(x, y)

    clear xp1 xm Xs

    N=length(x); %number of points
    b=1:N;       %bins

    x=x-x(1); %for routine to calculate freq increment, require first x-coordinate to be zero
    xp1=[-(x(2)),x];
    xm=[x,x(length(x))+x(2)]-xp1;
    format long
    Xs=mean(xm);

    if range (xm)>Xs
        disp('error - input interval not found')
        return
    end

    fs=1/Xs;     %sampling interval in reciprocal space

    Ay = fft(y);
    Pyy = 4 * Ay.* conj(Ay) / N^2;

    f = (b-1)/N*fs;

    clear x y
return
```

B.8 fft_to_diff.m

```
%Function to transform a FFT profile to diffraction profile

function [P,qx_fft]=fft_to_diff(Pyy,fraw);
    P=fftshift(Pyy);
    qx_fft=2*pi*fftshift(fraw);
        for i=1:floor(length(qx_fft/2))
            qx_fft(i)=-qx_fft(length(qx_fft)-i+1);
        end
return
```

B.9 extract_cross_section.m

```
%Function to extract cross-section in a certain orientation

function [sampleataz_z, sampleataz_xy, sample_z_marked, sampleataz_x, sampleataz_y]=...
                                extract_cross_section(sample_x, sample_y, sample_z, az, real_steps, periods)

    sample_z_marked=sample_z;

    i_scan_start=1;
    j_scan_start=1;

    i=i_scan_start;
    j=j_scan_start; %set initial values of the data selection indices from the array sample_z

    size_x=max(size(sample_x));
    size_y=max(size(sample_y));
    element_size_steps=floor(real_steps/periods);

    for h=1:element_size_steps

        k=1;

            while (k<real_steps+1);
                    sampleataz_z(k,h)=sample_z(i,j);
                    sampleataz_x(k,h)=sample_x(j);
                    sampleataz_y(k,h)=sample_y(i);

                    sample_z_marked(i,j)=sample_z_marked(i,j)+1.5; %mark the selected beam footprint on a copy of the array

                    sampleataz_xy(k,h)=sqrt(sample_x(i)*sample_x(i)+sample_y(j)*sample_y(j));

                    if atan((j-j_scan_start+1)/(i-i_scan_start+1))<az
                        j=j+1;
                    else
                        i=i+1;
                    end

                    k=k+1;
            end

            if az>pi/4 %choose whether to go upwards or along from bottom corner of array, ...
                            %...in order to ensure profile width covers all periodicities
                    i_scan_start=i_scan_start+1;
                    i=i_scan_start;
                    j=1;
            else
                    j_scan_start=j_scan_start+1;
                    j=j_scan_start;
                    i=1;
            end

    end

return
```

B.10 variable_resfunc.m

```
%Function to calculate a variable resolution function

function [Ivr]=variable_resfunc(qx_interp, Iscatt, geometry_factor, var_res_lower, var_res_upper)
    clear ra                                                        %clear any previous resolution matrix
    array_size=length(qx_interp);                                   %calculate size needed for resolution matrix
    resolution_width=linspace(var_res_lower,var_res_upper, array_size);   %calculate variation of resolution width with qx
    qxsq=transpose(qx_interp.^2); rwsq=transpose(resolution_width.^2);    %calculate terms in Gaussian resolution function
    ra=zeros(array_size, array_size);                               %create n empty resolution matris=x
    for i=1:array_size
        ra(:,i)=exp(-(transpose((qx_interp+qx_interp(i)).^2)/rwsq(i))).*resolution_width';   %calculate variable resolution matrix
    end

    for i=1:length(Iscatt); if isnan(Iscatt(i))==1; Iscatt(i)=0; end; end %remove any not-a-number values
    Ivr=ra*Iscatt'.*geometry_factor';                               %multiple diffraction output by variable resolution matrix
return
```

Appendix C. FORTRAN code for generating randomised arrays with Raith electron beam lithography systems

```
program ebdesrand
!
! Fortran program to write array coordinates to file for Raith Lithograhy system
! David Eastwood, University of Durham, 15 January 2006
!
implicit none
real::radius_x, radius_y, periodicity_x, periodicity_y
integer:: array_x, array_y!, circsteps
integer::i, j!, k
real::x_coord, y_coord
!real::pi
real::rand_displacement_fwhm

real::rand_displacement, rand_angle
real::rand_displacement_value, rand_angle_value

!pi=4.0*atan(1.0)

radius_x=0.3
radius_y=0.2
periodicity_x=0.75
periodicity_y=3
array_x=800
array_y=200
!circsteps=24

rand_displacement_fwhm=0.1

write(*,*)''
write(*,*)'------------------------------------------------------------'
write(*,*)'Large rectangle array writer for Raith Lithograhy System'
write(*,*)'              David Eastwood 16 January 2006'
write(*,*)'------------------------------------------------------------'
write(*,*)''
write(*,*)'radius_x = ',radius_x,' microns'
write(*,*)'radius_y = ',radius_y,' microns'
write(*,*)'periodicity_x = ',periodicity_x, ' microns'
write(*,*)'periodicity_y = ',periodicity_y, ' microns'

write(*,*)'periods in x = ', array_x
write(*,*)'periods in y = ', array_y
!write(*,'(A47,I3)')' number of steps around element circumference = ', circsteps
write(*,*)'randomness', rand_displacement_fwhm



open(8,file='ebdesrand_fout_w03h02_p075-3_800-200.asc')
open(9,file='ebdesrand_fout__w03h02_p075-3_800-200dataonly.asc')
open(11, file='ebdesrand_fout_w03h02_p075-3_800-200_disponly.asc')
open(12, file='ebdesrand_fout_w03h02_p075-3_800-200_angonly.asc')

37 format(A7)
38 format(F8.4,A1,F8.4)
39 format(A1)
40 format(F8.4)

write(*,*)''
write(*,*)'Calculating coordinates and writing to file...'

do i=1, array_x, 1
        do j=1, array_y, 1
                write(8,37)'1 100 0'

                                rand_displacement_value=rand_displacement(rand_displacement_fwhm)
                                rand_angle_value=rand_angle()

  !                     write(11, 40)rand_displacement_value
  !                     write(12, 40)rand_angle_value

                !do k=1, circsteps, 1


                        x_coord=real(i)*periodicity_x+rand_displacement_value*sin(rand_angle_value)

                                        !+sin(real(k)/real(circsteps)*2.0*pi)*radius_x
                        y_coord=real(j)*periodicity_y+rand_displacement_value*cos(rand_angle_value)
                                        !+cos(real(k)/real(circsteps)*2.0*pi)*radius_y

                        write(8,38)x_coord,' ', y_coord
                                write(9,38)x_coord,' ', y_coord

                        x_coord=real(i)*periodicity_x+rand_displacement_value*sin(rand_angle_value)&
                                                +radius_x
                                y_coord=real(j)*periodicity_y+rand_displacement_value*cos(rand_angle_value)

                                        !+cos(real(k)/real(circsteps)*2.0*pi)*radius_y
                        write(8,38)x_coord,' ', y_coord
                                write(9,38)x_coord,' ', y_coord

                          x_coord=real(i)*periodicity_x+rand_displacement_value*sin(rand_angle_value)&
                                                +radius_x
                                y_coord=real(j)*periodicity_y+rand_displacement_value*cos(rand_angle_value)&
                                                +radius_y
                                        !+cos(real(k)/real(circsteps)*2.0*pi)*radius_y
                        write(8,38)x_coord,' ', y_coord
                                write(9,38)x_coord,' ', y_coord
```

```
                        x_coord=real(i)*periodicity_x+rand_displacement_value*sin(rand_angle_value)
                                y_coord=real(j)*periodicity_y+rand_displacement_value*cos(rand_angle_value)&
                                        +radius_y
                                    !+cos(real(k)/real(circsteps)*2.0*pi)*radius_y
                          write(8,38)x_coord,' ', y_coord
                                write(9,38)x_coord,' ', y_coord

                    !end do

                    write(8,39)'#'
            end do
end do

close(8)
close(9)
close(11)
close(12)

write(*,*)'...complete'

stop
end program ebdesrand


function rand_displacement(rand_displacement_fwhm)
! function to calculate a random displacement with gaussian distribution with input FWHM

implicit none
real::x, rand_displacement, pi
real, intent(in)::rand_displacement_fwhm

pi=4.0*atan(1.0)

call random_number(x)
rand_displacement=0!rand_displacement_fwhm/log(2.0)*sqrt(log(1.0/x))  !1.0-erf(1.2*x)
return

end function rand_displacement

function rand_angle()
! function to calculate a random angle over the range zero to two pi

implicit none
real::rand_angle, y
real::pi

pi=4.0*atan(1.0)

!call random_seed
call random_number(y)
rand_angle=y*2.0*pi

return

end function rand_angle
```